



12-2013

## **Fundamental Studies of Single Crystal Alpha Alumina Microstructures Produced by Irradiation with Zirconium Ions**

Younes Sina

*University of Tennessee - Knoxville, ysina@utk.edu*

Follow this and additional works at: [https://trace.tennessee.edu/utk\\_graddiss](https://trace.tennessee.edu/utk_graddiss)

 Part of the [Materials Science and Engineering Commons](#)

---

### **Recommended Citation**

Sina, Younes, "Fundamental Studies of Single Crystal Alpha Alumina Microstructures Produced by Irradiation with Zirconium Ions. " PhD diss., University of Tennessee, 2013.  
[https://trace.tennessee.edu/utk\\_graddiss/2616](https://trace.tennessee.edu/utk_graddiss/2616)

This Dissertation is brought to you for free and open access by the Graduate School at TRACE: Tennessee Research and Creative Exchange. It has been accepted for inclusion in Doctoral Dissertations by an authorized administrator of TRACE: Tennessee Research and Creative Exchange. For more information, please contact [trace@utk.edu](mailto:trace@utk.edu).

To the Graduate Council:

I am submitting herewith a dissertation written by Younes Sina entitled "Fundamental Studies of Single Crystal Alpha Alumina Microstructures Produced by Irradiation with Zirconium Ions." I have examined the final electronic copy of this dissertation for form and content and recommend that it be accepted in partial fulfillment of the requirements for the degree of Doctor of Philosophy, with a major in Materials Science and Engineering.

Carl J. McHargue, Major Professor

We have read this dissertation and recommend its acceptance:

Kurt E. Sickafus, William J. Weber, Ali Passian, Claudia Rawn

Accepted for the Council:

Carolyn R. Hodges

Vice Provost and Dean of the Graduate School

(Original signatures are on file with official student records.)

**Fundamental Studies of Single Crystal Alpha Alumina Microstructures**

**Produced by Irradiation with Zirconium Ions**

A Dissertation Presented for the

Doctor of Philosophy

Degree

The University of Tennessee, Knoxville

Younes Sina

December 2013

Copyright © 2013 by Younes Sina

All rights reserved.



**Dedication**

This dissertation is dedicated to my dear wife and daughter Minoo and Media with love and appreciation, and to my mother, brothers and sisters, and to the memory of my father.

## **Acknowledgements**

I thank to my advisor, Professor Carl J. McHargue, for his guidance, valuable suggestions, and insights regarding the ideas presented in the dissertation also for financially supporting me. My sincere gratitude is due to my co-adviser professor Kurt E. Sickafus, Materials Science and Engineering (MSE) Professor and department head, my advisory committee member Dr. William J. Weber, MSE Professor and Governor's Chair and director of ion beam materials laboratory (IBML) at UTK for assisting me and for many good discussions and suggestions.

Many thanks for Dr. Claudia J. Rawn Assistant Professor in MSE Department and Director of Center for Materials Processing (CMP), researcher at Materials Science & Technology Division Oak Ridge National Laboratory; Dr. Ali Passian researcher and development staff at Measurement Science and Systems Engineering (MSSE), Oak Ridge National Laboratory and Adjunct Professor at the Department of Physics, University of Tennessee (UTK), Knoxville, for their support and accepting the responsibility to be on my advisory committee.

I also thank to Dr. Yanwen Zhang, Associate Professor at MSE department and deputy director of IBML at UTK and all the other IBML facility manager and staffs.

I am particularly grateful to Dr. Eduardo Alves Professor at Instituto Superior Técnico (IST)/Instituto Tecnológico e Nuclear (ITN), Portugal and Manabu Ishimaru MSE Professor at Kyushu Institute of Technology (KIT), Fukuoka, Japan for their support.

I am thankful to Dr. Charles L. Melcher Research Professor and Director of Scintillation Materials Research Center (SMRC) at UTK, Dr. Marry Koschan Research Associate III at SMRC and Mohit Tyagi post-doctoral research associate at SMRC, for helping me to optically analyze and anneal my samples.

I appreciate Dr. Peter D. Townsend Professor in university of Sussex, UK for advising me for the results of optical absorption and photoluminescence and related calculations.

I also acknowledge Dr. Gerd Duscher ORNL/UTK joint faculty in the scanning transmission electron microscopy (STEM) group (Materials Science & Technology Division Oak Ridge National Laboratory) for help to analyze one of my samples, Dr. Claudia Cantoni from Superconductive & Energy Efficient Materials Group of Materials Science & Technology Division in Oak Ridge National Laboratory for her help with the EELS spectra and Claudiu Muntele from Center for Irradiation of Materials in Department of Physics of A&M University of Alabama.

## Abstract

This research has discovered the following new information:

- a) The threshold fluence for amorphization of single crystal  $\alpha$ -Al<sub>2</sub>O<sub>3</sub> [alpha alumina] samples irradiated with 175 keV Zr<sup>+</sup> [Zr+] ions at room temperature is  $1.5 \times 10^{16}$  [1.5E16] Zr/cm<sup>2</sup> [Zr+/cm2] which is a much lower fluence than the previously thought.
- b) A buried amorphous layer sandwiched between two highly-damaged crystalline regions was observed in samples irradiated with 175 keV Zr<sup>+</sup> to a fluence of  $1.5 \times 10^{16}$  Zr<sup>+</sup>/cm<sup>2</sup> and higher at room temperature. The amorphous region contains short range order similar to  $\gamma$ -Al<sub>2</sub>O<sub>3</sub> [gamma alumina]; it is deficient in oxygen containing Zr-rich nano-clusters.
- c) Ion-beam induced epitaxial recrystallization occurred at room temperature due to oxygen irradiation of the amorphous phase. It is the first observation at low temperature.
- d) Irradiation of Zr-implanted  $\alpha$ -Al<sub>2</sub>O<sub>3</sub> [alpha alumina] samples with oxygen decreased the F-type centers concentrations.
- e) Post irradiation thermal annealing of Zr-implanted  $\alpha$ -Al<sub>2</sub>O<sub>3</sub> samples induced amorphous to  $\gamma$ -Al<sub>2</sub>O<sub>3</sub> transformation at the interface between amorphous and damaged regions.

## Preface

The threshold fluence for amorphization of sapphire due to ion irradiation with zirconium shows an anomaly compared to other ions with atomic weights similar to zirconium. Comparing zirconium ( $Z=40$ ,  $M=91$ ), to niobium ( $Z=41$ ,  $M=93$ ) an amorphous structure is produced by irradiation to threshold fluences of  $\phi \approx 1.5 \times 10^{16}$   $\text{Zr}^+/\text{cm}^2$  and  $>5 \times 10^{16}$   $\text{Nb}^+/\text{cm}^2$ , for Zr and Nb, respectively (irradiation at room temperature). In other words,  $\text{Al}_2\text{O}_3$  is more than twice as susceptible to irradiation-induced amorphization by Zr compared to irradiation with ions of other elements with masses similar to Zr. In case of  $\alpha\text{-Al}_2\text{O}_3$  irradiated with  $\text{Zr}^+$  ions, energy deposited by nuclear processes (elastic collisions) is not totally responsible for producing the amorphous structure. A chemical effect may be responsible for the “Zr anomaly”. This study describes  $\alpha\text{-Al}_2\text{O}_3$  microstructures produced by  $\text{Zr}^+$  ions irradiation. For this purpose five selected highlighted results are presented on the effect of Zr irradiation as well as Zr plus O irradiation on microstructure of single crystal  $\alpha\text{-Al}_2\text{O}_3$ .

First, the threshold fluence for amorphization of 175 keV Zr ions for amorphization of  $\alpha\text{-Al}_2\text{O}_3$  is investigated using transmission electron microscopy (TEM), and Rutherford backscattering techniques. Then displacement damage dose in units of dpa as well as Zr concentration in unit of atomic % is discussed for the interface between amorphous region and two surrounding highly damaged crystalline  $\text{Al}_2\text{O}_3$ . This study relies on results of scanning transmission electron microscopy (STEM) and TEM examination of  $\alpha\text{-Al}_2\text{O}_3$  samples irradiated with 175 keV to fluences of  $1.5 \times 10^{16}$   $\text{Zr}^+/\text{cm}^2$ ,  $2 \times 10^{16}$   $\text{Zr}^+/\text{cm}^2$ , and  $4 \times 10^{16}$   $\text{Zr}^+/\text{cm}^2$ . Electron energy loss spectroscopy (EELS)

measurement is used to obtain important information for the sample irradiated with 175 keV  $\text{Zr}^+$  to a fluence of  $4 \times 10^{16} \text{ Zr}^+/\text{cm}^2$ .

Post implantation process study is one of the most important studies to understand the effect of impurities on microstructure of host materials. In this study microstructure of  $\alpha\text{-Al}_2\text{O}_3$  samples irradiated with 175 keV to fluences of  $1.5 \times 10^{16} \text{ Zr}^+/\text{cm}^2$  and  $2 \times 10^{16} \text{ Zr}^+/\text{cm}^2$  followed by irradiation of 48 and 55 keV oxygen to different fluences are investigated. Although there have been many thermal annealing studies of materials irradiated with different ions, there are few reports of post irradiation with another ion implanted sample. This work is the first report of ion beam-induced epitaxial recrystallization (IBIER) in  $\text{Al}_2\text{O}_3$  at room temperature. The result of nano-beam electron diffraction (NBED) patterns obtained from different regions of  $\alpha\text{-Al}_2\text{O}_3$  sample irradiated to a fluence of  $1.5 \times 10^{16} \text{ Zr}^+/\text{cm}^2$  plus 55 keV  $\text{O}^+$  ions to a fluence of  $2.3 \times 10^{16} \text{ O}^+/\text{cm}^2$ , indicate the presence of a phase that is not  $\alpha\text{-Al}_2\text{O}_3$ . Indexing the individual reflections reveals that two phases of  $\alpha\text{-Al}_2\text{O}_3$  and  $\gamma\text{-Al}_2\text{O}_3$  are present. They are arranged with a special crystallographic relationship.

The effect of Zr fluences and the effect of post implantation oxygen ions into pre-Zr-implanted samples were also investigated by photoluminescence (PL) and optical absorption (OA). The presence of both F and  $\text{F}^+$  centers were confirmed by PL and OA measurements. The OA spectra showed that the concentration of F and  $\text{F}^+$ -centers increases with increasing of Zr fluences. OA results showed that post irradiation of oxygen into pre-Zr-implanted samples reduces the concentration of both F-type centers. The reducing of the concentration of these color centers is ascribed to IBIER.

Over the last forty years, the kinetics of phase transformations in alumina and the effects of impurities have been studied. Most of these kinetics studies have used techniques such as X-ray diffraction (XRD), differential thermal analysis (DTA) thermogravimetric analysis (TGA), and time resolved reflectivity (TRR). These techniques are not able to differentiate the nucleation and growth stages of the transformation. Most researchers have used alumina powders mixed with selected impurities and report a variety of activation energies. In the majority of these studies, only the kinetics of  $\gamma \rightarrow \alpha$  transformation has been studied. A few studies discuss the effect of doping on the kinetics of transition from amorphous to crystalline aluminum oxides, using non powder alumina. Amorphizing single crystal sapphire samples by ion irradiation at low temperatures or with certain ions at room temperature are among the techniques that can be used as techniques to investigate the growth stage in absence of a nucleation stage. Another technique is to prepare a thin film of amorphous alumina on a sapphire substrate using electron-beam evaporation of alumina containing the appropriate dopants or co-evaporation of the high purity metal with a second e-beam gun. The technique used in the current work is based on irradiation of  $\alpha\text{-Al}_2\text{O}_3$  with  $\text{Zr}^+$  ions at room temperature. This technique provides a thin amorphized film sandwiched between two crystalline regions. The sample can be annealed in order to study the phase transformation in the absence of a nucleation stage. The amorphous region forms a new phase ( $\gamma$ ) by solid-phase epitaxial growth from an underlying planar crystalline substrate during annealing. In this study three different post-irradiation annealing temperatures 800, 900, and 1000 °C, and different residence times were used. Under ion irradiation

conditions, the energetic particles travel through the material, and store a significant amount of energy in the subsurface region in the form of stress. The stored stresses which act as a thermodynamic driving force tends to be relaxed during irradiation or during the thermal annealing process. The related difficulties associated with kinetics study are discussed due to this fact that in the presence of irradiation, thermodynamical concepts cannot be directly applied for the materials. Transmission electron microscopy (TEM), electron energy loss spectroscopy (EELS), and Rutherford backscattering spectrometry with ion channeling (RBS-C) are the major characterization methods employed in this part of the study.

Another phase of this work is the study of annealing after dual irradiation. Samples were irradiated with  $\text{Zr}^+$  ions to a fluence of  $2 \times 10^{16} \text{ Zr}^+/\text{cm}^2$  followed by 48 keV  $\text{O}^+$  ions to a fluence of  $3 \times 10^{16} \text{ O}^+/\text{cm}^2$  and annealed at 800, 900, and 1000 °C. The TEM bright-field (BF) images and RBS-C results reveal interesting details about the microstructure of defected  $\alpha\text{-Al}_2\text{O}_3$ . Stopping and range of ions in matters (SRIM-2013) is used throughout this research to calculate many features of Zr and O ions transport in  $\alpha\text{-Al}_2\text{O}_3$ .



## Table of Contents

Chapter 1 .....	1
Introduction and General Information .....	1
1.1 Single crystal of $\alpha$ -alumina (sapphire) .....	1
1.2 Applications of alumina .....	2
1.2.1 Use in Jewelry Industry .....	3
1.2.2 Use in Engineering .....	3
1.2.3 Use in Optics .....	5
1.2.4 Use in Medicine .....	6
1.3 Structure and properties .....	7
1.4 Metastable alumina polymorphs .....	11
1.4.1 $\gamma$ - $\text{Al}_2\text{O}_3$ .....	15
1.5 Solid phase epitaxial growth (SPEG) .....	16
1.6 Crystal growth kinetics .....	18
1.7 Methods to produce metastable $\text{Al}_2\text{O}_3$ and amorphous alumina .....	20
1.7.1 Vapor deposition techniques .....	20
1.7.2 Alumina melt .....	21
1.7.3 Amorphous anodic $\text{Al}_2\text{O}_3$ films .....	22
1.7.4 Thermal oxidation of aluminum .....	23
1.7.5 Other precursors for metastable aluminas and the sequence of transformation .....	23
1.8 Ion Implantation .....	24
1.9 Ion implantation-induced amorphization .....	28
1.10 Statement of the problem and background of the study .....	29
1.10.1 Importance of microstructure study of $\alpha$ - $\text{Al}_2\text{O}_3$ during ion irradiation and kinetics study of alumina transformation .....	30
1.10.2 Effects of dopants in $\alpha$ - $\text{Al}_2\text{O}_3$ on kinetics of alumina transformation .....	35
1.10.3 Objective of this Study .....	39
Chapter 2 .....	41
Literature Review .....	41
2.1 Ion-beam induced amorphization in sapphire .....	41
2.2 Single crystalline $\alpha$ - $\text{Al}_2\text{O}_3$ irradiation with Zr .....	48
2.3 Effect of post ion irradiation on a pre-ion-implanted $\alpha$ - $\text{Al}_2\text{O}_3$ .....	50
2.4 Effect of annealing .....	53
2.4.1 Annealing of $\alpha$ - $\text{Al}_2\text{O}_3$ irradiated with iron followed by oxygen .....	54
2.4.2 Annealing of pre-amorphized $\text{Al}_2\text{O}_3$ produced by ion-beam irradiation .....	55
2.4.3 Annealing of zirconium implanted sapphire .....	58
2.5 Doping effects on the kinetics of solid-phase epitaxial growth of amorphous $\rightarrow \gamma \rightarrow \alpha$ -alumina .....	58

2.6 Phase transformation under irradiation .....	64
2.7 Ion beam induced recrystallization in $\alpha$ -Al <sub>2</sub> O <sub>3</sub> .....	68
Chapter 3 .....	71
Materials and methods .....	71
3.1 Ion irradiation condition .....	71
3.1.1 Sample preparation for irradiation .....	72
3.2 Rutherford backscattering spectrometry (RBS).....	75
3.2.1 Basic concept of Rutherford backscattering spectroscopy .....	75
3.2.2 Samples characterization using Rutherford backscattering spectroscopy .....	78
3.3 Transmission electron microscopy (TEM) .....	80
3.3.1 Sample Preparation for TEM .....	82
3.3.2 Samples characterization using STEM/TEM.....	86
3.4 Electron energy loss spectroscopy (EELS).....	88
3.5 Optical measurements .....	89
3.5.1 Ultraviolet and visible (UV-Vis) absorption spectroscopy.....	90
3.5.2 Photoluminescence .....	90
3.6 Thermal annealing .....	91
3.7 Arrhenius equation.....	94
3.8 Cross-cut technique.....	94
3.10 SRIM calculations.....	96
3.9.1 The SRIM calculated results .....	97
Chapter 4.....	103
Results and discussion .....	103
4.1 The effect of zirconium irradiation on the structure of sapphire and threshold fluence for amorphization .....	103
4.2 A study of the amorphous $\rightarrow \gamma \rightarrow \alpha$ transformation in Zr-irradiated $\alpha$ -alumina..	133
4.3 Ion-beam induced epitaxially recrystallization (IBIER) in $\alpha$ -Al <sub>2</sub> O <sub>3</sub> , due to oxygen irradiation effect on Zr-implanted $\alpha$ -Al <sub>2</sub> O <sub>3</sub> .....	161
4.4 Optical study of Zr-implanted $\alpha$ -Al <sub>2</sub> O <sub>3</sub> samples followed by oxygen irradiation.	175
4.5 Dual effect of oxygen irradiation and thermal annealing on Zr-implanted $\alpha$ -Al <sub>2</sub> O <sub>3</sub> .....	184
Chapter 5.....	203
Conclusions and recommendation .....	203
5.1 Conclusions.....	203
5.2 Recommendation .....	206
List of References .....	208
Vita.....	227

## List of Tables

Table 1 Common processing routes for producing different $\text{Al}_2\text{O}_3$ polymorphs and the sequences of phase transformations toward $\alpha\text{-Al}_2\text{O}_3$ with approximate hcp and fcc packing of oxygen for the metastable $\text{Al}_2\text{O}_3$ structures .....	12
Table 2 Structure and properties of alumina polymorphs.....	14
Table 3 Summary of studies about the effect of dopants in alumina phase transformation .....	32
Table 4 Summary of growth kinetics studies results .....	37
Table 5 Summary of ion irradiation studies in sapphire .....	45
Table 6 Summary of samples irradiation conditions .....	74
Table 7 Thermal annealing conditions for Zr irradiated samples .....	93
Table 8 Thermal annealing conditions for Zr plus O irradiated samples .....	93
Table 9 Summary information obtained from STEM/TEM and calculated SRIM results regarding the interface between highly damaged and amorphous regions for all the studied samples. ....	132
Table 10 The absorption and emission bands associated with specific lattice defects in single crystals $\alpha\text{-Al}_2\text{O}_3$ .....	176
Table 11 True absorption coefficient of the induced bands.....	182
Table 12 The concentration of F-type centres estimated by Smakula's equation .....	183

## List of Figures

Figure 1 Optical transmission spectrum of a 3 mm thick sapphire crystal of thickness 3 mm .	5
Figure 2 Arrangement of aluminum and oxygen in a three dimension ball-and-stick model from visualization for electronic and structural analysis (VESTA).....	9
Figure 3 Distribution of aluminum ions and holes on the simple hexagonal lattice.....	10
Figure 4 The atomic processes during crystal growth, Solute molecules enter kinks either directly from solution or after adsorbing and diffusing across terraces.....	19
Figure 5 Selected literature data on the growth temperatures of different $\text{Al}_2\text{O}_3$ polymorphs using various vapor deposition techniques .....	21
Figure 6 Effect of atomic mass of ions on the range. Calculated with full damage cascade SRIM-2013. ....	26
Figure 7 The variation of the electronic and nuclear stopping power of zirconium into sapphire as a function of Zr ion energy .....	27
Figure 8 Minimum yield for Al-sublattice ( $\chi_{\text{Al}}$ ) as a function of displacement damage dose (in units of dpa) for different ions calculated based on information on .....	44
Figure 9 Phase diagram of $\text{ZrO}_2\text{-Al}_2\text{O}_3$ .....	52
Figure 10 Schematic illustration of the evolution during ion irradiation of a solid target processes. The grey shaded processes correspond to long term effects. ....	54
Figure 11 Annealing effect in Fe-implanted sapphire a) annealing in air b) annealing in Ar-4% $\text{H}_2$ atmosphere.....	56
Figure 12 Schematic representation of behavior observed during annealing of an amorphous film .....	62
Figure 13 A schematic diagram showing a film under residual compressive stress .....	66
Figure 14 Schematic diagram of the semi-coherent interface between two different phases of alumina .....	67
Figure 15 The 210 kV Ion implanter has a chamber allowing the implantation of an area of $20 \times 20 \text{ cm}^2$ . It is possible to carry on implantation samples in the temperatures range of 77 K up to 1273 K, in a controlled way.....	72
Figure 16 beam control panel for the irradiation of samples .....	73
Figure 17 Schematic representation of the experimental setup for Rutherford backscattering analysis.....	76
Figure 18 Components of energy loss for an ion beam that scatters from depth t. First, incident beam loses energy through interaction with electrons $\Delta E_{\text{in}}$ . Then energy lost occurs due to scattering $E_c$ . Finally outgoing beam loses energy for interaction with electrons $\Delta E_{\text{out}}$ .....	78
Figure 19 Geometry of the chamber with three detectors at different angles.....	79
Figure 20 A 2.5 MV Van de Graaff accelerator with three experimental beam lines, with all the relevant ion beam techniques available: RBS, PIXE, NRA, Channeling, ERDA and NRB with (p, g)......	80
Figure 21 The Ion Beam Materials Laboratory (IBML) at the University of Tennessee, Knoxville (UTK).....	81

Figure 22 Diagram of a multilayer sample prepared using the sandwich technique for tripod thinning.....	83
Figure 23 A thined Zr-irradiated sapphire sample under optical microscope that was made by sandwich technique using tripod thinning .....	84
Figure 24 Mechanical polishing process for one of the Zr-irradiated sapphire samples using Allied multyprep system polisher at the joint institute for advanced materials (JIAM) at UTK .....	85
Figure 25 Ion milling process for one of the Zr-irradiated sapphire samples using Gatan model 691 at the Joint Institute for Advanced Materials (JIAM) at UTK.....	86
Figure 26 Working on the samples with scanning transmission electron microscope (STEM) at the scanning transmission electron microscopy (STEM) group (Materials Science & Technology Division Oak Ridge National Laboratory) .....	87
Figure 27 A typical EELS spectrum with the different parts indicated.....	89
Figure 28 Cross-cut procedure from isothermal annealing curves to determine the activation energy .....	95
Figure 29 SRIM calculated range and displacement damage dose (in units of dpa) dpa versus target depth for $\text{Al}_2\text{O}_3$ irradiated with 175 keV $\text{Zr}^+$ ions to a fluence of $7.5 \times 10^{15} \text{ Zr}^+/\text{cm}^2$ , followed by irradiation with 55 keV $\text{O}^+$ ions to a fluence of and $1.1 \times 10^{15} \text{ O}^+/\text{cm}^2$ .....	97
Figure 30 SRIM calculated range and displacement damage dose (in units of dpa) dpa versus target depth for $\text{Al}_2\text{O}_3$ irradiated with 175 keV $\text{Zr}^+$ ions to a fluence of $1.5 \times 10^{16} \text{ Zr}^+/\text{cm}^2$ , followed by irradiation with 55 keV $\text{O}^+$ ions to a fluence of and $2.3 \times 10^{16} \text{ O}^+/\text{cm}^2$ .....	98
Figure 31 Range and concentration profile of 175 keV $\text{Zr}^+$ ions to a fluence of $2 \times 10^{16} \text{ Zr}^+/\text{cm}^2$ during implantation into sapphire .....	99
Figure 32 Range and concentration profile of 175 keV $\text{Zr}^+$ ions to a fluence of $4 \times 10^{16} \text{ Zr}^+/\text{cm}^2$ during implantation into sapphire .....	100
Figure 33 Nuclear and electronic energy loss for 175 keV $\text{Zr}^+$ ions into sapphire.....	101
Figure 34 SRIM calculated nuclear and electronic energy loss for $\text{Al}_2\text{O}_3$ irradiated with 55 keV $\text{O}^+$ ions, after the formation of buried amorphous layer due to prior "high dose" irradiation with $\text{Zr}^+$ ions.....	102
Figure 35 RBS-C spectra obtained from $\alpha\text{-Al}_2\text{O}_3$ sample irradiated with $2 \times 10^{15} \text{ Zr}^+/\text{cm}^2$ . This is "low- dose" sample in the sense that the Zr displacement damage dose is less than the threshold dose for amorphization. Arrows labeled "Zr", "Al", and "O", indicate the surface elastic scattering energies for Zr, Al, and O atoms respectively. Scattering angle of $165^\circ$ was used for this measurement. ....	104
Figure 36 RBS-C spectra obtained from $\alpha\text{-Al}_2\text{O}_3$ sample irradiated with $2 \times 10^{15} \text{ Zr}^+/\text{cm}^2$ . This is "low- dose" sample in the sense that the Zr displacement damage dose is less than the threshold dose for amorphization. Arrows labeled "Zr", "Al", and "O", indicate the surface elastic scattering energies for Zr, Al, and O atoms respectively. Scattering angle of $165^\circ$ was used for this measurement. ....	105
Figure 37 (a) TEM cross section image and (b) Selected area electron diffraction (SAED) patterns obtained from $\alpha\text{-Al}_2\text{O}_3$ sample irradiated with $7.5 \times 10^{15} \text{ Zr}^+/\text{cm}^2$ . This is	

“low- dose” sample in the sense that the Zr displacement damage dose is less than the threshold dose for amorphization.....	106
Figure 38 RBS-C spectra obtained from $\alpha$ -Al <sub>2</sub> O <sub>3</sub> sample irradiated with $1.5 \times 10^{16}$ Zr <sup>+</sup> /cm <sup>2</sup> . This is “high dose” sample in the sense that the Zr displacement damage dose is in excess of the threshold dose for amorphization. Arrows labeled “Zr”, “Al”, and “O”, indicate the surface elastic scattering energies for Zr, Al, and O atoms respectively. Scattering angle of 165 ° was used for this measurement. ....	108
Figure 39 TEM cross section image obtained from $\alpha$ -Al <sub>2</sub> O <sub>3</sub> sample irradiated with $1.5 \times 10^{16}$ Zr <sup>+</sup> /cm <sup>2</sup> . This is “high dose” sample in the sense that the Zr displacement damage dose is in excess of the threshold dose for amorphization. ....	109
Figure 40 RBS-C spectra obtained from $\alpha$ -Al <sub>2</sub> O <sub>3</sub> sample irradiated with $2 \times 10^{16}$ Zr <sup>+</sup> /cm <sup>2</sup> . This is “high dose” sample in the sense that the Zr displacement damage dose is in excess of the threshold dose for amorphization. Arrows labeled “Zr”, “Al”, and “O”, indicate the surface elastic scattering energies for Zr, Al, and O atoms respectively. Scattering angle of 170 ° was used for this measurement. ....	110
Figure 41 TEM cross section image obtained from $\alpha$ -Al <sub>2</sub> O <sub>3</sub> sample irradiated with $2 \times 10^{16}$ Zr <sup>+</sup> /cm <sup>2</sup> . This is “high dose” sample in the sense that the Zr displacement damage dose is in excess of the threshold dose for amorphization.....	111
Figure 42 RBS-C spectra obtained from $\alpha$ -Al <sub>2</sub> O <sub>3</sub> sample irradiated with $2 \times 10^{16}$ Zr <sup>+</sup> /cm <sup>2</sup> . This is “high dose” sample in the sense that the Zr displacement damage dose is in excess of the threshold dose for amorphization. Arrows labeled “Zr”, “Al”, and “O”, indicate the surface elastic scattering energies for Zr, Al, and O atoms respectively. ....	112
Figure 43 High angle annular dark field cross section image of $\alpha$ -Al <sub>2</sub> O <sub>3</sub> implanted with Zr ions .....	114
Figure 44 High angle annular dark field (HAADF) cross section image of $\alpha$ -Al <sub>2</sub> O <sub>3</sub> irradiated with Zr ions from amorphous region shows nearly spherical Zr-rich clusters .....	115
Figure 45 (a) High angle annular dark field, (b) bright field, (c–e) bright field, and (f–h) fast Fourier transform (FFT) from the three regions of zirconium implanted-sapphire. ....	117
Figure 46 EELS Al-L spectra from (a) bulk region, (b) near surface damaged and deeper damaged regions, and (c) amorphous region .....	119
Figure 47 The results of MS calculations for the Al L <sub>2,3</sub> -ELNES of: (a) tetrahedral AlO <sub>4</sub> with Al–O distances equal to 0.17 nm and (b) octahedral AlO <sub>6</sub> with Al–O distances equal to 0.19 nm [212]. ....	120
Figure 48 Al L <sub>2,3</sub> -EELS spectra for different regions of the $\alpha$ -Al <sub>2</sub> O <sub>3</sub> sample irradiated with 175 keV Zr <sup>+</sup> ions to a fluence of $4 \times 10^{16}$ Zr/cm <sup>2</sup> : the $\alpha$ -Al <sub>2</sub> O <sub>3</sub> edge is rounder and shifted to a lower energy like (purple spectrum). ....	121
Figure 49 Electron energy loss spectroscopy (EELS) oxygen-K edge obtained from sample of $\alpha$ -Al <sub>2</sub> O <sub>3</sub> irradiated with 175 keV Zr ions to a fluence of $4 \times 10^{16}$ Zr/cm <sup>2</sup> at room temperature. (a) spectrum from subsurface and deeper damaged regions (b) spectrum from the amorphous region .....	123

- Figure 50 TEM cross section image and SAED patterns obtained from  $\alpha$ -Al<sub>2</sub>O<sub>3</sub> samples irradiated with  $7.5 \times 10^{15}$  Zr<sup>+</sup>/cm<sup>2</sup>. These are “low- dose” samples in the sense that the Zr displacement damage dose is less than the threshold dose for amorphization. Also shown are SRIM calculated profiles for the Zr displacement damage dose (in units of dpa) as a function of target sample depth and the implanted Zr concentration versus depth. .... 126
- Figure 51 TEM bright-field (BF) image obtained from cross-sectional samples of  $\alpha$ -Al<sub>2</sub>O<sub>3</sub> irradiated with  $1.5 \times 10^{16}$  Zr<sup>+</sup>/cm<sup>2</sup>. Also shown are SRIM calculated profiles for the Zr displacement damage dose (in units of dpa) as a function of target sample depth and the implanted Zr concentration versus depth. .... 127
- Figure 52 TEM bright-field (BF) image obtained from cross-sectional samples of  $\alpha$ -Al<sub>2</sub>O<sub>3</sub> irradiated with  $2 \times 10^{16}$  Zr<sup>+</sup>/cm<sup>2</sup>. Also shown are SRIM calculated profiles for the Zr displacement damage dose (in units of dpa) as a function of target sample depth and the implanted Zr concentration versus depth. .... 129
- Figure 53 TEM bright-field (BF) image obtained from cross-sectional samples of  $\alpha$ -Al<sub>2</sub>O<sub>3</sub> irradiated with  $4 \times 10^{16}$  Zr<sup>+</sup>/cm<sup>2</sup>. Also shown are SRIM calculated profiles for the Zr displacement damage dose (in units of dpa) as a function of target sample depth and the implanted Zr concentration versus depth. .... 130
- Figure 54 The bright-field image for the sample irradiated to fluence of  $2 \times 10^{15}$  Zr<sup>+</sup>/cm<sup>2</sup> ..... 133
- Figure 55 RBS-C spectra using 2 MeV He<sup>+</sup> obtained from  $\alpha$ -Al<sub>2</sub>O<sub>3</sub> samples irradiated with 175 keV Zr<sup>+</sup> ions to a fluence of  $2 \times 10^{16}$  Zr/cm<sup>2</sup>. The RBS-chamber had IBM geometry with detector scattering angle of +170° with a detector resolution of about 15 keV. Arrows labeled “Zr”, “Al”; “O” indicate the surface elastic scattering energies for Zr, Al, and O atoms respectively. Scattering angle of 170 ° was used for this measurement. .... 134
- Figure 56 A closer view of Al-sublattice in the RBS-C spectra using 2 MeV He<sup>+</sup> obtained from  $\alpha$ -Al<sub>2</sub>O<sub>3</sub> samples irradiated with 175 keV Zr<sup>+</sup> ions to a fluence of  $2 \times 10^{16}$  Zr/cm<sup>2</sup> ions. The RBS-chamber had IBM geometry with detector scattering angle of +170° with a detector resolution of about 15 keV. Arrow labeled “Al” indicates the surface elastic scattering energy for Al atom. Scattering angle of 170 ° was used for this measurement. .... 135
- Figure 57 (a) cross-sectional TEM-BF image obtained from the as-irradiated  $\alpha$ -Al<sub>2</sub>O<sub>3</sub> sample irradiated with  $2 \times 10^{15}$  Zr<sup>+</sup>/cm<sup>2</sup> (b) High resolution transmission electron microscopy (HRTEM) image obtained from the subsurface region and (c) NBED patterns obtained from different regions. .... 137
- Figure 58 The bright-field image for the irradiated sample with  $2 \times 10^{16}$  Zr/cm<sup>2</sup> and annealed at 800 °C for 30 minutes ..... 139
- Figure 59 RBS-C spectra using 2 MeV He<sup>+</sup> obtained from  $\alpha$ -Al<sub>2</sub>O<sub>3</sub> samples irradiated with 175 keV Zr<sup>+</sup> ions to a fluence of  $2 \times 10^{16}$  Zr/cm<sup>2</sup> and annealed at 800 °C for 30 minutes. The RBS-chamber had IBM geometry with detector scattering angle of +140° with a detector resolution of about 15 keV. Arrows labeled “Zr”, “Al”, “O” indicates the surface elastic scattering energies for Zr, Al, and O atoms respectively. Scattering angle of 165 ° was used for this measurement..... 140

- Figure 60 A closer view of Al-sublattice in the RBS-C spectra using 2 MeV  $\text{He}^+$  obtained from  $\alpha\text{-Al}_2\text{O}_3$  samples irradiated with 175 keV  $\text{Zr}^+$  ions to a fluence of  $2 \times 10^{16}$   $\text{Zr}/\text{cm}^2$  ions and annealed at 800 °C for 30 minutes. The RBS-chamber had IBM geometry with detector scattering angle of  $+140^\circ$  with a detector resolution of about 15 keV. Arrow labeled “Al” indicates the surface elastic scattering energy for Al atom. Scattering angle of  $165^\circ$  was used for this measurement. .... 141
- Figure 61 The bright-field image for the irradiated sample with  $2 \times 10^{16}$   $\text{Zr}/\text{cm}^2$  and annealed at 900 °C for 60 minutes ..... 143
- Figure 62 (a) Cross-sectional TEM-BF image obtained from the irradiated sample with  $2 \times 10^{16}$   $\text{Zr}/\text{cm}^2$  and annealed at 900 °C for 60 minutes. (b) NBED patterns obtained from different regions ..... 145
- Figure 63 (a) Cross-sectional TEM-BF Image obtained from the irradiated sample with  $2 \times 10^{16}$   $\text{Zr}/\text{cm}^2$  and annealed at 900 °C for 60 minutes. (b) HRTEM images obtained from sub-surface and deeper damaged regions (c) HRTEM images obtained from sub-surface and deeper damaged regions after  $30^\circ$  rotation. .... 146
- Figure 64 RBS-C spectra using 2 MeV  $\text{He}^+$  obtained from  $\alpha\text{-Al}_2\text{O}_3$  samples irradiated with 175 keV  $\text{Zr}^+$  ions to a fluence of  $2 \times 10^{16}$   $\text{Zr}/\text{cm}^2$  and annealed at 900 °C for 60 minutes. The RBS-chamber had IBM geometry with detector scattering angle of  $+140^\circ$  with a detector resolution of about 15 keV. Arrows labeled “Zr”, “Al”, “O” indicates the surface elastic scattering energies for Zr, Al, and O atoms respectively. Scattering angle of  $165^\circ$  was used for this measurement. .... 147
- Figure 65 A closer view of Al-sublattice in the RBS-C spectra using 2 MeV  $\text{He}^+$  obtained from  $\alpha\text{-Al}_2\text{O}_3$  samples irradiated with 175 keV  $\text{Zr}^+$  ions to a fluence of  $2 \times 10^{16}$   $\text{Zr}/\text{cm}^2$  ions and annealed at 900 °C for 60 minutes. The RBS-chamber had IBM geometry with detector scattering angle of  $+140^\circ$  with a detector resolution of about 15 keV. Arrow labeled “Al” indicates the surface elastic scattering energy for Al atom. Scattering angle of  $165^\circ$  was used for this measurement. .... 148
- Figure 66 The bright-field image for the irradiated sample with  $2 \times 10^{16}$   $\text{Zr}/\text{cm}^2$  and annealed at 1000 °C for 30 minutes ..... 149
- Figure 67 The bright-field image for the irradiated sample with  $2 \times 10^{16}$   $\text{Zr}/\text{cm}^2$  and annealed at 1000 °C for 30 minutes ..... 151
- Figure 68 RBS-C spectra using 2 MeV  $\text{He}^+$  obtained from  $\alpha\text{-Al}_2\text{O}_3$  samples irradiated with 175 keV  $\text{Zr}^+$  ions to a fluence of  $2 \times 10^{16}$   $\text{Zr}/\text{cm}^2$  and annealed at 1000 °C for 30 minutes. The RBS-chamber had IBM geometry with detector scattering angle of  $+140^\circ$  with a detector resolution of about 15 keV. Arrows labeled “Zr”, “Al”, “O” indicate the surface elastic scattering energies for Zr, Al, and O atoms respectively. .... 152
- Figure 69 A closer view of Al-sublattice in the RBS-C spectra using 2 MeV  $\text{He}^+$  obtained from  $\alpha\text{-Al}_2\text{O}_3$  samples irradiated with 175 keV  $\text{Zr}^+$  ions to a fluence of  $2 \times 10^{16}$   $\text{Zr}/\text{cm}^2$  ions and annealed at 1000 °C for 30 minutes. The RBS-chamber had IBM geometry with detector scattering angle of  $+140^\circ$  with a detector resolution of about 15 keV. Arrow labeled “Al” indicates the surface elastic scattering energy for Al atom. .... 153



- Figure 70 The bright-field images of the irradiated samples with  $2 \times 10^{16} \text{ Zr}^+/\text{cm}^2$  shows the effect of thermal annealing at different temperatures and times. (Left) as-irradiated sample, (Middle) after annealing at 800 °C for 30 minutes, and (Right) after annealing at 900 °C for 60 minutes..... 154
- Figure 71 Effect of fluence on solid changes during irradiation of  $\alpha\text{-Al}_2\text{O}_3$  with Zr ions. The bright-field images obtained from the irradiated sample to fluences of a)  $7.5 \times 10^{15} \text{ Zr}^+/\text{cm}^2$  b)  $1.5 \times 10^{16} \text{ Zr}^+/\text{cm}^2$  c)  $2 \times 10^{16} \text{ Zr}^+/\text{cm}^2$  d) The high resolution TEM image obtained from the irradiated sample to a fluence of  $1.5 \times 10^{16} \text{ Zr}^+/\text{cm}^2$  obtained from subsurface region e) Z-contrast image obtained from the irradiated sample to a fluence of  $4 \times 10^{16} \text{ Zr}^+/\text{cm}^2$  ..... 156
- Figure 72 A schematic representation of the changes to a solid caused by increasing ion fluence. .... 157
- Figure 73 Plot of effect of free energy for a hypothetical system. Irradiation condition alters phases free energies..... 160
- Figure 74 TEM cross section images and SAED patterns obtained from  $\alpha\text{-Al}_2\text{O}_3$  samples irradiated with: (a) 175 keV  $\text{Zr}^+$  ions to a fluence of  $7.5 \times 10^{15} \text{ Zr}^+/\text{cm}^2$  and (b) 175 keV  $\text{Zr}^+$  ions to a fluence of  $7.5 \times 10^{15} \text{ Zr}^+/\text{cm}^2$  plus 55 keV  $\text{O}^+$  to a fluence of  $1.1 \times 10^{16} \text{ O}^+/\text{cm}^2$ . These are “low- dose” samples in the sense that the Zr displacement damage dose is less than the threshold dose for amorphization. Also shown are SRIM calculated profiles for the Zr displacement damage dose (in units of dpa) as a function of target sample depth and the implanted Zr concentration versus depth. The label “surface” indicates the  $\alpha\text{-Al}_2\text{O}_3$  sample surface and the arrows indicate the direction of the incident ions. .... 162
- Figure 75 RBS-C spectra obtained from  $\alpha\text{-Al}_2\text{O}_3$  samples irradiated with: (a) 175 keV  $\text{Zr}^+$  ions to a fluence of  $7.5 \times 10^{15} \text{ Zr}^+/\text{cm}^2$  and (b) 175 keV  $\text{Zr}^+$  ions to a fluence of  $7.5 \times 10^{15} \text{ Zr}^+/\text{cm}^2$  plus 55 keV  $\text{O}^+$  to a fluence of  $1.1 \times 10^{16} \text{ O}^+/\text{cm}^2$ . For reference, aligned RBS-C spectra are shown in both and from unirradiated (virgin) single crystal  $\alpha\text{-Al}_2\text{O}_3$  samples. These are “high dose” samples in the sense that the Zr displacement damage dose is in excess of the threshold dose for amorphization. Arrows labeled “Zr”, “Al”, “O” indicate the surface elastic scattering energies for Zr, Al, and O atoms respectively. .... 164
- Figure 76 TEM cross-sectional bright-field (BF) images obtained from “high-dose” samples of  $\alpha\text{-Al}_2\text{O}_3$  irradiated with: (a) 175 keV  $\text{Zr}^+$  ions to a fluence of  $1.5 \times 10^{16} \text{ Zr}^+/\text{cm}^2$  and (b) 175 keV  $\text{Zr}^+$  ions to a fluence of  $1.5 \times 10^{16} \text{ Zr}^+/\text{cm}^2$  plus 55 keV  $\text{O}^+$  ions to a fluence of  $2.3 \times 10^{16} \text{ O}^+/\text{cm}^2$ . Also shown are SRIM calculated profiles for the Zr displacement damage dose (in units of dpa) as a function of target sample depth and the implanted Zr concentration versus depth. Comparing the two TEM-BF images, it is apparent that the buried amorphous region in the  $\alpha\text{-Al}_2\text{O}_3$  substrate is recrystallized during the subsequent oxygen implantation. .... 166
- Figure 77 (a) Nano-beam electron diffraction (NBED) patterns obtained from different regions of a “high-dose”  $\alpha\text{-Al}_2\text{O}_3$  sample irradiated with 175 keV  $\text{Zr}^+$  ions to a fluence of  $1.5 \times 10^{16} \text{ Zr}^+/\text{cm}^2$  plus 55 keV  $\text{O}^+$  ions to a fluence of  $2.3 \times 10^{16} \text{ O}^+/\text{cm}^2$ ; (b) cross-sectional TEM-BF image from the same sample. The NBED pattern from the deeper damaged region is consistent with an  $\alpha\text{-Al}_2\text{O}_3$  phase (B=

- $\langle 11\bar{2}0 \rangle$ ). The arrows in the uppermost NBED pattern, in (a) obtained from the near-surface damaged and recrystallized regions, indicate the presence of a phase that is not  $\alpha$ -Al<sub>2</sub>O<sub>3</sub>. The structure of this phase is identified in Figure 78. .... 168
- Figure 78 The same NBED pattern as the uppermost pattern in Fig. 77a, with indexing of some of the principal reflections (displayed using reverse contrast). Indexing the individual reflections reveals that two phases of Al<sub>2</sub>O<sub>3</sub> are responsible for this diffraction pattern. In particular both  $\alpha$ -Al<sub>2</sub>O<sub>3</sub> and  $\gamma$ -Al<sub>2</sub>O<sub>3</sub> are present and they are arranged with a special crystallographic relationship. The incident beam direction is  $[11\bar{2}0]$  for  $\alpha$ -phase Al<sub>2</sub>O<sub>3</sub> and  $[1\bar{1}\bar{2}]$  for  $\gamma$ -phase Al<sub>2</sub>O<sub>3</sub>. The red and black indices correspond  $\alpha$ -Al<sub>2</sub>O<sub>3</sub> and  $\gamma$ -Al<sub>2</sub>O<sub>3</sub>, respectively. .... 170
- Figure 79 SRIM calculated range and displacement damage dose (in units of dpa) dpa versus target depth. For Al<sub>2</sub>O<sub>3</sub> irradiated with 175 keV Zr<sup>+</sup> ions to a fluence of  $1.5 \times 10^{16}$  Zr<sup>+</sup>/cm<sup>2</sup>, followed by irradiation with 55 keV O<sup>+</sup> ions to a fluence of  $2.3 \times 10^{16}$  O<sup>+</sup>/cm<sup>2</sup>. For the oxygen SRIM calculation, densities of 3.98 and 3.1 g/cm<sup>3</sup> were used for the highly-damaged and amorphous regions of the Al<sub>2</sub>O<sub>3</sub>, respectively. .... 172
- Figure 80 (a) SRIM calculated nuclear and electronic energy loss for Al<sub>2</sub>O<sub>3</sub> irradiated with 55 keV O<sup>+</sup> ions, after the formation of buried amorphous layer due to prior "high dose" irradiation with Zr<sup>+</sup> ions; (b) TEM cross-section BF image obtained from "high dose" sample irradiated with 175 keV Zr<sup>+</sup> ions to a fluence of  $1.5 \times 10^{16}$  Zr<sup>+</sup>/cm<sup>2</sup>; (c) TEM cross-section BF image obtained from a "high dose" sample irradiated with 175 keV Zr<sup>+</sup> ions to a fluence of  $1.5 \times 10^{16}$  Zr<sup>+</sup>/cm<sup>2</sup> plus 55 keV O<sup>+</sup> ions to a fluence of  $2.3 \times 10^{16}$  O<sup>+</sup>/cm<sup>2</sup>. The model for the SRIM calculation in (a) assumes that the Al<sub>2</sub>O<sub>3</sub> substrate contains a buried amorphous layer with a lower density (3.1 g/cm<sup>3</sup>) compared to the density of pristine  $\alpha$ -Al<sub>2</sub>O<sub>3</sub> (3.98 g/cm<sup>3</sup>). .... 174
- Figure 81 Optical absorption spectra with the absorption from a virgin crystal subtracted ..... 179
- Figure 82 Photoluminescence of Zr and Zr + O irradiated sapphire ..... 180
- Figure 83 The bright-field image for the sample irradiated with 175 keV Zr<sup>+</sup> ions to a fluence of  $2 \times 10^{16}$  Zr/cm<sup>2</sup> plus 48 keV O<sup>+</sup> ions to a fluence of  $3 \times 10^{16}$  O/cm<sup>2</sup> ..... 185
- Figure 84 RBS-C spectra using 2 MeV He<sup>+</sup> obtained from  $\alpha$ -Al<sub>2</sub>O<sub>3</sub> sample irradiated with 175 keV Zr<sup>+</sup> ions to a fluence of  $2 \times 10^{16}$  Zr/cm<sup>2</sup> plus 48 keV O<sup>+</sup> ions to a fluence of  $3 \times 10^{16}$  O/cm<sup>2</sup>. The RBS-chamber had IBM geometry with detector scattering angle of +170° with a detector resolution of about 15 keV. Arrows labeled "Zr", "Al", "O" indicate the surface elastic scattering energies for Zr, Al, and O atoms respectively. .... 186
- Figure 85 A closer view of Al-sublattice in the RBS-C spectra using 2 MeV He<sup>+</sup> obtained from  $\alpha$ -Al<sub>2</sub>O<sub>3</sub> samples irradiated with 175 keV Zr<sup>+</sup> ions to a fluence of  $2 \times 10^{16}$  Zr/cm<sup>2</sup> plus 48 keV O<sup>+</sup> ions to a fluence of  $3 \times 10^{16}$  O/cm<sup>2</sup>. The RBS-chamber had IBM geometry with detector scattering angle of +170° with a detector resolution of about 15 keV. Arrow labeled "Al" indicates the surface elastic scattering energy for Al atom. .... 187
- Figure 86 (a) cross-sectional TEM-BF image obtained from the as-irradiated  $\alpha$ -Al<sub>2</sub>O<sub>3</sub> sample irradiated with  $2 \times 10^{16}$  Zr<sup>+</sup>/cm<sup>2</sup> and  $3 \times 10^{16}$  (b) SAED pattern obtained from

- the sample (c) High resolution transmission electron microscopy (HRTEM) image obtained from the subsurface, amorphous and deeper damaged regions and (d) NBED patterns obtained from different regions..... 189
- Figure 87 The bright-field image for the sample irradiated with 175 keV  $\text{Zr}^+$  ions to a fluence of  $2 \times 10^{16} \text{ Zr/cm}^2$  plus 48 keV  $\text{O}^+$  ions to a fluence of  $3 \times 10^{16} \text{ O/cm}^2$  and annealed at 800 °C for 30 minutes. .... 191
- Figure 88 RBS-C spectra using 2 MeV  $\text{He}^+$  obtained from  $\alpha\text{-Al}_2\text{O}_3$  samples irradiated with 175 keV  $\text{Zr}^+$  ions to a fluence of  $2 \times 10^{16} \text{ Zr/cm}^2$  plus 48 keV  $\text{O}^+$  ions to a fluence of  $3 \times 10^{16} \text{ O/cm}^2$  and annealed at 800 °C for 30 minutes. The RBS-chamber had IBM geometry with detector scattering angle of  $-165^\circ$  with a detector resolution of about 15 keV. Arrows labeled “Zr”, “Al”, “O” indicate the surface elastic scattering energies for Zr, Al, and O atoms respectively..... 192
- Figure 89 A closer view of Al-sublattice in the RBS-C spectra using 2 MeV  $\text{He}^+$  obtained from  $\alpha\text{-Al}_2\text{O}_3$  samples irradiated with 175 keV  $\text{Zr}^+$  ions to a fluence of  $2 \times 10^{16} \text{ Zr/cm}^2$  plus 48 keV  $\text{O}^+$  ions to a fluence of  $3 \times 10^{16} \text{ O/cm}^2$  and annealed at 800 °C for 30 minutes. The RBS-chamber had IBM geometry with detector scattering angle of  $-165^\circ$  with a detector resolution of about 15 keV. Arrow labeled “Al” indicates the surface elastic scattering energy for Al atom..... 193
- Figure 90 The bright-field image for the sample irradiated with 175 keV  $\text{Zr}^+$  ions to a fluence of  $2 \times 10^{16} \text{ Zr/cm}^2$  plus 48 keV  $\text{O}^+$  ions to a fluence of  $3 \times 10^{16} \text{ O/cm}^2$  and annealed at 800 °C for 30 minutes. .... 195
- Figure 91 (a) Cross-sectional TEM-BF image obtained from  $\alpha\text{-Al}_2\text{O}_3$  sample irradiated with 175 keV  $\text{Zr}^+$  ions to a fluence of  $2 \times 10^{16} \text{ Zr/cm}^2$  plus 48 keV  $\text{O}^+$  ions to a fluence of  $3 \times 10^{16} \text{ O/cm}^2$  and annealed at 900 °C for 60 minutes. (b) HRTEM image and (c) NBED patterns obtained from the affected regions..... 196
- Figure 92 The bright-field image for the sample irradiated with 175 keV  $\text{Zr}^+$  ions to a fluence of  $2 \times 10^{16} \text{ Zr/cm}^2$  plus 48 keV  $\text{O}^+$  ions to a fluence of  $3 \times 10^{16} \text{ O/cm}^2$  and annealed at 1000 °C for 30 minutes. .... 197
- Figure 93 RBS-C spectra using 2 MeV  $\text{He}^+$  obtained from  $\alpha\text{-Al}_2\text{O}_3$  samples irradiated with 175 keV  $\text{Zr}^+$  ions to a fluence of  $2 \times 10^{16} \text{ Zr/cm}^2$  plus 48 keV  $\text{O}^+$  ions to a fluence of  $3 \times 10^{16} \text{ O/cm}^2$  and annealed at 1000 °C for 30 minutes. The RBS-chamber had IBM geometry with detector scattering angle of  $-165^\circ$  with a detector resolution of about 15 keV. Arrows labeled “Zr”, “Al”, “O” indicate the surface elastic scattering energies for Zr, Al, and O atoms respectively..... 198
- Figure 94 A closer view of Al-sublattice in the RBS-C spectra using 2 MeV  $\text{He}^+$  obtained from  $\alpha\text{-Al}_2\text{O}_3$  samples irradiated with 175 keV  $\text{Zr}^+$  ions to a fluence of  $2 \times 10^{16} \text{ Zr/cm}^2$  plus 48 keV  $\text{O}^+$  ions to a fluence of  $3 \times 10^{16} \text{ O/cm}^2$  and annealed at 1000 °C for 30 minutes. The RBS-chamber had IBM geometry with detector scattering angle of  $-165^\circ$  with a detector resolution of about 15 keV. Arrow labeled “Al” indicates the surface elastic scattering energy for Al atom..... 199
- Figure 95 The TEM bright-field image for the samples irradiated with 175 keV  $\text{Zr}^+$  ions to a fluence of  $2 \times 10^{16} \text{ Zr/cm}^2$  plus 48 keV  $\text{O}^+$  ions to a fluence of  $3 \times 10^{16} \text{ O/cm}^2$  before and after annealing at different temperatures and times ..... 200

Figure 96 BF-TEM, HRTEM, and NBED patterns showing the effect of O irradiation and annealing on Zr-irradiated sample .....	202
--	-----

**List of abbreviations**

AS: angular scanning

BF: bright field

CD: compact disk

CEMS: conversion electron energy Mössbauer spectroscopy

CEMS: conversion-electron Mossbauer spectroscopy

COF: coefficient friction

CVD: chemical vapor deposition

DF: dark field

DFT: density functional theory

dpa: displacement per atom

DSC: differential scanning calorimetry

DTA: differential thermal analysis

EELS: electron energy loss spectroscopy

ELNES: energy loss near-edge structure

EPR: electron paramagnetic resonance

EXELFS: Extended energy loss fine structure spectroscopy

fcc: face center cubic

GXRD: grazing-angle X-ray diffraction

HAADF: high angle annular dark-field

hcp: hexagonal close packed

HPPMS: high power pulsed magnetron sputtering

HRTEM: high resolution TEM

IBIER: ion-beam induced epitaxial recrystallization

IC: integrated circuit

IR: infra-red

LED: light-emitting diode

MH: micro hardness

MS: magnetron sputtering

MS: multiple scattering

NBED: nano-beam electron diffraction

NMR: Nuclear magnetic resonance

NPD: neutron powder diffraction

OA: optical absorption

OM optical microscope

PECVD: plasma enhanced CVD

PL: photoluminescence

PLE: photoluminescence excitation

RBS: Rutherford backscattering spectrometry

RBS-C: Rutherford backscattering spectrometry with channeling

RF: radio-frequency

RHEED: reflection high energy electron diffraction

RT: room temperature

SAED: selected area electron diffraction

SEM: secondary electron microscope

SOS: silicon on sapphire

SPEG: solid phase epitaxial growth

SRIM: stopping and range of ions in matter

SRO: short range order

STEM: scanning transmission electron microscopy

TCVD: thermal CVD

TEM: transmission electron microscopy

TRR: time resolved reflectivity

TSK: terrace step kink

UHF: ultra-high frequencies

UV: ultra violet

XPS: X-ray photoemission spectroscopy

XRD: X-ray diffraction

## Chapter 1

### Introduction and General Information

In this chapter, general information about applications and importance of alumina followed by a description of its crystal structures are presented. Important metastable alumina polymorphs as well as the methods to produce these alumina polymorphs are also discussed. At the end of this chapter, statement of the problem and background of the study are described.

There are many different forms of aluminum oxide ( $\text{Al}_2\text{O}_3$ ) or alumina. In this dissertation alumina refers generally to aluminum oxide. Sapphire means single crystal of  $\alpha\text{-Al}_2\text{O}_3$  and corundum means single crystal alumina that occurs naturally in the form of sapphire (mineral name). Alumina also has a number of metastable polymorphs beside the thermodynamically stable  $\alpha$ -phase. Among them  $\gamma$ ,  $\chi$ ,  $\delta$ ,  $\theta$ ,  $\kappa$ ,  $\lambda$  phases are well known. The beta phase of alumina also exists, although not in pure alumina but with the incorporation of sodium ions in the lattice. Polycrystalline alumina is aluminum oxide that is composed of many crystallites of varying size and orientation.

#### 1.1 Single crystal of $\alpha$ -alumina (sapphire)

Sapphire has a great chemical stability and high electrical resistivity with a limited solubility of impurities. The high optical transmission range of sapphire makes it a useful material for optical purposes. Due to its extreme hardness, chemical inertness, high melting point and wide bandgap, sapphire has been used in different applications



from mechanical to medical and electronics devices. Undoped sapphire also plays an important role in semiconductor technology as the substrate for epitaxial growth of Si and the other semiconductor materials.

Over the last few years, there has been a great interest in use of additives to sapphire in order to improve its surface-related properties. By using ion irradiation (or implantation) techniques, a variety of metal ions have been implanted in sapphire to alter its physical, chemical, electrical, optical, and mechanical properties [1]. Sapphire is also of significant interest from fundamental studies and theoretical point of view. Many computational studies have been reported for sapphire to relate theoretical models to its structural and transport properties [2].

## **1.2 Applications of alumina**

Alumina is an important insulating material due to its dielectric and excellent thermal shock properties. Due to its unique mechanical properties, alumina ceramics can be used for abrasive and cutting tools. It is also widely used in the electronics industry.

Alumina is widely used in very high frequencies (UHF), as interconnection, resistances, capacitors, hybrid circuits, multi-layer interconnection circuits, materials for type II condensers, and hyper frequency resonators (mobile phones). Alumina is also used for making extrusion and sanding nozzles and for parts of machinery (particularly in the mining industry) where wear resistant qualities are critical. It is also used for making iceskate blades and some friction parts such as wear-resistant seals in piston engines. Due to its shock-resisting quality alumina can be used as armor plating for protection of tanks

and helicopters as well as for bullet-proof jackets and in aeronautics for protection of hydraulic parts. Some of the applications of alumina are described briefly below:

### **1.2.1 Use in Jewelry Industry**

As early as 3,000 years ago, humans began to use natural sapphire and rubies as gems having the value of diamond. At the beginning of twentieth century, synthetic corundum (sapphire) was introduced for use as jewel. Techniques for deposition of impurities into sapphire produced colored sapphire (ruby, star sapphire, etc.). Trace amounts of impurities such as iron, titanium, chromium, copper or magnesium can give corundum blue, yellow, pink, purple, orange or greenish color. Chromium impurities in corundum yield the red gemstone called ruby. The common techniques to change the color of sapphire crystals are irradiation, ion implantation, and thermal and thermochemical treatments. Using one or a combination of these techniques precious jewels can be made.

### **1.2.2 Use in Engineering**

Sapphire is suitable for friction pads and scratch resistant windows due to its hardness (Moh 9), reasonable cost, stable quality, and wear resistance. For “ruby-steel” pad the coefficient friction (COF) is 0.25 at a pressure on the order of 3.7 GPa. Sapphire is also used as watch glasses by all well-known manufacturers of high-quality watches. These watches are scratch resistance [3].

A glass sandwich of sapphire sheet, armored glass and transparent plastic with a total thickness of about 30 mm is used for the windows of military helicopters and special purpose vehicles. The sapphire sheet can absorb the greater part of the kinetic energy of

bullets and the rest of bullet energy can be absorbed in the layer of glass and plastic. A similar result but a heavier window can be achieved in the absence of the sapphire sheet by using a 100 mm armored glass.

When two solid surfaces are in sliding, rubbing, or rolling contact one or both of the solids can remove material from one or both. This process is called wear. Among the oxides sapphire has the highest hardness and it is considered as a heat and wear resistant ceramic. These properties made sapphire as a one of the best cutting tools, bearings, seals, and other sliding/rolling application [4]. Experimental data has shown that sapphire nozzles in sand blaster and water-jet cutting tools serve up to 30 times longer than steel nozzles [3]. Sapphire cutters produce high quality surface finishes in applications for cutting metals, alloys and nonmetallic materials. Extremely sharp and abrasive crystal particles of  $\alpha\text{-Al}_2\text{O}_3$  are widely used in blast finishing and surface preparation due to their hardness, cost and longevity. In the opinion of Dobrovinskaya et al. [3], CD disks fabricated of sapphire will be substitutes for polycarbonate CDs in the near future due to ability of sapphire CDs for long-term data storage. They have also mentioned the application of sapphire as chemical wares, capillaries, and fibers to reinforce metallic and ceramic composites.

Sapphire is used in the semiconductor industry as a non-conducting substrates for epitaxial deposition of thin films such as GaN for use in the manufacture of bright blue and green LED's. Thin sapphire wafers are also used in integrated circuit (IC) industries as an insulating substrate. For example silicon on sapphire or "SOS" chips have applications in high-power radio-frequency (RF) such as cellphones, radio and satellite

communication systems. The reason for choosing sapphire as wafer is that sapphire is a good electrical insulator while it can conduct the significant heat generated in all operating ICs.

In ceramic-metal joining technology such as the moly-manganese process, sapphire can be coupled with different metals to develop seals for use in thermionic converters which are capable of long life at temperatures in excess of 1500°C [5] .

### 1.2.3 Use in Optics

Sapphire transmits about 80-90% of wavelengths in the range 0.2-2.2 microns in the UV-visible, and ~ 5.5 microns in the IR (Fig.1) and is often used as window materials where the temperature is very low or high or resistance against scratch is required.

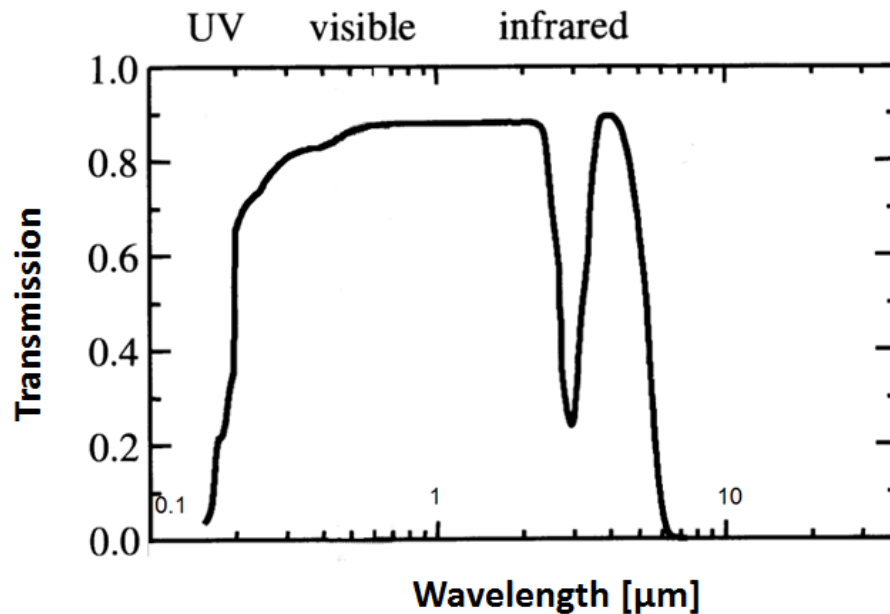


*Figure 1 Optical transmission spectrum of a 3 mm thick sapphire crystal of thickness 3 mm [6].*

It has applications in various devices that work on the ground, under water, and in outer space. Sapphire is used in different sizes with diameters from several millimeters to several hundreds of millimeters in a wide range of pressures and temperatures from cryogenic to high temperatures. Sapphire is also used for the scanner windows of cash registers that read bar codes.

Another application of high quality sapphire is in optical components such as lenses, prisms, reflecting mirrors for laser beam control due to its high refractive index. Sapphire optical fibers are especially attractive for fabricating thermal sensors for the harsh high-temperature harsh temperature environment, where quartz and the other optical glasses cannot preserve their optical properties or service abilities. Sapphire domes are used for making the heads of IR-radiation guided missiles. Sapphire can also be used as shells for sodium high-pressure lamps, focusing cones, X-ray interferometers and monochromators [3].

#### **1.2.4 Use in Medicine**

Based on medical-biological studies, sapphire is not toxic for humans and does not cause changes in the functions of the central nervous system, liver, kidneys, protein and fat metabolism, and general reactivity. In contrast to metals, electrically neutral sapphire is not carried by electrochemical reactions into lymph nodes and other parts of the body, does not cause immunodepressions or other changes in the immune system, and does not lead to demineralization of adjacent bone tissue. This biocompatibility of sapphire along with unique inertness, including electrolytic passiveness, corrosion resistance, and hardness characteristic of sapphire, define the main fields of application in

medicine: implants, surgery, and medical instrument. In surgical and dental applications sapphire can be used as implants and in Despite the above-mentioned application of sapphire implants, some analysis has shown osteogenic activity in vivo.

### 1.3 Structure and properties

Sapphire is the single crystal form of corundum, also known as alpha-alumina ( $\alpha$ - $\text{Al}_2\text{O}_3$ ) or single crystal  $\text{Al}_2\text{O}_3$ . Because sapphire is the purest form of aluminum oxide with no porosity or grain boundaries, it is theoretically the densest form of aluminum oxides ( $3.99 \text{ gr/cm}^3$ ) [7].

Sapphire belongs to the  $R\bar{3}c$  space group with lattice parameters  $a = 0.4789 \text{ nm}$  and  $c = 1.2991 \text{ nm}$ . It consists of a close-packed oxygen sublattice arranged in an approximately hexagonal array with the  $\text{Al}^{3+}$  ions placed on octahedral coordination. Two third of the octahedral sites are occupied by  $\text{Al}^{3+}$  cations and one-third of the octahedral sites are structural vacancies. The presence of the vacant sites make sapphire a non-perfect close-packed crystal, but these sites provide the overall electrical neutrality for the crystal with the maximum separation of like charges and a minimum separation of unlike charges [8].

In sapphire the oxygen layers are in an ABABAB stacking sequence, where the O atoms are bonded to four Al atoms in a distorted  $\text{sp}^3$  arrangement, and the Al atoms are bonded to six nearest neighbor oxygen atoms [9] (Figs.2 and 3). The deviation from a perfect close-packed crystal is noted by a rhombohedral angle of  $55^\circ 17'$  in sapphire compare with  $53^\circ 47'$  in a perfect rhombohedral unit cell. The Al ions are bonded to six nearest neighbor oxygen, but three Al ions have a bond length of  $0.1858 \text{ nm}$  and the other

three Al ions have a bond length of 0.1971 nm instead of six equal distances arranged on the vertices of an octahedron in a perfect rhombohedral unit cell [10] . Sapphire possesses a mixture of covalent and ionic bonding. The ionicity percent of sapphire based on the Pauling electronegativity scale is 63%. The sharing of covalent bonds (~20% ) is a probable cause of the excellent mechanical properties of sapphire [3].

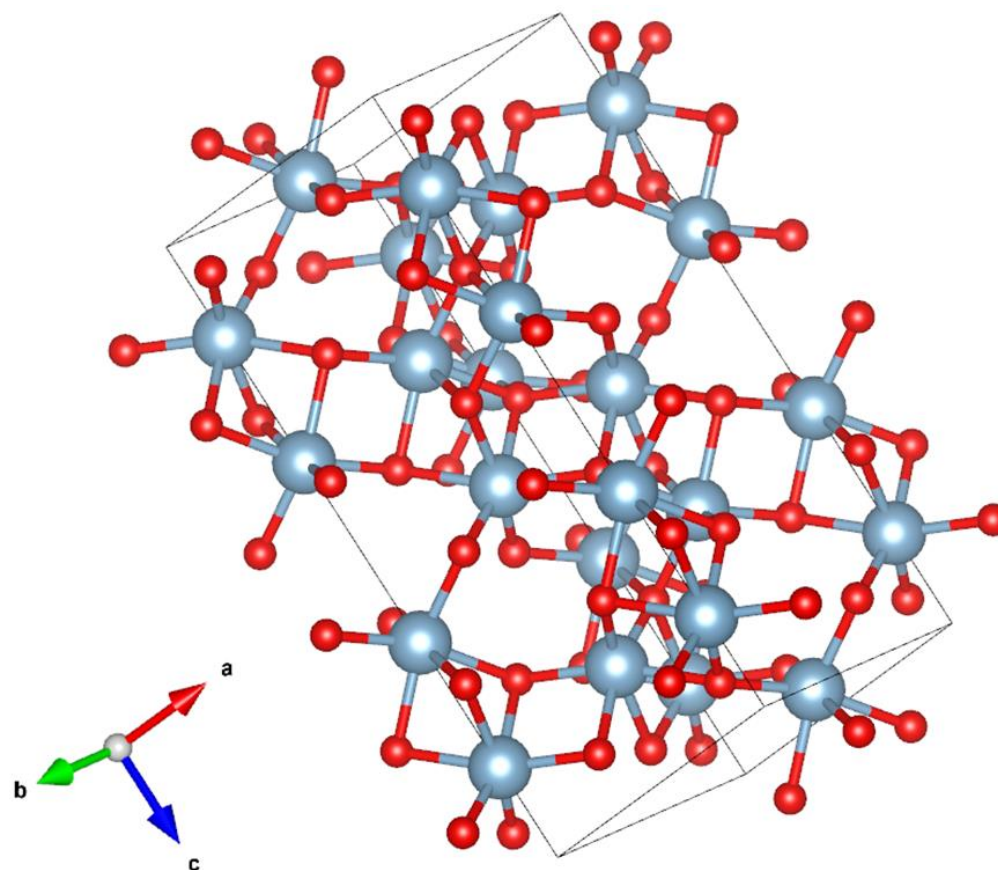


*Figure 2 Arrangement of aluminum and oxygen in a three dimension ball-and-stick model from visualization for electronic and structural analysis (VESTA), red and grey balls represent oxygen and aluminum atoms respectively*



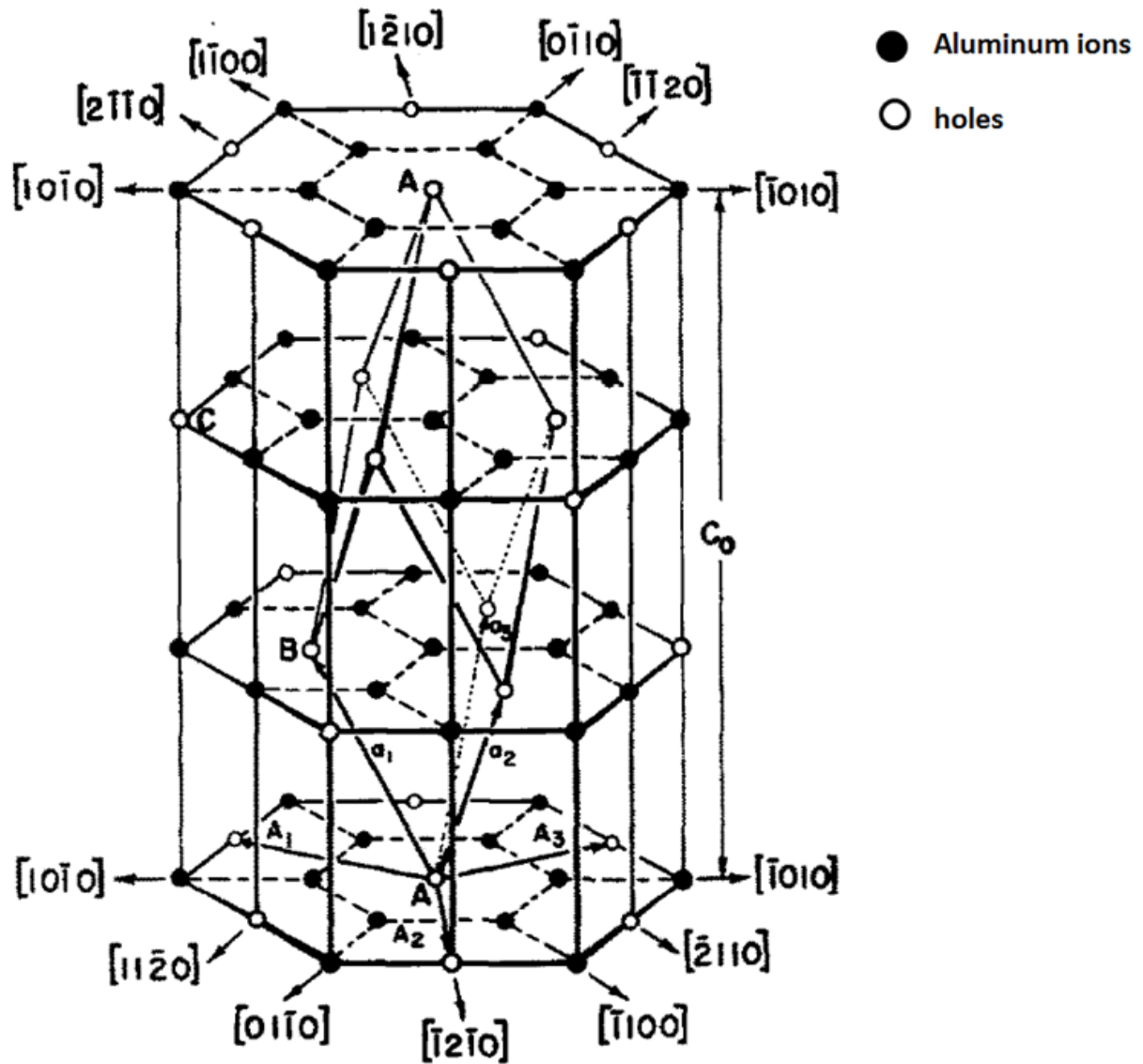


Figure 3 Distribution of aluminum ions and holes on the simple hexagonal lattice

The smallest rhombohedral cell which correctly describes the positions of the cations is shown along with the corresponding hexagonal cell vectors (after Kronberg, [8])

### 1.4 Metastable alumina polymorphs

In addition to the importance of alumina for its applications and fundamental studies, alumina is also important from the point of view that it has many metastable polymorphs such as  $\kappa$ -,  $\gamma$ -,  $\delta$ -,  $\theta$ - $\text{Al}_2\text{O}_3$  besides the thermodynamically stable  $\alpha$ - $\text{Al}_2\text{O}_3$ . Among the several metastable polymorphs of alumina (transition alumina phases),  $\gamma$ -alumina is important due to its application in industry as catalyst, adsorbents, coatings, and soft abrasives. The metastable phases are generally divided into two structural categories depending on the O anion arrangement: face centered cubic (fcc) and hexagonal close packed (hcp). Metastable phases of  $\gamma$ ,  $\eta$  (cubic),  $\delta$  (either tetragonal or orthorhombic), and  $\theta$  (monoclinic) with ABCABC stacking sequence have the fcc structure while metastable phase of  $\kappa$  (orthorhombic),  $\chi$  (hexagonal) and thermodynamically stable phase of  $\alpha$  (trigonal) with ABAB stacking sequence have the hcp structure [7].

Table 1 summarizes the processing routes to produce different metastable  $\text{Al}_2\text{O}_3$  phases. All these phases can be observed at room temperature but the sequence of transformation is not reversible. It can be observed from Table 1, that gibbsite is the only aluminum hydroxide that produces  $\chi$ -alumina crystals by thermal dehydroxilation [11].  $\kappa$ - $\text{Al}_2\text{O}_3$  can form from heating  $\chi$ - $\text{Al}_2\text{O}_3$  at about 700 °C or by thermal dehydroxilation of tohite at 700-800 °C [7]. The  $\kappa$ - $\text{Al}_2\text{O}_3$  phase can be also produced from amorphized sapphire by megatron sputtering and from thermal chemical vapor deposition (CVD) [12]. In all most cases  $\kappa$ - $\text{Al}_2\text{O}_3$  can be converted into  $\alpha$ -alumina by further heating. It is expected that  $\chi$ - and  $\kappa$ - $\text{Al}_2\text{O}_3$  crystals would have very similar structures [11].

*Table 1 Common processing routes for producing different  $Al_2O_3$  polymorphs and the sequences of phase transformations toward  $\alpha$ - $Al_2O_3$  with approximate hcp and fcc packing of oxygen for the metastable  $Al_2O_3$  structures [7, 12, 13]*

Approximate packing of oxygen for the metastable $Al_2O_3$ structures (hcp)	Approximate packing of oxygen for the metastable $Al_2O_3$ structures (fcc)
$\alpha$ -AlOOH (diaspore) $\xrightarrow{700^\circ-800^\circ C}$ $\alpha$ - $Al_2O_3$	$\gamma$ -AlOOH (boehmite) $\xrightarrow{300^\circ-500^\circ C}$ $\gamma$ $\xrightarrow{700^\circ-800^\circ C}$ $\delta$ $\xrightarrow{900^\circ-1000^\circ C}$ $\theta$ $\xrightarrow{1000^\circ-1100^\circ C}$ $\alpha$ - $Al_2O_3$
$\gamma$ -Al(OH) <sub>3</sub> (gibbsite) $\xrightarrow{150^\circ-300^\circ C}$ $\chi$ $\xrightarrow{650^\circ-750^\circ C}$ $\kappa$ $\xrightarrow{1000^\circ C}$ $\alpha$ - $Al_2O_3$	$\alpha$ -Al(OH) <sub>3</sub> (bayerite) $\xrightarrow{200^\circ-300^\circ C}$ $\eta$ $\xrightarrow{600^\circ-800^\circ C}$ $\theta$ $\xrightarrow{1000^\circ-1100^\circ C}$ $\alpha$ - $Al_2O_3$
$5Al_2O_3 \cdot H_2O$ (tohdite) $\xrightarrow{700^\circ-800^\circ C}$ $\kappa'$ $\xrightarrow{750^\circ C}$ $\kappa$ $\xrightarrow{900^\circ C}$ $\alpha$ - $Al_2O_3$	Melt $\longrightarrow \gamma \longrightarrow \delta, \theta \longrightarrow \alpha$ - $Al_2O_3$
Vapor (thermal CVD) $\gamma \xrightarrow{800^\circ C} \kappa \xrightarrow{820^\circ C} \alpha$ - $Al_2O_3$	Cathodic arc $\xrightarrow{420-590^\circ C} \gamma \longrightarrow \alpha$ - $Al_2O_3$
Vapor (thermal CVD) $\gamma \xrightarrow{800^\circ C} \kappa \xrightarrow{820^\circ C} \alpha$ - $Al_2O_3$	Amorphous (plasma enhanced CVD) $\xrightarrow{350-500^\circ C} \gamma \xrightarrow{550-570^\circ C} \alpha$ - $Al_2O_3$
Amorphous (magnetron sputtering) $\xrightarrow{220-440^\circ C} \kappa \xrightarrow{440-550^\circ C} \gamma \xrightarrow{550-650^\circ C} \alpha$ - $Al_2O_3$	Amorphous (ion implantation) $\longrightarrow \gamma \longrightarrow \alpha$ - $Al_2O_3$

Table 1 show that  $\gamma\text{-Al}_2\text{O}_3$  can be produced by several different routes: (a) dehydroxilation of monohydroxide boehmite in air, at 300 °C, (b) from amorphous alumina anodic films, (c) from melt (d) from cathodic arc, (e) from amorphous by plasma enhanced CVD, and (f) from amorphous alumina produced by ion implantation. According to Zywitzki et al. and Schneider et al. [14-17],  $\gamma\text{-Al}_2\text{O}_3$  can be formed by heating  $\kappa\text{-Al}_2\text{O}_3$  produced by magnetron sputtering. Cao et al. reported the formation of  $\gamma\text{-Al}_2\text{O}_3$  directly from pulsed-laser irradiated sapphire. They believe the  $\gamma\text{-Al}_2\text{O}_3$  was formed because laser irradiation is a rapid heating and cooling process in which thin surface layer is heated and melted and evaporated during a 41-ns pulse duration [18]. Also  $\delta\text{-Al}_2\text{O}_3$  is produced only from  $\gamma\text{-Al}_2\text{O}_3$ ; indicating that the transformation is pseudomorphic either from boehmite or from amorphous and melt. The metastable phase of  $\theta\text{-Al}_2\text{O}_3$  may be produced by three routes: (a) from  $\delta\text{-Al}_2\text{O}_3$ ; (b) from  $\eta\text{-Al}_2\text{O}_3$ ; (c) from  $\gamma\text{-Al}_2\text{O}_3$ . Metastable phase of  $\eta\text{-Al}_2\text{O}_3$  may be produced from bayerite. The presence of  $\delta\text{-Al}_2\text{O}_3$  in the transformation sequence of  $\gamma\text{-Al}_2\text{O}_3$  to  $\theta\text{-Al}_2\text{O}_3$  has been speculated from studies of Zhou [19] and Gan [20]. Based on NMR and IR data, Pecharroman has suggested that the  $\delta\text{-Al}_2\text{O}_3$  detected in the transformation sequence of  $\gamma\text{-Al}_2\text{O}_3$  to  $\theta\text{-Al}_2\text{O}_3$  actually is not a single  $\delta\text{-Al}_2\text{O}_3$  phase but a heterogeneous mixture of well crystallized  $\gamma\text{-Al}_2\text{O}_3$  and  $\theta\text{-Al}_2\text{O}_3$  metastable phases [21].

Santos et al. have reported that  $\eta\text{-Al}_2\text{O}_3$  can be produced from gelatinous boehmite. No information exists on pseudomorphism from these crystals [11]. A brief summary on the structures and properties of common alumina polymorphs is presented in Table 2 [7, 22, 23].

*Table 2 Structure and properties of alumina polymorphs*

Phase	Structure (arrangement of oxygen)	Space group	Density [g/cm <sup>3</sup> ]	Cations/unit cell	Lattice parameter [Å]
$\alpha$	hcp	R- $\bar{3}c$ hR10	3.99	10 30	5.128 a = 4.789 c = 12.991
$\gamma$	fcc	$Fd\bar{3}m$	3.65-3.67	64/3	7.9
$\delta$	fcc	$P\bar{4}m2$	3.60-3.65	64	a=7.9 b=15.8 c=11.85
$\theta$	fcc	C2/m	3.60-3.65	8	a=11.85 b=2.793 c=5.586
$\kappa$	hcp	Pna2 <sub>1</sub>	3.98	8	a=4.834 b=8.310 c=8.93

Although the exact structures and properties of some metastable aluminas are still not well understood, the transition aluminas have found significant attention for use in industry. For instance  $\kappa$ -Al<sub>2</sub>O<sub>3</sub> has application in wear resistance coatings on cement carbide cutting tools. The metastable phase,  $\delta$ -Al<sub>2</sub>O<sub>3</sub>, is used in bioactive bone cement composites as an alternative to  $\alpha$ -Al<sub>2</sub>O<sub>3</sub> due to a greater osteoblastic activity for in-vivo bone formation. Ultra-high purity polycrystalline  $\alpha$ -Al<sub>2</sub>O<sub>3</sub> can be produced from  $\theta$ -Al<sub>2</sub>O<sub>3</sub>. All the transition phases are widely used in heterogeneous catalysis, metal production,

adsorbents, etc. [24]. The  $\gamma$ -  $\text{Al}_2\text{O}_3$  phase is a very fine-grained material making it very difficult to impossible to sinter into a dense body. Therefore  $\gamma$ -  $\text{Al}_2\text{O}_3$  powder has a very high specific surface area  $\approx 100 \text{ m}^2/\text{g}$  compare with the  $\alpha$ - $\text{Al}_2\text{O}_3$  with the surface area of  $\approx 5 \text{ m}^2/\text{g}$ .

#### 1.4.1 $\gamma$ - $\text{Al}_2\text{O}_3$

The structure of  $\gamma$ -alumina has been described as a defect spinel ( $\text{Fd}\bar{3}m$ ) with the formula  $\text{Al}_{21+1/3}\square_{2+2/3}\text{O}_{32}$ , where  $\square$  denotes a vacancy. The 32 oxygen anions are distributed over the fcc packing, while  $64/3$  Al ions and vacancies are distributed over octahedral (16d) and tetrahedral (8a) positions of the ideal spinel structure [25]. The deviations from an ideal spinel arise from the assumption that the  $2+2/3$  aluminum vacancies are randomly distributed over the tetrahedral or octahedral sites. Different researchers have reported different percentage of aluminum ion occupancy in the octahedral and tetrahedral positions. Shirasuka et al. and John et al. respectively have reported that the aluminum ions occupancy of the two 16-fold octahedral sites are 62.5% and 65% and they assumed the remaining aluminum ions are distributed equally over the eightfold and the 48-fold tetrahedral sites [26, 27]. These percentages are reported to be 63% and 70% respectively in the work of Shelberg et al. and Lee et al. [28, 29]. A similar disagreement can be found in case of the aluminum vacancy distribution. The studies show that the aluminum vacancies are situated entirely in octahedral positions [30-32].

A study by Jayaram [33] concluded that these aluminum vacant sites are entirely in tetrahedral positions. Lippens et al. believe whether the vacant sites will occur in octahedral or in tetrahedral positions, the greatest disorder is to be expected for the atoms

in tetrahedral positions [34]. Most of density functional theory (DFT) studies along with experimental works indicate the aluminum vacancies to reside at both tetrahedral and octahedral sites [35-38].

### 1.5 Solid phase epitaxial growth (SPEG)

Epitaxy refers to the process of growing a crystal as an overlayer on another crystalline substrate. The orientation of the growing crystal is determined by the underlying crystal. For instance, for epitaxial growth of copper on the surface of silver, copper lies with the (111) face in registry with the (111) face of the substrate and the  $\langle 110 \rangle$  direction of the copper is parallel to the  $\langle 110 \rangle$  direction of the silver underlying crystal;  $(111) \langle 110 \rangle_{\text{Cu}} \parallel (111) \langle 110 \rangle_{\text{Ag}}$ . If the deposited compound grows with a random orientation with respect to the underlying crystal, this is called non-epitaxial growth. Although parallel epitaxial orientation is the most observed case of deposition, epitaxy does not require parallelism of low-index crystallographic direction. The deposition of silver on the surface of GaAs at temperatures lower than 200 °C is an example of non-parallel epitaxial growth with the orientation of  $(011) \langle 111 \rangle_{\text{Ag}} \parallel (00\bar{1}) \langle \bar{1}10 \rangle_{\text{GaAs}}$  [39].

Epitaxial films may be grown from gaseous, liquid or solid precursors. The substrate act as a seed for growing the film, and temperature determine the epitaxial orientation. In homoepitaxy the growth films are made up of the same material as the underlying crystal, whereas in hetroepitaxy the films are of a material different from the substrate. The driving force for epitaxial growth in homoepitaxy is mainly due to lattice misfit and for hetroepitaxy is due to different in chemistry. In the vapor and liquid phase

epitaxy, growth occurs at the vapor-solid and liquid-solid interface respectively. Solid phase epitaxial growth (SPEG) is a layer-by-layer process that occurs at the crystal-amorphous interface. In solid phase epitaxy a thin amorphous layer is first recrystallized on the crystalline substrate then the post annealing process convert the thin film into a crystalline layer.

Deposition of Si on doped Si single crystal is among many studies to investigate SPEG in semiconductor compounds [40]. In these studies, usually a thin layer of amorphous region is produced using ion irradiation. Annealing of this layer, results in the recrystallization of the amorphous phase by SPEG. Doping of oxides with optically activated dopants also is used to study SPEG, leading to synthesize the materials proper for optical device technology. There are a few studies that focused on the SPEG of insulators. For example Sklad et al. studied the phase transformation of amorphous alumina to  $\gamma$ -alumina to  $\alpha$ -alumina by annealing of amorphized sapphire formed by irradiation of Al and O at liquid nitrogen [13]. SPEG has also been reported for amorphous alumina films on sapphire substrates at temperatures as low as 400° C. Zhou et al. [41] observed SPEG in films prepared by implantation of In at 77 K followed by 1.5 MeV Si irradiation at 400° C. They observed the same transformation path as in thermal annealing, e.g.,  $A \rightarrow \gamma \rightarrow \alpha$ . The results appeared to be insensitive to the presence of indium in the amorphous layer.

Yu et al. [42, 43] observed SPEG in alumina films prepared by electron beam deposition on sapphire (0001) surfaces during subsequent ion irradiation at temperatures



in the range 400 to 600° C. Beams of oxygen (180 keV) and argon (360 keV) were chosen such that the projected ranges were beyond the amorphous/substrate interface. The amorphous layer first transformed to  $\gamma$ -phase followed by a  $\gamma \rightarrow \alpha$  epitaxial transformation. The quality of the films was much lower than those thermally regrown. These investigators also attributed the observed IBIER effects to energy deposited in nuclear processes (elastic collisions). They also reported that the presence of iron dopants inhibits the process.

### **1.6 Crystal growth kinetics**

There are two major models describing the epitaxial thin-film growth in crystals: layer-by-layer and island. These models are two regimes of the Terrace Step Kink (TSK) model that apply for different conditions based on temperature, flux and step density. The layer-by-layer regime applies at low temperature, high flux and low step density. The island regime applies for the atoms that have stronger bounds with each other than with underlying or neighboring atoms. The kinetics of growth is determined by counting broken and formed bounds. Figure 4 shows the atomic processes during crystal growth. The surface consists of terraces and steps which themselves contain kinks. Molecules that attach the kinks make more bonds to neighboring molecules compared to the molecules that attach to traces or step edges. The molecules that leave the amorphous region can easily stick and are more likely to do so, on the kinks. The concentration of kinks and roughening steps play an important role in kinetics of growth.

Molecules are constantly attaching and detaching to the steps due to thermally activation. The strength of bounds between molecules and their neighboring determine if

molecules detach from the crystal or adhere to it. Therefore temperature is a dominant parameter in growth since the strength of bonding is a function of temperature rather than the flux. In contrast, the diffusion flux to the surface is proportional to the concentration and decomposition of molecules in amorphous phase. Presence of impurities in the amorphous phase, play an important role on the diffusion flux and consequently on the kinetics of the growth. Since in most crystals, the bonds are anisotropic and the energy barrier seen by the molecules are different, the edges are usually fuzzy [44, 45].

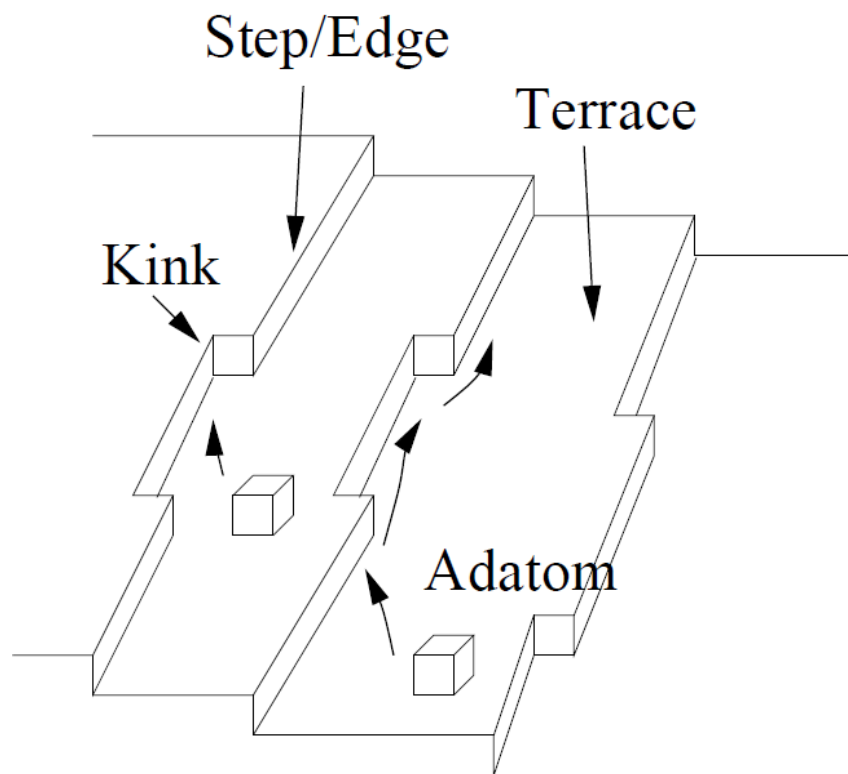


*Figure 4 The atomic processes during crystal growth, Solute molecules enter kinks either directly from solution or after adsorbing and diffusing across terraces.*

## **1.7 Methods to produce metastable $\text{Al}_2\text{O}_3$ and amorphous alumina**

### **1.7.1 Vapor deposition techniques**

One important method for synthesis of  $\alpha\text{-Al}_2\text{O}_3$  and alumina polymorphs in industry is thermal chemical vapor deposition (CVD). Higher deposition temperatures increase the chance of phase transformation as well as producing cracks and poor adhesion. To avoid this problem, bombarding of energetic ions which are available in plasma based physical and chemical vapor deposition techniques can be used. Besides the ion energy and the growth temperature the phase formation is also influenced by the presence of “seeds” in the substrates. Oxygen pressure has also been reported as a controlling factor for synthesis of alumina polymorphs [46]. Figure 5 summarizes selected reported data on the growth temperatures of different  $\text{Al}_2\text{O}_3$  polymorphs using various vapor deposition techniques [12].

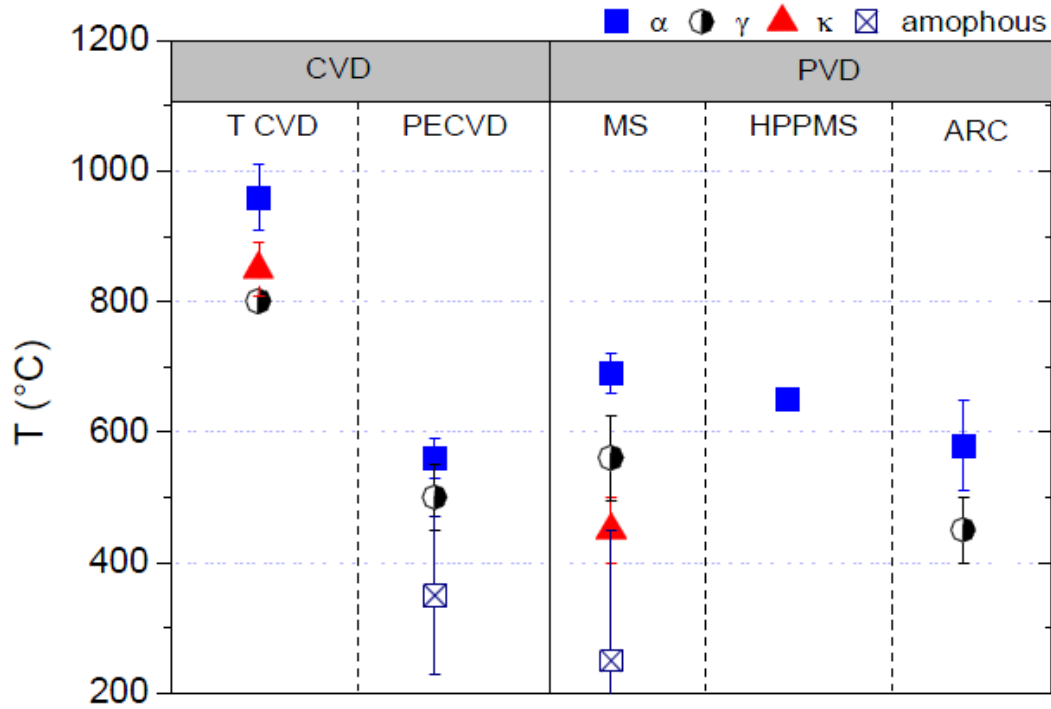


Figure 5 Selected literature data on the growth temperatures of different  $\text{Al}_2\text{O}_3$  polymorphs using various vapor deposition techniques [12]

### 1.7.2 Alumina melt

The structure of alumina melt is not been well understood. Based on work by Ansell et al. [47],  $\text{Al}_2\text{O}_3$  undergoes a structural rearrangement on melting, with a change of the aluminum cation coordination from octahedral, in  $\alpha\text{-Al}_2\text{O}_3$ , to predominantly tetrahedral in the  $\text{Al}_2\text{O}_3$  melt. Waseda et al. [48] has reported octahedrally coordinated aluminum as the fundamental cluster configuration in the melt. Although  $\text{Al}_2\text{O}_3$  is not a glass former, quenching of alumina melt at high cooling rates of more than  $10^5$  K/s can formed amorphous alumina as a thin film. Amorphous alumina consequently can

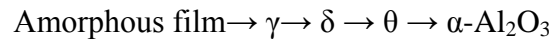
crystallize to form  $\gamma$ - $\text{Al}_2\text{O}_3$  or the other transition alumina phases, all containing tetrahedrally coordinated aluminum. Based on work by Lee et al., a thin film of amorphous alumina contains 95% four- and five-coordinated species, while six-coordinated species comprise 5% [49]. Therefore the average coordination number of  $\text{Al}_2\text{O}_3$  melts was suggested to be 4.5 [50]. Annealing the thin film amorphous alumina at 800 °C cause the five-coordinated species convert to four- and six-coordinated species through a mechanism involves the formation of edge-sharing tetrahedrons and octahedrons, indicating the onset of crystallization of  $\text{Al}_2\text{O}_3$  [51].

### **1.7.3 Amorphous anodic $\text{Al}_2\text{O}_3$ films**

Amorphous aluminum oxide can be made by anodic oxidation. An Al substrate can be oxidized with boiling water to form a hydrous oxide, and then to anodize in a neutral borate solution at high temperature. The hydrous oxide is pseudoboehmite (PB), an oxyhydroxide containing excess water with approximate composition  $\text{AlOOH} \cdot \text{H}_2\text{O}$ . During anodization, amorphous alumina grows under the PB layer by anion transport to the metal interface [52]. Another way to form amorphous  $\text{Al}_2\text{O}_3$  films is anodization of aluminum in acid solution. Nonporous amorphous  $\text{Al}_2\text{O}_3$  films are formed in solutions that do not dissolve  $\text{Al}_2\text{O}_3$ , whereas porous  $\text{Al}_2\text{O}_3$  films are developed in acid solutions, where partial solubility is possible. Amorphous  $\text{Al}_2\text{O}_3$  films commonly have been assumed to contain a mixture of tetragonally and octahedrally coordinated aluminum. Dense  $\text{Al}_2\text{O}_3$  films contain 80% of aluminum cations in octahedral sites and 20% in tetrahedral sites. The aluminum cations in the porous  $\text{Al}_2\text{O}_3$  films predominantly have tetrahedral or even lower coordination [7] .

#### 1.7.4 Thermal oxidation of aluminum

Aluminum oxide is produced almost instantaneously by aluminum or its alloys in the presence of any environment containing oxygen. This aluminum oxide consists of amorphous alumina and prevents additional oxidation of aluminum and its alloys at low temperatures. At elevated temperatures, the common route of phase transformations in alumina film grown on aluminum surface by thermal oxidation as:



Jeurgens et al. found that there is a critical thickness for amorphous alumina. When the thickness of this layer exceeds the critical value, it starts to transform to the crystalline forms [53]. The critical thickness depends on temperature and the crystallographic orientation of the aluminum substrate. In the temperature range of 20-600 °C, the specific values of the critical thickness are close to 0.5, 2.5, and 5 nm for the (111), (100), and (110) crystallographic faces of aluminum, respectively [53]. After reaching the critical thickness, the thin layer of amorphous alumina transform to metastable  $\gamma$ -alumina. In range of 950-1250 °C,  $\gamma$ -alumina transforms into the thermodynamically stable  $\alpha$ -alumina via intermediate phases of  $\delta$ -, and  $\theta$ -alumina.

#### 1.7.5 Other precursors for metastable aluminas and the sequence of transformation

The most common  $\text{Al}_2\text{O}_3$  precursors for metastable aluminas are aluminum trihydroxide ( $\text{Al}(\text{OH})_3$ ), monohydroxide ( $\text{AlOOH}$ ), gibbsite ( $\gamma\text{-Al}(\text{OH})_3$ ), boehmite ( $\gamma\text{-AlOOH}$ ), and tohdite ( $5\text{Al}_2\text{O}_3 \cdot \text{H}_2\text{O}$ ). Table 1 and 2 summarize the thermal processing

routes to form different metastable  $\text{Al}_2\text{O}_3$  structures as well as the sequence of the transformations [7].

### **1.8 Ion Implantation**

The transistor era started in 1947 when Brattain and Bardeen at Bell Labs showed that doping of some atoms which accept electrons could amplify signals of a Ge crystal. Since then doping of materials in a controlled way has been challenged [54]. The use of particle accelerator was a solution for this problem. Particle accelerators are usually very precise for controlling fluence. Impurity depth and concentration can be controlled independently using particle accelerators. The ability to produce complex as well as retrograde profiles in a short time is another advantage. The parameters of the ion beam such as flux, energy, species and charge state and direction (and divergence) are all easily can be quantified and controlled.

Particle accelerators (ion beam accelerators) also provide a unique technique for researchers to study the structure of materials under nonequilibrium condition. It has been recognized for years that ion beam radiation might make changes in material to improve some properties of interest, mostly because of the damage processes. Mechanical, electrical, optical, magnetic, and superconducting properties all are affected by the presence of the foreign ions and the damages produced by them. Mimicking damages in nuclear reactor components and other systems is another use of these studies.

Among the ion beam applications, ion irradiation and ion implantation is an attractive technique to change the properties of a wide range of materials. The atomic species to be implanted in the target material are first ionized and then accelerated to

energies of 25-200 KeV. The incident ions penetrate the surface of the material and form an ion enriched layer [55]. Beside the injection of impurity or alloying, ions, other structural changes may result from ion beam bombardment of the surface such as stretching bond, breaking bond, surface adatoms, sputtering of atoms from the surface, formation of surface and bulk defects (vacancies, dislocations, interstitials), amorphizing the bombarded zone, developing damaged layers for thickness greater than mean projectile range, and finally inducing changes in optical, electrical, magnetic, mechanical properties [56]. The depth of penetration is a function of the atomic numbers and masses of both the ions and target atoms and the rate of energy transfer. For example Fig.6 shows the result of irradiation of  $\text{Al}_2\text{O}_3$  with different ions each, with energy of 175 keV. The ion range decreases with increasing the atomic mass of ion species. The irradiation and implantation of ions into target materials can lead to the production of amorphous or metastable polymorphs. The mobile ions during implantation may form new precipitates with the target atoms. The precipitation produces high density of point defects which develop compressive stresses. The generation of compressive stress on the surface results in mechanical properties changes. Ion irradiation process has been carried out on metals, ceramics and polymers [55].



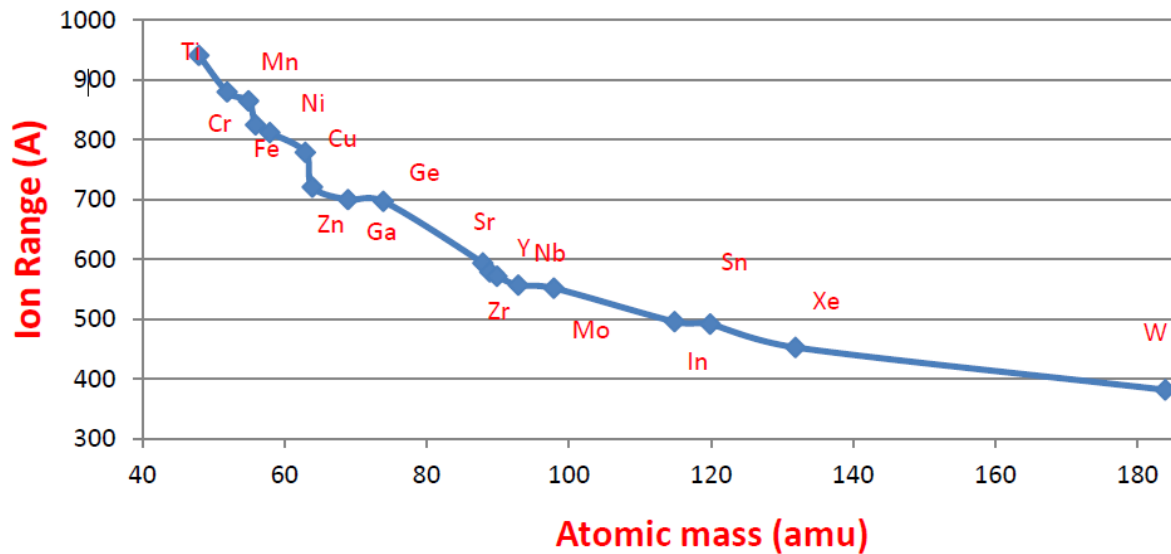


*Figure 6 Effect of atomic mass of ions on the range. Calculated with full damage cascade SRIM-2013. For the calculation the species energy and the angle of the incident ion considered to be 175 keV and 7° respectively.*

The energy of an accelerated ion colliding with a material is dissipated by two fundamental mechanisms: inelastic (electronic) and elastic (nuclear) collision. The nuclear energy loss that dominates at low energies (typically below 10 keV/amu) is caused by the scattering of the projectile by the screened nuclear potential of the target atoms. The electronic loss causes excitation or ionization of atoms in the target. Each collision leads to a slowing down of the moving projectile and also a deflection of the trajectory that gives rise to the term of scattering. The rate of energy transfer for each process is a function of the mass and charge of the incoming ions, the target material and the incident energy. The nuclear collision displaces lattice ions and can result in damage cascades. Both stopping powers increase with increasing energy until they reach a

maximum value, and thereafter decrease [54]. The best known simulation program SRIM (Stopping and Range of Ions in Matter), has been developed to calculate the motion of ions in a medium, by simulating the collisions with nuclei in the medium [57].

Figure 7 shows the distribution of the electronic and nuclear stopping power of zirconium into sapphire as a function of Zr ion energy. Fig. 7 shows that the ballistic (nuclear) energy loss dominates at energies lower than about 1 MeV and it is this process that is primarily responsible for the lattice damage. At higher ion energy the electronic energy loss dominates.

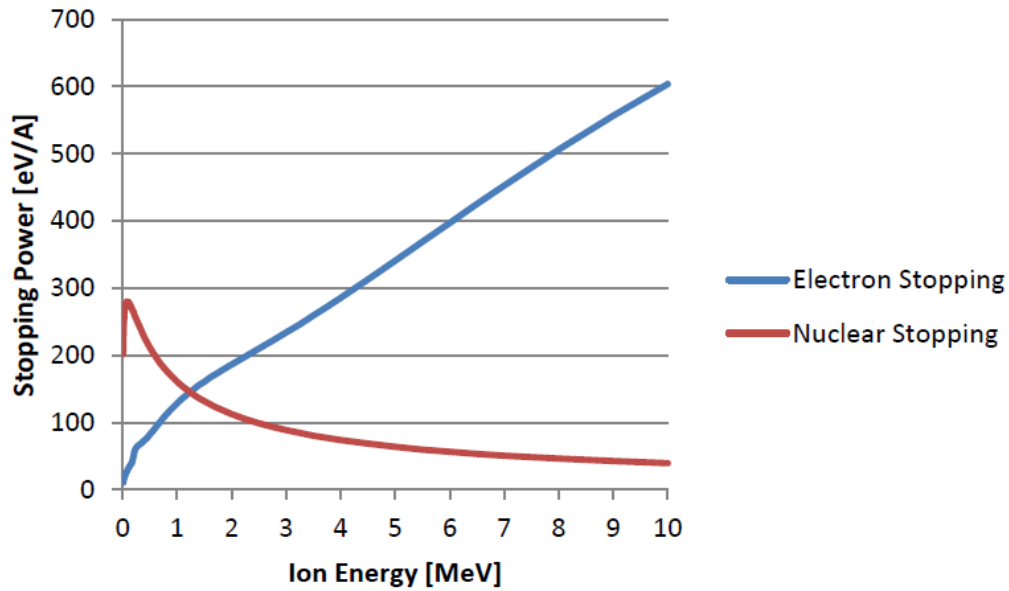


*Figure 7 The variation of the electronic and nuclear stopping power of zirconium into sapphire as a function of Zr ion energy (calculated by SRIM-2013)*

### 1.9 Ion implantation-induced amorphization

Ion implantation-induced amorphization has been observed during irradiation at temperatures sufficiently far below the crystallization temperature of the amorphous phase. Covalently bonded systems are particularly conducive to amorphization (even pure elements Si and Ge). In contrast, there has been no observation of amorphization under irradiation for pure metal even at irradiation temperatures below 10 K. In ionic crystals the position of the implanted ion in the lattice, the lattice disorder and the presence of impurities determine the chemical state of the implant. In covalent compounds the formation and rupture of bonds is an additional factor. In general the important factors that affect amorphization during ion irradiation are temperature, ion mass, ion energy, dose rate, and the properties of the target material [58]. Chemical effect (changes in the chemical structure and composition of the targets induced by the irradiation) is another important factor that affects ion irradiation-induced amorphization. Among these factors the ion energy (accelerating voltage) in general is not of major importance for amorphization [59].

Upon entering the target lattice, the incident ions will at first suffer few atomic collisions due to their high velocity and will lose energy slowly by ionizing the host atoms. As the ion energy is reduced, the probability of nuclear collisions increases. Hence, after traveling some distance without causing atomic displacement, they undergo a catastrophic loss in energy due to nuclear collisions with the target lattice atoms. This results in the formation of a large number of interstitial atoms or ions and vacant lattice

sites. As a result the crystal is most heavily damaged at a depth near  $R_p$  where  $R_p$  is the projected range of the incident ions.

There are two models to explain how a material can be amorphized: direct impact and defect accumulation. The direct impact model mostly applies for ions and targets of relatively high atomic number and for ion beam energies usually employed in ion implantation. In this model the energy lost by the ion is concentrated in a “thermal spike” which can lead to amorphization along a single ion cascade by the melting of a small region followed by rapid cooling similar to liquid quenching. The defect accumulation model mostly applies for relatively light atoms and moderate energies. In this model, the ions make the material amorphous due to an accumulation of defects produced by independent atomic displacements rather than a collective, thermal process [60, 61]. During ion irradiation the ions displace atoms from lattice sites and create vacancy-interstitial pairs and other associated defects.

### **1.10 Statement of the problem and background of the study**

Among alumina's many polymorphs,  $\alpha$ -alumina and  $\gamma$ -alumina have important applications in different areas. For example the thermodynamically stable  $\alpha$ - phase is widely used in protective coatings and wear-resistant, due to its chemical inertness, good mechanical properties, and thermal stability and  $\gamma$ -alumina is used in catalysts for automotive emission control, adsorbents, and soft abrasives applications due to its high surface area. In high-temperature applications, a problem with the use of the  $\gamma$ -phase is its transform into the  $\alpha$ -phase at  $>800^\circ\text{C}$ . Therefore, formation and control of the different

phases of alumina is of great interest. This has led to the experimental research on doping of alumina to increase its thermal stability.

#### **1.10.1 Importance of microstructure study of $\alpha$ - $\text{Al}_2\text{O}_3$ during ion irradiation and kinetics study of alumina transformation**

Due to high surface area and desired mechanical, chemical, and thermal properties as well as low cost,  $\gamma$ - $\text{Al}_2\text{O}_3$  is one of the most important material used as a support in the metal catalyst industry. Gamma alumina facilitates the formation of extremely small metal particles with a high proportion of the atoms at the surface and has a remarkable thermal stability. This support allows the incorporation of beneficial additives, usually known as promoters. In some catalyst applications, such as automotive emission control, the molecular length scale of open internal surfaces of porous gamma alumina, provide active sites for the heterogeneous catalysts. Therefore gamma alumina due to its distinctive properties is one of the most promising advanced materials for metal catalyst industry.

Because the catalyst activity is closely related to the structure of the support and its stability, structural transformations during the operation at elevated temperatures is a key factor. In high-temperature applications, a limitation to the use of  $\gamma$ -phase is that it transforms into the  $\alpha$ -phase at a temperature above 800 °C. Therefore, control the formation of, and transformations between, the different phases of alumina is of great interest. This has led to the experimental research on doping of alumina to increase its thermal stability.

There are many studies of the effect of dopants on alumina phase transformation and related areas [1, 10, 24, 29, 62-125]. Some of these studies showed that doping of different atoms and oxides has a great influence on the retarding or accelerating of structural transformation. Ragan [126] summarized many of these studies (shown in Table 4). A similar effect for the addition of metallic oxides also has been investigated. The study of oxide additives has shown that among  $B_2O_3$ ,  $SiO_2$ ,  $ZrO_2$ ,  $Li_2O$ ,  $LiF$ ,  $V_2O_5$ ,  $CuO$ ,  $Cu_2O$ ,  $TiO_2 + MnO / Mn_2O_3$ ,  $TiO_2 + CuO / Cu_2O$ , and  $ZnF_2$ , zirconium oxide ( $ZrO_2$ ) strongly retards the  $\gamma \rightarrow \alpha$  transformation whereas  $B_2O_3$  and  $SiO_2$  have less effect. Reports on implantation of many cations into  $\alpha-Al_2O_3$  indicate that irradiation of Zr results in an amorphous region at much lower fluence than many other species. Therefore, the recrystallized gamma alumina from the amorphous region has a lower concentration of the doped material compare with the other atoms. These studies suggest that Zr may be a good candidate for thermal stabilization of  $\gamma$  -alumina. In spite of this fact that doping has been found to inhibit this phase transformation, there is not an atomistic understanding of the mechanism [127]. This study is directed to shed light on the microstructure of  $\alpha-Al_2O_3$  during Zr and Zr plus O irradiation as well as effect of thermal annealing.

*Table 3 Summary of studies about the effect of dopants in alumina phase transformation*

Cation	Cationic Radius [nm]	Kinetics $\gamma \rightarrow \alpha$	Characterization method	Researcher
B <sup>3+</sup>	0.027	retarded	DTA,XRD	L.A Xue et al.
Si <sup>4+</sup>	0.04	retarded	DTA,XRD	L.A Xue et al.
V <sup>5+</sup>	0.054	accelerated	DTA,XRD	L.A Xue et al. D. Tsai et al.
Co <sup>3+</sup>	0.0545	accelerated	DTA	M. Ozawa et al.
Ti <sup>4+</sup>	0.0605	accelerated	DTA,XRD	D. Tsai et al.
Cr <sup>3+</sup>	0.0615	retarded	XRD	G.C.Bye
Cr <sup>3+</sup>	0.0615	retarded	TRR	N. Yu
Cr <sup>3+</sup>	0.0615	accelerated	DTA	M. Ozawa et al.
Cr <sup>3+</sup>	0.0615	accelerated	TGA,XRD	M. W. Brumm
Ga <sup>3+</sup>	0.062	accelerated	DTA, XRD	P.Burtin
Mn <sup>3+</sup>	0.0645	accelerated	DTA	M. Ozawa et al.
Fe <sup>3+</sup>	0.0645	accelerated	XRD	A.D. Polli et al. G. C. Bye

*Table 3 continue*

Cation	Cationic Radius [nm]	Kinetics $\gamma \rightarrow \alpha$	Characterization method	Researcher
Fe <sup>3+</sup>	0.0645	accelerated	DTA	M. Ozawa et al.
Fe <sup>3+</sup>	0.0645	accelerated	DTA,XRD	D. Tsai et al.
Fe <sup>3+</sup>	0.0645	accelerated	RBS,TEM	C.W. White et al.
Fe <sup>3+</sup>	0.0645	accelerated	TRR	N. Yu et al.
Ni <sup>2+</sup>	0.069	accelerated	DTA	M. Ozawa et al.
Mg <sup>2+</sup>	0.072	accelerated	XRD	M. Pijolat et al.
Mg <sup>2+</sup>	0.072	accelerated	DTA, XRD	P. Burtin et al.
Mg <sup>2+</sup>	0.072	retarded	DTA,XRD	D. Tsai et al. P. Bown et al.
Zr <sup>4+</sup>	0.072	retarded	XRD	M. Pijolat et al. P. Burtin et al.
Zr <sup>4+</sup>	0.072	retarded	DTA, XRD	L.A. Xue et al.
Zr <sup>4+</sup>	0.072	accelerated	DTA, XRD	D. Tsai et al.
Cu <sup>2+</sup>	0.073	accelerated	DTA	M. Ozawa et al.
Cu <sup>2+</sup>	0.073	accelerated	DTA,XRD	L. A. Xue et al.



Table 3 continue

Cation	Cationic Radius [nm]	Kinetics $\gamma \rightarrow \alpha$	Characterization method	Researcher
Zn <sup>2+</sup>	0.074	accelerated	DTA,XRD	L. A. Xue et al.
In <sup>3+</sup>	0.08	accelerated	DTA, XRD	P. Burtin et al.
Ce <sup>4+</sup>	0.087	retarded	DTA,XRD	M. Ozawa et al.
Y <sup>3+</sup>	0.09	retarded	DTA, XRD	D. Tsai et al. P. Bown et al.
Y <sup>3+</sup>	0.09	retarded	XRD	B. A. Pint et al.
Th <sup>4+</sup>	0.094	retarded	DTA, XRD	P. Burtin et al.
Ca <sup>2+</sup>	0.10	retarded	DSC,XRD	A. Douy
Ca <sup>2+</sup>	0.10	retarded	DTA, XRD	D. Tsai et al. P. Burtin et al.
La <sup>3+</sup>	0.1032	retarded	DTA, XRD	P. Burtin et al. M. Ozawa et al. H. Schaper et al
La <sup>3+</sup>	0.1032	retarded	NPD	C. K. Loong et al.
Sr <sup>2+</sup>	0.118	retarded	DSC,XRD	A. Douy
Ba <sup>2+</sup>	0.135	retarded	DSC,XRD	A. Douy

### 1.10.2 Effects of dopants in $\alpha$ -Al<sub>2</sub>O<sub>3</sub> on kinetics of alumina transformation

Many studies investigated the effect of dopants on the kinetics of phase transformations in alumina. Most researchers have employed alumina's powder and used characterization techniques such as X-ray diffraction (XRD) and differential thermal analysis (DTA). Almost all previous researches have focused on the  $\gamma$  to  $\alpha$  transformation and very few papers have been published on the formation of  $\gamma$ -alumina from amorphous alumina. These studies did not distinguish the nucleation stage and the subsequent growth kinetics. Some of the studies have considered the impurities or trace particles in  $\alpha$ -alumina to act as seeds to nucleate the epitaxial growth of the new phase. There is no explanation to clarify why some of these impurities accelerate and some decelerate the transformation. Table 4 contains results for four independent kinetic studies of Zr effects on the  $\gamma \rightarrow \alpha$ -alumina transformation. All studies used a similar characterization method to measure the rate of phase transformation. The study by Xue et al. reported that the Zr retarded the rate whereas Tsai et al. reported that Zr accelerate the phase transformation. Different activation energies have been reported for effect of particular dopants on the phase transformations. The effect of Zr on the  $\gamma \rightarrow \alpha$ -alumina transformation studied by Pijolate et al and Burtin et al. also reports that Zr retards the rate of the transformation. In almost all the studies, the nature of short range order (SRO) in amorphous alumina has not been studied.

Among the kinetics studies of alumina's transformation there are two different types of work that haven't used alumina's powder. One group studied a thin film of amorphous alumina on a single crystal sapphire substrate. This group used a soluble salt

of the dopant mixed with the alumina powder. After drying, pressing and sintering using electron beam evaporator technique, they evaporated impregnated alumina powder on the sapphire substrate. Time resolved reflectivity (TRR) was used as the main technique to analyze the kinetic study [128]. Another group of researchers used single crystal alumina and used ion beam irradiation at liquid nitrogen temperature to produce a layer of amorphous region then by annealing the sample they have produced gamma and alpha alumina. RBS and TEM were used as their measurement techniques [129]. These former studies used a technique in which growth stage can be investigated in the absence of nucleation stage. The technique consists of recrystallization of amorphous region to a new phase ( $\gamma$ -alumina) on a preexisting substrate of  $\alpha$ -alumina by solid-phase epitaxial growth. In this method the single crystal of sapphire substrate acts as a nucleation site therefore the measured rate of transformation is directly related to the growth kinetics.

The type of additives, concentration of additives, nature of the gaseous atmosphere, and crystallographic orientation of the underlying substrate that have important influences on the kinetics of the phase transformation investigated in the former studies. Table 5 summarizes the result of different literatures for activation energy chosen from the former studies. In none of the above mentioned studies effect of residual stress has discussed.

Table 4 Summary of growth kinetics studies results

Doped ion	Activation energy [eV]	Related phase transformation	Rate of transformation	Measurement technique	Work of
Er (6 ppm), Y (24, 72 ppm)	5.2±0.1	$\gamma \rightarrow \alpha$	decrease	TRR	Ragan et al. [130]
Er (6 ppm), Y (12,24,200 ppm)	4.1±0.1	$A \rightarrow \gamma$	increase	TRR	Ragan et al. [130]
Er (32 ppm)	4.1±0.1	$A \rightarrow \gamma$	decrease	TRR	Ragan et al. [130]
Cr (2.8 at. %)	5.1±0.2	$\gamma \rightarrow \alpha$	decrease	RBS, TRR	Yu et al. [131]
Fe (2.2 at. %)	5.2±0.2	$\gamma \rightarrow \alpha$	increase	TRR	Yu et al. [131]
Fe (4.5 at. %)	4.9±0.2	$\gamma \rightarrow \alpha$	increase	RBS	Yu et al. [131]
undoped	5.2±0.1	$\gamma \rightarrow \alpha$	-	RBS, TRR	Yu et al. [131]
Fe	3.6	$\gamma \rightarrow \alpha$	increase	RBS, TEM	White et al. [132]
Stoichiometric implant	3.6	$\gamma \rightarrow \alpha$		RBS, TEM	White et al. [132]
Stoichiometric implant	1.6	$A \rightarrow \gamma$		In situ TEM, TEM	Sklad et al. [13]
Stoichiometric implant	7.8	$\gamma \rightarrow \alpha$		In situ TEM, TEM	Sklad et al. [13]
Fe	0.23 (IBIER)	$A \rightarrow \gamma$	decrease	RBS	Yu et al [43]
Fe	5.0 (SPER)	$A \rightarrow \gamma$	decrease	RBS	Yu et al. [43]
Stoichiometric implant	3.57	$A \rightarrow \gamma$	-	TRR	McCallum et al. [133]
Stoichiometric implant	5.2±0.3	$\gamma \rightarrow \alpha$	-	TRR	McCallum et al. [133]
undoped	4.5	$A \rightarrow \gamma$	-	TRR	Simpson et al. [134]
undoped	5.2	$\gamma \rightarrow \alpha$	-	TRR	Simpson et al. [134]
In	0.7, 1.28	$A \rightarrow \alpha$	decrease	RBS, RHEED, SEM	Sood and Gao [135, 136]

Residual stresses are commonly generated during the deposition process of thin films. The residual stresses generated during ion irradiation-synthesized thin film processes and processes such as sputtering and e-beam evaporation can affect the properties, performance and long-term reliability of thin films. Some common effects of residual stresses are film cracking, delamination from the substrate, stress-induced voiding and undesired modifications of physical properties [137]. The fundamental origins of the residual stresses are critical to kinetics study. The residual stress on the thin films can be on the order of few GPa. An ion irradiation produces compressive stresses in the thin film. Ion irradiation-induced phase transformation can produce tensile stresses due to densification of a film constrained by the substrate. Suggested sources of the stress generation include dopant incorporation, grain growth during annealing, and coalescence. The grain boundaries in the film can contribute to densification as sinks for excess vacancies, or by eliminating excess boundary volume as a result of grain growth. Grain boundaries can also play a role in the relaxation of stresses by plastic flow, either as obstacles to dislocations or as sources and sinks in diffusional flow. The high magnitude of stresses depends on the synthesis parameters mainly ion species and their energies that can be expressed simply as ion flux, or as the average energy deposited per atom [138]. Based on this fact, calculated activation energies differ depends on the thin film synthesis parameters.

### 1.10.3 Objective of this Study

The microstructure of  $\alpha$ -Al<sub>2</sub>O<sub>3</sub> irradiated with 175 keV Zr<sup>+</sup> ions plus 55 or 48 keV O<sup>+</sup> ions to different fluences is investigated. The effect of different mechanisms in phase transformation such as irradiation induced-stress relaxation and irradiation induced-phase transformation on kinetics of phase transformation during thermal annealing is discussed. Highlighted results are presented which help understand the microstructure of  $\alpha$ -Al<sub>2</sub>O<sub>3</sub> produced during Zr irradiation and by post implantation processes.

During the phase transformation study, the concentration of additives, nature of the gaseous atmosphere, and crystallographic orientation of the underlying substrate remained fixed. In this work the irradiated samples are studied only at room temperature. Recrystallization of the amorphous layer is studied and compared during thermal annealing and oxygen irradiation on the samples previously implanted with Zr. TEM studies showed that irradiation of single crystal  $\alpha$ -Al<sub>2</sub>O<sub>3</sub> with 175 keV Zr<sup>+</sup> ions produces an amorphous layer sandwiched between two highly damaged layers at fluences  $2 \times 10^{16}$  Zr/cm<sup>2</sup> [139]. This fluence for amorphization of sapphire is very much lower than that reported for other ions with atomic weights similar to zirconium. In this study the exact threshold fluence for amorphization of single crystal  $\alpha$ -Al<sub>2</sub>O<sub>3</sub> during 175 keV Zr<sup>+</sup> ions is determined. Single crystal  $\alpha$ -Al<sub>2</sub>O<sub>3</sub> samples are irradiated with from  $2 \times 10^{15}$  Zr/cm<sup>2</sup> to  $4 \times 10^{16}$  Zr/cm<sup>2</sup>, and the defect structures of the samples are analyzed using TEM and RBS-C. High angle annular dark-field (HAADF) and bright-field (BF) images along with Z-contrast images obtained from aberration-corrected STEM and TEM are presented to reveal microstructure of different regions. The studies show that the amorphous material

during irradiation of  $\alpha$ -Al<sub>2</sub>O<sub>3</sub> with different ions contained short-range-order (SRO) and the details of the SRO depend upon the implanted species [140, 141] . For example the Al-O first near-neighbor distance in amorphous stoichiometric-implanted is  $\gamma$ -Al<sub>2</sub>O<sub>3</sub>, whereas in the amorphous Fe-implanted sample it is  $\alpha$ -Al<sub>2</sub>O<sub>3</sub> [89] . In this study the SRO and the details of the SRO in Zr implanted  $\alpha$ -Al<sub>2</sub>O<sub>3</sub> are discussed.

The effect of post implantation oxygen ions into pre-Zr-implanted samples were also investigated in this study using characterization techniques such as STEM, TEM, RBS, photoluminescence (PL) and optical absorption (OA). This study for the first time reports that during post irradiation with oxygen ions of pre-Zr-implanted sample, ion beam-induced epitaxial recrystallization (IBIER) occur in Al<sub>2</sub>O<sub>3</sub> at room temperature. Nano-beam electron diffraction (NBED) patterns indicate the presence of a  $\gamma$  phase in the recrystallized region.

## **Chapter 2**

### **Literature Review**

#### **2.1 Ion-beam induced amorphization in sapphire**

Important factors that affect a material to be amorphized during ion irradiation are sample temperature, ion mass, ion energy, fluence, and the target material. Different studies show that thermodynamic stability, topology of the atomic scale structure, physical properties and the ease of glass formation play an important role on susceptibility of a material to amorphization [142].

During ion irradiation the ions displace atoms from lattice sites and create vacancy-interstitial pairs and other associated defects. By further ion bombardment an equilibrium defect concentration can be reached and recombination of defects can occur with the same rate as their production. In other cases amorphization is the result of damages during ion bombarding especially at low temperatures [60]. Defects in crystals can be recovered by recrystallization at higher temperature, resulting in a strong dependency of amorphization on temperature. Studies have shown that some amorphizable crystals amorphize only at low or cryogenic temperatures. Usually amorphization does not occur above a threshold value of temperature. Similar to the threshold temperature there is a critical radiation fluence representing a critical accumulated displacement damage dose in units of dpa, above which amorphization occurs below the critical temperature [143]. For instance, Weber found SiC can be amorphized with different ions at room temperature at about 0.5 dpa [144], however SiC



undergoes dislocation climb-driven void swelling with doses of  $>100$  dpa at 1000 K but it remains crystalline [143]. Inui works showed that a dose of 1MeV electrons make silicon carbide amorphous at 77 K [145-148].

Ionic materials such as alkali halides or oxides with the rocksalt or fluorite structures are impossible or nearly impossible to amorphize by ion irradiation. In covalently bonded materials, a dose of 0.1 to 1 dpa make them amorphous, whereas other material with a medium range of ionicity such as  $\text{Al}_2\text{O}_3$ ,  $\text{ZrO}_2$ , and  $\text{MgO}$  require damage greater than 50 dpa to be amorphized [143, 149]. Based on Specht's work, amorphization of sapphire at room temperature requires ion fluences producing damage levels on the order of 100 dpa [60]. Fig. 8 shows the  $\chi_{\text{Al}}$  as a function of displacement damage dose (in units of dpa) for different ions. Among these ions Zr amorphizes sapphire at much lower dpa than the others. A value of unity for  $\chi=1$  indicates random scattering or "amorphous" matter.

Many of the ion irradiation studies in sapphire are summarized in Table 6. There are other studies on the effect of implantation of various ions on polycrystalline/single crystal alumina. Table 6 summarizes the studies of ions only with the energy of less than or equal to 400 keV on single crystalline  $\alpha\text{-Al}_2\text{O}_3$ .

Another important factor for radiation-induced amorphization is the chemistry between irradiated ions and host material. Chemical reaction of the implanted ion with the host atoms is known as "chemical effect". Zinkle proposed that thermal diffusion may be enhance by a chemical effect whereas it is negligible at the absence of a chemical reaction. Enhanced diffusion can propagate amorphization from end-range through the

mid-range. As a result of chemical effect the relatively low concentrations of implanted species which come to rest in the midrange with no diffusion may lead to amorphization by inhibiting damage recovery mechanisms [60]. White noted that having a preference for a specific oxidation state may lead to stabilization of the amorphous phase in the host materials, but at this stage this has not been proven categorically [150]. Hunt et al and Werner et al stated that a chemical effect can occur if the Gibbs free energy of the reaction of the ion and the host material is negative [151, 152].

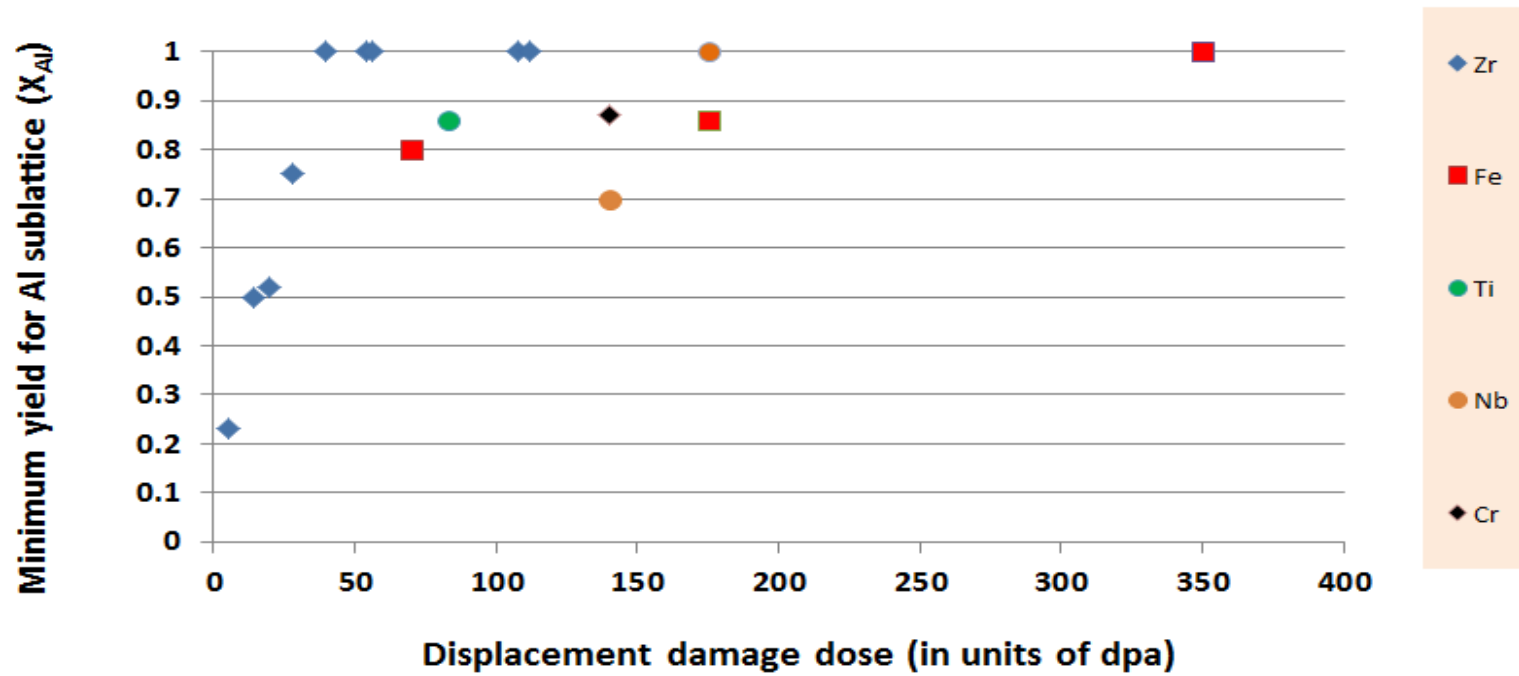


Figure 8 Minimum yield for Al-sublattice ( $\chi_{Al}$ ) as a function of displacement damage dose (in units of dpa) for different ions calculated based on information on [153-155]

Table 5 Summary of ion irradiation studies in sapphire

Ion	Ion energy [keV]	Fluence [ion/cm <sup>2</sup> ]	Temp. [°C]	Amorphization	Characterization technique	Reference
Fe	100	$4 \times 10^{16}$	-200	N	TEM, XRD, CEMS	[156]
Fe	160	$7 \times 10^{16}$	25	N	RBS, TEM, CEMS	[156]
Fe	160	$2 \times 10^{17}$	25	N	RBS, TEM	[10, 157-159]
Fe	400	$1 \times 10^{17}$	240	N	TEM, XRD, VSM	[160, 161]
Fe	160	$4 \times 10^{16}$	45	N	RBS, TEM	[162]
Br	150	$3 \times 10^{16}$	25	Y	SEM.OM	[163, 164]
Br	175	$4 \times 10^{16}$	25	Y	RBS, TEM	[165]
Mn	150	$4 \times 10^{16}$	25	N	RBS, TEM	[162]
Zr	150	$2-4 \times 10^{16}$	25	Y	RBS, TEM	[139, 166-168]
W	250	$1.5 \times 10^{16}$	25	N	RBS, TEM	[162, 165]
W	160	$1 \times 10^{16}$	25	Y	RBS, AS	[169]
Cu	130	$4 \times 10^{16}$	25	N	RBS, TEM	[162, 165]
Ni	160	$4 \times 10^{16}$	45	N	TEM, XPS, GXR	[170]
Xe	900	Flux= $10-20 \times 10^{16}$ /cm <sup>2</sup> /s	-183-25	Y	TEM	[171]
Kr	600	Flux= $10-20 \times 10^{16}$ /cm <sup>2</sup> /s	-136	Y	TEM	[171]
Al/O	90/55	$4 \times 10^{16}/6 \times 10^{16}$	LN	Y	RBS, TEM	[129]
Al	90	$4 \times 10^{16}$	25	N	RBS, TEM	[162]
Ti	150	$3 \times 10^{16}$	25	N	RBS, EPR, MH	[168]
Ti	150	$5 \times 10^{16}$	25	Y	RBS, TEM, PL	[172]
Ti	150	$1-5 \times 10^{16}$	25	N	RBS, TEM, PL	[172]
Ti	100, 150	$0.1-5 \times 10^{16}$	25	N	RBS, TEM, OA, PL	[173]
Ti	100, 150	$5 \times 10^{16}$	25	Y	RBS, TEM, OA, PL	[173]
Cr	280	$4 \times 10^{16}$	25	N	RBS	[168]
Cr	280	$4 \times 10^{16}$	-196	Y	RBS, TEM	[167]
Cr	280	$4 \times 10^{17}$	25, 367	N	RBS, EPR, MH	[168]
Cr	300	$1-10 \times 10^{16}$	25	N	RBS, TEM	[153, 154]
Cr	150	$1-10 \times 10^{16}$	25	N	RBS, OA	[174]
Cr	150	$2.9 \times 10^{17}$	25	Y	RBS, OA	[174]
Nb	220	$4 \times 10^{16}$	25	N	RBS	[10]
Ga	135	$4 \times 10^{16}$	25	N	RBS, TEM	[162]
Mo	130	$2 \times 10^{16}$	25	N	RBS, TEM	[162]
Zn	165	$4 \times 10^{16}$	25	Y	RBS, TEM	[174]

Table 5 continue

Ion	Ion energy [keV]	Fluence [ion/cm <sup>2</sup> ]	Fluence [ion/cm <sup>2</sup> ]	Amorphization	Characterization technique	Reference
Zr	155	$4 \times 10^{16}$	25	Y	RBS, TEM	[140]
Zr	175	$7.5 \times 10^{15}$	25	N	RBS, TEM	[141]
Zr	175	$1.5 \times 10^{16}$	25	Y	RBS, TEM	[141]
Zr	175	$2 \times 10^{16}$	25	Y	RBS, TEM	[141]
Fe	160	$7 \times 10^{16}$	-185	Y	RBS, TEM	[175]
Fe	160	$1 \times 10^{17}$	-185	Y	RBS, TEM	[175]
Fe	380	$1 \times 10^{17}$	25			[176]
Fe	160	$1 \times 10^{17}$	25	N	RBS, TEM, OA, PL	[177, 178]
Fe	160	$4 \times 10^{17}$	25	Y	RBS, TEM, OA, PL	[177, 178]
Fe	85	$4 \times 10^{16}$	25	N	CEMS	[176]
Fe	85	$1 \times 10^{17}$	25	N	CEMS	[176]
Fe	160	$2 \times 10^{17}$	25	Y	RBS, TEM, OA, PL	[178]
Co	100, 150	$0.1-5 \times 10^{16}$	25	N	RBS, TEM, OA, PL	[173]
Co	100, 150	$2 \times 10^{17}$	25	Y	RBS, TEM, OA, PL	[173]
Cu	160	$2 \times 10^{16}$	25	N	RBS, TEM, OA	[179]
Cu	130	$4 \times 10^{16}$	25	N	RBS, TEM	[162]
Ag	1500	$2-20 \times 10^{16}$	-200	N	RBS, TEM, OA	[179]
Pt	30	$1-2 \times 10^{16}$	25	N	RBS	[180]
In	160	$4 \times 10^{16}$	25	N	RBS, TEM	[162, 174]
Pb	50	$4.08 \times 10^{15}$	25	Y	RBS, OA	[174]
Fe	160	$4 \times 10^{16}$	LN	Y	RBS, TEM	[85]
Sn	180	$4 \times 10^{16}$	77	Y	RBS	[181]
Sn	180	$1-10 \times 10^{16}$	25	Y	RBS, TEM	[182, 183]
Sn	180	$1 \times 10^{15}$	25	N	RBS, TEM	[182, 183]
Nb	150	$1-5 \times 10^{16}$	25	N	RBS, XPS	[184]
Nb	150	$5-10 \times 10^{16}$	25	Y	RBS, XPS	[184]
C	150	$1-10 \times 10^{16}$	25	N	RBS, TEM, EELS	[185]
C	150	$1-10 \times 10^{16}$	1000	N	RBS, TEM, EELS	[185]
C	150	$1 \times 10^{17}$	25	Y	RBS, TEM, EELS	[185]
N	150	$1-10 \times 10^{16}$	25, 1000	N	RBS, TEM, EELS	[185]
Mn	150	$4 \times 10^{16}$	25	N	RBS, TEM	[162]
W	250	$1.5 \times 10^{16}$	25	N	RBS, TEM	[162]
Ge	50-150	$3-8 \times 10^{15}$	25	N	RBS, TEM	[186]
Hg	100	$0.1-1 \times 10^{15}$	25	N	RBS	[187]
Hg	100	$>1 \times 10^{15}$	25	Y	RBS	[187]
Pt	100	$0.1-1 \times 10^{16}$	25	N	RBS	[169, 187]
Pt	100	$>1 \times 10^{16}$	25	Y	RBS	[187]

Further evidence for the complex nature of the interactions among the implanted species, irradiation-produced defects and the host material is found in the studies using Conversion Electron Energy Mössbauer Spectroscopy (CEMS) on sapphire irradiated with iron [159, 188]. Although iron in the incident beam carried a single charge,  $\text{Fe}^+$ , samples implanted at 300 K contained iron as  $\text{Fe}^{2+}$ ,  $\text{Fe}^0$  (metallic) and  $\text{Fe}^{4+}$ . Moreover, multiple distinctly different local environments for each  $\text{Fe}^{2+}$  and  $\text{Fe}^{4+}$  could be identified. Charge compensation was provided by the formation of complexes with oxygen vacancies. The same valence states are found for samples irradiated at 77 K but the ratios between each state were different from those implanted at room temperature.

Irradiation of sapphire with 180 keV tin ions to a fluence of  $4 \times 10^{16} \text{ Sn/cm}^2$  also produced an amorphous (disordered) phase at room temperature. The transmission electron microscope (TEM) studies indicated the presence of two amorphous “phases” and the CEMS measurements detected tin in two states,  $\text{Sn}^{2+}$  and  $\text{Sn}^{4+}$  [94].

Burnett and Page attempted to correlate the formation of the amorphous state in several ceramics with a critical deposited energy value with limited success [149]. They also proposed a relationship between the energy density for amorphization and the bonding characteristics, i.e. the degree of ionicity or covalency. A critical deposited energy density for  $\text{Al}_2\text{O}_3$  was proposed to be between 3.4 and 6.8 keV per atom.

It should be noted that the concentration of implanted ions with the high fluences generally for required amorphization of ceramics that have a high degree of ionic bonding represent a major deviation from stoichiometry for the host material. Fluences of  $\sim 10^{17} \text{ ions/cm}^2$  produce peak concentrations of 0.2 to 0.4 implanted impurities for each

cation. There is a major excess positive charge in the crystal unless there is a precipitation in the metallic state of one type of cation.

Short-range order in the amorphous phase of sapphire produced by ion irradiation has been detected by Extended Energy Loss Fine Structure Spectroscopy (EXELFS). Sklad, Angelini and Sevely determined the partial radial distribution functions for samples implanted at 77 K with iron or with aluminum followed by oxygen [189]. The first near-neighbor distance for the iron-irradiated sample suggests a structure of  $\alpha$ -Al<sub>2</sub>O<sub>3</sub>, whereas, that for the sample implanted with Al followed by oxygen is  $\gamma$ -Al<sub>2</sub>O<sub>3</sub>.

Formation of  $\gamma$ -Al<sub>2</sub>O<sub>3</sub> from  $\alpha$ -Al<sub>2</sub>O<sub>3</sub> can be produced by processes other than ion irradiation. Cao et al. reported the formation of  $\gamma$ -Al<sub>2</sub>O<sub>3</sub> directly from pulsed-laser irradiated sapphire. They proposed that the  $\gamma$ -Al<sub>2</sub>O<sub>3</sub> was formed because laser irradiation is a rapid heating and cooling process in which thin surface layer is heated and melted and evaporated during a 41-ns pulse duration [18].

## **2.2 Single crystalline $\alpha$ -Al<sub>2</sub>O<sub>3</sub> irradiation with Zr**

Irradiation of zirconium in sapphire is of special interest since previous studies indicated that irradiation of zirconium into single crystalline  $\alpha$ -Al<sub>2</sub>O<sub>3</sub> produced an amorphous region, whereas, some ions of similar mass and energy, e.g., Nb, produced only highly disordered crystalline regions [129, 167]. The results for irradiation of different ion species in sapphire has been summarized in reference [132]. The authors compared different studies to show that type of ion species as well as the temperature of the substrate during ion irradiation has a significant effect on damage retained as a result of irradiation. White et al. suggested a "chemical effect" to justify why in some cases the

critical dose required for amorphization is lower compare with another ion with a similar mass. For an example of such a chemical effect, they compare the specimens irradiated with  $\text{Zr}^+$  ions to a fluence of  $2 \times 10^{16} \text{ Zr/cm}^2$  to that implanted with Nb and Mo (elements of similar mass) to a fluence of  $5 \times 10^{16}$  at room temperature. In the case of zirconium ions, a buried amorphous layer was detected but the irradiation of Nb and Mo did not produce amorphous layers [132]. Recent studies have shown that the threshold fluence for sapphire amorphization with zirconium even is lower than that reported by White et al. The threshold fluence for amorphization of sapphire with 175 keV  $\text{Zr}^+$  ions was reported to be between  $7.5 \times 10^{15}$  and  $1.5 \times 10^{16} \text{ Zr/cm}^2$  [141]. The irradiation energy for threshold for amorphization by Zr appears to have little, if any, effect in the limited range of 150 to 300 keV studied [94, 132, 159, 162, 167].

Other studies have also suggested that “chemical effects” may play a role in defining the implanted structure of sapphire. Alves et al. propose that Pt and Hg show different defect behaviors during the irradiation in sapphire with similar fluences although both species have very close masses [187]. Farlow et al. measured the fraction of implanted ions that substituted for Al on the Al-sublattice using Rutherford backscattering spectroscopy with ion channeling (RBS-C). The RBS-C for irradiation of Cr, Ti, Fe, W, Ga, Mn, Ni, Cu, Nb or Mo did not show any simple relationship between atomic size, valence or electronegativity of the implanted species and lattice position. However, they found no detectable substitution of Zr for Al [162].

An alternation explanation for the irradiation-induced amorphization with Zr has been proposed based on the equilibrium chemical thermodynamics observation that the



free energies of formation of  $\text{Al}_2\text{O}_3$  and  $\text{ZrO}_2$  are nearly the same at high temperatures, perhaps permitting the Zr ions to preferentially react with the oxygen ions [152]. Since any reaction, either among the injected ions and defects or zirconium with oxygen, occurs under highly nonequilibrium irradiation conditions, further studies are necessary to clarify the reason(s) for the observed behavior.

### **2.3 Effect of post ion irradiation on a pre-ion-implanted $\alpha\text{-Al}_2\text{O}_3$**

There have been many studies of annealing as a post-irradiation process for ion irradiated  $\alpha\text{-Al}_2\text{O}_3$ . A few studies investigated the post ion irradiation on a pre-implanted sapphire sample. McHargue et al. studied the effect of oxygen irradiation on a pre-Fe-implanted  $\alpha\text{-Al}_2\text{O}_3$ . Another study by Sina et al. discusses the optical absorption properties of oxygen irradiation on a pre-Zr-implanted sapphire. The optical absorption and RBS results from this study showed that oxygen irradiation reduces the number of color centers. In the current work, TEM results show that oxygen irradiation recrystallizes the amorphous region adjacent to the deeper damaged region due to ion beam-induced epitaxial recrystallization (IBIER). So far there have been no reports of oxygen bubble formation.

According to the published phase diagrams,  $\text{ZrO}_2$  is not soluble in  $\text{Al}_2\text{O}_3$  at any temperature below  $1600^\circ\text{C}$  but to a very little amount at above that temperature (Fig.9). Ternary phases have not been reported for the Al-O-Zr system and there is no evidence that monoclinic  $\alpha\text{-ZrO}_2$  dissolves in  $\text{Al}_2\text{O}_3$ . According to work of Alper et al., the solubility of  $\text{ZrO}_2$  in  $\text{Al}_2\text{O}_3$  is 0.83 mol% at  $1600^\circ\text{C}$  [190]. Jerebtsov found that the solubility of  $\text{ZrO}_2$  in  $\text{Al}_2\text{O}_3$  is even smaller than reported by Alper et al. (0.008 mol%

ZrO<sub>2</sub>) [191]. Therefore we do not expect any solid solution, (Al<sub>x</sub>Zr<sub>(1-x)</sub>)<sub>2</sub>O<sub>3</sub> formation during oxygen implantation, but precipitation of compound(s) as second precipitate(s) is possible.

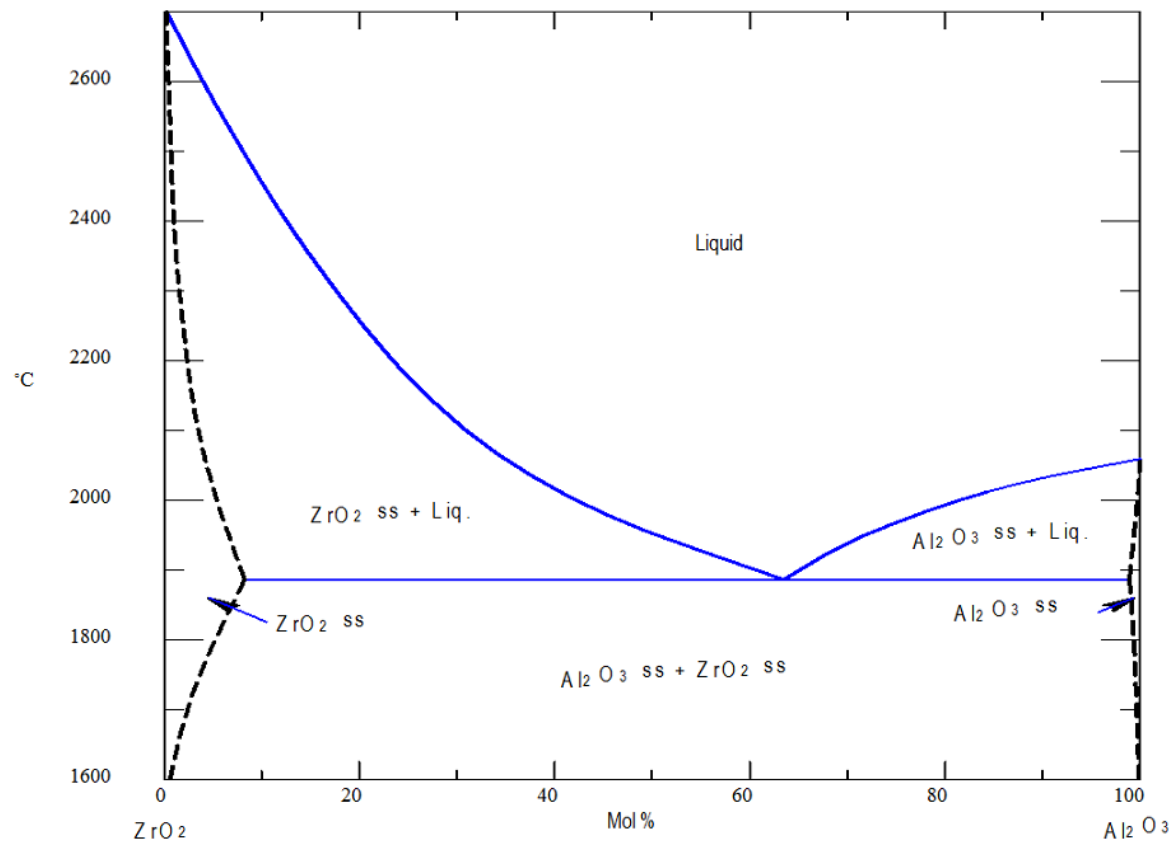


Figure 9 Phase diagram of  $\text{ZrO}_2\text{-Al}_2\text{O}_3$  [192]

Since ion irradiation is a process far from equilibrium, possible effects of ion irradiation of oxygen on the Zr-implanted  $\text{Al}_2\text{O}_3$  include: (a) compound formation and precipitation due to reactions during the cascade produced by the energetic oxygen ions; (b) interactions of the injected oxygen with Zr and/or displaced Al ions in the cascades to stabilize the disorder created by the “thermal spike”; (c) enhanced recovery of the disorder caused by the Zr-implantation.

The proposed study will investigate the structure(s) produced during irradiation and after annealing in order to further our understanding of the proposed “chemical effects.

## **2.4 Effect of annealing**

Figure 10 illustrates the wide variety of defects introduced in a crystalline target during ion irradiation. Whereas, many of the defects are eliminated by dynamic annealing process during bombardment, many are trapped to leave the sample in a thermodynamic metastable state. Upon annealing, thermal activated processes (e.g. diffusion and phase changes) drive the system toward the equilibrium state. Regions rendered amorphous by irradiation, recrystallize at elevated temperatures.

Bull and Page suggested a quantitative model that indicates the activation energy for annealing of the amorphous material during irradiation (dynamic annealing) is very much lower than might be expected for post-implantation thermal annealing of the same material [193]. There have been many studies on post-implantation annealing recovery of disorder, implanted species distribution, and phase formation. Two cases pertain to this proposed study:

- 1) Annealing of damaged but crystalline structures
- 2) Recrystallization and epitaxial regrowth of implanted amorphous  $\text{Al}_2\text{O}_3$

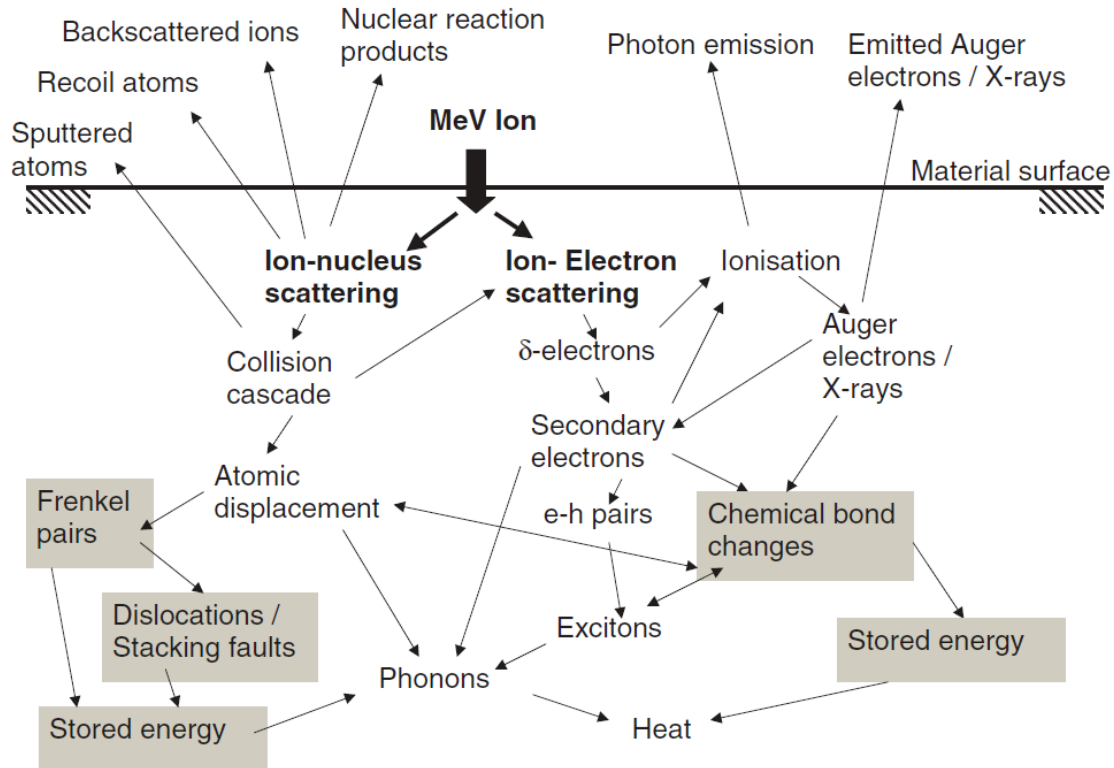


*Figure 10 Schematic illustration of the evolution during ion irradiation of a solid target processes. The grey shaded processes correspond to long term effects. After Zhang and Whitlow [194]*

#### 2.4.1 Annealing of $\alpha\text{-Al}_2\text{O}_3$ irradiated with iron followed by oxygen

McHargue et al. irradiated c-cut sapphire single crystals with 160 keV  $\text{Fe}^+$  ions to a fluence of  $4 \times 10^{16} \text{ Fe/cm}^2$ , followed by 54 keV  $\text{O}^+$  ions to a fluence of  $6 \times 10^{16} \text{ O/cm}^2$ .

The samples were annealed for one hour at 500, 800 and 1200 °C in an oxidizing or a reducing (Ar-4% H<sub>2</sub>) atmosphere. The residual damage (disorder) was determined by RBC-C spectroscopy. All samples retained about 90% of the disorder after 1 hour at 500 °C in both annealing atmospheres. The retained disorder (20-25%) was similar for the conditions annealed in the oxidizing atmosphere at 800 °C but significantly more (~53%) for the sample irradiated with iron only. The sample irradiated only with iron also retained more disorder after annealing at 1200 °C in both atmospheres (Figure 11). Hence, the irradiation of iron plus oxygen accelerated the recovery process(s) at temperatures above 500 °C in both annealing atmospheres [195]. Implanted species may migrate toward the surface during recrystallization but under certain conditions, the implant can be trapped at defects or create a second phase. Mouritz et al studied annealing of low melting point metals implanted into sapphire in an argon atmosphere. They found the retained concentration of these metals such as Zn, In, and Pb is independent of both implanted fluence and phase diagram consideration [174].

#### **2.4.2 Annealing of pre-amorphized Al<sub>2</sub>O<sub>3</sub> produced by ion-beam irradiation**

White et al summarized the studies on annealing samples in an inert (Ar) atmosphere that have an amorphous surface layer produced by irradiation with aluminum ions followed by oxygen ions at 77 K [129]. The amorphous layer first transforms to  $\gamma$ -Al<sub>2</sub>O<sub>3</sub> containing subgrains. Further annealing grows the subgrains of  $\gamma$ -Al<sub>2</sub>O<sub>3</sub> and the  $\alpha$ -Al<sub>2</sub>O<sub>3</sub> sub-region epitaxially grows into the  $\gamma$ -phase and eventually converts the entire surface to a single crystal of  $\alpha$ -Al<sub>2</sub>O<sub>3</sub> coherent to the subsurface. Sklad et al found the

same sequence during annealing samples irradiated with iron at 77 K. They followed the redistribution and precipitation of the implantation in both reducing and oxidizing atmospheres [196]. White et al reported that the presence of Fe in the amorphous region increases the kinetics of crystallization significantly but does not change the nature of the crystallization behavior [129].

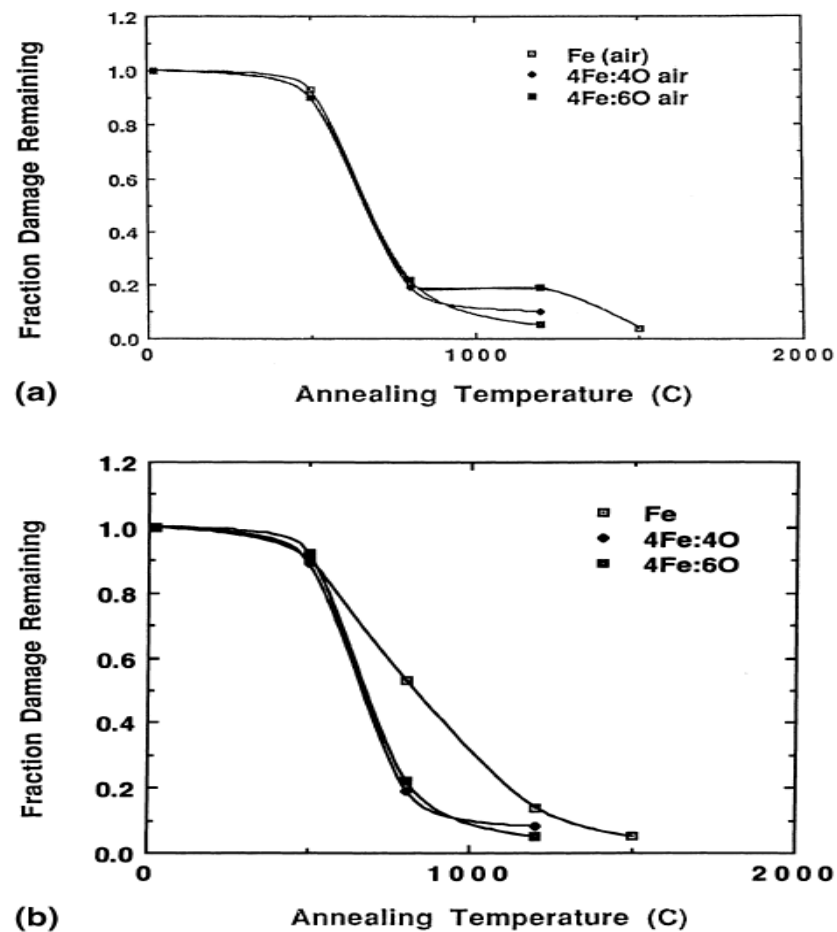


Figure 11 Annealing effect in Fe-implanted sapphire a) annealing in air b) annealing in Ar-4% H<sub>2</sub> atmosphere [195]

Romana et al., produced an amorphous surface layer on c-axis  $\alpha$ - $\text{Al}_2\text{O}_3$  irradiated with 180 keV  $\text{Sn}^+$  ions to a fluence of  $4 \times 10^{14} \text{ Sn/cm}^2$  at room temperature. During annealing in a reducing atmosphere, the recrystallization occurred in the same manner (amorphous  $\rightarrow \gamma$ - $\text{Al}_2\text{O}_3 \rightarrow \alpha$ - $\text{Al}_2\text{O}_3$ ) as described above at temperature above 1233 K. In this case, precipitates of  $\text{SnAl}_2\text{O}_3$  formed at 1233 K. Thermal annealing at 1373 K resulted in the loss of 97% of the implanted Sn. The start of recrystallization of the amorphous region was delayed to 1373 K in the oxidizing atmosphere. In this case, the surface layer consisted of  $\text{SnO}_2$  coherent with  $\gamma$ - $\text{Al}_2\text{O}_3$ . The  $\text{SnO}_2$  precipitates appear to stabilize the  $\gamma$  structure [94].

Annealing of a Sn implanted sample into sapphire has been also reported by Xiang et al. Tetragonal Sn nanoparticles of  $\sim 15 \text{ nm}$  diameter in  $\text{Al}_2\text{O}_3$  produced by direct Sn irradiation at room temperature oxidized after thermal annealing at  $1000^\circ\text{C}$  in oxygen. The irradiation-induced amorphous region, recrystallized and the Sn nanoparticles turned into  $\text{SnO}_2$  nanoparticles with an average diameter of  $\sim 30 \text{ nm}$  [197].

Marques et al studied amorphization of a c-cut  $\text{Al}_2\text{O}_3$  sample by irradiation with 150 keV  $\text{Ti}^+$  ions to a fluence of  $5 \times 10^{16} \text{ Ti/cm}^2$ . Annealing in oxidizing environment led to complete recovery of the amorphous region and segregation of Ti (in form of  $\text{Ti}_3\text{O}_5$ ) to the surface. In the reducing atmosphere the competition between Al and Ti favors the formation of titanium oxide to lower the energy. In the amorphous region, a Ti rich layer and a depletion of Al were detected [172].



Although the disorder as determined from RBS-C measurements reaches the random value and the TEM examinations detect no coherently scattering regions in the amorphous layer, the extended loss fine structure (EXELFS) indicates short-range order (SRO) to be present [159]. This SRO is similar to crystalline  $\alpha$ -Al<sub>2</sub>O<sub>3</sub> in Fe-implanted amorphous layers but similar to crystalline  $\gamma$ -Al<sub>2</sub>O<sub>3</sub> in stoichiometrically (Al+O) irradiated samples. This SRO appears to influence the kinetics of the recrystallization but not the path.

#### **2.4.3 Annealing of zirconium implanted sapphire**

There are only a few studies about the effect of annealing in zirconium implanted in sapphire. The thermal annealing behavior of irradiation with 150 keV with Zr<sup>+</sup> ions to a fluence of  $2 \times 10^{16}$  Zr/cm<sup>2</sup> in  $\alpha$ -Al<sub>2</sub>O<sub>3</sub> has been investigated by Naramoto et al. Annealing in an oxidizing atmosphere to temperatures as high as 1600 °C showed that there is little if any redistribution in depth of Zr [168].

### **2.5 Doping effects on the kinetics of solid-phase epitaxial growth of amorphous $\rightarrow \gamma \rightarrow \alpha$ -alumina**

There are few studies that discuss the effect of doping on the kinetics of the transition from amorphous to crystalline aluminum oxides, using non powder alumina. Amorphizing single crystal sapphire samples by ion irradiation at low temperatures or using proper fluences of ions at room temperature are techniques that can be used to investigate growth stage in absence of nucleation stage. Another technique used for this purpose is depositing a thin film of amorphous alumina on a sapphire substrate using

electron-beam evaporation of alumina containing the appropriate dopants or co-evaporation of the high purity metal with a second *e*-beam gun.

Ragan et al. used deposition of a thin amorphous alumina film technique to prepare the amorphous thin film. The effect of Cr (0.1 at %), Y (0.2, 1, 2 at %), and Er (0.1, 1, 2 at %) deposited into the film with a substrate of c-axis sapphire at different temperatures were studied. Time resolved reflectivity measurements were used to quantify the growth kinetics during phase transformation. The activation energies for amorphous-to- $\gamma$  and for  $\gamma$ -to- $\alpha$  transformation were calculated to be 4.1 and 5.2 eV respectively for the doped and undoped samples. Ragan found that Er retards the amorphous-to- $\gamma$  transformation relative to undoped alumina whereas yttrium and chromium accelerate it. Yttrium and chromium ions decrease the  $\gamma$ -to- $\alpha$  transformation velocity in proportion to their concentration. Concentrations of Er as low as ~6 ppm retard the  $\gamma$ -to- $\alpha$  transformation and concentrations of 32 ppm essentially stop the  $\alpha$  phase transformation [130].

Yu et al. studied the effects of Fe (2.2 and 4.5 ct. %) and Cr (2.8 ct. %) on the kinetics of solid-phase epitaxial growth of amorphous alumina. They made a 200- 265 nm thick amorphous alumina deposited on c-axis single crystal  $\alpha$ -  $\text{Al}_2\text{O}_3$  using electron-beam evaporation. TRR and RBS were employed to study the kinetics of the epitaxial growth at 800–1050 °C in flowing oxygen gas. During the thermal annealing, the amorphous alumina transformed to gamma then to alpha alumina. Yu et al. found that the activation energy of  $\gamma$ -to- $\alpha$  is  $5.0 \pm 0.2$  eV, independent of the presence of dopants. The

Arrhenius plot of the growth rate of  $\gamma$ -to- $\alpha$  transformation showed that Fe enhances while Cr slows the growth rate relative to the undoped case [131].

Clarke studied the epitaxial regrowth of an amorphous thin film containing iron or chromium on a pure sapphire single crystal. He deposited a thin film of amorphous alumina on (0001) sapphire substrates, by electron-beam evaporation from doped, sintered alumina target. Iron (2.2 and 4.5 atomic %) or chromium atoms (2.8 atomic %) were uniformly doped into the films during deposition. Clarke studied the kinetics of the amorphous-to- $\gamma$  and  $\gamma$ -to- $\alpha$  transformation for different orientations of the underlying sapphire substrate by thermal annealing the samples at 1000 °C for 1, 2.5 and 5 h. In situ time-resolved reflectivity (TRR) techniques and Rutherford backscattering spectrometry with ion channeling (RBS-C) techniques were used to analyze the samples. The activation energies for amorphous-to- $\gamma$  and for  $\gamma$ -to- $\alpha$  alumina were found to be 4.6 and 5.2 eV respectively, independent of the presence of dopants and underlying orientation. The different rates on the different substrate orientations were attributed to the differences in step mobility. Clarke found that Fe enhances while Cr slows the growth rate relative to the undoped case [128].

White et al. produced a thin layer of amorphous alumina by irradiated Al and O with the same stoichiometric ratio of  $\text{Al}_2\text{O}_3$  at liquid nitrogen temperature. They annealed the samples in Ar ambient to recrystallize the amorphous film (~160 nm thick) to  $\gamma$  phase followed by the transformation of the  $\gamma$  to the  $\alpha$ -phase. They studied the kinetics of phase transformation at 800-1000 °C by RBS and TEM measurement. They observed that a few minutes annealing of the samples at 800 °C transformed the entire amorphous phase to  $\gamma$ -

alumina phase. Thermal annealing at 800 °C required approximately 100 hours to transform about 80 nm of  $\gamma$  into the  $\alpha$ -phase. Annealing the samples with about 160 nm thick amorphous region at 1600 °C, require a few minute to transform to  $\alpha$  phase. White et al. measured the activation energy of the  $\gamma$ -to- $\alpha$  transformation about 3.6 eV [129, 132].

A similar experiment using iron ion-irradiation at liquid nitrogen temperature has used to investigate the effects of impurities on the nature and kinetics of the recrystallization of the amorphous  $\text{Al}_2\text{O}_3$  [129, 132]. White et al. produced an amorphous layer  $\sim 150$  nm thick by irradiation with 160 keV  $\text{Fe}^+$  ions to a fluence of  $4 \times 10^{16}$   $\text{Fe}/\text{cm}^2$  at liquid nitrogen temperature. Thermal annealing at 800-1200 °C in flowing Ar was carried out. It found out that the addition of Fe to the amorphous film accelerate the rate of  $\gamma$ -to- $\alpha$  transformation (Fig.12).

Sklad et al. produced a thin layer of amorphous alumina ( $\approx 170$  nm) by irradiation with 90 keV  $\text{Al}^+$  ions to a fluence of  $2 \times 10^{16}$   $\text{Al}/\text{cm}^2$  and 55 keV  $\text{O}^+$  ions to a fluence of  $3 \times 10^{16}$   $\text{O}/\text{cm}^2$  into single crystal  $\alpha$ -alumina at -185 °C. The kinetics of phase transformation was studied after post-irradiation annealing in the temperature range from 700 to 800 °C by in situ transmission electron microscopy (TEM) and conventional TEM. Sklad et al. reported activation energies of  $\approx 1.6$  and 7.8 eV for the low and high temperature regions respectively for the amorphous-to- $\gamma$  transformation [13].

Another study by McCallum et al. investigated the effect of annealing environment on the on the kinetics of phase transformation. McCallum et al. produced a thin layer of amorphous alumina using irradiation with 160 keV  $\text{Fe}^+$  ions to a fluence of

$4 \times 10^{16}$  Fe/cm<sup>2</sup> at liquid nitrogen temperature. The samples then were thermally annealed at temperatures of 900, 960 and 1100 °C in an oxidizing environment (flowing O<sub>2</sub>) or in a reducing environment (flowing 96% Ar, 4% H<sub>2</sub>). The samples were analyzed by RBS-C and TEM to study of dependence of regrowth of the amorphous alumina on the annealing atmosphere. The results of annealing in oxidizing atmosphere showed that at the first stage of annealing the amorphous layer first transforms to  $\gamma$ -Al<sub>2</sub>O<sub>3</sub>, and then epitaxial growth of  $\alpha$ -Al<sub>2</sub>O<sub>3</sub> follows where the Fe redistributes relatively uniformly into the  $\gamma$ -phase.

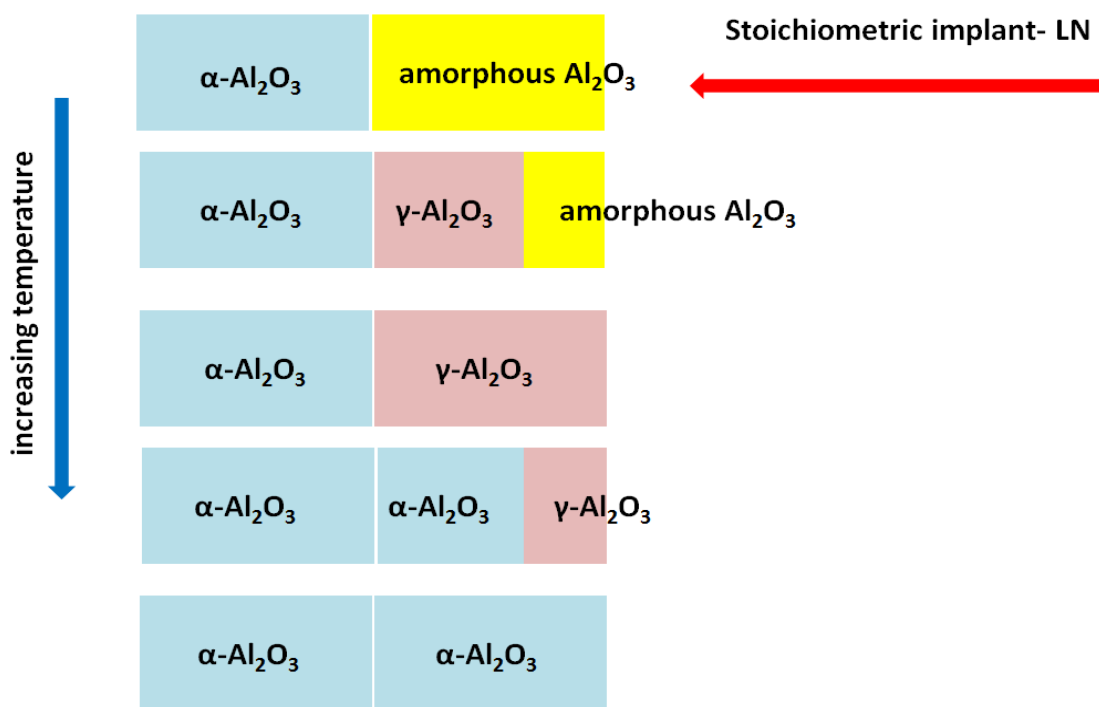


*Figure 12 Schematic representation of behavior observed during annealing of an amorphous film*

At the second stage of annealing process in flowing  $O_2$  the Fe appears to be present as substitutional  $(Al_{1-x}Fe_x)_2O_3$  or in the form of small particles of diamond cubic  $Fe_3O_4$  containing Al distributed in the  $\alpha-Al_2O_3$ . During annealing in flowing 96% Ar, 4%  $H_2$ , the Fe preferentially segregated in the  $\gamma$ -phase because it is largely insoluble in the recrystallized  $\alpha-Al_2O_3$  layer. By continuing the annealing process, the Fe was moved to the surface in front of the  $\alpha-Al_2O_3$  / $\gamma-Al_2O_3$  interface [85].

Sood and Cao irradiated a-axis  $Al_2O_3$  ( $\langle 1\bar{2}10 \rangle$  orientation) single crystal with 100 keV  $In^+$  ions to fluences of  $0.8 \times 10^{16} \text{ In/cm}^2$  (low dose) and  $6 \times 10^{16} \text{ In/cm}^2$  (high dose) at 77 K. The samples then underwent to an isothermal annealing in flowing high purity Ar gas atmosphere at 600, 700, 800, and 1000 °C for 10 minutes to 24 hours. They characterized the samples with RBS-C, reflection high energy electron diffraction (RHEED) and scanning electron microscopy (SEM) [135, 136].

In low dose regime, the amorphous phase undergoes to epitaxial growth from amorphous/crystalline interface towards the surface. They found out that regrowth velocity is decelerated as the concentration of indium increases. The activation energy of 0.7 and 1.28 were reported for initial faster growth and further anneal times respectively. The study showed that the amorphous phase transforms directly to  $\alpha-Al_2O_3$  without any evidence to an intermediary  $\gamma$ -phase [135].

In the high dose regime, all indium atoms migrated to the surface within 10 minutes and form islands of  $In_2O_3$ . The longer anneal time up to 24 hours had no effect in indium atoms redistribution. Although annealing was performed in flowing high purity Ar gas ambient, the source of oxygen to produce indium oxide is not clear [136].

## 2.6 Phase transformation under irradiation

Irradiation induced-phase transformation involves changes in crystal structure such as polymorphic phase transformations and amorphization. The irradiation generally enhances the defect concentration resulting in an increase of crystal entropy. The irradiation-induced amorphization is a result of damage accumulation leading to microstructure evolution and changes of material properties. An irradiation induced-phase transformation involves radiation-enhanced diffusion processes resulting in acceleration of the phase transformation kinetics. Therefore under irradiation condition, creating phases might be possible and easier to obtain, compare with a thermal condition [198]. For example when the energetic particles travel through the material, the significant amount of deposited energy can be stored in a subsurface region by the stresses which acts as a thermodynamic driving force when tends to relax the stresses [199].

In the absence of irradiation, the Gibbs free energy change between two phases determines phase transformation. In the presence of irradiation, thermodynamical concepts cannot be directly applied for the materials. The irradiation process is a non-equilibrium process from thermodynamics point of view. The energy of irradiation should be added to the difference in free energy between the phases without irradiation to analyze the effect of irradiation on phase stability. In many cases this energy is stored as a biaxial compressive stress. Energetic ions implanted into the affected area expand the material near the surface and this leads to biaxial compressive stresses. Also during irradiation-induced amorphization or phase transformation, stress can arise from

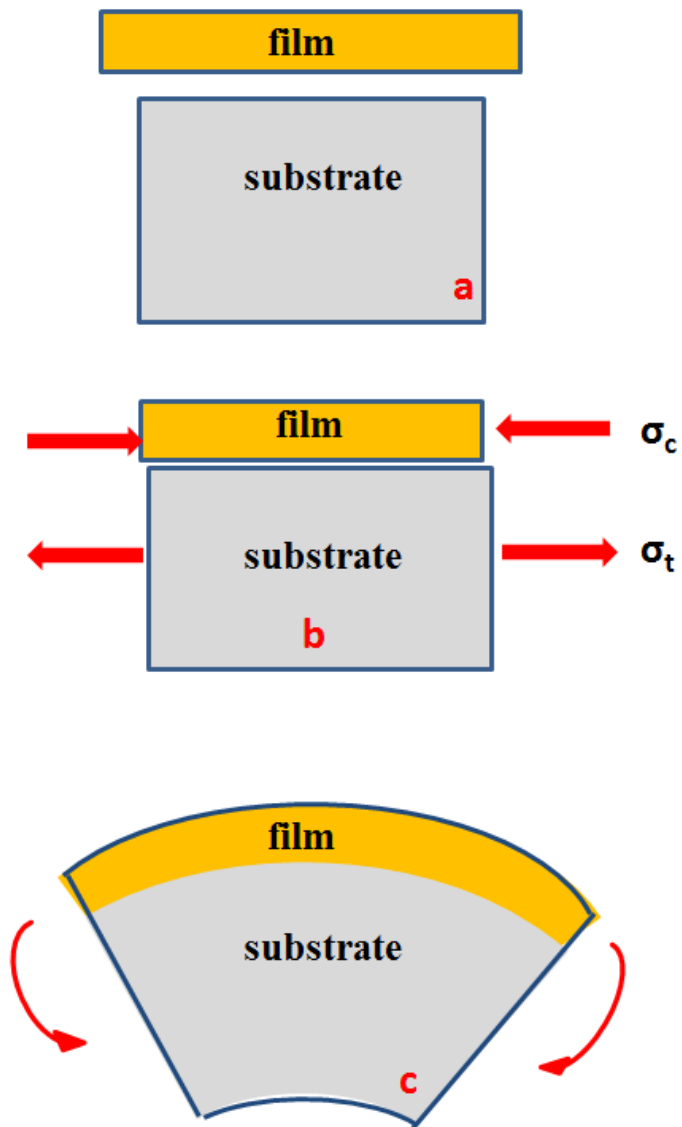
incompatibilities between the film and the substrate due to differences in thermal expansion, phase transformations with volume changes, densification of the film, and epitaxial effects. For instance, irradiation of  $\alpha$ -Al<sub>2</sub>O<sub>3</sub> with energetic ions causes an increase in volume due to introduction of a number of defects such as vacancies and interstitial atoms. Because the volume expansion of the damaged layer is restricted by the very thicker-undamaged substrate, it yields a lateral compressive stress. Irradiation of  $\alpha$ -Al<sub>2</sub>O<sub>3</sub> with 300 keV nickel ions using different fluences showed that irradiation induced surface lateral compressive stress in room temperature is three to nine times less than that obtain by low temperature irradiation [200].

Figure 13 illustrates the stresses and strains associated with the affected region (film) and the related bending. Fig 13a shows the volume expanded film free of the substrate. Fig. 13 shows a compressive stress in film and a tensile stress in the substrate when the film is bonded rigidly to the substrate. The final state is when both the film and substrate deform to make a concave curvature so that they again fit together perfectly.

Another type of stress under irradiation condition is epitaxial stresses. For example during ion beam irradiation induced epitaxial recrystallization in  $\alpha$ -Al<sub>2</sub>O<sub>3</sub>, a thin crystalline layer of  $\gamma$ -Al<sub>2</sub>O<sub>3</sub> forms form perfectly coherent boundaries with the substrate. The recrystallized  $\gamma$ -Al<sub>2</sub>O<sub>3</sub> film and  $\alpha$ -Al<sub>2</sub>O<sub>3</sub> substrate must be match up at the interface by elastically strained for the two lattices. Figure 14 shows misfit dislocations due to difference in the lattice constants of an epitaxial recrystallized region (film) and its substrate. There is strain and stress in the film, because it must be squeezed in order to fit with the substrate. The simplest way of obtaining some stress relief is plastic



deformation, i.e. producing and moving some dislocations. If the stress in a perfectly epitaxial thin film exceeds some critical value dislocations and stacking faults and possibly even new crystallites with different orientations might be formed in the growing film.



*Figure 13 A schematic diagram showing a film under residual compressive stress*

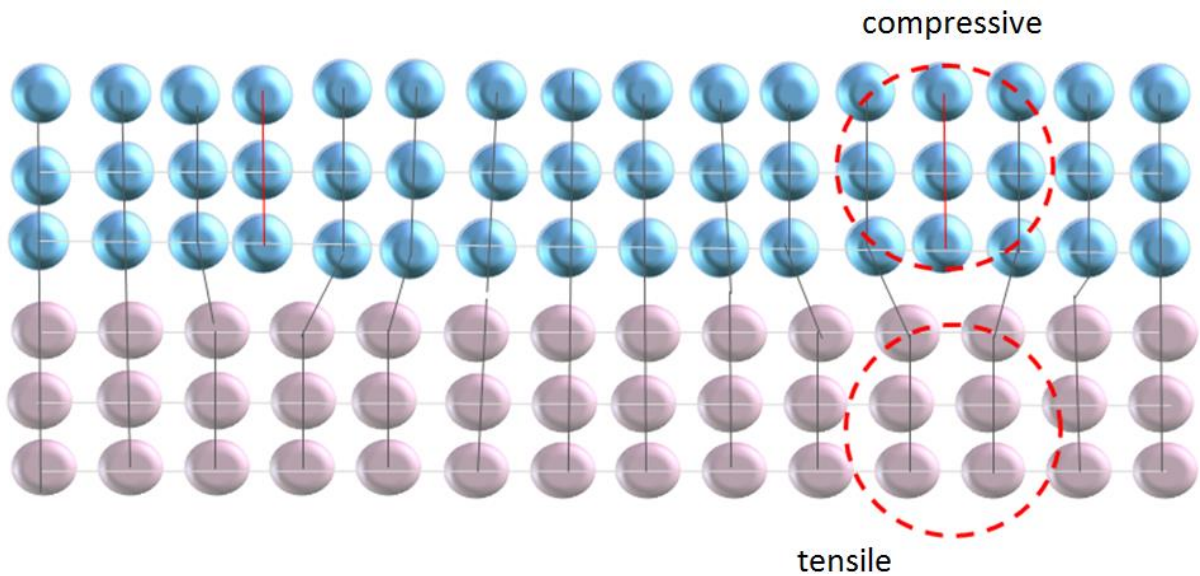


*Figure 14 Schematic diagram of the semi-coherent interface between two different phases of alumina*

When a new crystalline phase grows, conditions are expected to be nonequilibrium due to defects such as excess vacancy concentration in the new phase. There are various possible sites to develop stress such as free surface, film/substrate interface, voids, and grain boundaries. Usually developing stress due to vacancy annihilation is associated with volume changes in the film.

Almost all ion-irradiated surfaces are in a state of stress. The majority of these stresses are a result of the accumulating defects that are built under ion irradiation (intrinsic stress). Irradiation induced- heat also develops thermal stress. The thermal stress is a result of thermal expansion coefficients differences between the irradiated region and the substrate. In hard and high- melting point materials such as alumina,

thermal stress is negligible compared with intrinsic stresses. However thermal stress is significant during thermal annealing post irradiation.

The intrinsic stresses formed under irradiation and the internal stresses formed in cold worked material are similar. In both cases, the stresses develop from the strain due to various lattice defects formation. However, the density of defects present in a irradiated material can be two orders of magnitude higher than that produced by cold-work treatment [199].

Most of the energies introduced by energetic ions during ion irradiation stored by stress tend to be released by a phenomenon that is known as recovery (stress relaxation). These stored energies in form of stress can be released by stress relaxation such as vacancy, interstitial, and dislocation movement or by recrystallization of the strained regions into new strain-free grains. Therefore stress relaxation acts as a thermodynamic driving force. Mechanism of strained region relaxation during ion irradiation and the role of interaction of ions are still poorly understood.

## **2.7 Ion beam induced recrystallization in $\alpha$ -Al<sub>2</sub>O<sub>3</sub>**

In addition to the thermodynamically stable  $\alpha$ -phase (corundum structure), Al<sub>2</sub>O<sub>3</sub> has several metastable forms which depend upon the preparation technique. Among them is the  $\gamma$ -phase (cubic). Amorphous Al<sub>2</sub>O<sub>3</sub> can be transformed into the  $\gamma$ -phase at elevated temperatures. Then this metastable form transforms to the  $\alpha$ -phase upon annealing in the temperature range of about 650 to 1000° C [7].

White et al.[2] studied amorphous layers in Al<sub>2</sub>O<sub>3</sub> produced by ion-irradiation at 77 K , during thermal annealing in the temperature range of 850 to 1050° C. The

transformation followed the path of  $A \rightarrow \gamma \rightarrow \alpha$ , with  $\gamma$  epitaxially-oriented with respect to the  $\alpha$ -substrate. Yu et al. [131] and Clarke [6] found the same sequence to be followed during thermal annealing at 1050 °C of amorphous films produced by electron beam deposition. In all of these studies, impurities were found to have significant effects on the rate of the  $\gamma \rightarrow \alpha$  transformation (e. g., Fe enhances whereas Cr retards the growth rate). To summarize, thermal annealing can induce epitaxial recrystallization of amorphous  $\text{Al}_2\text{O}_3$  (an  $A \rightarrow C$  transformation). Similarly, ion beam irradiation can be used to induce epitaxial recrystallization of amorphous solids. In this paper, we will refer to this phenomenon as ion beam induced epitaxial recrystallization (IBIER). For instance, in Si, IBIER occurs with the formation of high quality single crystal silicon at temperatures as low as 250° C [201-203]. In Si, recrystallization is attributed to the deposited nuclear energy.

IBIER has also been reported for amorphous alumina films on sapphire substrates at temperatures as low as 400° C. Zhou et al. [41] observed IBIER in films prepared by implantation of In at 77 K followed by 1.5 MeV Si irradiation at 400° C. They observed the same transformation path as in thermal annealing, e.g.,  $A \rightarrow \gamma \rightarrow \alpha$ . The results appeared to be insensitive to the presence of indium in the amorphous layer.

Yu et al. [42, 43] observed IBIER in alumina films prepared by electron beam deposition on sapphire (0001) surfaces during subsequent ion irradiation at temperatures in the range 400 to 600° C. Beams of oxygen (180 keV) and argon (360 keV) were chosen such that the projected ranges were beyond the amorphous/substrate interface. The amorphous layer first transformed to  $\gamma$ -phase followed by a  $\gamma \rightarrow \alpha$  epitaxial

transformation. The quality of the films was much lower than those thermally regrown. These investigators also attributed the observed IBIER effects to energy deposited in nuclear processes (elastic collisions). They also reported that the presence of iron dopants inhibits the process.

## Chapter 3

### Materials and methods

#### 3.1 Ion irradiation condition

The irradiations were performed at the Instituto Tecnológico e Nuclear (ITN) facility in Portugal using a 210 kV ion implanter (Fig.15). The 210kV ion implanter has a chamber allowing the implantation of an area of  $20 \times 20 \text{ cm}^2$ . It is possible to carry on implantation samples in the temperatures range of 77 K up to 1273 K, in a controlled way. The connection of the implanter to the RBS chamber of the van der Graaff Accelerator, allows in situ analysis.

Samples were irradiated at room temperature with the incidence ions  $\sim 7^\circ$  off [0001] axis to avoid channeling effects. The sapphire samples were irradiated with 175 keV  $\text{Zr}^+$  ions to fluence of  $2 \times 10^{15}$ -  $4 \times 10^{16} \text{ Zr/cm}^2$ . Some of the irradiated  $\alpha\text{-Al}_2\text{O}_3$  samples with 175 keV Zr then were irradiated with 55 or 48 keV oxygen ions to fluences  $1.1 \times 10^{16}$ -  $3 \times 10^{16}$ . The zirconium and oxygen ions fluxes were on the order of  $1.25 \mu\text{A/cm}^2$  to avoid significant heating of the sample. Table 7 shows the summary of sample irradiation conditions for both species Zr and O. The values in black and red are corresponding to Zr and O respectively. Figure 16 shows the beam control information for irradiation of one of the samples.



*Figure 15 The 210 kV Ion implanter has a chamber allowing the implantation of an area of  $20 \times 20 \text{ cm}^2$ . It is possible to carry on implantation samples in the temperatures range of 77 K up to 1273 K, in a controlled way. The connection of the implanter to the RBS chamber of the van der Graaff Accelerator, allows in situ analysis.*

### **3.1.1 Sample preparation for irradiation**

High-purity and strain free  $\alpha\text{-Al}_2\text{O}_3$  single crystals discs 1 inch diameter and 0.04 inch thick with the c-axis normal to the surface and with an optical polish (Crystal Systems, Inc., Salem, MA) were annealed for 120 h at 1400 °C in air to remove any residual polishing damage or surface contamination.

Table 6 shows the summary of samples irradiation conditions.

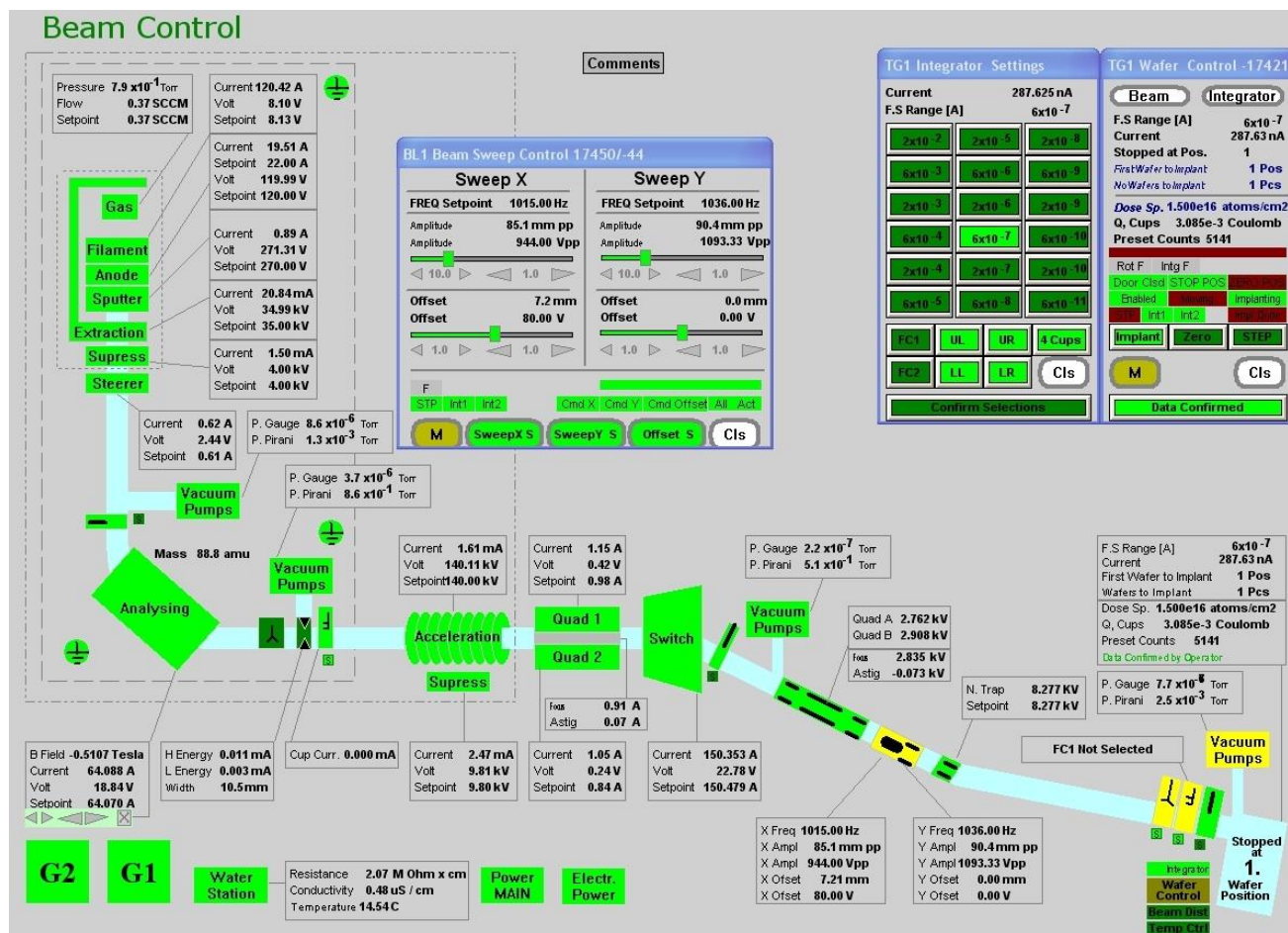


Figure 16 beam control panel for the irradiation of samples



*Table 6 Summary of samples irradiation conditions*

<b>Ion Energy [keV]</b>	<b>Ion Fluence [Zr<sup>+</sup>/cm<sup>2</sup>], [O<sup>+</sup>/cm<sup>2</sup>]</b>	<b>Zr/O Concentration (at%) at Range [Zr/cm<sup>3</sup>], [O/cm<sup>3</sup>]</b>	<b>Ion Flux [Zr<sup>+</sup>/cm<sup>2</sup>.S] [O<sup>+</sup>/cm<sup>2</sup>.S]</b>	<b>Ion Range [nm]</b>	<b>Zr/O dpa Peak [nm]</b>	<b>Elapsed time [hr]</b>	<b>Temperature [K]</b>
<b>175</b>	<b>2×10<sup>15</sup></b>	<b>0.4</b>	<b>1×10<sup>12</sup></b>	<b>57</b>	<b>5</b>	<b>0.55</b>	<b>300</b>
<b>175</b> <b>55</b>	<b>7.5×10<sup>15</sup></b> <b>1.1×10<sup>16</sup></b>	<b>~1.5%</b> <b>~1.5%</b>	<b>1×10<sup>12</sup></b> <b>1×10<sup>12</sup></b>	<b>57</b> <b>86</b>	<b>~20</b> <b>~5</b>	<b>2.08</b> <b>3.05</b>	<b>300</b>
<b>175</b> <b>55</b>	<b>1.5×10<sup>16</sup></b> <b>2.3×10<sup>16</sup></b>	<b>~3%</b> <b>~3%</b>	<b>1×10<sup>12</sup></b> <b>1×10<sup>12</sup></b>	<b>57</b> <b>86</b>	<b>~40</b> <b>~10</b>	<b>4.16</b> <b>6.38</b>	<b>300</b>
<b>175</b> <b>48</b>	<b>2×10<sup>16</sup></b> <b>3×10<sup>16</sup></b>	<b>4%</b> <b>5.5%</b>	<b>1×10<sup>12</sup></b> <b>1×10<sup>12</sup></b>	<b>57</b> <b>74</b>	<b>53.6</b> <b>~17</b>	<b>5.55</b> <b>8.3</b>	<b>300</b>
<b>175</b>	<b>4×10<sup>16</sup></b>	<b>7.9</b>	<b>1×10<sup>12</sup></b>	<b>57</b>	<b>105</b>	<b>11.11</b>	<b>300</b>

### **3.2 Rutherford backscattering spectrometry (RBS)**

One of the most significant challenge regarding thin film materials is measurement of structure and properties. Rutherford backscattering spectroscopy (RBS) is a unique non destructive analysis method for this purpose. RBS is able to determine some critical parameters of thin films such as the thickness, composition of material and impurities at the surface. RBS can also provide useful information regarding in-depth profiling in detection limit and depth resolution of  $\sim 1$  and  $\sim 10$  nm respectively. RBS does not provide any chemical bonding information which must be obtained from some other thin film analysis techniques.

#### **3.2.1 Basic concept of Rutherford backscattering spectroscopy**

RBS is based on the electrostatic repulsion between high energy incident ions and target nuclei. The specimen is usually bombarded with monoenergetic beam of  $^4\text{He}^+$  ions (typically 2 MeV) and the elastically backscattered ions are detected by the detector-analysis system which measures the energies of the particles (Fig. 17). During the collision, energy is transferred from the incident particle to the target specimen atoms; the change in energy of the scattered particle depends on the masses of incoming and target atoms. Using kinematic factor ( $k$ ), which is the ratio of the particle energy before and after the collision, and definition of  $k$ , the film elements can be identified.

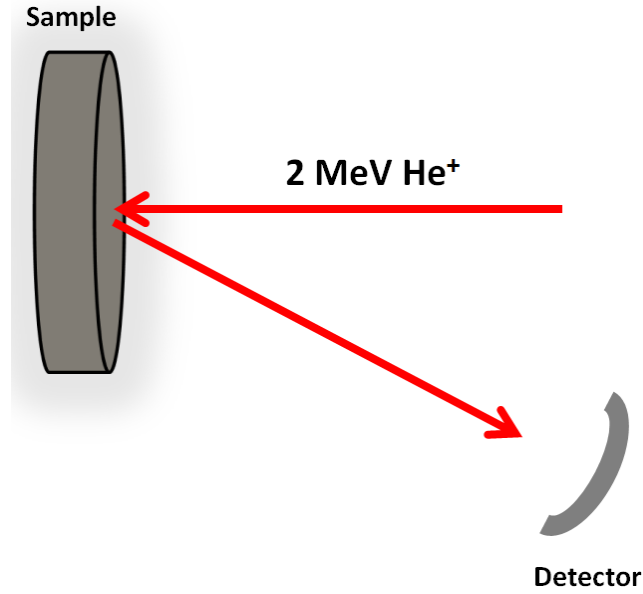


*Figure 17 Schematic representation of the experimental setup for Rutherford backscattering analysis.*

Equation (1) expresses the dependency of  $k$  on the masses of the incident particle ( $M_1$ ) and target atom ( $M_2$ ), and the scattering angle ( $\theta$ ).

$$k = \left[ \frac{(M_2^2 - M_1^2 \sin^2 \theta)^{1/2} + M_1 \cos \theta}{M_1 + M_2} \right]^2 \quad (1)$$

The probability of scattering event can also be expressed as a function of scattering cross section which is proportional to the  $Z_1 Z_2$  when a particle with charge  $Z_1$  approaches the target atom with charge  $Z_2$ .

$$\frac{d\sigma}{d\Omega} = \left( \frac{Z_1 Z_2 e^2}{2E} \right)^2 \frac{1}{\sin^4 \theta} \frac{\left\{ \left[ 1 - \frac{M_1^2}{M_2^2} \sin^2 \theta \right]^{1/2} + \cos \theta \right\}^2}{\left[ 1 - \left( \frac{M_1}{M_2} \right)^2 \sin^2 \theta \right]^{1/2}} \quad (2)$$

where  $E$  is the incident ion energy,  $\Omega$  is the detector solid angle, and  $d\sigma$  is the effective differential cross section for the scattering of a particle (Equation 2).

As the helium ions traverse the solid, they lose energy due to interaction with electrons in the target and usually do not scatter at the surface. After collision the  $\text{He}^+$  ions lose further energy on their way out to the detector. Figure 18 shows schematic of energy loss for an ion scatters from depth  $t$ . The rate of energy loss or stopping power ( $dE/dx$ ) is a critical component in backscattering experiments as it determines the depth profile in a given experiment. To avoid complications to calculate energy loss, it is convenient to assume that total energy loss is linearly proportional to depth  $t$ .

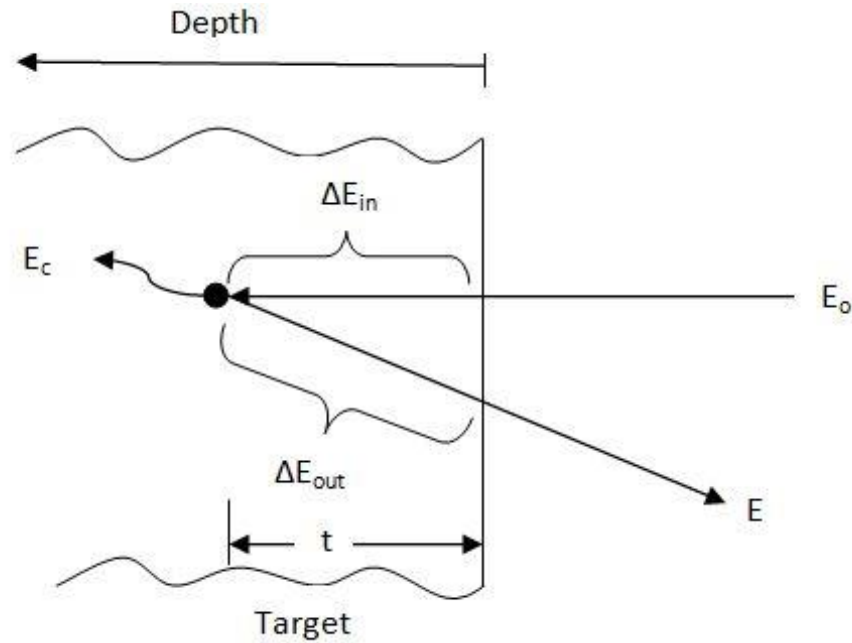


*Figure 18 Components of energy loss for an ion beam that scatters from depth  $t$ . First, incident beam loses energy through interaction with electrons  $\Delta E_{in}$ . Then energy lost occurs due to scattering  $E_c$ . Finally outgoing beam loses energy for interaction with electrons  $\Delta E_{out}$  (adapted from [204]).*

### 3.2.2 Samples characterization using Rutherford backscattering spectroscopy

For characterization of the disorder on the Al-sublattice, distribution of implanted species and verification of presence (or absence) of an amorphous phase, all specimens were analyzed by Rutherford backscattering spectroscopy with ion channeling (RBS-C) using 2.0 MeV  $\text{He}^+$  at scattering angles of  $170^\circ$ ,  $-165^\circ$ , and  $-140^\circ$  in the standard IBM geometry (Fig. 19). The RBS experimental beam line of the 2.5 MV Van de Graaff accelerator in the Ion Beam Laboratory (ITN) (Fig. 20), 3MV tandem accelerator in the

Ion Beam Materials Laboratory (IBML) at the University of Tennessee, Knoxville (UTK) (Fig. 21), and the 3.6 MeV NEC Pelletron in the ion beam laboratory at IBM Almaden Research Center were used to characterization of the samples.

For the results of RBS-C carried out in IBM Almaden Research Center, the channel number converted to energy using calibration samples with 100nm of Cr on SiO<sub>2</sub> (quartz) and 100nm of Au on graphite. Similar measurements were carried out in ITN, using calibration samples with V, Nb and Ta thin film (over SiO<sub>2</sub>) and with Au and Ni thin film over Si in IBML-UTK. The film thickness was below the energy resolution of all the experimental set-up.

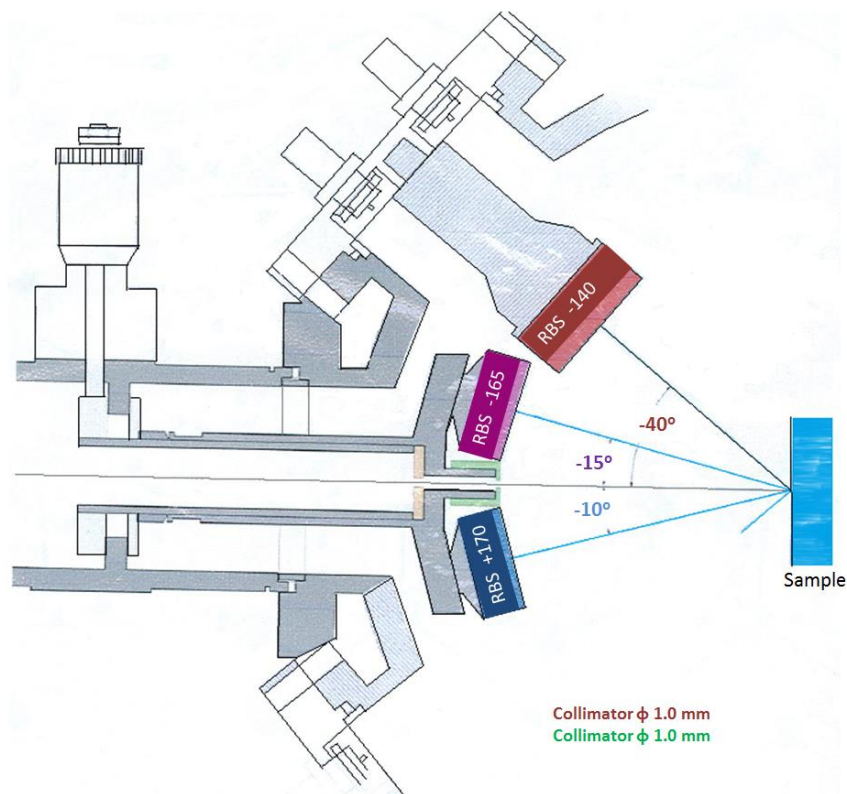


*Figure 19 Geometry of the chamber with three detectors at different angles*

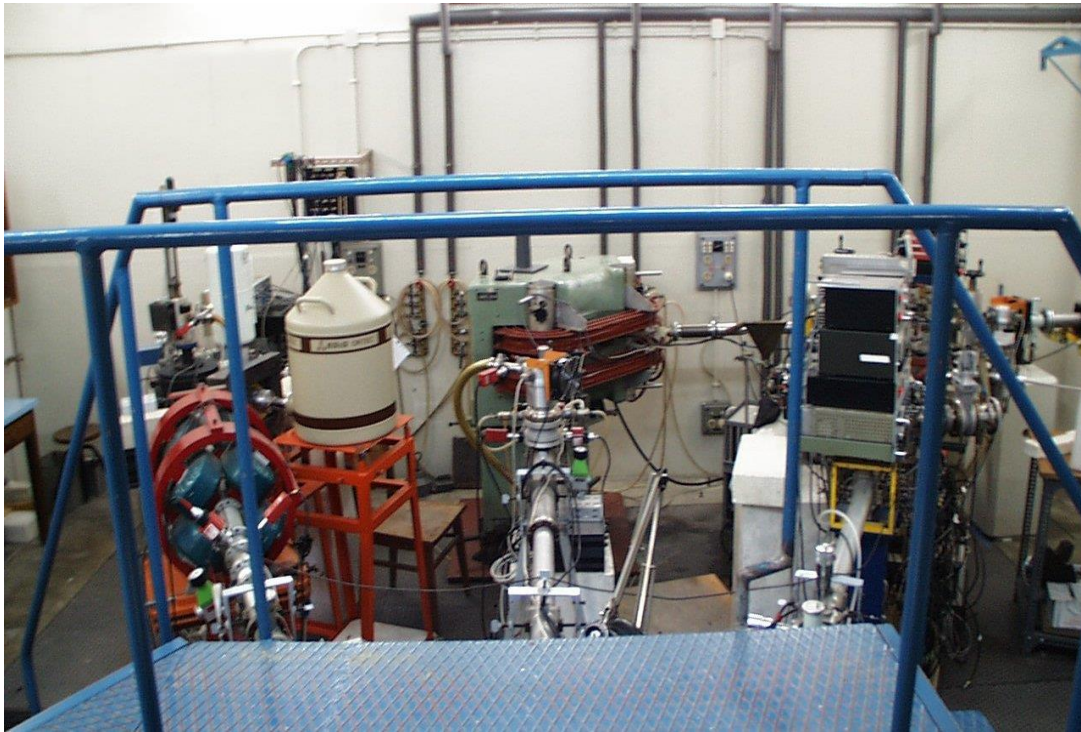


*Figure 20 A 2.5 MV Van de Graaff accelerator with three experimental beam lines, with all the relevant ion beam techniques available: RBS, PIXE, NRA, Channeling, ERDA and NRB with (p, g).*

### **3.3 Transmission electron microscopy (TEM)**

The basic principle of a transmission electron microscope (TEM) is the same as a light microscope but uses electrons instead of light and electromagnetic lenses instead of glass lenses. Using an electron source in a microscope makes it possible to get a resolution a thousand times greater than with a light microscope. Electrons have characteristic wavelengths of less than an angstrom, and come close to seeing atomic detail. For example, the wavelength of electrons produced in a 50 kV and 200 kV TEM is

0.05 and 0.025 Å respectively compared with the wavelength of Cu K $_{\alpha}$  used in X-ray diffraction of 0.154 Å.



*Figure 21 The Ion Beam Materials Laboratory (IBML) at the University of Tennessee, Knoxville (UTK)*

Among the electron microscopy techniques, scanning transmission electron microscopy (STEM) has become a very popular and widespread technique during the last two decades. It can be used for the characterization of nanostructures, providing a range of different imaging modes with the ability to provide information on elemental composition and electronic structure at the ultimate sensitivity, that of a single atom. In scanning transmission electron microscopy, a focused beam of electrons ( $\sim 1\text{--}10^\circ\text{\AA}$ ) is



moved in a television-style raster pattern across the specimen [205]. Various data can be acquired in synchronization with the raster scan such as emitted x-rays, secondary electrons, or backscattered electrons. Using scanning transmission electron microscopy, chemical mapping in a specimen can be obtained by electron energy loss spectroscopy (EELS) and energy-dispersive X-ray (EDX) analysis. Z-contrast imaging also allows for some degree of quantitative elemental mapping through the strong atomic number dependence of the signal [206].

### **3.3.1 Sample Preparation for TEM**

Since in TEM the electrons must penetrate the specimen, and penetration depth of the electrons is small, but the specimen should also represent the bulk material in both structure and composition, the sample has to be very thin. The thickness of samples is typically less than 100 nm depending on the average atomic number of the material. A thickness on the order of 20 to 30 nm is recommended for a high resolution Image.

A common technique used to thin the multilayer materials such as materials that undergo ion irradiation is sandwich technique. Figure 22 illustrates the sandwich technique of a multilayer sample prepared by multyprep system polisher or tripod thinning. The cross-sectional preparation of such materials enables the researchers to observe the implantation depth and the density of the ions or particles [207]. Figure 23 shows a thinned Zr-irradiated sapphire sample under optical microscope that was made by sandwich technique using multyprep system thinning.

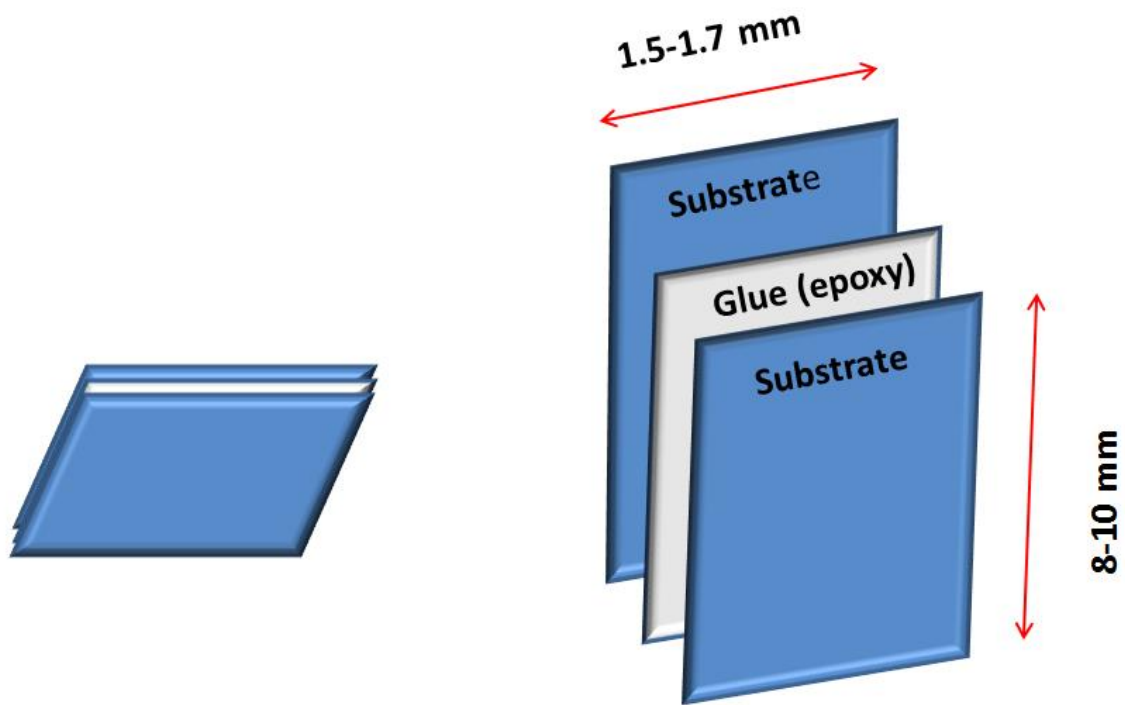


*Figure 22 Diagram of a multilayer sample prepared using the sandwich technique for tripod thinning*

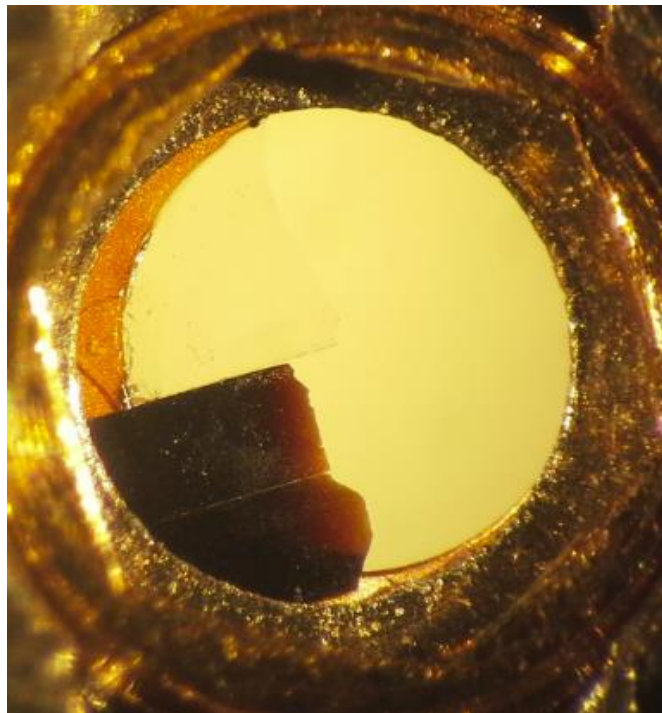


*Figure 23 A thined Zr-irradiated sapphire sample under optical microscope that was made by sandwich technique using tripod thinning*

A mechanical polishing technique, using diamond lapping films was employed for thinning the samples to about 10 micron ( $\mu$ ) (Figure 24). Then the ion milling polishing technique that consists of abrading the sample using ion bombardment was applied to thin the sample for the final step. Figure 25 shows the ion milling process for one of the Zr-irradiated sapphire samples using a Gatan precision ion polishing system (PIPS) model 691 at the Joint Institute for Advanced Materials (JIAM) at UTK. Usually if the ion milling process takes longer than 1 hour in the PIPS, the sample was not dimpled thin enough. The PIPS that uses a higher flux and lower angles is designed for short-term milling.

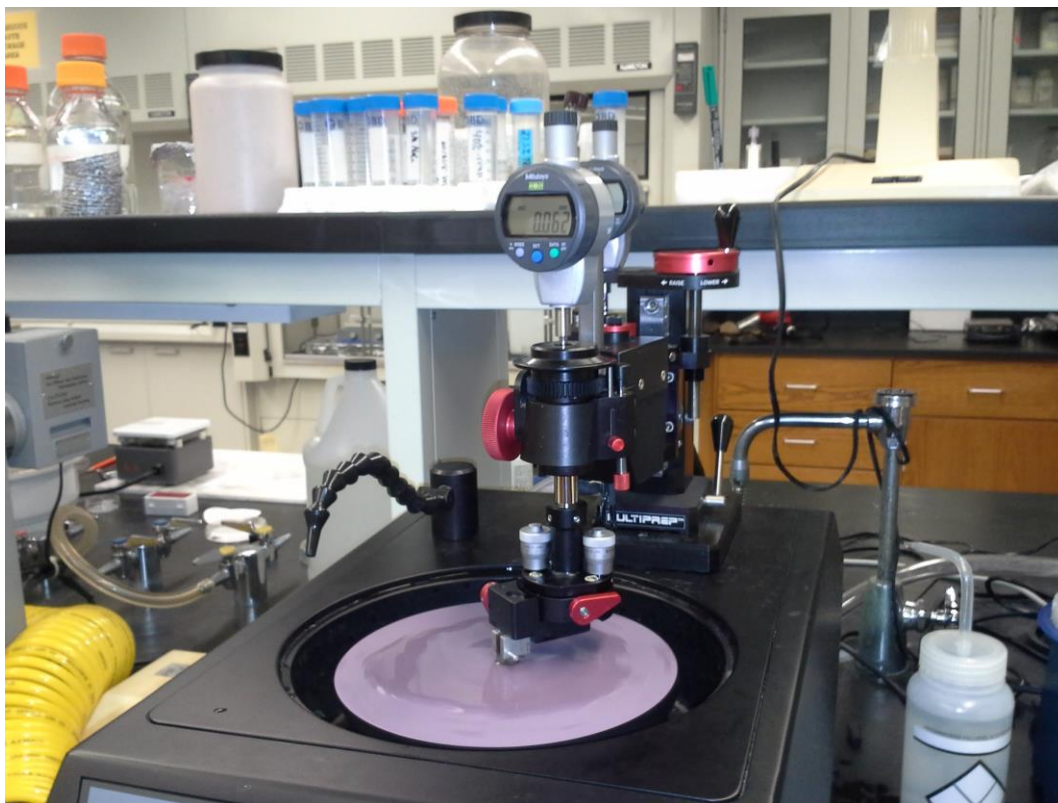


*Figure 24 Mechanical polishing process for one of the Zr-irradiated sapphire samples using Allied multyprep system polisher at the joint institute for advanced materials (JIAM) at UTK*

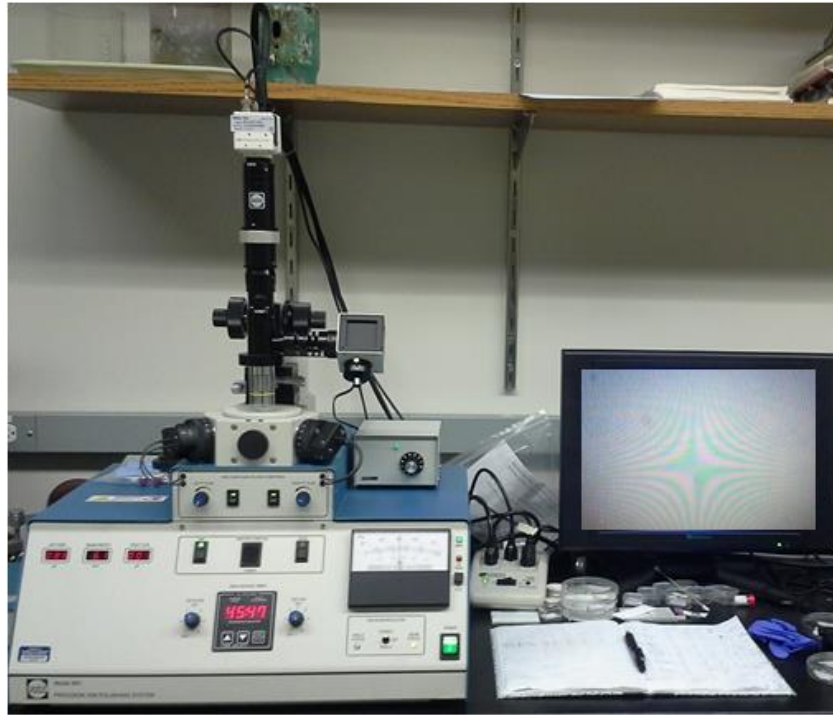


*Figure 25 Ion milling process for one of the Zr-irradiated sapphire samples using Gatan model 691 at the Joint Institute for Advanced Materials (JIAM) at UTK.*

### **3.3.2 Samples characterization using STEM/TEM**

The specimen that was irradiated with 175 keV  $\text{Zr}^+$  ions to a fluence of  $4 \times 10^{16}$   $\text{Zr}/\text{cm}^2$  was prepared by mechanical polishing followed by ion milling. Electron-energy loss spectroscopy (EELS) and Z-contrast and high angle annular dark field (HAADF) images were obtained in an aberration-corrected scanning transmission electron microscope (STEM), VG 501 STEM fitted with a Nion Mark II Cs corrector and a Gatan Enfina EEL spectrometer. The analysis was done at the scanning transmission electron microscopy (STEM) group (Materials Science & Technology Division Oak Ridge National Laboratory) (Fig. 26).

The other samples were analyzed using TEM at the Institute of Scientific and Industrial Research, Osaka University, Japan, using a JEOL JEM-3000F TEM operated at 300 kV. Cross sectional TEM specimens were also prepared by mechanical polishing followed by ion milling. Bright field (BF) and high resolution images, nano-beam electron diffraction (NBED) pattern, and selected area electron pattern (SAED) were obtained.



*Figure 26 Working on the samples with scanning transmission electron microscope (STEM) at the scanning transmission electron microscopy (STEM) group (Materials Science & Technology Division Oak Ridge National Laboratory)*

### 3.4 Electron energy loss spectroscopy (EELS)

When high energetic electrons in a scanning transmission electron microscope pass through a thin specimen, they interact with atoms of the solid. This interaction basically is a change in the kinetic energy of electrons due to inelastically scattering and energy transfer to the atoms. The amount of this electron energy loss is specific to the elements present at the specimen, their coordination, bonding, optical and electronic properties. Using an electro-magnetic prism, the electron beam can be deflected based on their velocities resulting on an electron energy-loss spectrum. Figure 27 is a typical spectrum for EELS with the different features indicated. Inelastic interactions include phonon excitations, inter- and intra-band transitions, plasmon excitations, inner shell ionizations, and Bremsstrahlung radiation. The inner-shell ionizations are particularly useful for detecting the elemental components of a material. The energy resolution of EELS obtained from a modern scanning transmission electron microscope is typically 1 eV but can approach 0.1 eV if an electron-beam monochromator is used. To obtain the chemical content of a sample, the shape of specific ionization edge (electron near edge structure) for the element is analyzed.

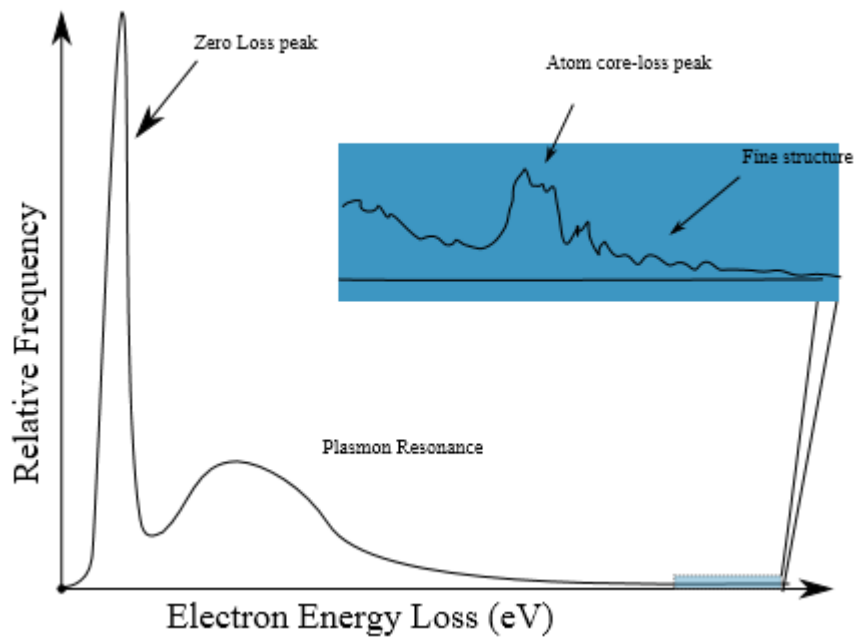


*Figure 27 A typical EELS spectrum with the different parts indicated*

### 3.5 Optical measurements

Studies of defects in ion irradiated insulators by optical absorption or luminescence techniques focus on defects and imperfections which extend over the range of the projectile. During an ion irradiation material process, variety of defects forms. Among them are simple point defects, interstitial and vacancies. These defects give rise to optical absorption bands. Specific ultraviolet absorption and luminescence bands are associated with F-type centers (oxygen vacancies with or without trapped electrons). Comparing the optical density for un-irradiated and irradiated samples in different spectral regions, it gives information about F-type centers concentration at the defected



region. The damaged region is so thin that one may follow coloration to very high optical absorption coefficients.

### **3.5.1 Ultraviolet and visible (UV-Vis) absorption spectroscopy**

Ultraviolet and visible (UV-Vis) absorption spectroscopy is the measurement of the intensity of a beam of light after it passes through a sample compared with the initial intensity. These measurements can be at a single wavelength or over an extended spectral range. The UV-Vis spectral range is approximately 190 to 900 nm. Obtaining short-wavelength  $<175$  nm requires a simple UV-Vis spectrometers with nitrogen gas. Working below 175 nm requires a vacuum spectrometer and a suitable UV light source. Ultraviolet and visible photons are energetic enough to promote electrons to higher energy states in molecules and materials. Therefore, UV-Vis spectroscopy is useful to the exploration of the electronic properties of materials such as semiconductors and insulators. The classic example is the F-type centers in which one or more electron(s) are trapped at an anion vacancy site. Substitutional impurities, especially transition metal ions can also provide absorption centers in crystals. For instance transition metal impurities such as  $\text{Cr}^{+3}$  are responsible for the colors of many gem-stones, such as ruby. Optical absorption spectroscopy requires a broadband excitation source, such as a tungsten-halogen lamp [208].

### **3.5.2 Photoluminescence**

When a semiconductor or a semi-insulator is illuminated by a light with photon energy greater than the band-gap energy ( $E_g$ ) of the material, electrons in the valence

band are excited to the conduction band. When electron and electron-hole recombines, it emits a photon. The emitted light has a wavelength characteristic of the occupied energy levels. This information can be used for investigating the electronic structure and impurity concentrations, identifying defect complexes, and measuring the band gap of materials. Photoluminescence (PL) spectroscopy is also a powerful technique for providing an excellent picture of overall crystal quality and purity. PL has a very good resolution for identifying F-type centers compared with OA. There are also more elaborate techniques, such as photoluminescence excitation (PLE), time-resolved PL, and resonant Raman scattering, but these techniques are more useful for basic scientific investigations than for routine crystal characterization [208] .

Optical absorption spectra were obtained using a double beam Varian Cary 5000 spectrophotometer in the 190–800 nm wavelength range at room temperature. The photoluminescence was measured for irradiation at 255 nm by a Varian Cary Eclipse 6000 spectrophotometer at room temperature.

### **3.6 Thermal annealing**

Post irradiation thermal annealing was used to induce recrystallization of the amorphized region of samples that were irradiated with Zr. To study of post irradiation thermal annealing, the irradiated samples were cut to a few pieces then were annealed at different temperatures and times. The first annealing temperature and residence time was chosen to be 800 °C and 30 minute based on previous studies to induce partial recrystallization of amorphous region to gamma. The temperature and the time for the samples were designed as shown in Table 8 and 9 to observe the phase changes in order

to study of the effect of annealing in oxygen irradiation  $\alpha$ -alumina. All anneals were performed using a clean 4" tube furnace in high purity Ar atmosphere. To avoid any possible contamination during the annealing process, the samples were placed at a pre-fired alumina crucible, and then the crucible was placed in to 2"-one-ended clean alumina tube. These were put at the tube furnace. After placing the samples in the furnace, the entire tube purged by Ar gas first by wide opening a flow for several minutes then to a rate of 4 lit/min for the entire annealing process. Both ramp and cooling rates were 3.3 °C/min.

*Table 7 Thermal annealing conditions for Zr irradiated samples*

Sample number	Zr fluence [ $\text{Zr}/\text{cm}^2$ ] (175 keV $\text{Zr}^+$ )	Post anneal conditions
31	$2 \times 10^{16}$	-
318	$2 \times 10^{16}$	800°C / 30 min.
5119	$2 \times 10^{16}$	900°C / 60 min.
51K	$2 \times 10^{16}$	900°C / 120 min.
31K	$2 \times 10^{16}$	1000°C / 30 min.

*Table 8 Thermal annealing conditions for Zr plus O irradiated samples*

Sample number	Zr fluence [ $\text{Zr}/\text{cm}^2$ ] (175 keV $\text{Zr}^+$ )	O fluence [ $\text{O}/\text{cm}^2$ ] (48 keV $\text{O}^+$ )	Post anneal conditions
32	$2 \times 10^{16}$	$3 \times 10^{16}$	-
328	$2 \times 10^{16}$	$3 \times 10^{16}$	800°C / 30 min.
5229	$2 \times 10^{16}$	$3 \times 10^{16}$	900°C / 60 min.
52K	$2 \times 10^{16}$	$3 \times 10^{16}$	900°C / 120 min.
32KZ	$2 \times 10^{16}$	$3 \times 10^{16}$	1000°C / 30 min.

### 3.7 Arrhenius equation

Experimental study of recrystallization has shown that recrystallization is a thermally activated process and the relation between the recrystallization rate and the temperature can be characterized by the Arrhenius expression:

$$V = V_0 \exp(-E_a/kT) \quad (3)$$

where  $V$  is recrystallization rate,  $V_0$  is the pre-exponential frequency factor,  $E_a$  is activation energy;  $k$  is Boltzmann constant; and  $T$  is temperature. The Arrhenius equation has been widely accepted and successfully applied to numerous reactions involving solids such as kinetic study of solid-phase epitaxy.

The Equation (3) can be written equivalently as:

$$\ln V = \ln V_0 - E_a/(kT) \quad (4)$$

From the plot of  $\ln V$  versus  $1/T$ , the value of the y-intercept and slope can be calculated equal to  $\ln V_0$  and  $-E_0/k$  [209].

### 3.8 Cross-cut technique

One method to determine the kinetics of the annealing process is the cross-cut method. In the cross cut method, activation energy is assumed to be single and constant. A set of identical samples are annealed at several temperatures for different times. The samples should contain the same initial concentration of defects,  $n_0$ . In a single activated process with constant activation energy, rate of defect concentration can be described by the following equation:

$$dn/dt = -F(n).K_0 \exp(-E_a/kT) \quad (5)$$

where  $n$  is the fractional concentration of the defect;  $F(n)$  is any continuous function of  $n$ ;  $K_0$  is a pre-exponential constant;  $E_a$  is activation energy;  $T$  is temperature and  $k$  is the Boltzmann factor. The Equation (3) can be rewritten as:

$$-dn/F(n) = K_0 t \cdot \exp(-E_a/kT) \quad (6)$$

Suppose that Fig. 28 is the isothermal annealing curves for these samples. The dashed line  $n_1$  and  $n_2$  represent a constant defect concentration over the isothermal annealing curves at different times. For each of these dashed lines the left-hand side of Equation (6) is a constant, therefore:

$$t \cdot \exp(-E_a/kT) = \text{constant} = C \quad (7)$$

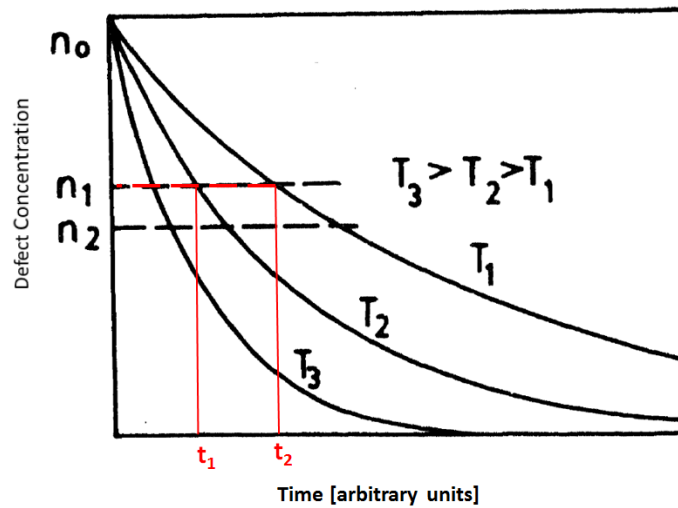


Figure 28 Cross-cut procedure from isothermal annealing curves to determine the activation energy

The activation energy can be determined by the following equation if two times,  $t_1$  and  $t_2$  reach a constant value of  $n_1$  at temperatures  $T_1$  and  $T_2$ :

$$\ln t_1/t_2 = E_a/k (1/T_1 - 1/T_2) \quad (8)$$

Using Equation (7) the times can be related to the temperature by:

$$\ln (t_i) = \ln C + E_a/kT_i \quad (9)$$

Equation (9) expresses a linear equation of the logarithm of  $t_i$  in  $1/T_i$  with the slope of  $E_a/k$ . If the constant  $C$  calculated from two cuts taken at points  $n_1$  and  $n_2$  is the same, the assumption that a single process with constant activation energy is operative can be checked [209].

### 3.10 SRIM calculations

SRIM is a collection of software packages which calculate many features of the transport of ions in matter such as: energy loss of ions in matter, range and straggling distributions. The basic of SRIM is the theory of the stopping of ions in matter with modified major parameters such as shell corrections, mean ionization potentials, the effective charge of ions and the Fermi velocity of solids. SRIM has also the capability to calculate displacements per atom (dpa) which is an important radiation damage exposure unit. Most researchers in the field of ion beams, use dpa as an indicator to evaluate the radiation damage associated with their irradiations.

In this study SRIM-2013 is used to calculate range, Zr distribution, vacancies, deposited energy and displacement per atom (dpa). Energies of displacement ( $E_d$ ) of 20 eV and 50 eV were used for Al and O respectively in the calculations [210]. The SRIM-

based calculations are based on densities of single crystal sapphire and amorphized alumina of 3.98 and 3.10 gr/cm<sup>3</sup> [7, 211].

### 3.9.1 The SRIM calculated results

Figure 29 shows SRIM calculated range and displacement damage dose (in units of dpa) dpa versus target depth for Al<sub>2</sub>O<sub>3</sub> irradiated with 175 keV Zr<sup>+</sup> ions to a fluence of  $7.5 \times 10^{15}$  Zr<sup>+</sup>/cm<sup>2</sup>, followed by irradiation with 55 keV O<sup>+</sup> ions to a fluence of  $1.1 \times 10^{15}$  O<sup>+</sup>/cm<sup>2</sup>.

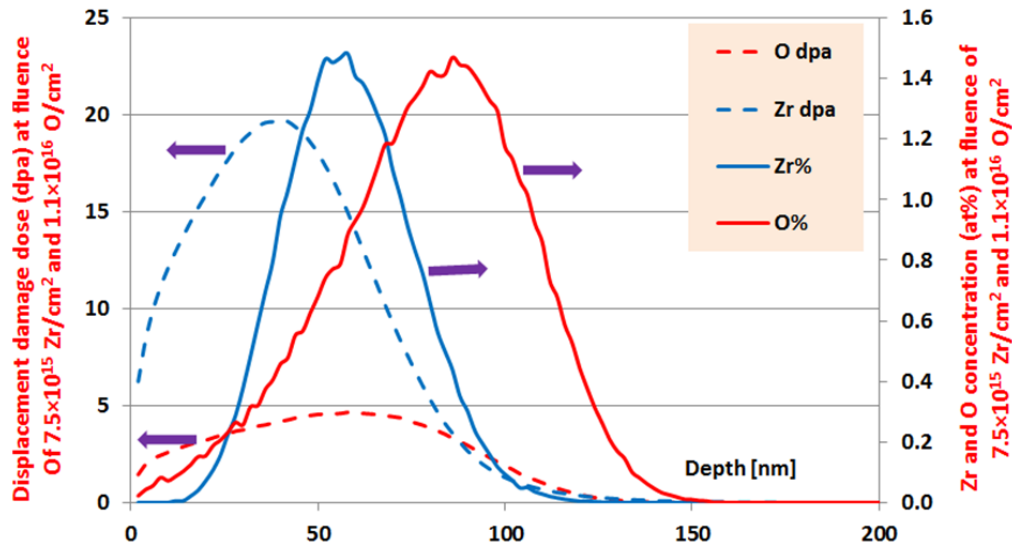


Figure 29 SRIM calculated range and displacement damage dose (in units of dpa) dpa versus target depth for Al<sub>2</sub>O<sub>3</sub> irradiated with 175 keV Zr<sup>+</sup> ions to a fluence of  $7.5 \times 10^{15}$  Zr<sup>+</sup>/cm<sup>2</sup>, followed by irradiation with 55 keV O<sup>+</sup> ions to a fluence of  $1.1 \times 10^{15}$  O<sup>+</sup>/cm<sup>2</sup>.



Figure 30 shows similar calculations for  $\text{Al}_2\text{O}_3$  irradiated with 175 keV  $\text{Zr}^+$  ions to a fluence of  $1.5 \times 10^{16} \text{ Zr}^+/\text{cm}^2$ , followed by irradiation with 55 keV  $\text{O}^+$  ions to a fluence of  $2.3 \times 10^{15} \text{ O}^+/\text{cm}^2$ .

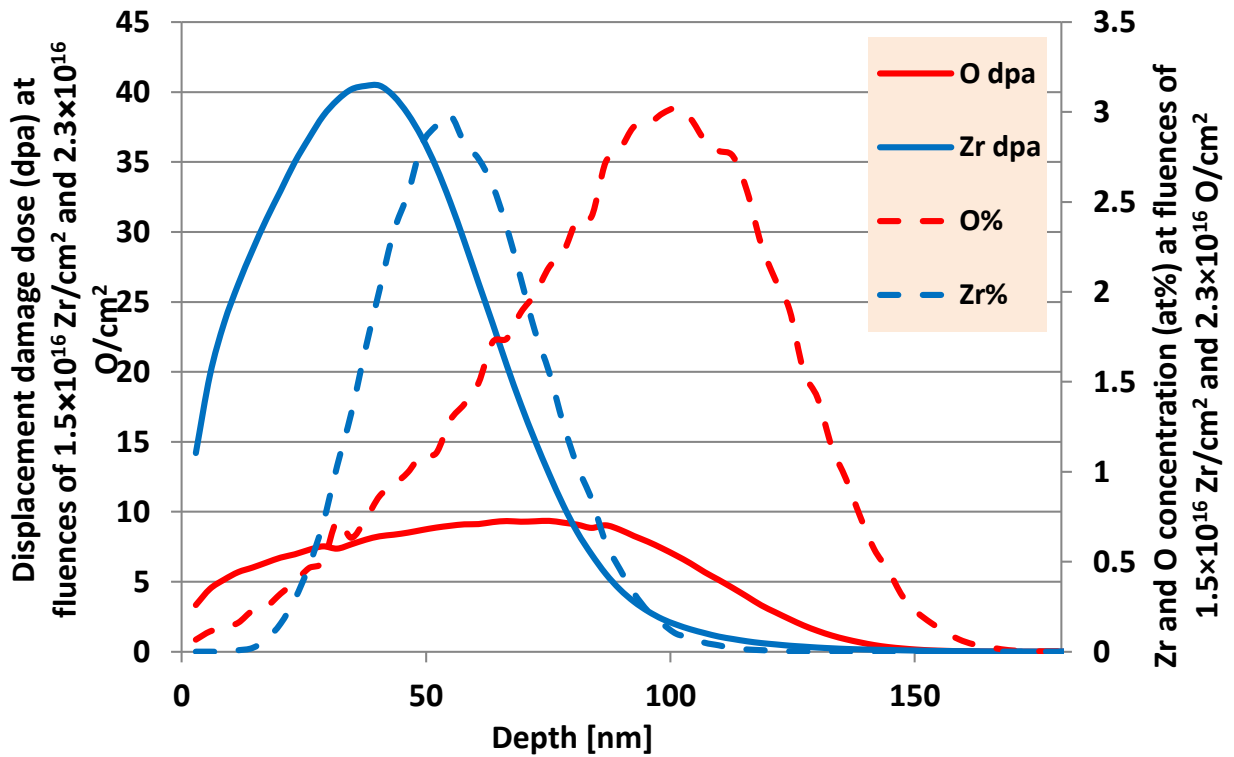


Figure 30 SRIM calculated range and displacement damage dose (in units of dpa) dpa versus target depth for  $\text{Al}_2\text{O}_3$  irradiated with 175 keV  $\text{Zr}^+$  ions to a fluence of  $1.5 \times 10^{16} \text{ Zr}^+/\text{cm}^2$ , followed by irradiation with 55 keV  $\text{O}^+$  ions to a fluence of  $2.3 \times 10^{15} \text{ O}^+/\text{cm}^2$ .

Figure 31 and 32 show SRIM calculated range and displacement damage dose (in units of dpa) dpa versus target depth for  $\text{Al}_2\text{O}_3$  irradiated with 175 keV  $\text{Zr}^+$  ions to a fluence of  $2 \times 10^{16} \text{ Zr}^+/\text{cm}^2$  and  $4 \times 10^{16} \text{ Zr}^+/\text{cm}^2$  respectively.

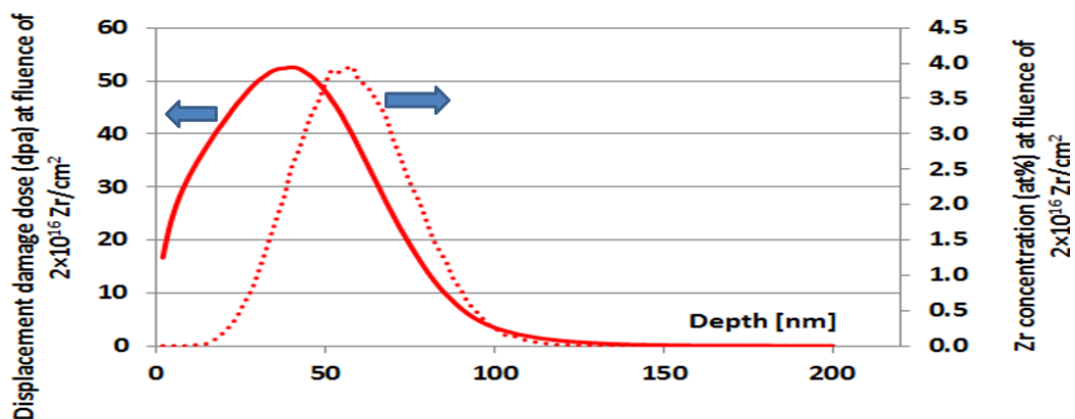


Figure 31 Range and concentration profile of 175 keV  $\text{Zr}^+$  ions to a fluence of  $2 \times 10^{16} \text{ Zr}/\text{cm}^2$  during implantation into sapphire

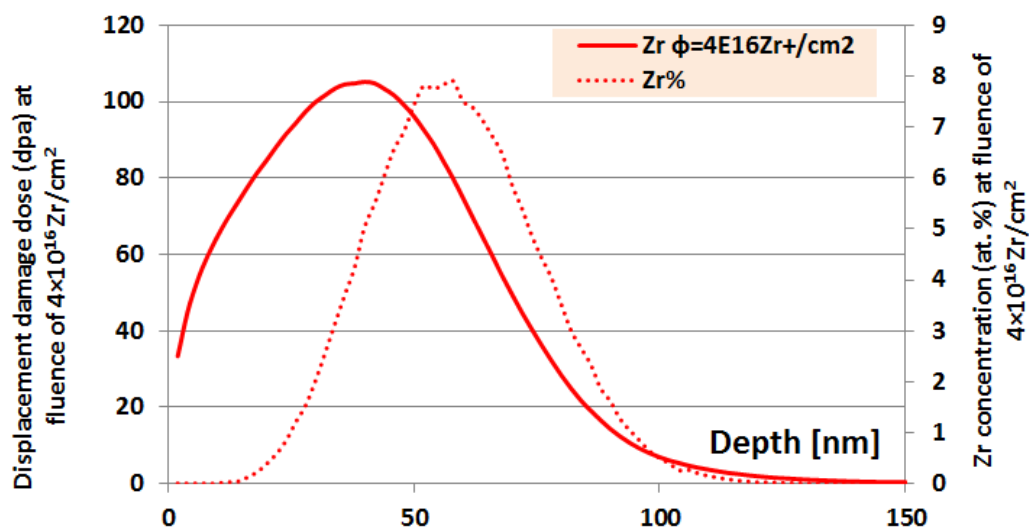


Figure 32 Range and concentration profile of 175 keV  $Zr^+$  ions to a fluence of  $4 \times 10^{16}$   $Zr/cm^2$  during implantation into sapphire

Figure 33 shows the distribution of energy loss during the penetration of energetic Zr (175 keV) over the depth of penetration till the ions come to rest. This energy loss has been separated to the nuclear and electronic energy loss. The ballistically energy loss in the amorphous phase is more dominant compared with the electronic collisions. In general, in the low energy regime the electronic energy loss that involves in excitations and ionization is small compared with the energy spent in nuclear elastic collisions. Usually electronic collisions do not change the ion trajectory, and their energy spend is not sufficient for lattice disordering. On the other hand, nuclear collisions can have significant role in angular deflection of the trajectory of the ions; also they are responsible for the lattice disorder.

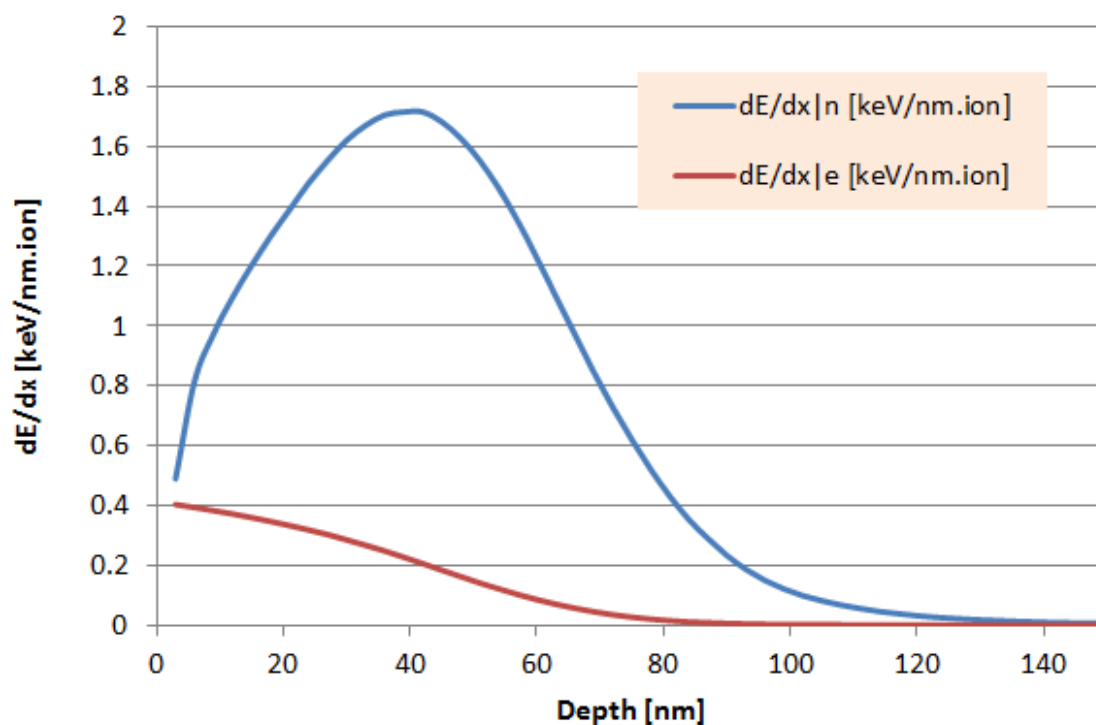


Figure 33 Nuclear and electronic energy loss for 175 keV  $Zr^+$  ions into sapphire

Figure 34 shows SRIM calculated nuclear and electronic energy loss for  $Al_2O_3$  irradiated with 55 keV  $O^+$  ions, after the formation of buried amorphous layer due to prior irradiation with  $Zr^+$  ions to a fluence of  $1.5 \times 10^{16} Zr^+/cm^2$ .

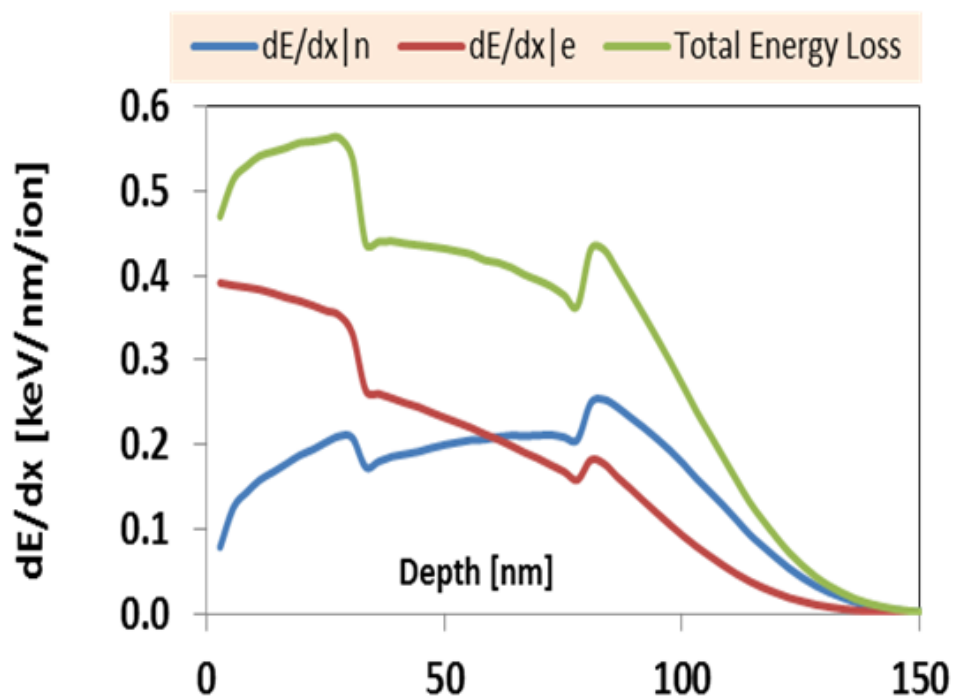


Figure 34 SRIM calculated nuclear and electronic energy loss for  $Al_2O_3$  irradiated with 55 keV  $O^+$  ions, after the formation of buried amorphous layer due to prior "high dose" irradiation with  $Zr^+$  ions

## Chapter 4

### Results and discussion

#### 4.1 The effect of zirconium irradiation on the structure of sapphire and threshold fluence for amorphization

Figure 35 shows RBC-C spectra obtained from a sample of  $\alpha$ -Al<sub>2</sub>O<sub>3</sub> irradiated with 175 keV Zr ions to a fluence of  $2 \times 10^{15}$  Zr/cm<sup>2</sup> at room temperature. The RBS-C shows that this fluence is not sufficient to amorphize the sample. The Zr profile in Fig. 35 is magnified ten times.

Figure 36 shows the RBS-C spectra for the sample irradiated to a fluence of  $7.5 \times 10^{15}$  Zr/cm<sup>2</sup> at room temperature. The aligned spectrum for this sample exhibits a minimum yield ( $\chi_m$ ) for Al of ~0.5.

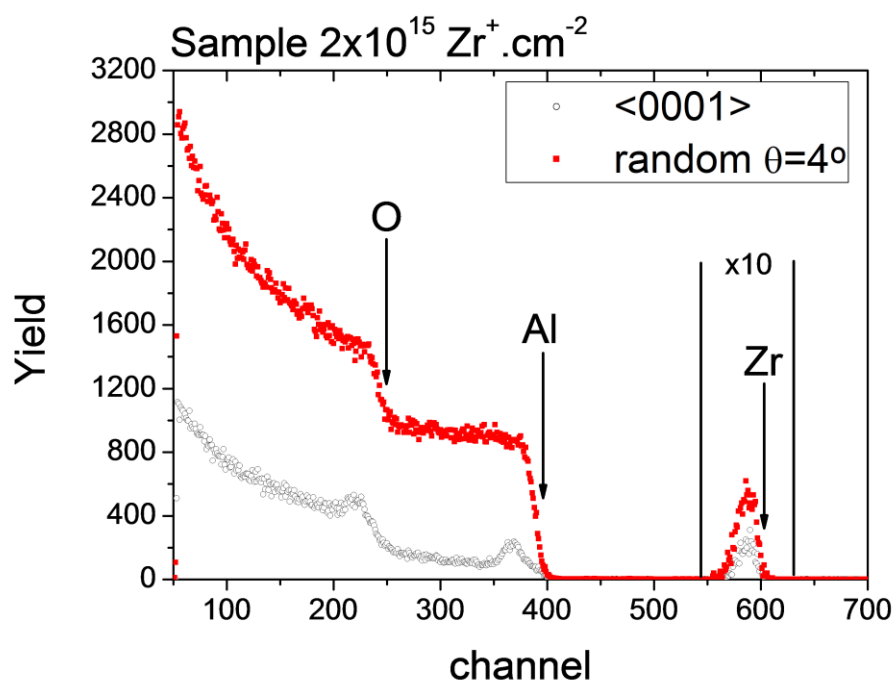


Figure 35 RBS-C spectra obtained from  $\alpha\text{-Al}_2\text{O}_3$  sample irradiated with  $2 \times 10^{15} \text{ Zr}^+/\text{cm}^2$ .

This is “low- dose” sample in the sense that the Zr displacement damage dose is less than the threshold dose for amorphization. Arrows labeled “Zr”, “Al”, and “O”, indicate the surface elastic scattering energies for Zr, Al, and O atoms respectively.

Scattering angle of  $165^\circ$  was used for this measurement.

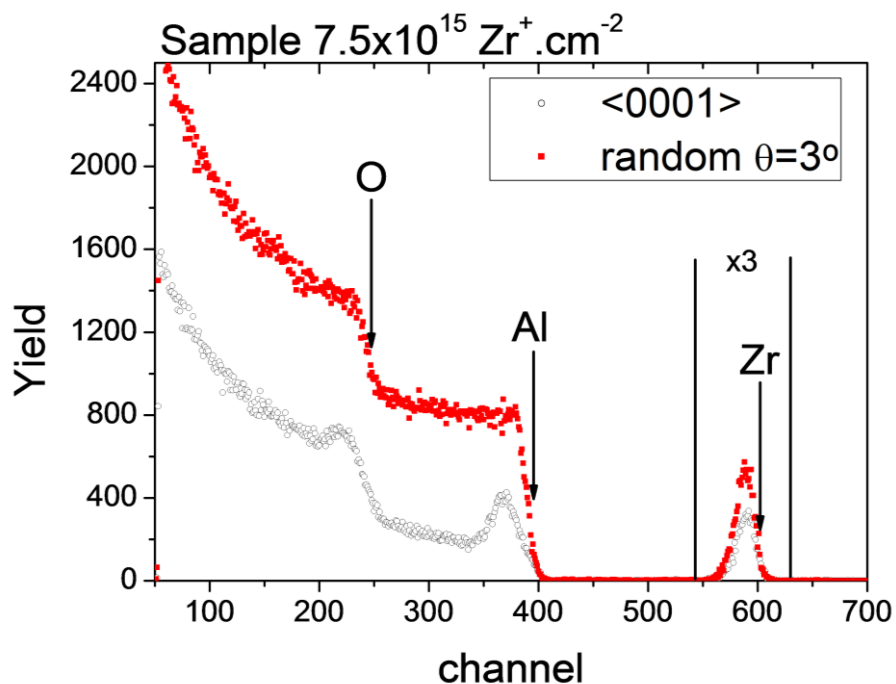


Figure 36 RBS-C spectra obtained from  $\alpha$ -Al<sub>2</sub>O<sub>3</sub> sample irradiated with  $2 \times 10^{15}$  Zr<sup>+</sup>/cm<sup>2</sup>.

This is “low- dose” sample in the sense that the Zr displacement damage dose is less than the threshold dose for amorphization. Arrows labeled “Zr”, “Al”, and “O”, indicate the surface elastic scattering energies for Zr, Al, and O atoms respectively.

Scattering angle of 165 ° was used for this measurement.

Figure 37 shows bright-field (BF) images obtained from cross-sectional TEM of the same sample. The Selected area electron diffraction (SAED) pattern confirms that this dose is “low- dose” in the sense that the Zr displacement damage dose is less than the threshold dose for amorphization. There is a highly damaged but crystalline region extending to more than 100 nm from the surface.



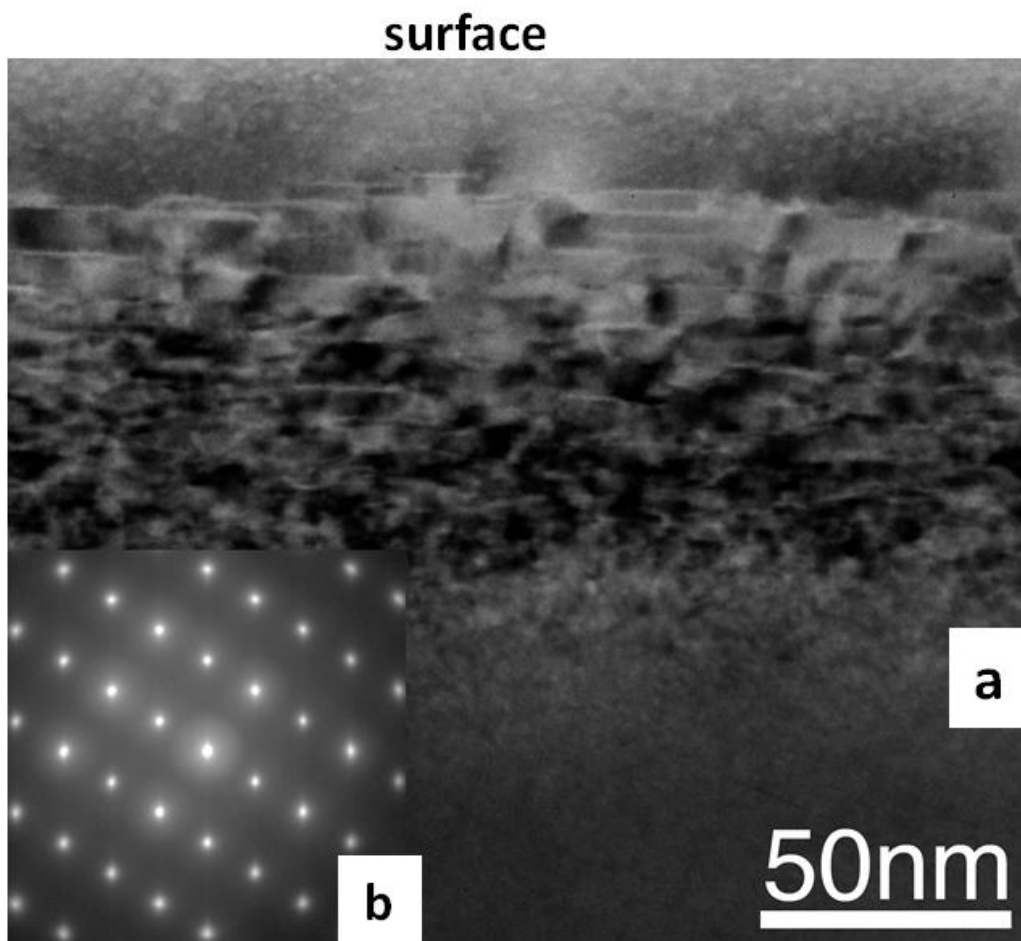


*Figure 37 (a) TEM cross section image and (b) Selected area electron diffraction (SAED) patterns obtained from  $\alpha$ - $\text{Al}_2\text{O}_3$  sample irradiated with  $7.5 \times 10^{15} \text{ Zr}^+/\text{cm}^2$ . This is “low-dose” sample in the sense that the Zr displacement damage dose is less than the threshold dose for amorphization.*

Figure 38 shows the RBS-C spectra for the samples irradiated to a fluence of  $1.5 \times 10^{16}$  Zr/cm<sup>2</sup>. The aligned spectra overlap the random spectra, suggesting the presence of a random scattering surface indicating an “amorphous” surface for the sample. Figure 39 shows bright-field (BF) images obtained from cross-sectional TEM samples of the same sample at room temperature. There is an amorphous region ~50 nm thick sandwiched between two highly damaged, crystalline regions. The near-surface and deeper highly damaged regions are about 23 and 75 nm thick respectively. Fig. 39 shows that the total defected regions of this sample including the amorphous region and two damaged regions is about 155 nm that is farther than the depth predicted by SRIM. This can be attributed to the damage produced by Al and O atoms recoil.

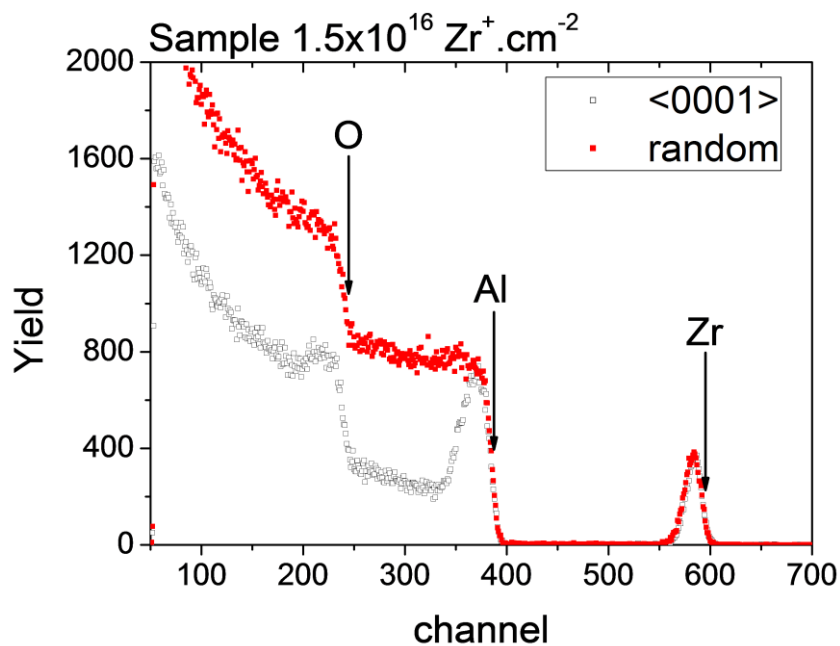
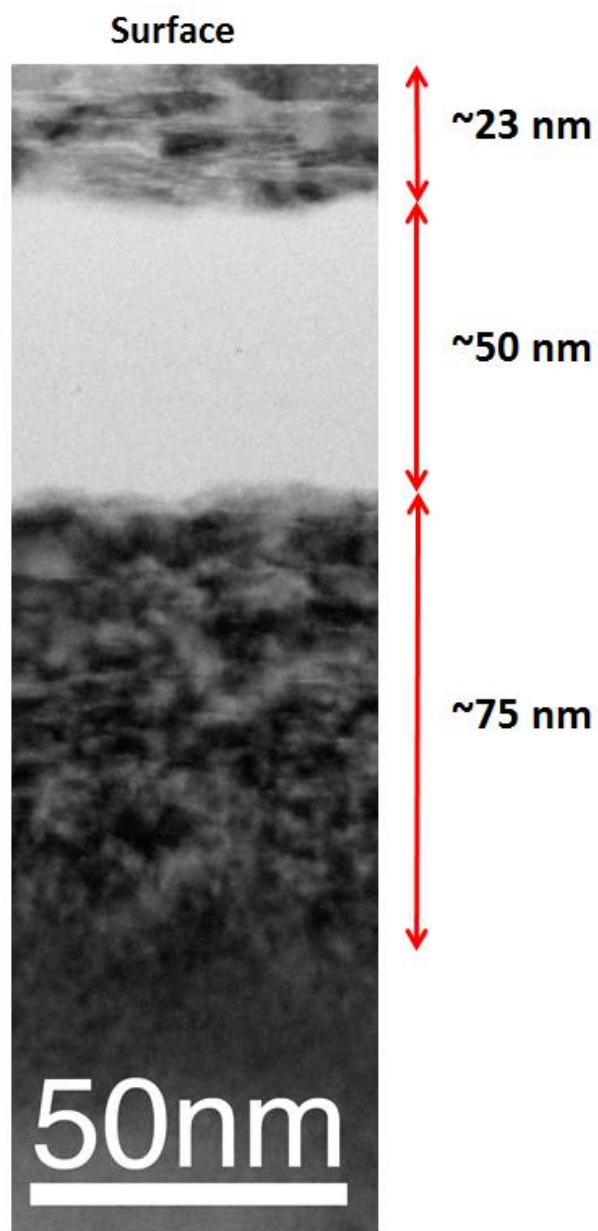


Figure 38 RBS-C spectra obtained from  $\alpha\text{-Al}_2\text{O}_3$  sample irradiated with  $1.5 \times 10^{16} \text{ Zr}^+/\text{cm}^2$ . This is “high dose” sample in the sense that the Zr displacement damage dose is in excess of the threshold dose for amorphization. Arrows labeled “Zr”, “Al”, and “O”, indicate the surface elastic scattering energies for Zr, Al, and O atoms respectively.

Scattering angle of  $165^\circ$  was used for this measurement.



*Figure 39 TEM cross section image obtained from  $\alpha$ - $\text{Al}_2\text{O}_3$  sample irradiated with  $1.5 \times 10^{16} \text{ Zr}^+/\text{cm}^2$ . This is “high dose” sample in the sense that the Zr displacement damage dose is in excess of the threshold dose for amorphization.*

Figure 40 shows the RBS-C spectra for the samples irradiated with Zr to a fluence of  $2 \times 10^{16}$  Zr/cm<sup>2</sup>. The aligned spectra overlap the random spectra, suggesting the presence of a random scattering surface indicating an “amorphous” surface for the sample.

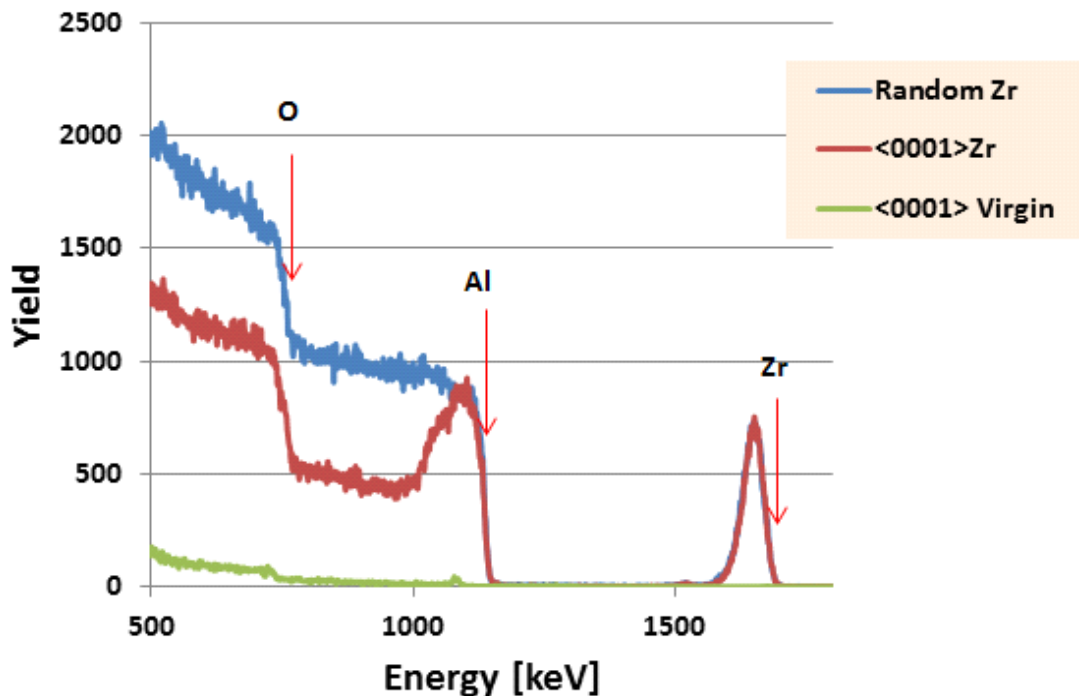
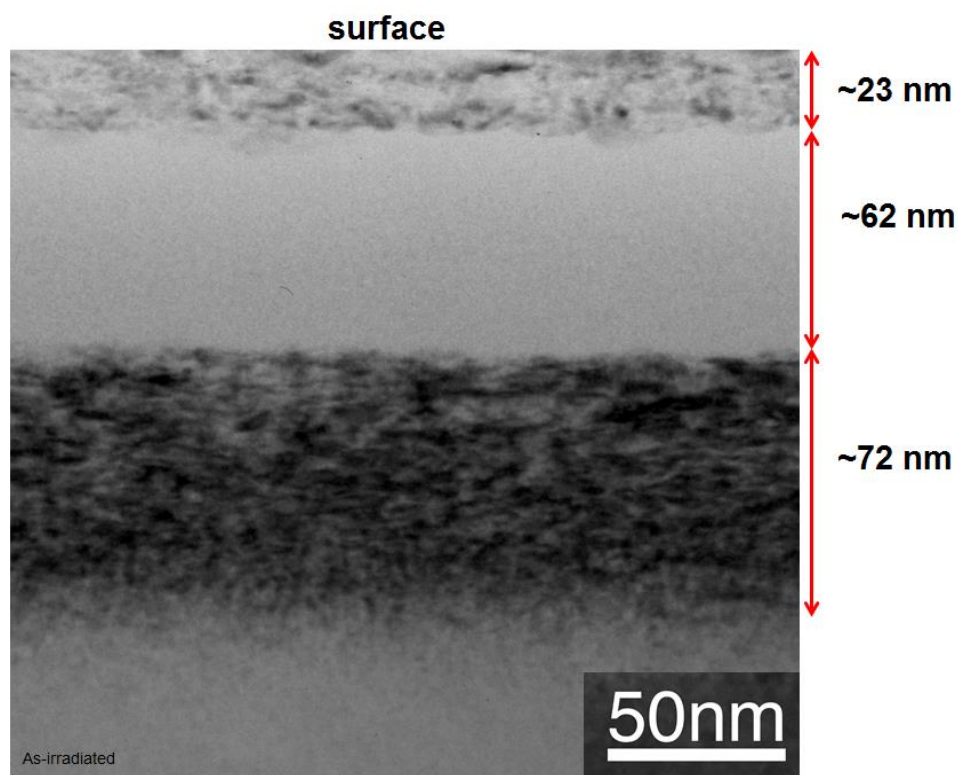


Figure 40 RBS-C spectra obtained from  $\alpha$ -Al<sub>2</sub>O<sub>3</sub> sample irradiated with  $2 \times 10^{16}$  Zr<sup>+</sup>/cm<sup>2</sup>.

This is “high dose” sample in the sense that the Zr displacement damage dose is in excess of the threshold dose for amorphization. Arrows labeled “Zr”, “Al”, and “O”, indicate the surface elastic scattering energies for Zr, Al, and O atoms respectively.

Scattering angle of 170 ° was used for this measurement.

Figure 41 shows bright-field (BF) images obtained from cross-sectional TEM samples of the same sample at room temperature. There is an amorphous region  $\sim 62$  nm thick sandwiched between two highly damaged, crystalline regions. The near-surface and deeper highly damaged regions are about 23 and 72 nm thick respectively. Comparing Figs. 39 and 41, it is apparent that the widths of two highly damaged regions remain almost the same but the width of amorphous region increases about 12 nm for the sample irradiated to a fluence of  $2 \times 10^{16} \text{ Zr/cm}^2$ .



*Figure 41 TEM cross section image obtained from  $\alpha\text{-Al}_2\text{O}_3$  sample irradiated with  $2 \times 10^{16} \text{ Zr}^+/\text{cm}^2$ . This is “high dose” sample in the sense that the Zr displacement damage dose is in excess of the threshold dose for amorphization.*

Figure 42 shows the RBS-C spectra for the samples irradiated with Zr to a fluence of  $4 \times 10^{16} \text{ Zr/cm}^2$ . The aligned and random spectra of the implanted region overlap in the energy range of 1.05– 1.1 MeV suggesting a buried “amorphous” region. The Zr spectra in Fig. 42 also exhibit no channeling, indicating random distribution of the implanted Zr ions.

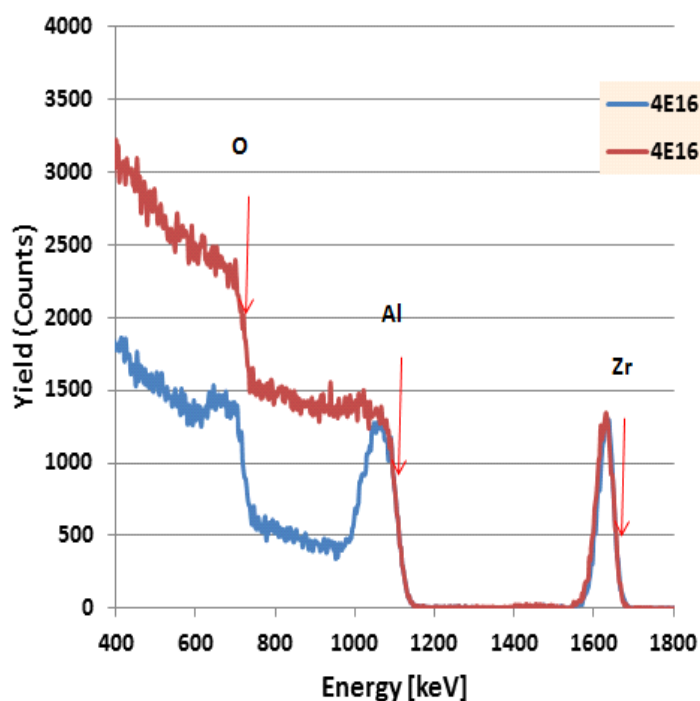


Figure 42 RBS-C spectra obtained from  $\alpha\text{-Al}_2\text{O}_3$  sample irradiated with  $2 \times 10^{16} \text{ Zr}^+/\text{cm}^2$ .

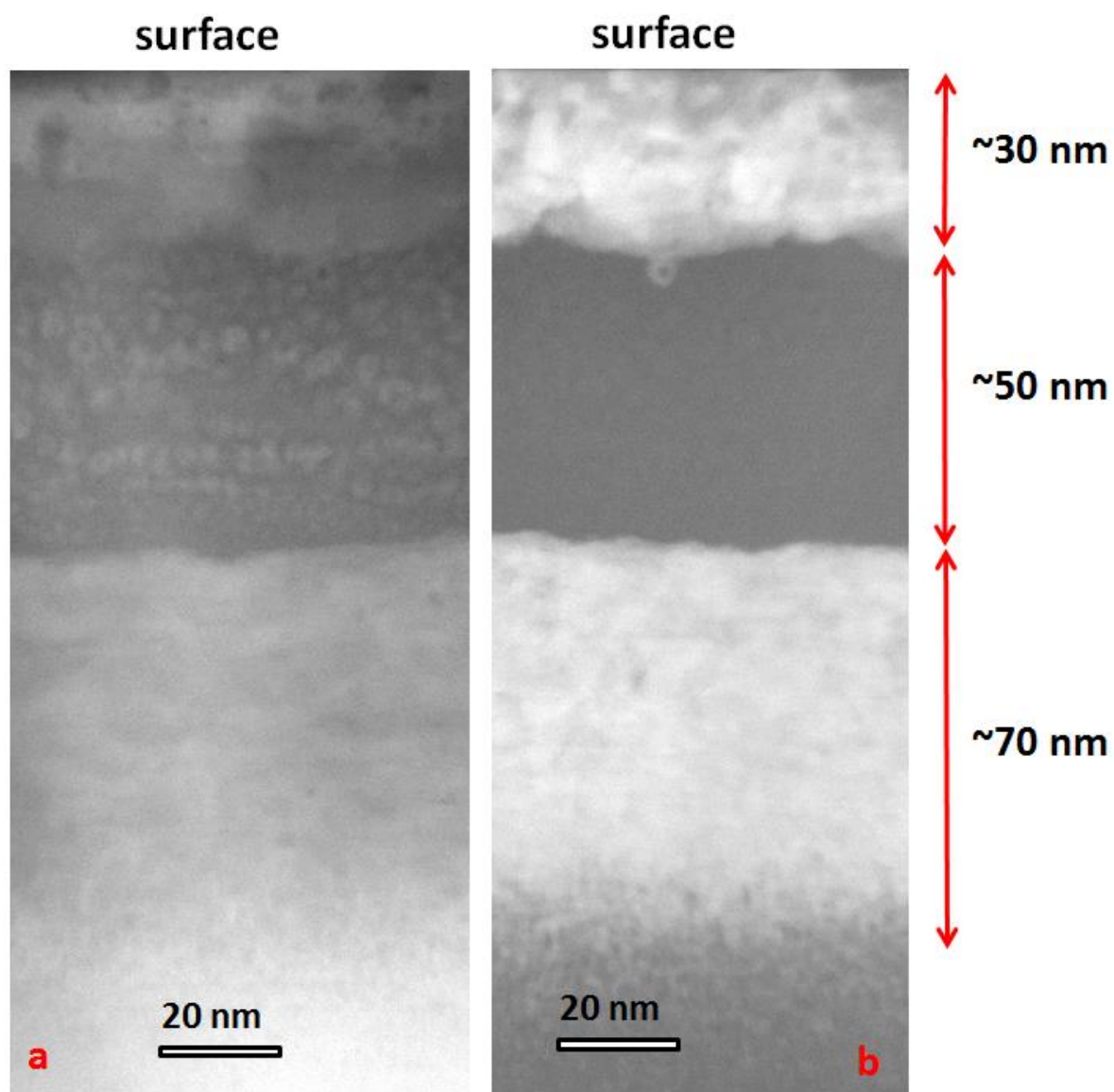
This is “high dose” sample in the sense that the Zr displacement damage dose is in excess of the threshold dose for amorphization. Arrows labeled “Zr”, “Al”, and “O”, indicate the surface elastic scattering energies for Zr, Al, and O atoms respectively.

Figure 43a,b are high angle annular dark field (HAADF) and bright-field images respectively obtained from cross-sectional aberration-corrected STEM sample of  $\alpha$ -Al<sub>2</sub>O<sub>3</sub> irradiated to a fluence of  $4 \times 10^{16}$  Zr/cm<sup>2</sup> at room temperature.

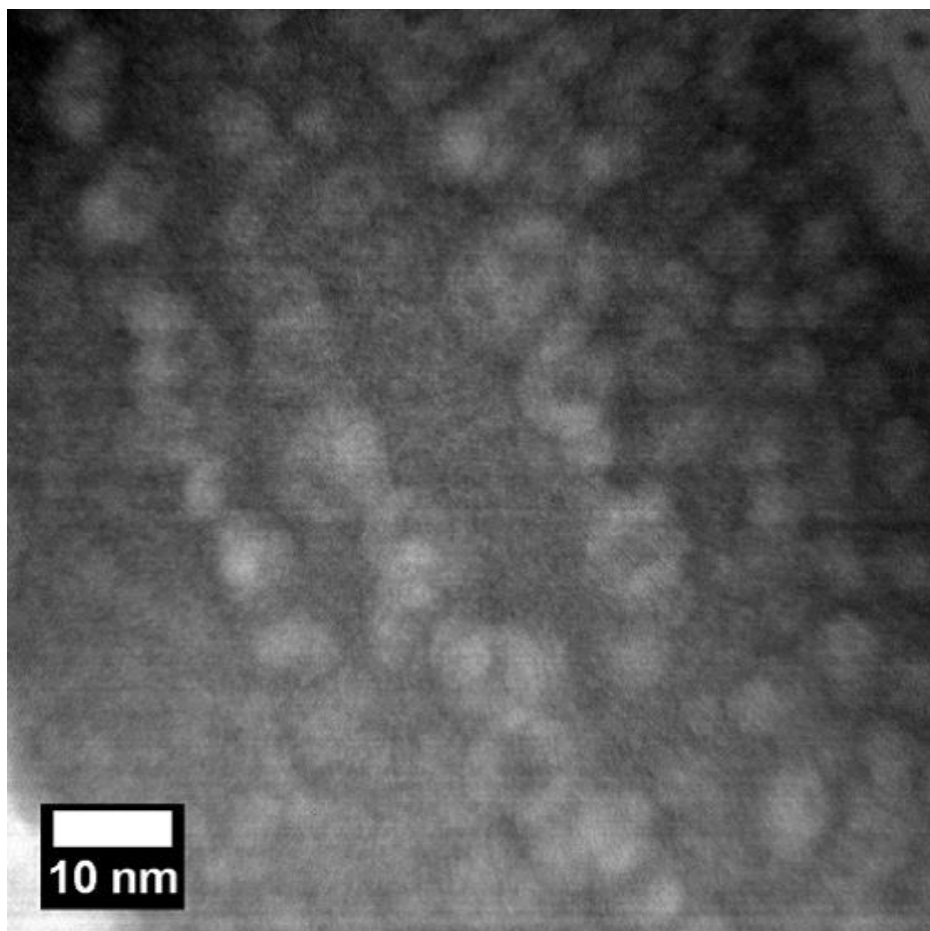
Embedded nanoparticles or clusters are present in the amorphous region. The Zr-rich clusters are distributed through a range of about 30–80 nm below the surface. The Z-contrast image shows a near-surface damaged layer about 30 nm thick, a subsurface region exhibiting “random” de-channeling ~50 nm thick, and a deeper damaged, crystalline zone ~70 nm thick.

Figure 44 shows HAADF image from the middle of the amorphous region. Nearly spherical Zr nano-clusters can be observed in this region. The average size of these nano-clusters is about 8 nm.





*Figure 43 High angle annular dark field cross section image of  $\alpha$ -Al<sub>2</sub>O<sub>3</sub> implanted with Zr ions*



*Figure 44 High angle annular dark field (HAADF) cross section image of  $\alpha$ - $\text{Al}_2\text{O}_3$  irradiated with Zr ions from amorphous region shows nearly spherical Zr-rich clusters*

Figure 45a, b shows a cross-sectional HAADF and BF images of the microstructure in  $\alpha$ -Al<sub>2</sub>O<sub>3</sub> irradiated to a fluence of  $4 \times 10^{16}$  Zr/cm<sup>2</sup>. In addition, Fig.45c, d, and e show bright field images obtained from various regions of the ion irradiated microstructure along with their corresponding images for Fourier transform (Fig 45f,g, and h) . Fig. 45 indicates that the subsurface region has lack of crystallinity, whereas the near surface and the deeper damaged layer have remained crystalline.

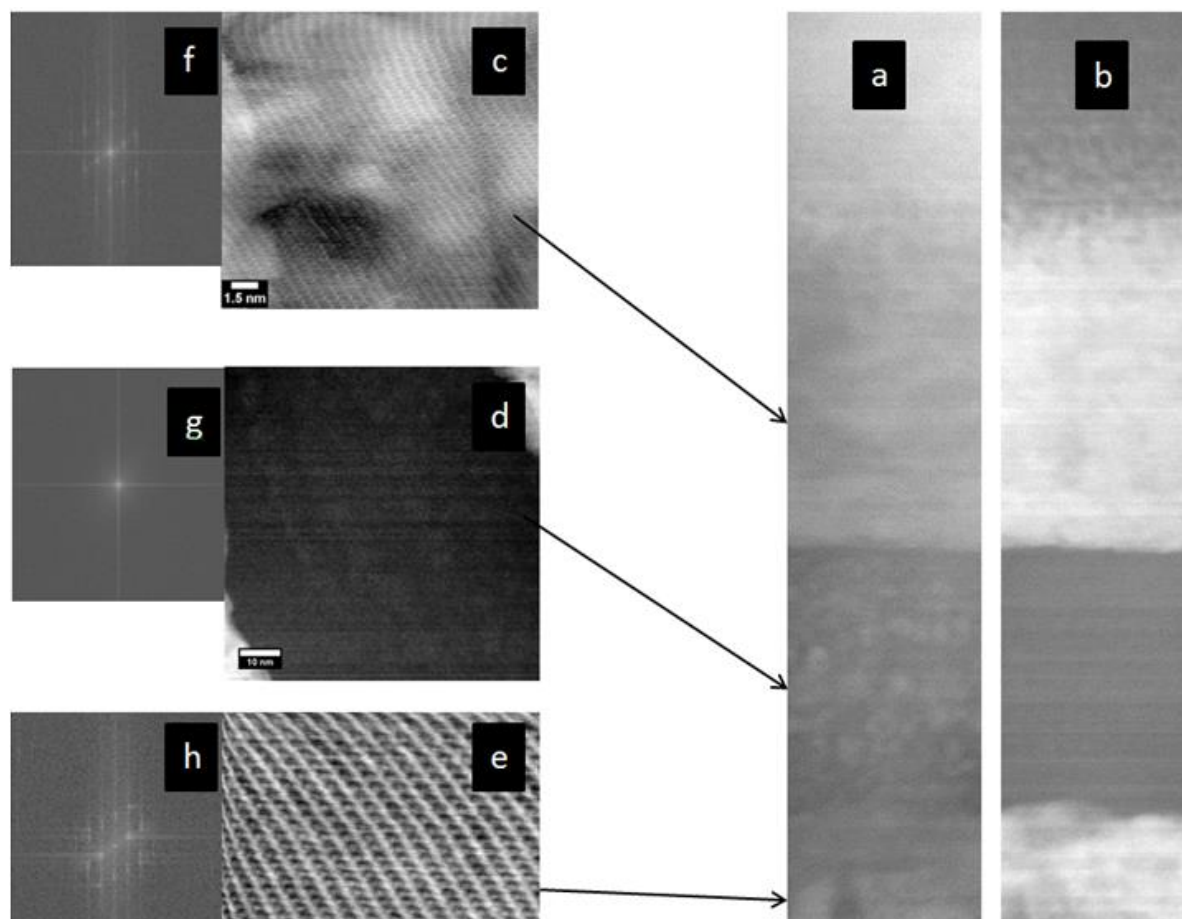


*Figure 45 (a) High angle annular dark field, (b) bright field, (c–e) bright field, and (f–h) fast Fourier transform (FFT) from the three regions of zirconium implanted-sapphire.*

Figure 46 shows the EELS Al-L<sub>2,3</sub> edge spectra for three different regions: (a) bulk, (b) sub-surface and deeper damaged, and (c) amorphous. Because the EELS Al-L<sub>2,3</sub> edge spectra for the subsurface and deeper damaged regions were identical, Fig. 46 shows the spectrum for the deeper damaged region as a representative for both. The bulk, subsurface damaged and deeper damaged have similar spectrum but the counts for the bulk region are higher because the sample is thicker there. Qualitatively, the sample shows two major regions: bulk-like  $\alpha$ -Al<sub>2</sub>O<sub>3</sub> and the amorphous regions. Figure 46 shows that the  $\alpha$ -Al<sub>2</sub>O<sub>3</sub> edge for the amorphous region is rounder and shifted to a lower energy. The Al-L<sub>2,3</sub>-edge of Al<sub>2</sub>O<sub>3</sub> spectrum from amorphous region has a different shape with two peaks compared with the Al<sub>2</sub>O<sub>3</sub> L-edge spectrum from bulk and subsurface and deeper damaged regions of one peak near 80 eV.

Brydson [212] proposed that multiple scattering (MS) theory combined with EELS measurements from a reference material might be used as a fingerprint. Figure 47 adapted from [212] shows that the results of MS calculations for the Al L<sub>2,3</sub>-energy loss near-edge structure (ELNES) of tetrahedral AlO<sub>4</sub> and octahedral AlO<sub>6</sub> may be used as a fingerprint of the local coordination. First principle calculations of band structures have shown that the L-edge for tetrahedrally coordinated Al has the first peak shifted to lower energy with respect to the peak near 80 eV for octahedrally coordinated Al (Figure 48). The first peak in Fig. 46c is less pronounced than the second, indicating that it is a  $\gamma$ -Al<sub>2</sub>O<sub>3</sub>-like edge. In  $\alpha$ -Al<sub>2</sub>O<sub>3</sub>, Al is in octahedral coordination, while in  $\gamma$ -Al<sub>2</sub>O<sub>3</sub> some Al are octahedrally coordinated and some are tetrahedrally coordinated to oxygen.

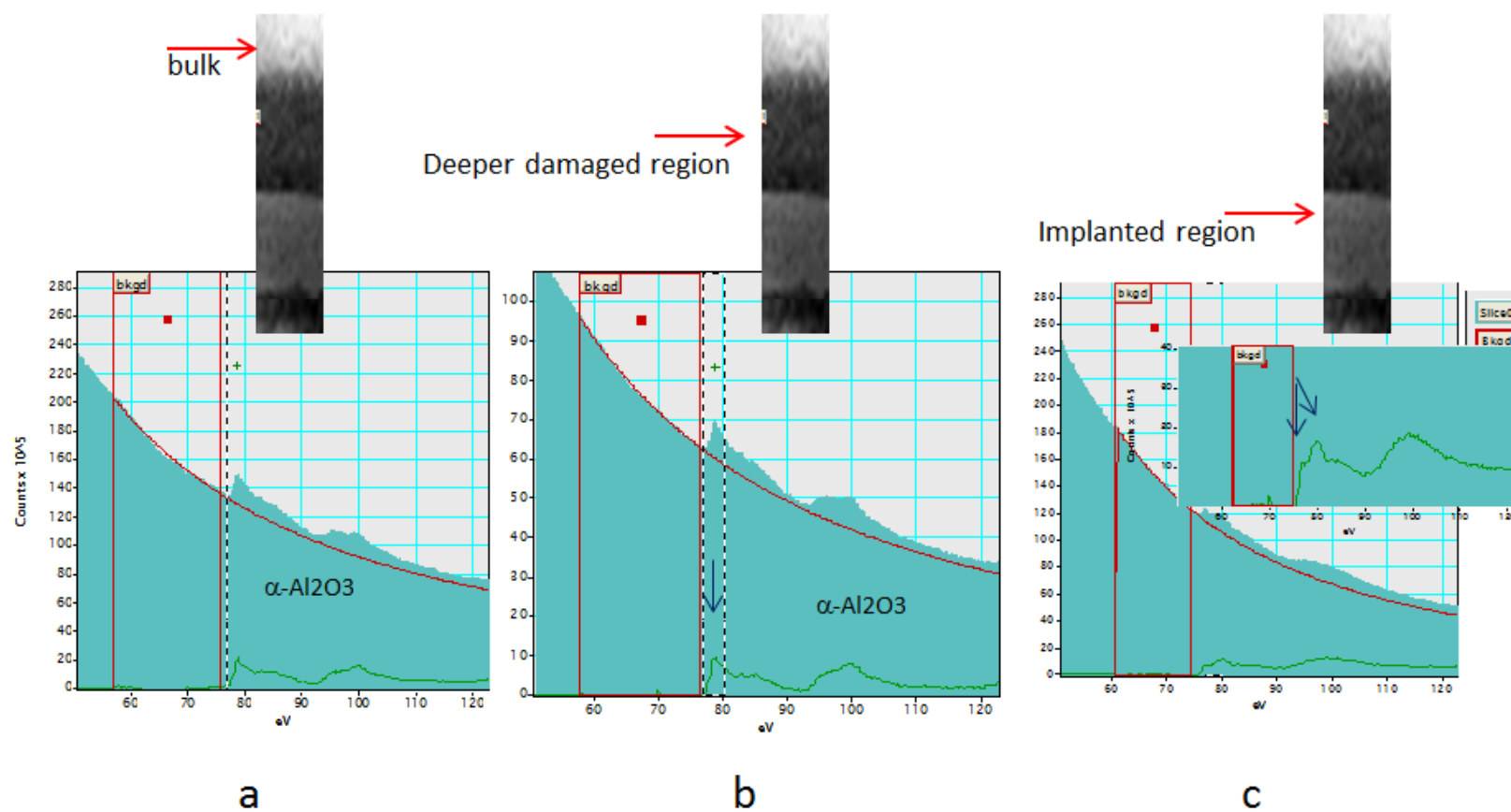


Figure 46 EELS Al-L spectra from (a) bulk region, (b) near surface damaged and deeper damaged regions, and (c) amorphous region

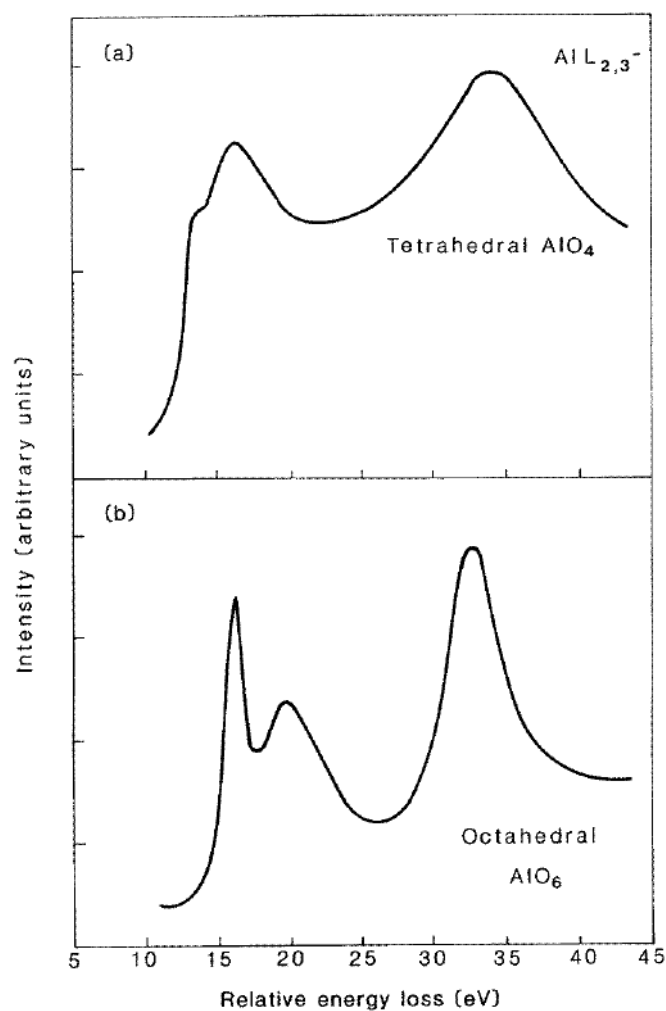


Figure 47 The results of MS calculations for the Al  $L_{2,3}$ -ELNES of: (a) tetrahedral  $AlO_4$  with Al–O distances equal to 0.17 nm and (b) octahedral  $AlO_6$  with Al–O distances equal to 0.19 nm [212].

Metallic Al shifts the spectrum toward a lower energy and rounds the edge. When the compound becomes more metallic a shift to lower energy can be seen. Based on Figure 46 and 48 there is no evidence of aluminum in metallic form.

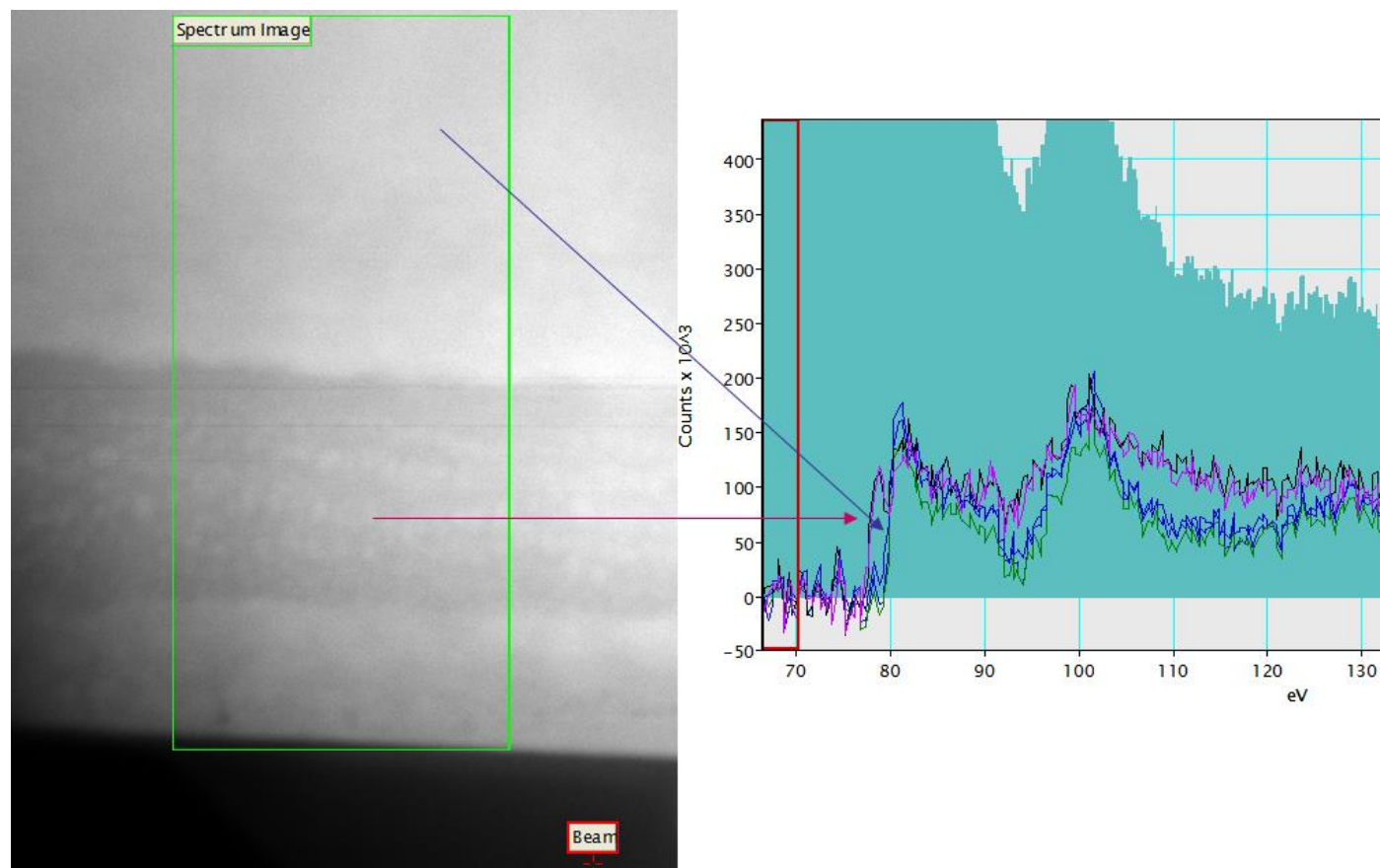


Figure 48 Al  $L_{2,3}$ -EELS spectra for different regions of the  $\alpha$ - $\text{Al}_2\text{O}_3$  sample irradiated with 175 keV  $\text{Zr}^+$  ions to a fluence of  $4 \times 10^{16} \text{ Zr/cm}^2$ : the  $\alpha$ - $\text{Al}_2\text{O}_3$  edge is rounder and shifted to a lower energy like (purple spectrum).



Figures 49 a and b show EELS oxygen-K edge obtained from sample of  $\alpha$ -Al<sub>2</sub>O<sub>3</sub> irradiated to a fluence of  $4 \times 10^{16}$  Zr/cm<sup>2</sup>. Comparison between O–K edge spectra from bulk-like and amorphous regions shows there is some oxygen deficiency in the amorphous region. The bulk-like region shows an O–K with three features, which are seen in  $\alpha$ -Al<sub>2</sub>O<sub>3</sub>.

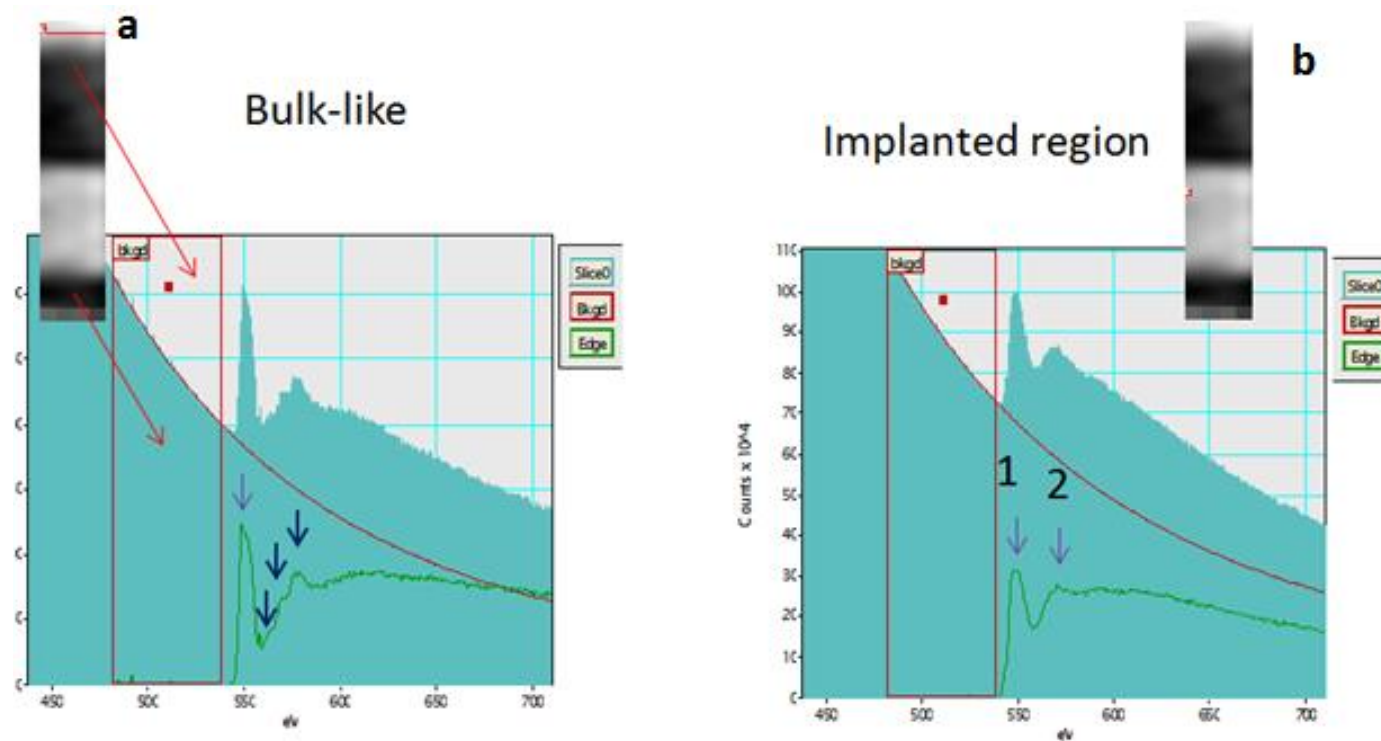


Figure 49 Electron energy loss spectroscopy (EELS) oxygen-K edge obtained from sample of  $\alpha\text{-Al}_2\text{O}_3$  irradiated with 175 keV Zr ions to a fluence of  $4 \times 10^{16}$  Zr/cm<sup>2</sup> at room temperature. (a) spectrum from subsurface and deeper damaged regions (b) spectrum from the amorphous region

The amorphous region does not have those features, which is consistent with  $\gamma$ - $\text{Al}_2\text{O}_3$ . However, if there weren't any oxygen deficiency the first peak (1) should be as high as in the bulk-like region. Instead the ratio of peak 1 to peak 2 is lower; the edge is more washed out indicating an oxygen deficiency. These results are interpreted as showing that the amorphous region exhibits short-range order similar to that of  $\gamma$ - $\text{Al}_2\text{O}_3$  with oxygen deficiency. In spite of this fact that there is no evidence for oxygen bubbles or aluminum precipitates, it is not clear where the oxygen atoms that were originally in the now oxygen-deficient amorphous region are.

The results of present work shows that the threshold fluence for sapphire amorphization with zirconium even is lower than that found by White et al. The threshold fluence for amorphization of sapphire is reported to be between  $7.5 \times 10^{15}$  and  $1.5 \times 10^{16}$   $\text{Zr}^+/\text{cm}^2$  (175 keV). Carter and Grant studied the effect of ion irradiation induced amorphization in different solids. They showed that with increasing ion fluence, accumulation and overlap of individual amorphous zone led to formation of an amorphous layer [213]. However the results of this work show that ion fluence and dpa alone are not responsible for amorphization.

Figure 50 shows TEM cross-section images and SAED patterns obtained from  $\alpha$ - $\text{Al}_2\text{O}_3$  samples irradiated with  $7.5 \times 10^{15}$   $\text{Zr}^+/\text{cm}^2$ . Also shown are SRIM calculated profiles for the Zr displacement damage dose (in units of dpa) as a function of target sample depth and the implanted Zr concentration versus depth. The specimen irradiated with Zr ions to a fluence of  $7.5 \times 10^{15}$   $\text{Zr}/\text{cm}^2$  contained only a damaged crystalline implanted zone. The displacement damage dose reached a value of  $\sim 20$  dpa over the

range of ~25 to ~65 nm from the surface but the Zr content ranged from 0.2 to 1.3% in this region.

Figure 51 indicates a TEM-BF cross section image and SAED patterns obtained from  $\alpha$ -Al<sub>2</sub>O<sub>3</sub> samples irradiated with  $1.5 \times 10^{16}$  Zr<sup>+</sup>/cm<sup>2</sup>. Along with the TEM-BF image also shown is SRIM calculated profiles for the Zr displacement damage dose (in units of dpa) as a function of target sample depth and the implanted Zr concentration versus depth. The specimen irradiated with Zr ions to a fluence of  $1.5 \times 10^{16}$  Zr/cm<sup>2</sup> contained an amorphous region sandwiched by subsurface and deeper damage regions. The amorphous/deeper damage interfaces lie at ~20 dpa and ~2.5% Zr.

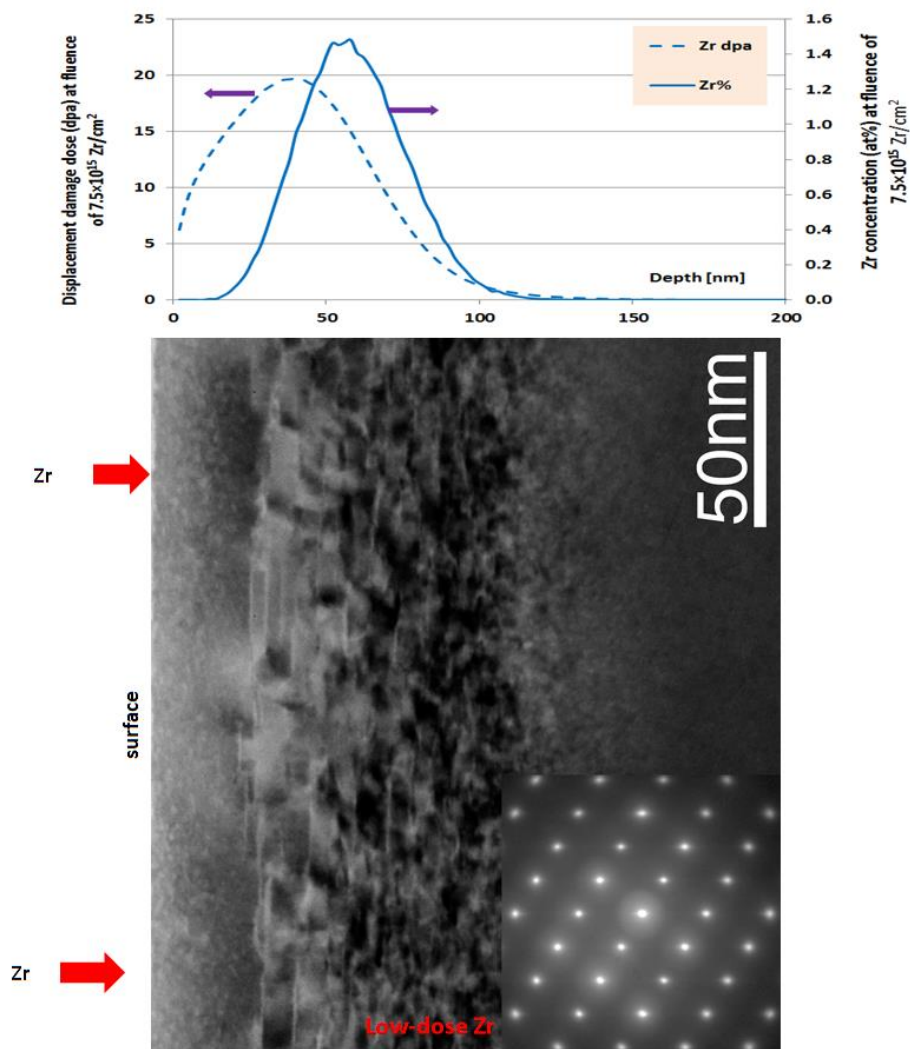


Figure 50 TEM cross section image and SAED patterns obtained from  $\alpha\text{-Al}_2\text{O}_3$  samples irradiated with  $7.5 \times 10^{15} \text{ Zr}^+/\text{cm}^2$ . These are “low- dose” samples in the sense that the Zr displacement damage dose is less than the threshold dose for amorphization. Also shown are SRIM calculated profiles for the Zr displacement damage dose (in units of dpa) as a function of target sample depth and the implanted Zr concentration versus depth.

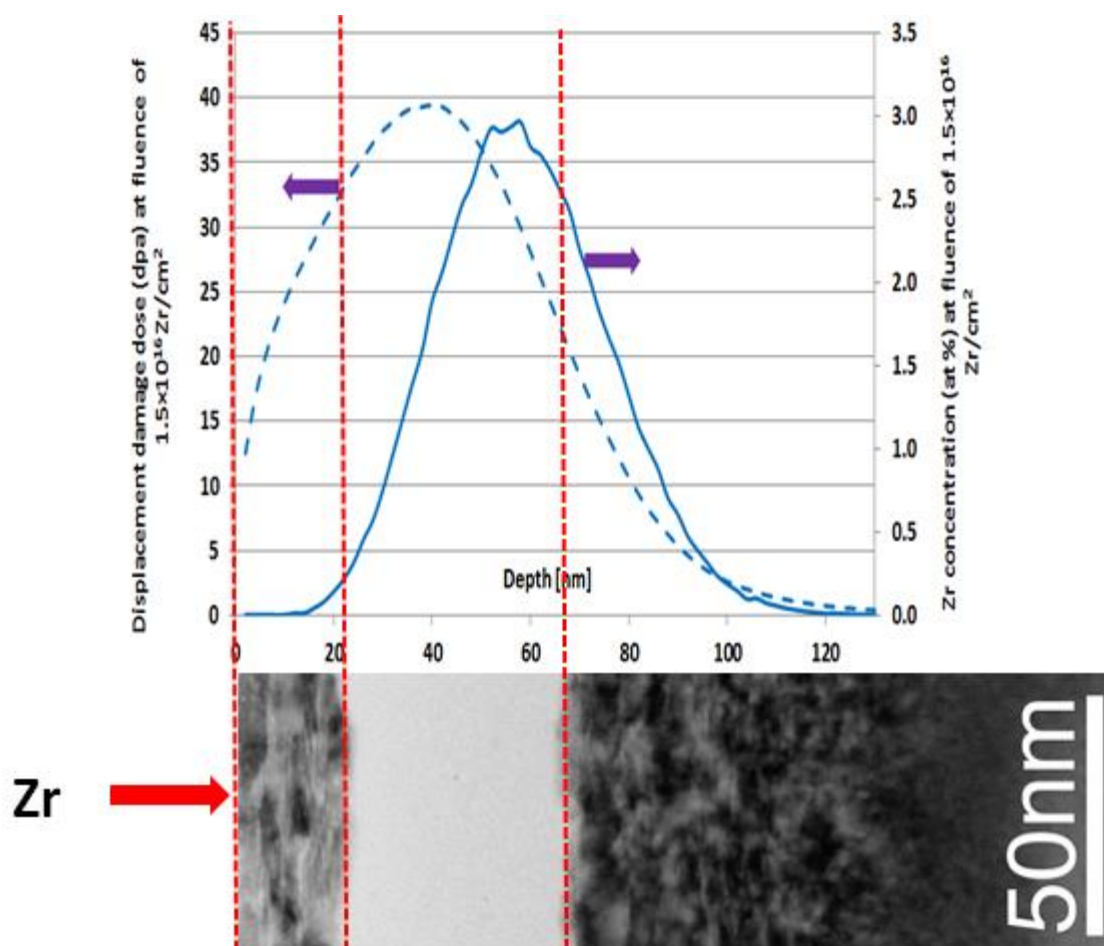


Figure 51 TEM bright-field (BF) image obtained from cross-sectional samples of  $\alpha\text{-Al}_2\text{O}_3$  irradiated with  $1.5 \times 10^{16} \text{ Zr}^+/\text{cm}^2$ . Also shown are SRIM calculated profiles for the Zr displacement damage dose (in units of dpa) as a function of target sample depth and the implanted Zr concentration versus depth.

Figure 52 shows a TEM cross section image and SAED patterns obtained from  $\alpha\text{-Al}_2\text{O}_3$  samples irradiated with  $2 \times 10^{16} \text{ Zr}^+/\text{cm}^2$ . Also shown are SRIM calculated profiles for the Zr displacement damage dose (in units of dpa) as a function of target sample depth

and the implanted Zr concentration versus depth. The specimen irradiated with Zr ions to a fluence of  $2 \times 10^{15} \text{ Zr/cm}^2$  contained an amorphous region sandwiched by subsurface and deeper damage regions. The width of this amorphous region is 62 nm that is about 12 nm more than of the amorphous region related to the sample irradiated with Zr ions to a fluence of  $1.5 \times 10^{15} \text{ Zr/cm}^2$ . The amorphous/deeper damage interfaces lie at  $\sim 8.5 \text{ dpa}$  and  $\sim 1\% \text{ Zr}$ .

Figure 53 indicates a Z-contrast image obtained from  $\alpha\text{-Al}_2\text{O}_3$  samples irradiated with  $4 \times 10^{16} \text{ Zr}^+/\text{cm}^2$ . Also shown are SRIM calculated profiles for the Zr displacement damage dose (in units of dpa) as a function of target sample depth and the implanted Zr concentration versus depth. The specimen irradiated with Zr ions to a fluence of  $4 \times 10^{15} \text{ Zr/cm}^2$  contained an amorphous region sandwiched by subsurface and deeper damage regions. The amorphous/deeper damage interfaces lie at  $\sim 40 \text{ dpa}$  and  $\sim 4.5\% \text{ Zr}$ .

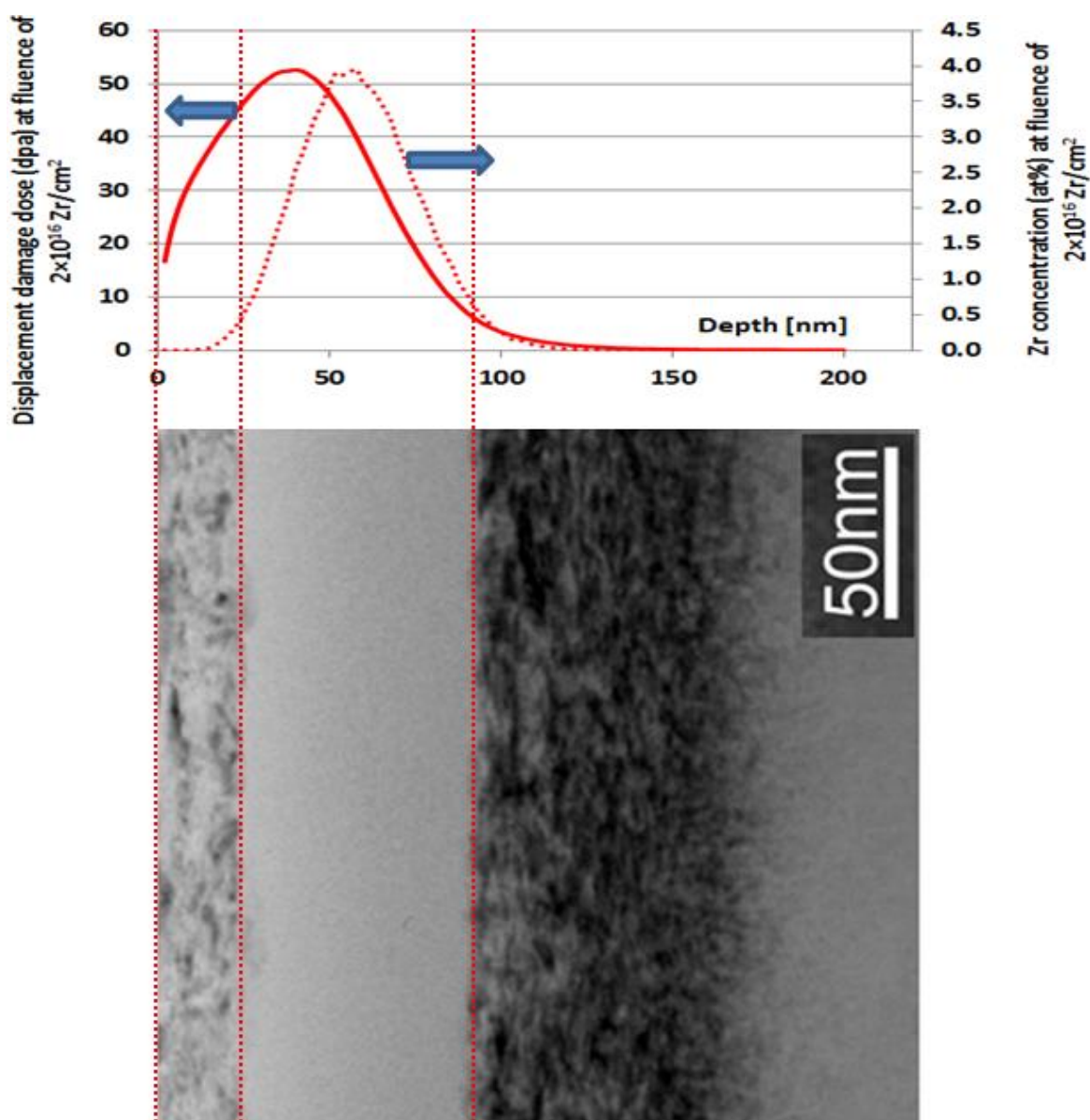


Figure 52 TEM bright-field (BF) image obtained from cross-sectional samples of  $\alpha\text{-Al}_2\text{O}_3$  irradiated with  $2 \times 10^{16} \text{ Zr}^+/\text{cm}^2$ . Also shown are SRIM calculated profiles for the Zr displacement damage dose (in units of dpa) as a function of target sample depth and the implanted Zr concentration versus depth.



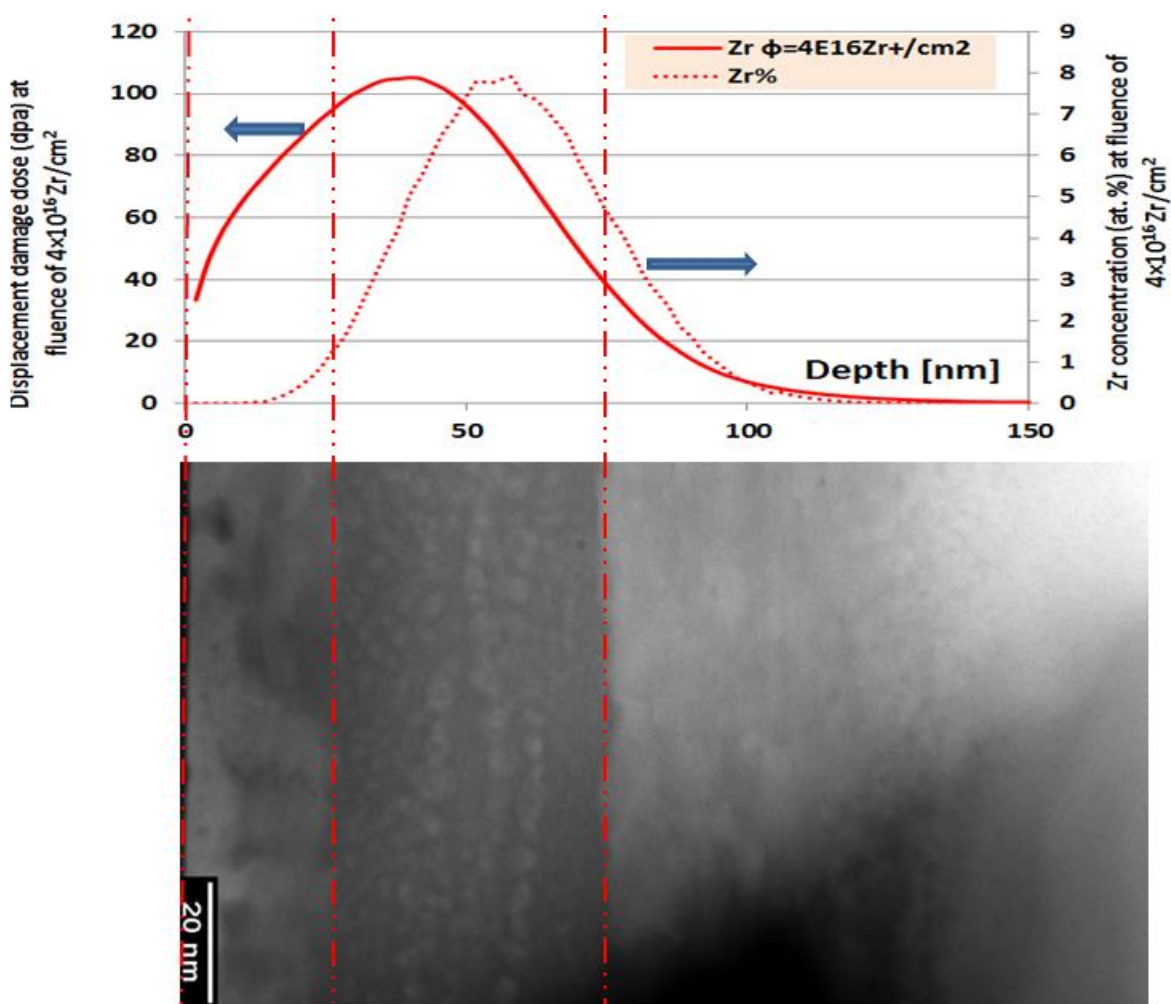


Figure 53 TEM bright-field (BF) image obtained from cross-sectional samples of  $\alpha\text{-Al}_2\text{O}_3$  irradiated with  $4 \times 10^{16} \text{ Zr}^+/\text{cm}^2$ . Also shown are SRIM calculated profiles for the Zr displacement damage dose (in units of dpa) as a function of target sample depth and the implanted Zr concentration versus depth.

Table 8 summarizes information revealed by TEM about the amorphous region along with calculated SRIM-2013 results for subsurface crystalline damaged/amorphous and amorphous/deeper crystalline damaged interfaces. Table 8 shows that by increasing fluence, the subsurface width increases and it is consistent with increasing the Zr% and dpa at crystalline/amorphous interface. For the deeper amorphous/crystalline interface the Zr content and dpa do not show a pattern, but dpa/Zr% could be a good parameter to predict about that interface. The ratio of dpa/Zr% is less than 9.

Table 8 shows that by increasing the fluence, the subsurface width increases and it is consistent with increasing the Zr% and dpa at crystalline/amorphous interface. For the deeper amorphous/crystalline interface the Zr content and dpa do not show a logical pattern, but dpa/Zr% for all the investigated samples show a value in range of 8-8.5.

*Table 9 Summary information obtained from STEM/TEM and calculated SRIM results regarding the interface between highly damaged and amorphous regions for all the studied samples.*

Fluence [ion/cm <sup>2</sup> ]	*Max dpa	*Max Zr%	Subsurface width [nm]	Amorphous width	Zr% at subsurface C/A interface	Zr% at deeper A/C interfa ce	dpa at subsurface C/A interface	dpa at deeper A/C interface	dpa/Zr % at C/A	dpa/Zr% at A/C
$7.5 \times 10^{15}$	19.7	1.5	-	-	0.2 <sup>°</sup>	1.4 <sup>•</sup>	17 <sup>°°</sup>	18 <sup>••</sup>	85	12.8
$1.5 \times 10^{16}$	39	3	23	50	0.2	2.5	38	20	190	8.3
$2 \times 10^{16}$	52	4	23	62	0.4	1.2	46	10	92	8.3
$4 \times 10^{16}$	105	7.9	30	50	2	3.5	98	29	57	8.3

*\*Depth at max dpa and max Zr% are 40 and 58 nm respectively for all the samples.*

*<sup>°</sup>Zr% at 25 nm, <sup>°°</sup>dpa at 25 nm, <sup>•</sup>Zr% at 50 nm, <sup>••</sup>dpa at 50 nm*

#### 4.2 A study of the amorphous $\rightarrow \gamma \rightarrow \alpha$ transformation in Zr-irradiated $\alpha$ -alumina

Figure 54 shows a bright-field TEM image obtained from the as-irradiated  $\alpha$ - $\text{Al}_2\text{O}_3$  sample irradiated with  $2 \times 10^{15} \text{ Zr}^+/\text{cm}^2$  at room temperature. The image shows a buried amorphous region, sandwiched by two highly damaged regions. The widths of these regions are about 23, 62, and 72 nm for the near-surface damaged, amorphous, and the deeper damaged regions respectively.

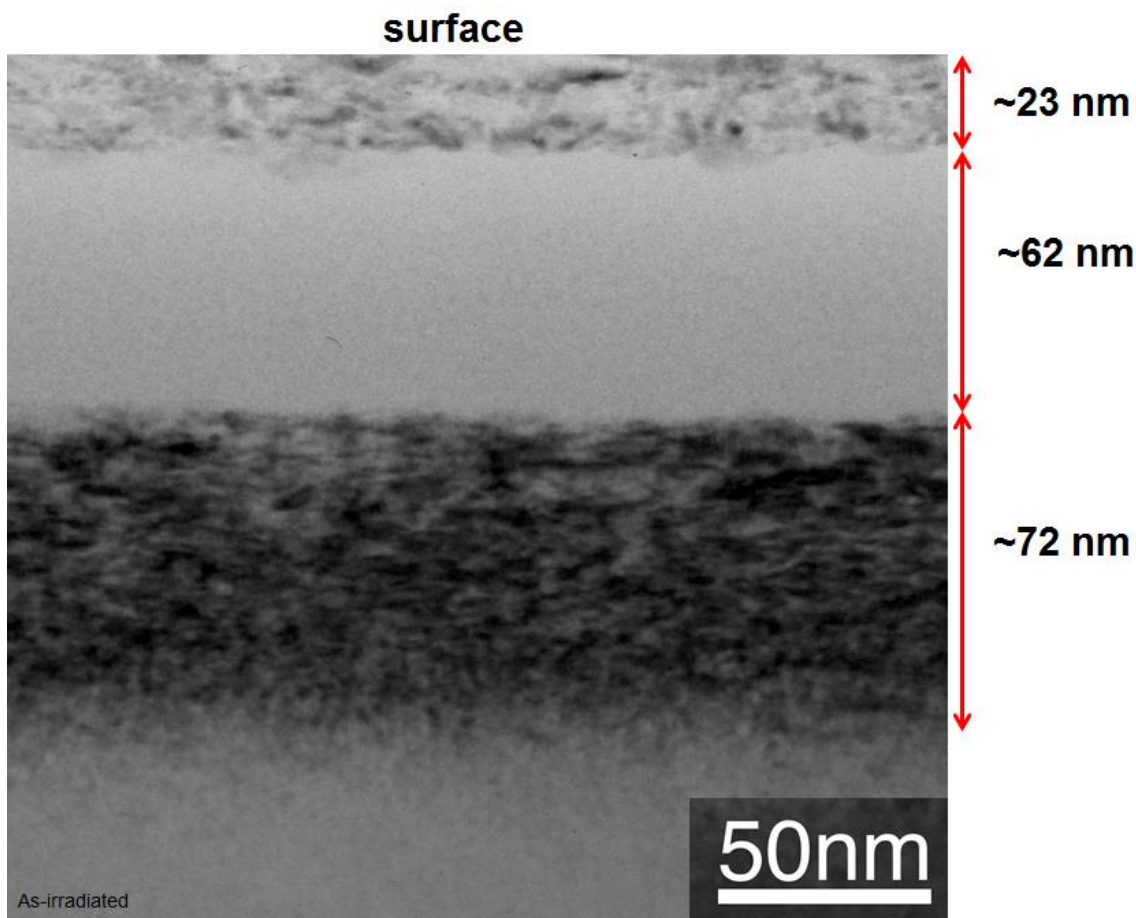


Figure 54 The bright-field image for the sample irradiated to fluence of  $2 \times 10^{15} \text{ Zr}^+/\text{cm}^2$

The RBS-C aligned and random spectra for the same sample are shown in Figure 55. Figure 56 shows a closer view of the Al-sublattice of the same spectra. The overlapped random and aligned spectra at the Al-sublattice can be attributed to amorphization of crystalline sample by Zr irradiation. The high yield from 1080 to 1110 keV is attributed to the deeper damage region.

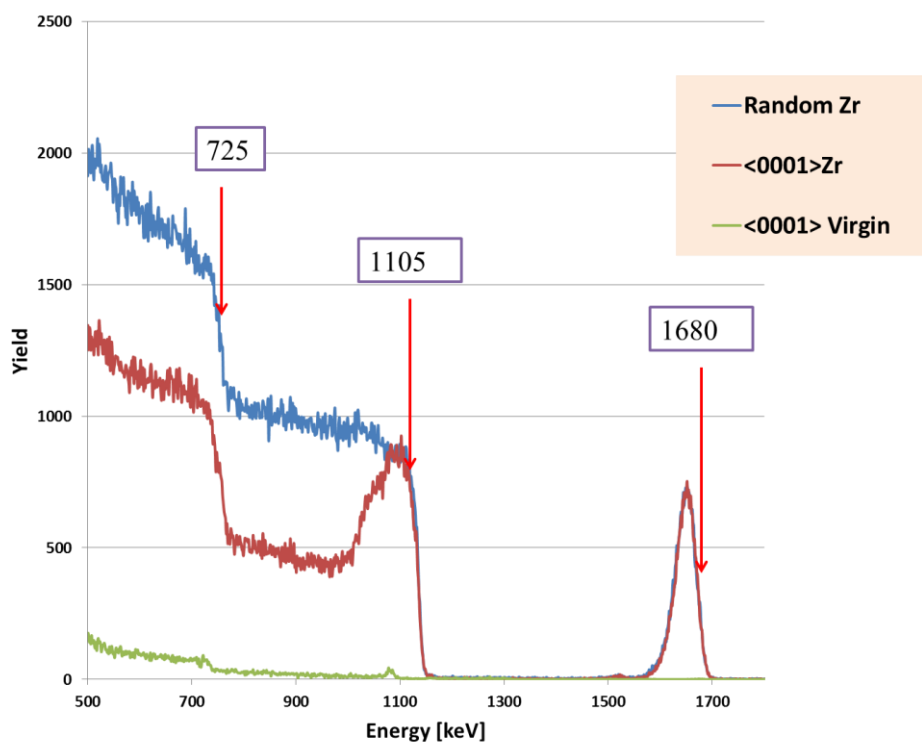


Figure 55 RBS-C spectra using 2 MeV  $\text{He}^+$  obtained from  $\alpha\text{-Al}_2\text{O}_3$  samples irradiated with 175 keV  $\text{Zr}^+$  ions to a fluence of  $2 \times 10^{16} \text{ Zr/cm}^2$ . The RBS-chamber had IBM geometry with detector scattering angle of  $+170^\circ$  with a detector resolution of about 15 keV. Arrows labeled “Zr”, “Al”; “O” indicate the surface elastic scattering energies for Zr, Al, and O atoms respectively. Scattering angle of  $170^\circ$  was used for this measurement.

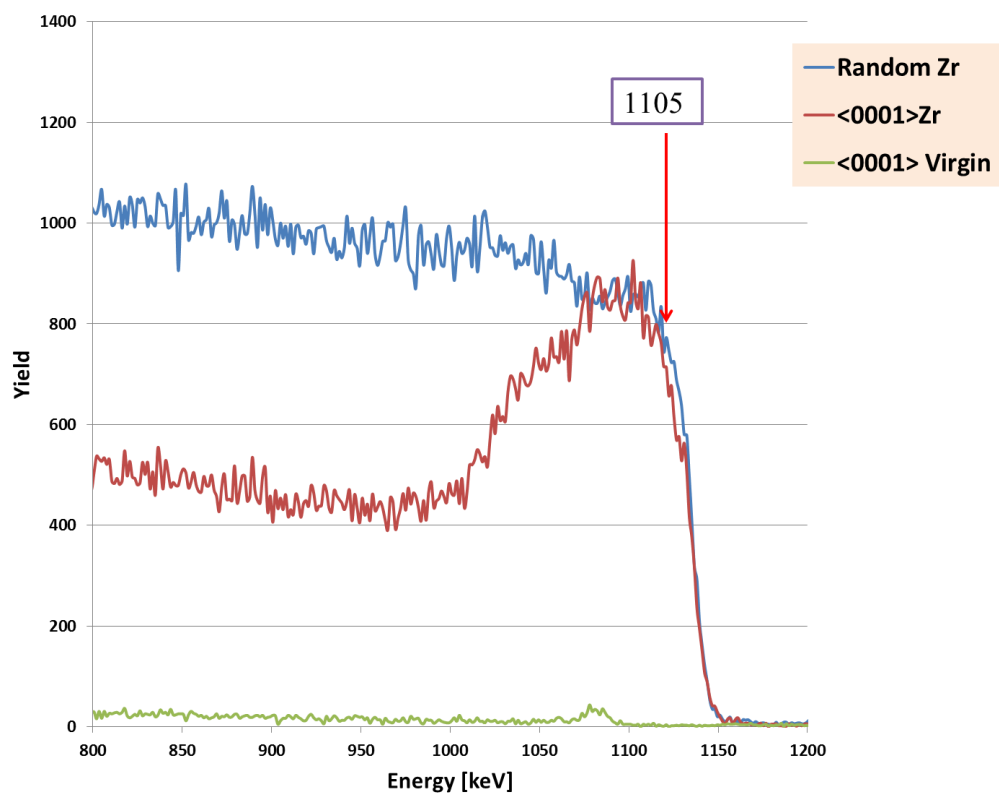


Figure 56 A closer view of Al-sublattice in the RBS-C spectra using 2 MeV He<sup>+</sup> obtained from  $\alpha$ -Al<sub>2</sub>O<sub>3</sub> samples irradiated with 175 keV Zr<sup>+</sup> ions to a fluence of  $2 \times 10^{16}$  Zr/cm<sup>2</sup> ions. The RBS-chamber had IBM geometry with detector scattering angle of +170° with a detector resolution of about 15 keV. Arrow labeled “Al” indicates the surface elastic scattering energy for Al atom. Scattering angle of 170 ° was used for this measurement.

Figure 57 shows the same bright-field TEM image demonstrated in Fig. 54, along with high resolution transmission electron microscopy (HRTEM) image obtained from the subsurface region and NBED pattern obtained from different regions. The HRTEM image obtained from the crystalline sub-surface region reveals the presence of an  $\alpha$ -Al<sub>2</sub>O<sub>3</sub> phase sandwiched with two  $\gamma$ -Al<sub>2</sub>O<sub>3</sub> phases. The NBED pattern obtained from this region confirms the presence of both  $\alpha$ -Al<sub>2</sub>O<sub>3</sub> and  $\gamma$ -Al<sub>2</sub>O<sub>3</sub> phases. The NBED pattern obtained from the deeper damaged region is consistent with  $\alpha$ -Al<sub>2</sub>O<sub>3</sub> phase (beam direction  $\vec{B} = \langle 11\bar{2}0 \rangle$ ). The NBED pattern from the middle region shows evidence diffuse rings, indicative of an amorphous Al<sub>2</sub>O<sub>3</sub> region.

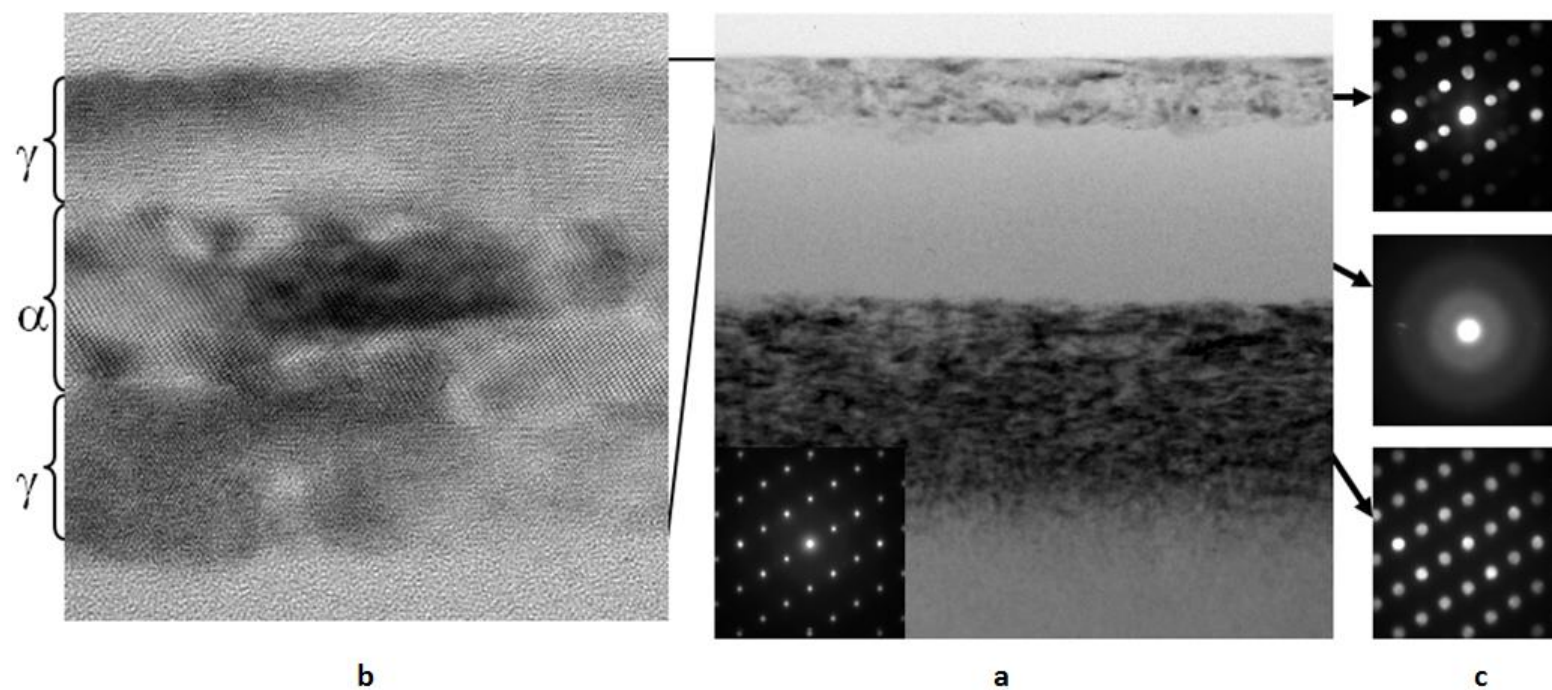
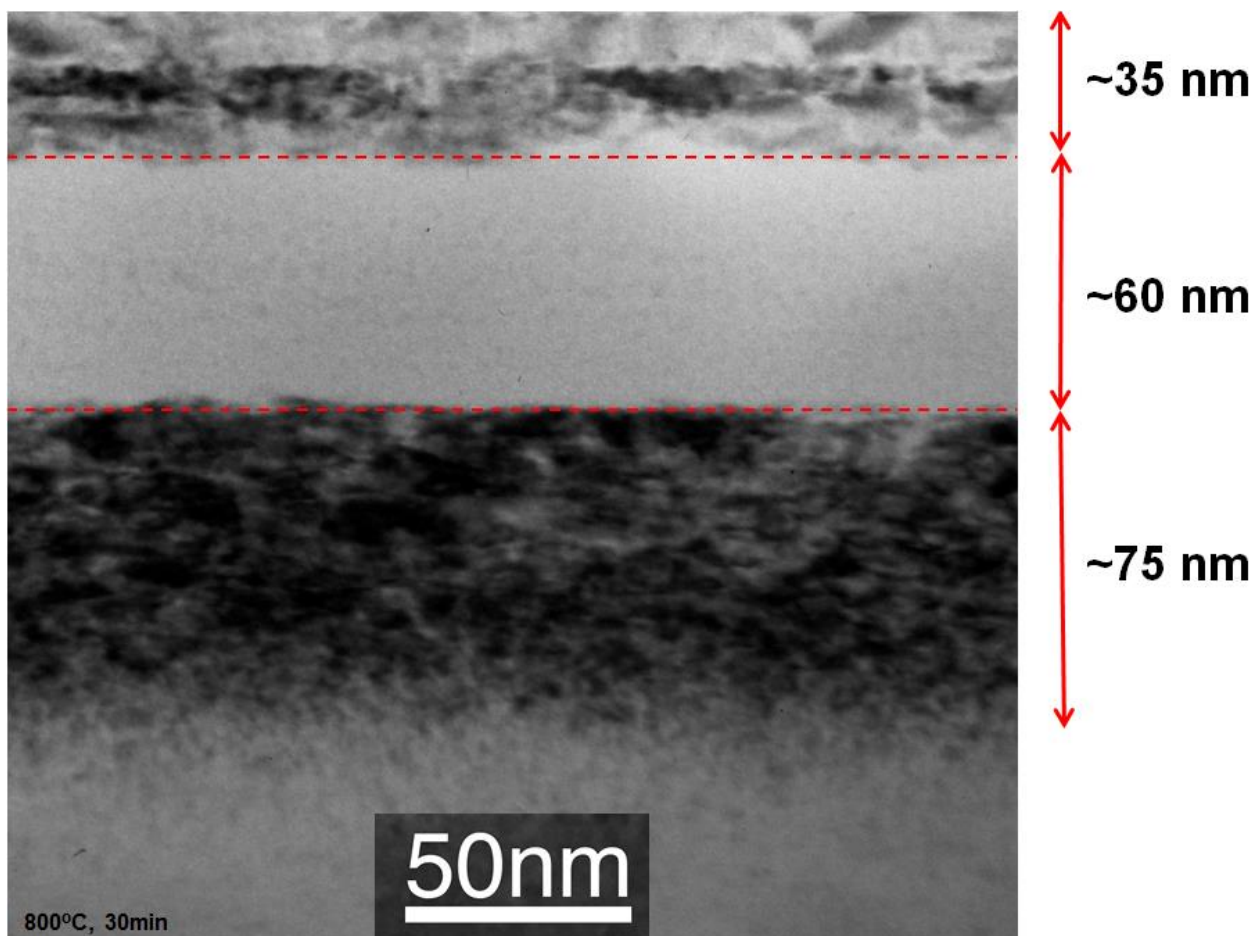


Figure 57 (a) cross-sectional TEM-BF image obtained from the as-irradiated  $\alpha\text{-Al}_2\text{O}_3$  sample irradiated with  $2 \times 10^{15} \text{ Zr}^+/\text{cm}^2$  (b) High resolution transmission electron transmission microscopy (HRTEM) image obtained from the subsurface region and (c) NBED patterns obtained from different regions.



Figure 58 shows a bright-field TEM image obtained from  $\alpha$ -Al<sub>2</sub>O<sub>3</sub> sample irradiated with  $2 \times 10^{15}$  Zr<sup>+</sup>/cm<sup>2</sup> at room temperature followed by thermal annealing at 800 °C for 30 minutes. The thermal annealing of this sample at 800 °C for 30 minutes results solid phase epitaxial growth of the subsurface amorphous layer. The regrowth appears to have initiated at the interface between the surface damaged and amorphous regions and has grown into the amorphous region. The thickness of the recrystallized layer with its substrate is about 35 nm.



*Figure 58 The bright-field image for the irradiated sample with  $2 \times 10^{16} \text{ Zr/cm}^2$  and annealed at 800 °C for 30 minutes*

Figure 59 shows the RBS-C aligned and random spectra for the same sample ( $2 \times 10^{15} \text{ Zr}^+/\text{cm}^2$  after thermal annealing at 800 °C for 30 minutes). Figure 60 shows a closer view of the Al-sublattice of the same spectra shown in Fig.50. The overlapped random and aligned spectra at the Al-sublattice can be attributed to amorphized region present in the sample.

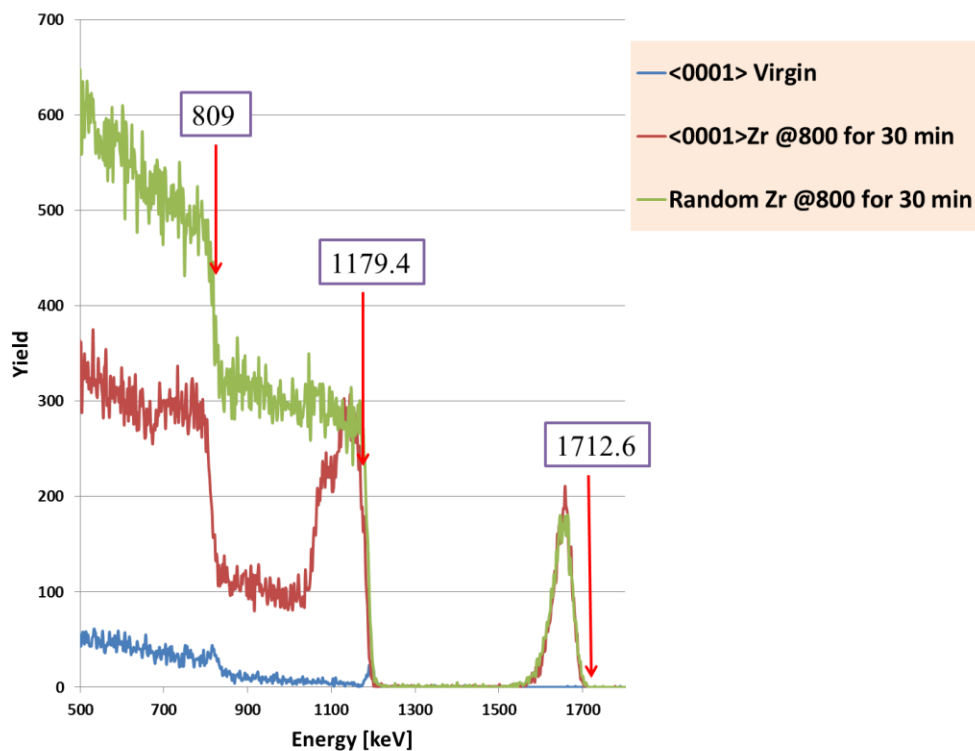


Figure 59 RBS-C spectra using 2 MeV  $\text{He}^+$  obtained from  $\alpha\text{-Al}_2\text{O}_3$  samples irradiated with 175 keV  $\text{Zr}^+$  ions to a fluence of  $2 \times 10^{16}$   $\text{Zr}/\text{cm}^2$  and annealed at 800 °C for 30 minutes. The RBS-chamber had IBM geometry with detector scattering angle of  $+140^\circ$  with a detector resolution of about 15 keV. Arrows labeled “Zr”, “Al”, “O” indicates the surface elastic scattering energies for Zr, Al, and O atoms respectively. Scattering angle of  $165^\circ$  was used for this measurement

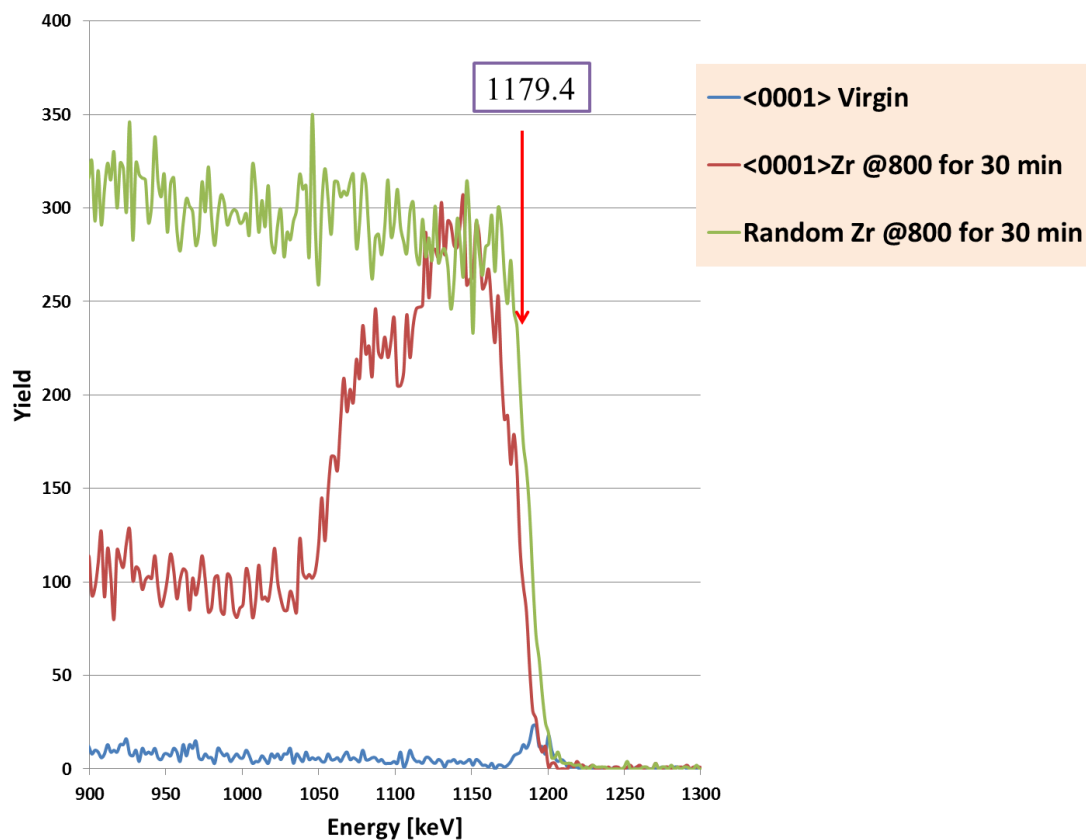
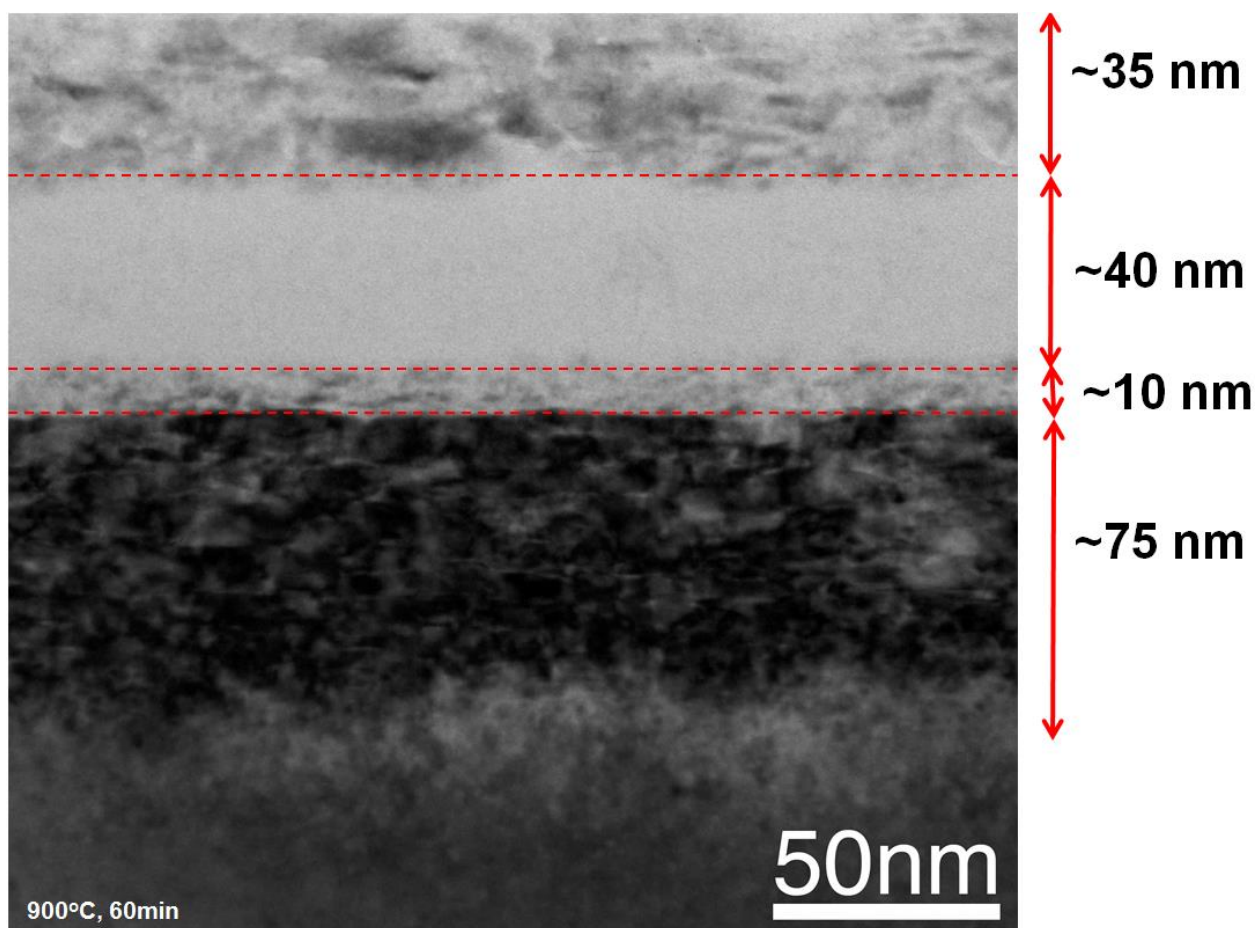


Figure 60 A closer view of Al-sublattice in the RBS-C spectra using 2 MeV  $\text{He}^+$  obtained from  $\alpha\text{-Al}_2\text{O}_3$  samples irradiated with 175 keV  $\text{Zr}^+$  ions to a fluence of  $2 \times 10^{16}$   $\text{Zr}/\text{cm}^2$  ions and annealed at 800 °C for 30 minutes. The RBS-chamber had IBM geometry with detector scattering angle of  $+140^\circ$  with a detector resolution of about 15 keV. Arrow labeled “Al” indicates the surface elastic scattering energy for Al atom. Scattering angle of  $165^\circ$  was used for this measurement.

Figure 61 shows a bright-field TEM image obtained from the irradiated  $\alpha$ -Al<sub>2</sub>O<sub>3</sub> sample irradiated with  $2 \times 10^{15}$  Zr<sup>+</sup>/cm<sup>2</sup> at room temperature followed by thermal annealing at 900 °C for 60 minutes. Comparing the as-irradiated  $\alpha$ -Al<sub>2</sub>O<sub>3</sub> sample, the  $\alpha$ -Al<sub>2</sub>O<sub>3</sub> sample irradiated with  $2 \times 10^{15}$  Zr<sup>+</sup>/cm<sup>2</sup> and annealed at 800 °C for 30 minutes, and the  $\alpha$ -Al<sub>2</sub>O<sub>3</sub> sample annealed at 900 °C for 60 minutes, it is apparent that the amorphous region recrystallizes to produce a thicker layer on the surface damaged region. The thickness of the recrystallized layer is about 35 nm compared with the as-irradiated sample. Figure 61 also shows a solid phase growth underlying the deeper damaged region. The depth of this thin recrystallized layer is about 10 nm.



*Figure 61 The bright-field image for the irradiated sample with  $2 \times 10^{16}$  Zr/cm<sup>2</sup> and annealed at 900 °C for 60 minutes*

Figure 62 shows the cross-sectional TEM-BF image obtained from the irradiated sample with  $2 \times 10^{16} \text{ Zr/cm}^2$  and annealed at 900 °C for 60 minutes along with the NBED patterns corresponding to different regions presence at the sample. The NBED patterns from the sub-surface and recrystallized region adjacent to the deeper damaged regions are consistent with the  $\gamma\text{-Al}_2\text{O}_3$  phase. The NBED patterns obtained from the deeper damaged region (bottommost Fig.62 b) is consistent with  $\alpha\text{-Al}_2\text{O}_3$  phase (beam direction  $(\vec{B}) = \langle 11\bar{2}0 \rangle$ ). The NBED pattern from the middle region shows evidence diffuse rings, indicative of an amorphous  $\text{Al}_2\text{O}_3$  region.

Figure 63a shows the same cross-sectional TEM-BF image shown in Fig. 62, along with HRTEM images obtained from sub-surface and recrystallized region adjacent to the deeper damaged region (Fig 63b). Fig. 63c that is a 30°-rotated HRTEM images shown in Fig.63b, indicates the presence of disorders in the form of twins in the recrystallized regions.

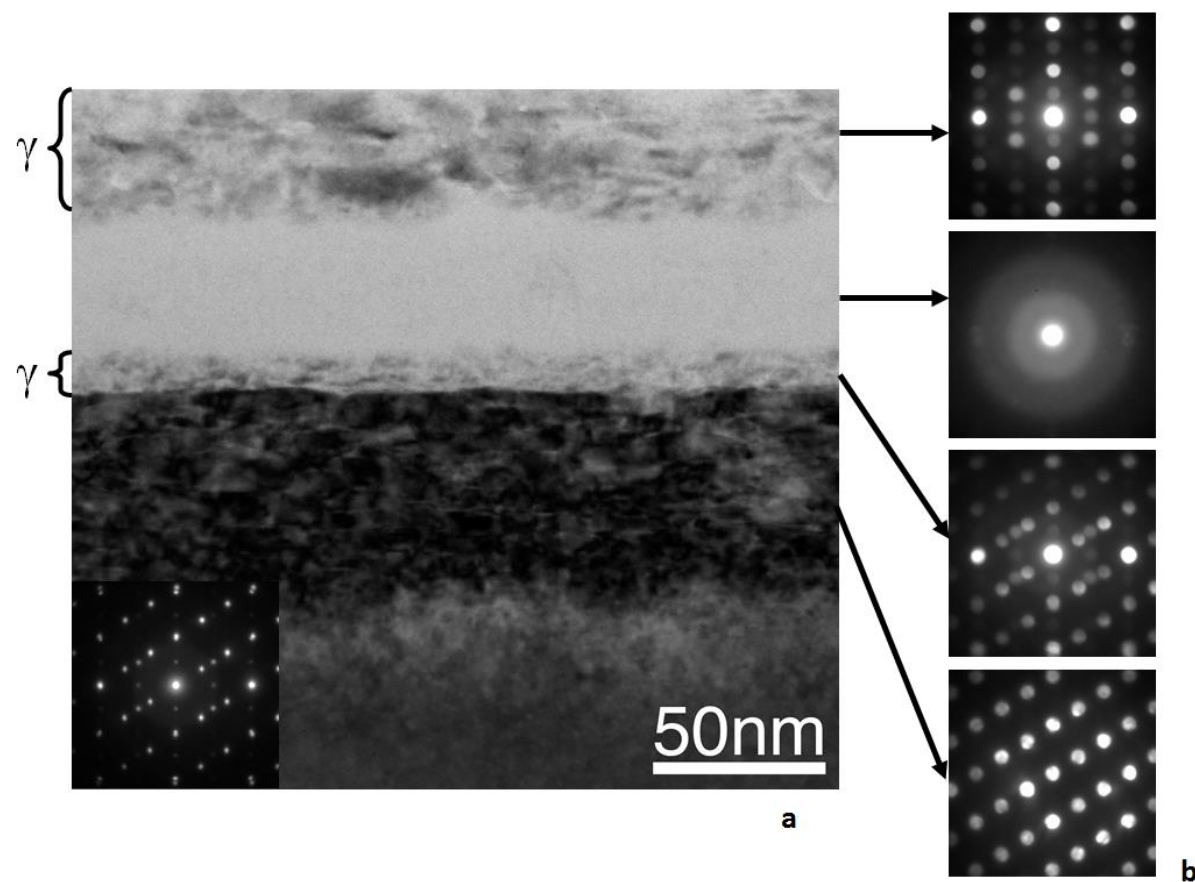


Figure 62 (a) Cross-sectional TEM-BF image obtained from the irradiated sample with  $2 \times 10^{16}$  Zr/cm<sup>2</sup> and annealed at 900 °C for 60 minutes. (b) NBED patterns obtained from different regions



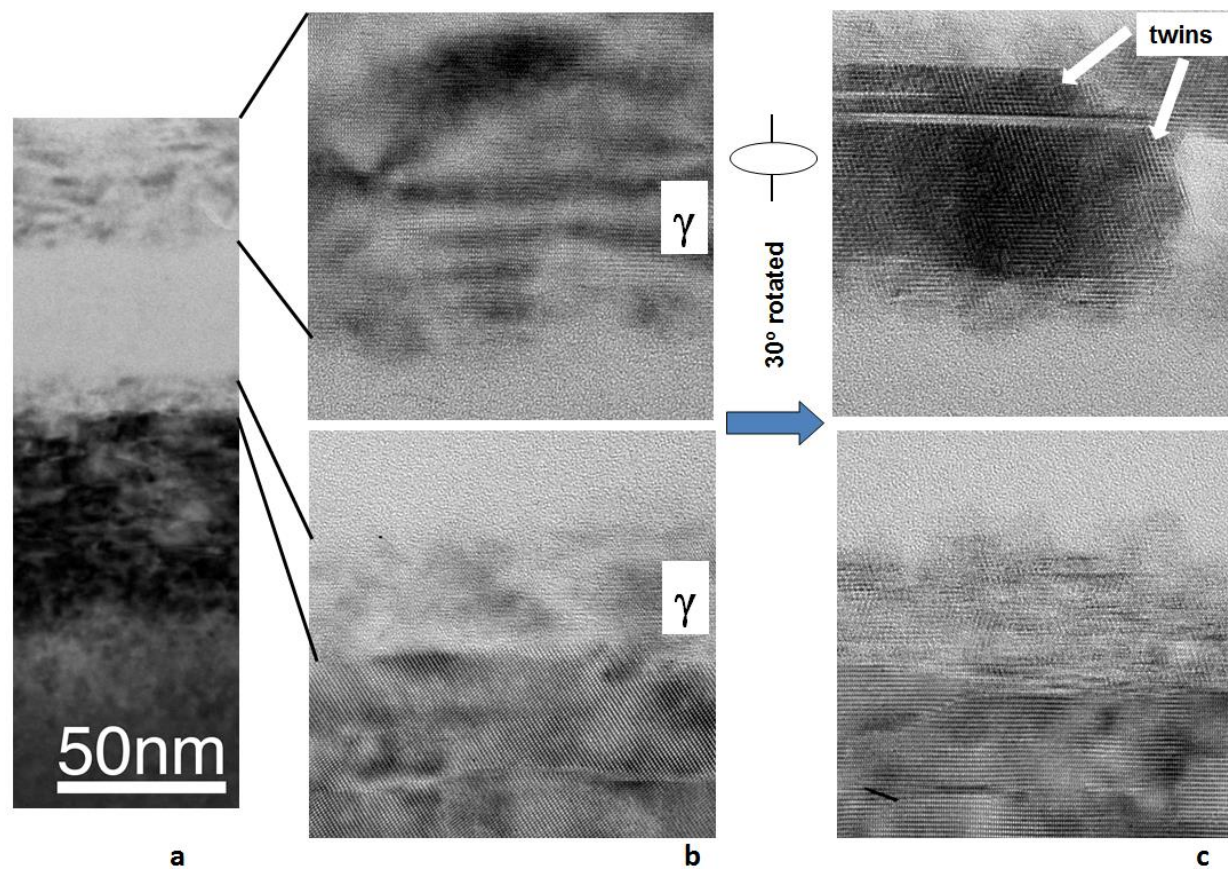
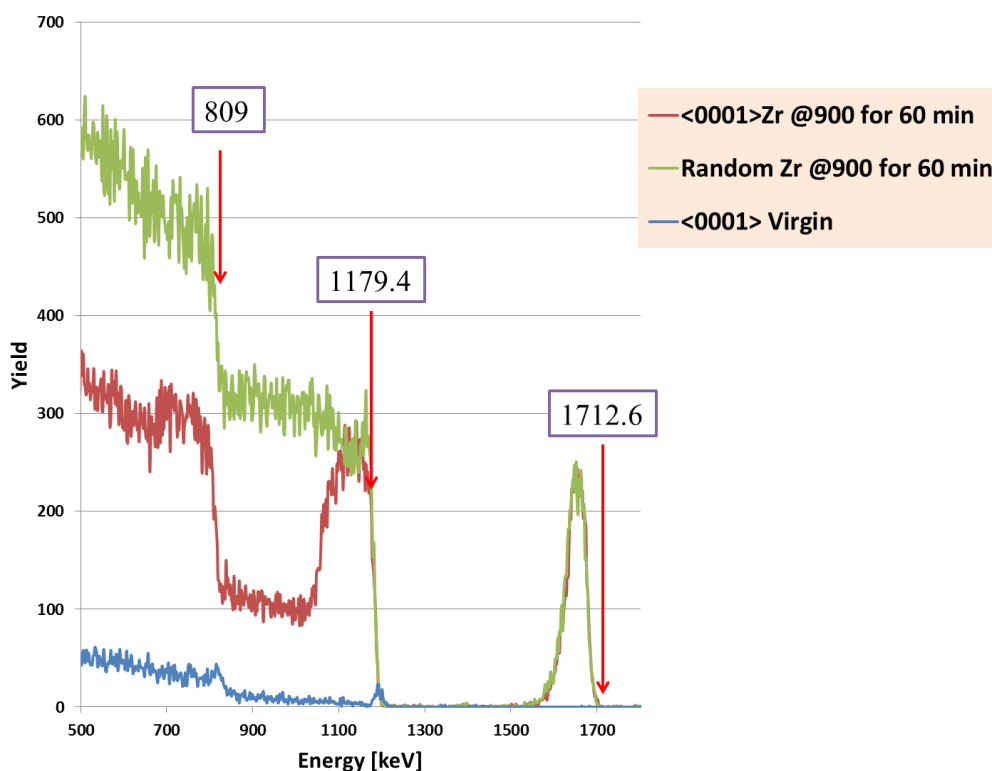


Figure 63 (a) Cross-sectional TEM-BF Image obtained from the irradiated sample with  $2 \times 10^{16}$  Zr/cm<sup>2</sup> and annealed at 900 °C for 60 minutes. (b) HRTEM images obtained from sub-surface and deeper damaged regions (c) HRTEM images obtained from sub-surface and deeper damaged regions after 30° rotation.

Figure 64 shows the RBS-C spectra for the  $\alpha$ -Al<sub>2</sub>O<sub>3</sub> samples irradiated with 175 keV Zr<sup>+</sup> ions to a fluence of  $2 \times 10^{16}$  Zr/cm<sup>2</sup> and annealed at 900 °C for 60 minutes. Figure 65 shows the Al-sublattice in the same spectra. The overlapped region of random and aligned spectra in Fig. 64 and 65 indicate the presence of the amorphous region.



*Figure 64 RBS-C spectra using 2 MeV He<sup>+</sup> obtained from  $\alpha$ -Al<sub>2</sub>O<sub>3</sub> samples irradiated with 175 keV Zr<sup>+</sup> ions to a fluence of  $2 \times 10^{16}$  Zr/cm<sup>2</sup> and annealed at 900 °C for 60 minutes. The RBS-chamber had IBM geometry with detector scattering angle of +140° with a detector resolution of about 15 keV. Arrows labeled “Zr”, “Al”, “O” indicates the surface elastic scattering energies for Zr, Al, and O atoms respectively. Scattering angle of 165 ° was used for this measurement.*

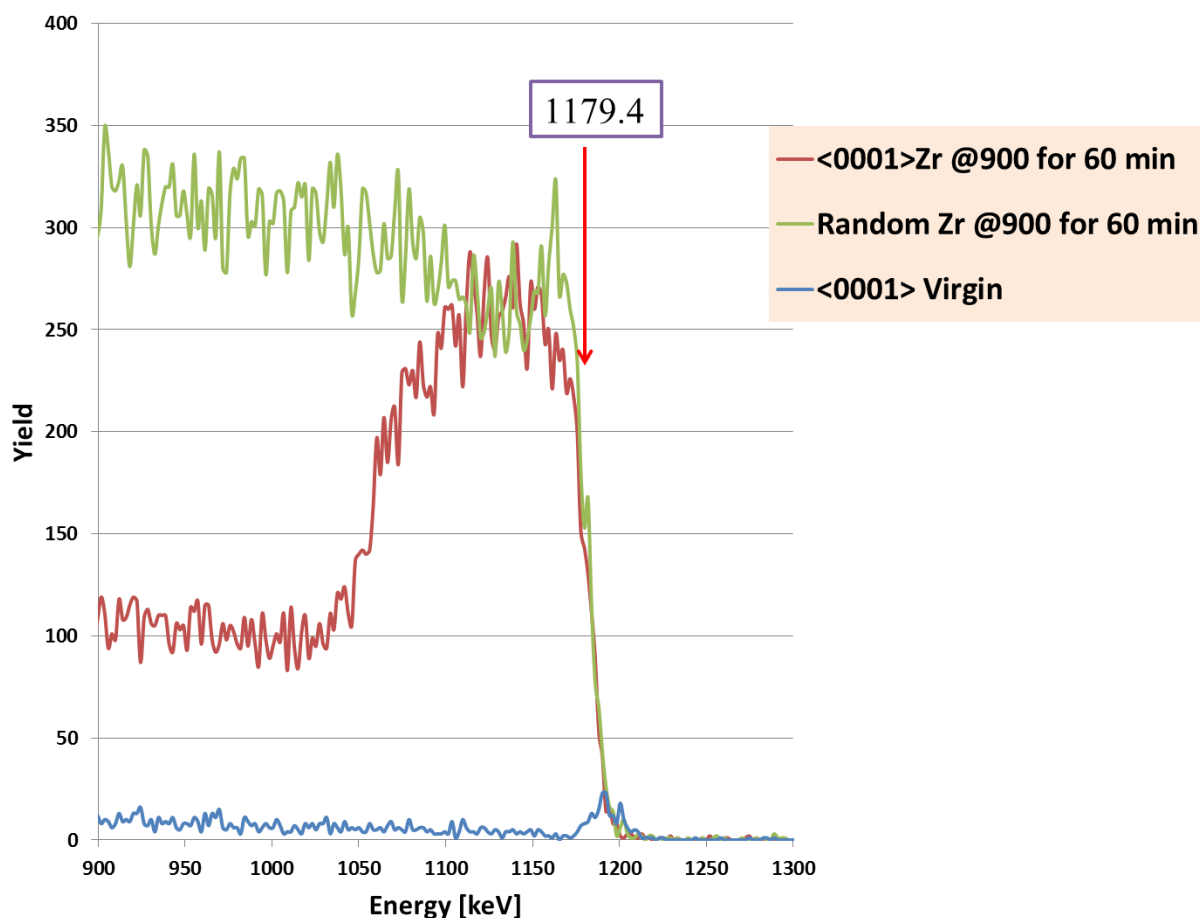
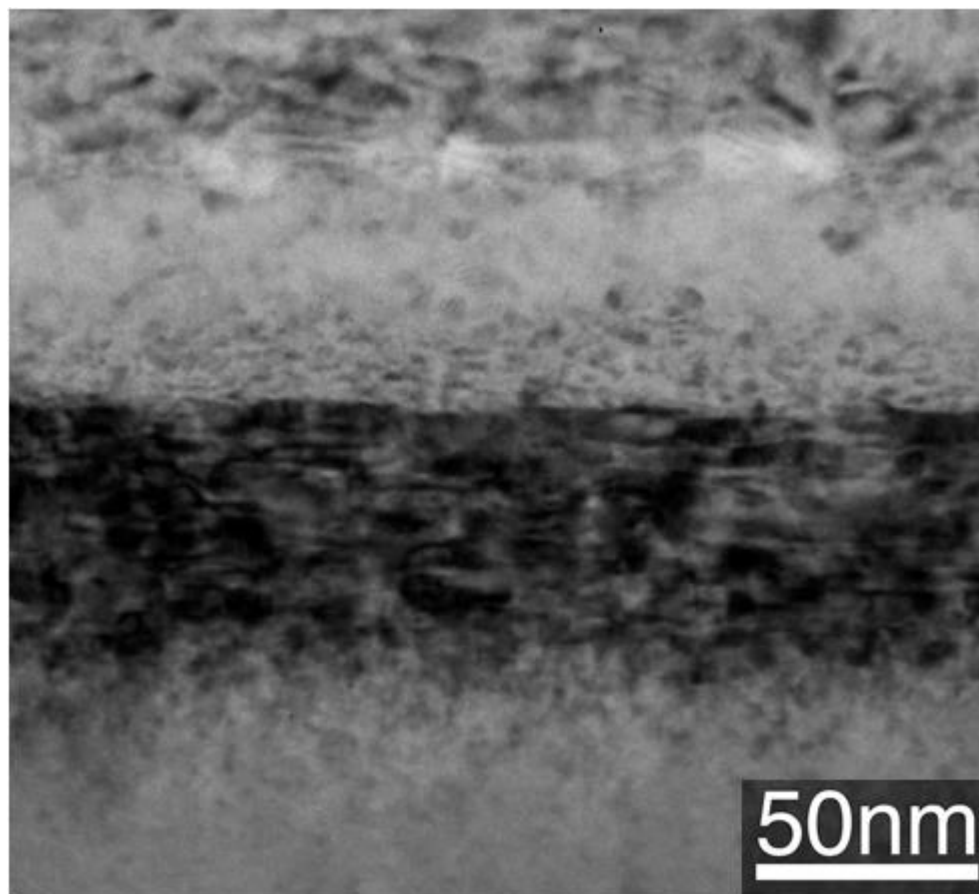


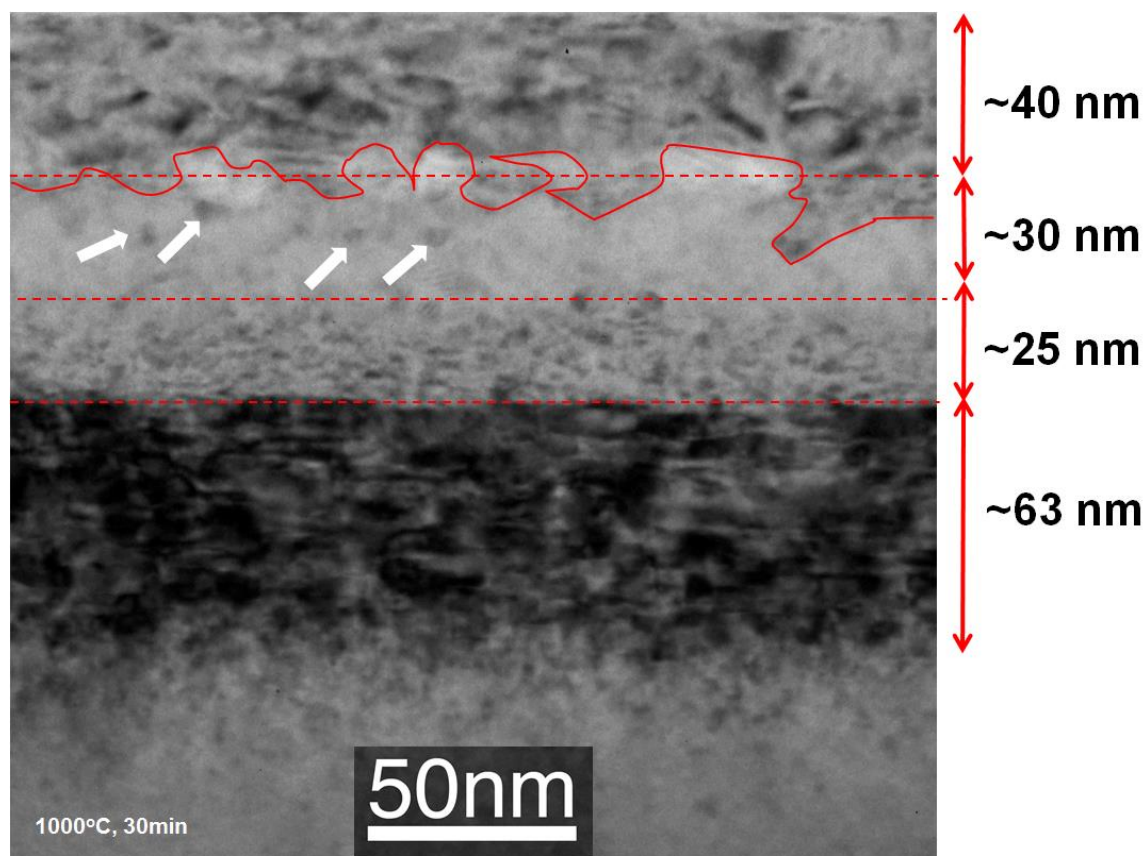
Figure 65 A closer view of Al-sublattice in the RBS-C spectra using 2 MeV  $\text{He}^+$  obtained from  $\alpha\text{-Al}_2\text{O}_3$  samples irradiated with 175 keV  $\text{Zr}^+$  ions to a fluence of  $2 \times 10^{16}$   $\text{Zr}/\text{cm}^2$  ions and annealed at 900 °C for 60 minutes. The RBS-chamber had IBM geometry with detector scattering angle of  $+140^\circ$  with a detector resolution of about 15 keV. Arrow labeled “Al” indicates the surface elastic scattering energy for Al atom. Scattering angle of  $165^\circ$  was used for this measurement.

Figure 66 shows a bright-field TEM image obtained from the irradiated  $\alpha$ -Al<sub>2</sub>O<sub>3</sub> sample irradiated with  $2 \times 10^{15}$  Zr<sup>+</sup>/cm<sup>2</sup> at room temperature followed by thermal annealing at 1000 °C for 30 minutes.



*Figure 66 The bright-field image for the irradiated sample with  $2 \times 10^{16}$  Zr/cm<sup>2</sup> and annealed at 1000 °C for 30 minutes*

Figure 67 is identical to Fig. 66 but indicates some more details. The white spots indicate lower density regions that pin recrystallization process. The interface between sub-surface recrystallized region and the amorphous region is not a smooth line. The average thickness of the sub-surface recrystallized, amorphous region and deeper recrystallized and damaged regions are 40, 30, 25, and 63 nm respectively. Fig. 67 shows also some spots inside the amorphous region, shown by small white arrows, corresponding to recrystallized micro regions not growing at the interfaces between amorphous and damaged crystalline regions. There is no more information about these micro regions.



*Figure 67 The bright-field image for the irradiated sample with  $2 \times 10^{16} \text{ Zr/cm}^2$  and annealed at 1000 °C for 30 minutes*

Figure 68, 69 show the RBS-C spectra for the same sample ( $2 \times 10^{16} \text{ Zr}^+/\text{cm}^2$  and annealed at 1000 °C for 30 minutes). Figure 69 is a closer view for the Al-sublattice of Fig. 68. The RBS spectra confirm the presence of an amorphous region during annealing of the sample at 1000 °C for 30 minutes.

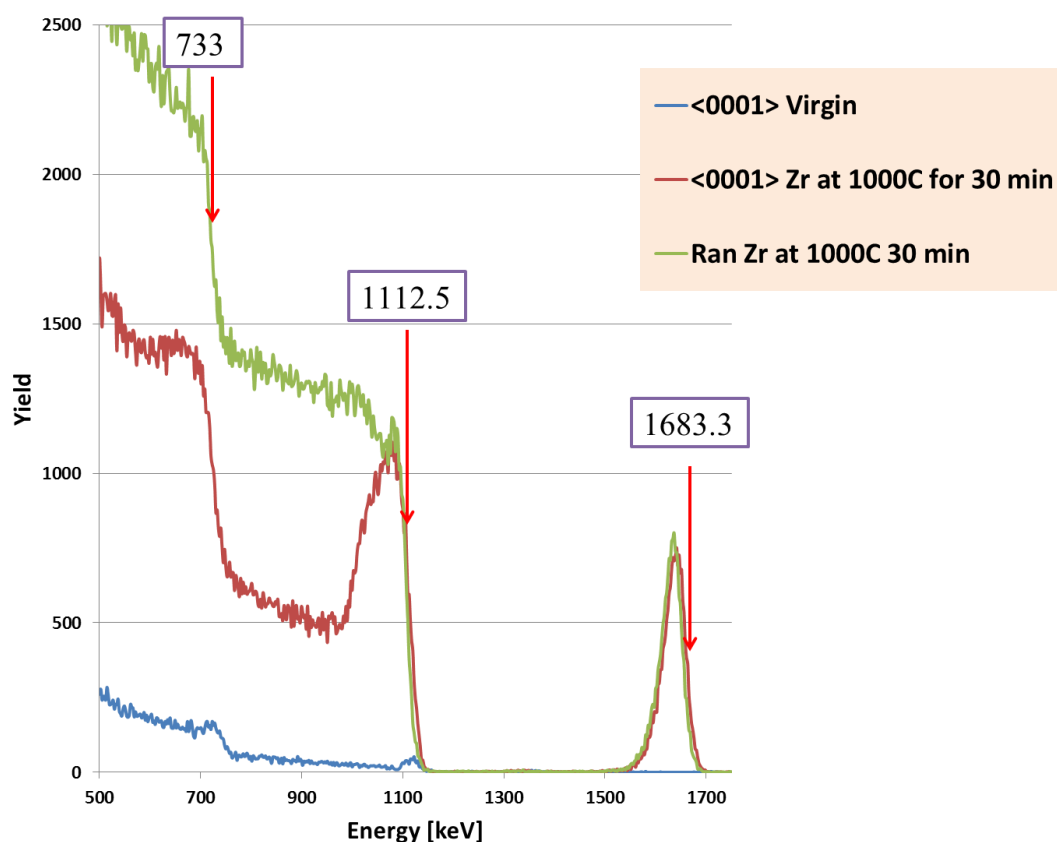


Figure 68 RBS-C spectra using 2 MeV  $\text{He}^+$  obtained from  $\alpha\text{-Al}_2\text{O}_3$  samples irradiated with 175 keV  $\text{Zr}^+$  ions to a fluence of  $2 \times 10^{16}$   $\text{Zr}/\text{cm}^2$  and annealed at 1000 °C for 30 minutes. The RBS-chamber had IBM geometry with detector scattering angle of  $+140^\circ$  with a detector resolution of about 15 keV. Arrows labeled “Zr”, “Al”, “O” indicate the surface elastic scattering energies for Zr, Al, and O atoms respectively.

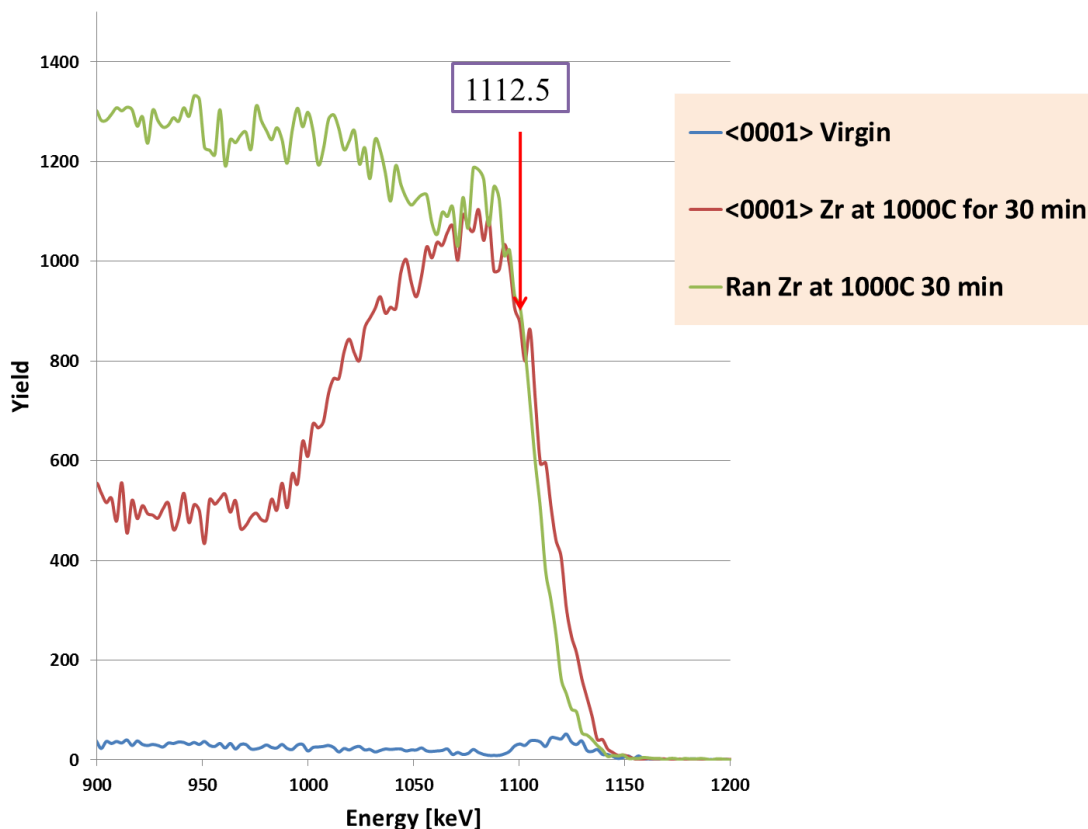
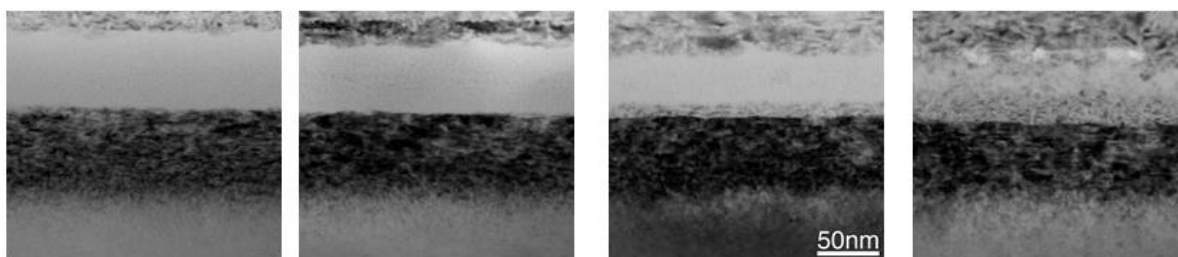


Figure 69 A closer view of Al-sublattice in the RBS-C spectra using 2 MeV  $\text{He}^+$  obtained from  $\alpha\text{-Al}_2\text{O}_3$  samples irradiated with 175 keV  $\text{Zr}^+$  ions to a fluence of  $2 \times 10^{16}$   $\text{Zr}/\text{cm}^2$  ions and annealed at 1000 °C for 30 minutes. The RBS-chamber had IBM geometry with detector scattering angle of  $+140^\circ$  with a detector resolution of about 15 keV. Arrow labeled “Al” indicates the surface elastic scattering energy for Al atom.

Figure 70 shows a composite of the TEM bright-field images for as-irradiated  $\alpha\text{-Al}_2\text{O}_3$  sample (Fig.54)) and the same sample annealed at 800 °C for 30 minutes (Fig.58), 900 °C for 60 minutes (Fig.61) and 1000 °C for 30 minutes (Fig.66). Fig. 70 shows that the interface between the amorphous and deeper damaged regions that has defected  $\alpha\text{-Al}_2\text{O}_3$  crystalline structure act as a substrate for epitaxially growth of  $\gamma\text{-Al}_2\text{O}_3$



at 900 °C and higher, however the similar growth starts at lower temperature from the surface damaged region. Fig. 70 also shows that  $\gamma$ -Al<sub>2</sub>O<sub>3</sub> recrystallization from deeper damaged region is significant at higher temperatures.



*Figure 70 The bright-field images of the irradiated samples with  $2 \times 10^{16} \text{ Zr}^+/\text{cm}^2$  shows the effect of thermal annealing at different temperatures and times. (Left) as-irradiated sample, (Middle) after annealing at 800 °C for 30 minutes, and (Right) after annealing at 900 °C for 60 minutes*

In this study, we observed three effects: (1) formation of an  $\alpha$ -Al<sub>2</sub>O<sub>3</sub> phase that is sandwiched by two  $\gamma$ -Al<sub>2</sub>O<sub>3</sub> phases at the surface damaged region for as-irradiated sample, (2) recrystallization of  $\gamma$ -Al<sub>2</sub>O<sub>3</sub> phases at both amorphous/crystalline interfaces during thermal annealing and (3) significant recrystallization at lower temperature at the surface crystalline/amorphous interface and remarkable recrystallization at higher temperature at the deeper amorphous /crystalline interface.

Figure 71 is a summary of the effects of fluence on solid changes during irradiation of  $\alpha$ -Al<sub>2</sub>O<sub>3</sub> with Zr ions. The bright-field images obtained from the irradiated

sample to fluence of  $7.5 \times 10^{15} \text{ Zr}^+/\text{cm}^2$  (Fig. 71a) shows formation of a defected region that has  $\alpha\text{-Al}_2\text{O}_3$  phase structure. Fig. 71b shows the bright-field images obtained from the irradiated sample to fluence of  $1.5 \times 10^{16} \text{ Zr}^+/\text{cm}^2$  indicating that increasing the fluence can result in damage accumulation. The accumulation of damages appears in form of an amorphous region. There are residual stresses in the interfaces between the crystalline and amorphous regions as well as between the damaged region and the substrate. By increasing the fluence to  $2 \times 10^{16} \text{ Zr}^+/\text{cm}^2$ , the width of amorphous region increases slightly and the sample undergoes to a stress relaxation in subsurface damaged region. This stress relaxation appear as volume expansion by phase transformation from highly stressed  $\alpha\text{-Al}_2\text{O}_3$  phase to  $\gamma\text{-Al}_2\text{O}_3$  phase (Fig. 71 d). Figure 71e shows Z-contrast image obtained from the irradiated sample to a fluence of  $4 \times 10^{16} \text{ Zr}^+/\text{cm}^2$ . The spherical bright spots in amorphous region are Zr-rich clusters. The formation of this cluster is attributed to compound formation as a subsequence of irradiation with a higher fluence. Figure 72 is a schematic representation of the changes to a solid caused by increasing ion fluence [214].

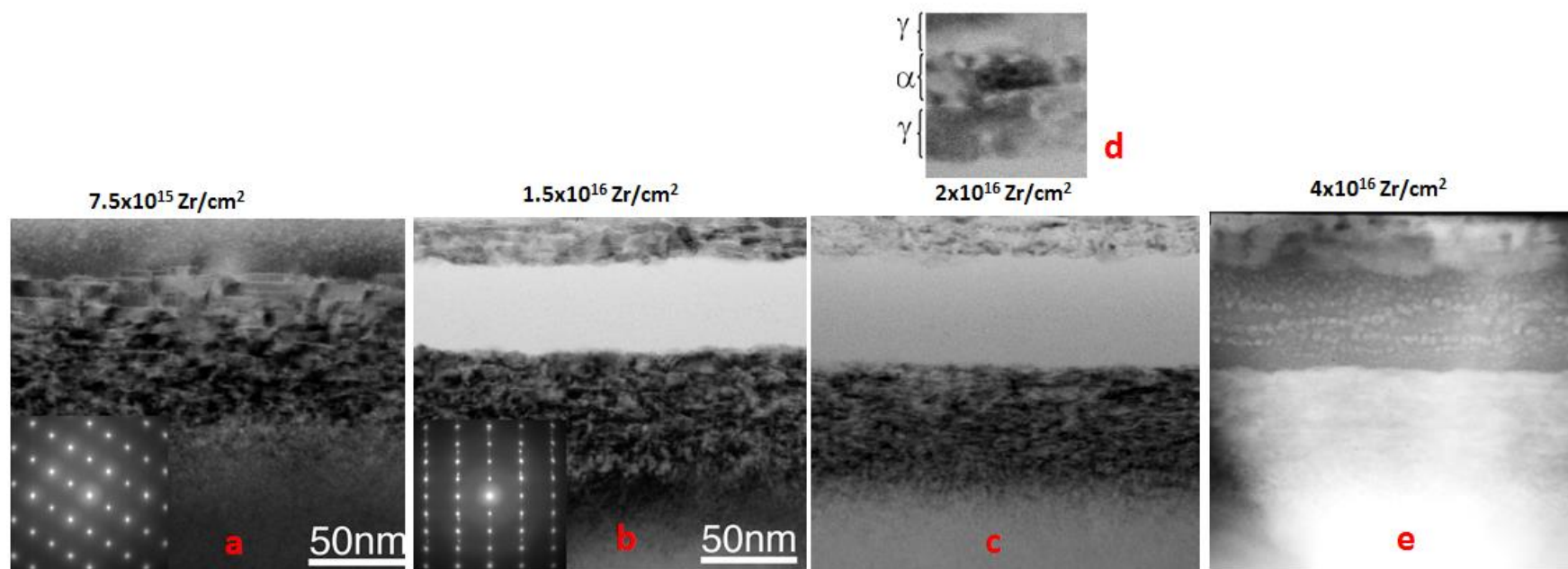


Figure 71 Effect of fluence on solid changes during irradiation of  $\alpha\text{-Al}_2\text{O}_3$  with Zr ions. The bright-field images obtained from the irradiated sample to fluences of a)  $7.5 \times 10^{15} \text{ Zr}^+/\text{cm}^2$  b)  $1.5 \times 10^{16} \text{ Zr}^+/\text{cm}^2$  c)  $2 \times 10^{16} \text{ Zr}^+/\text{cm}^2$  d) The high resolution TEM image obtained from the irradiated sample to a fluence of  $1.5 \times 10^{16} \text{ Zr}^+/\text{cm}^2$  obtained from subsurface region e) Z-contrast image obtained from the irradiated sample to a fluence of  $4 \times 10^{16} \text{ Zr}^+/\text{cm}^2$

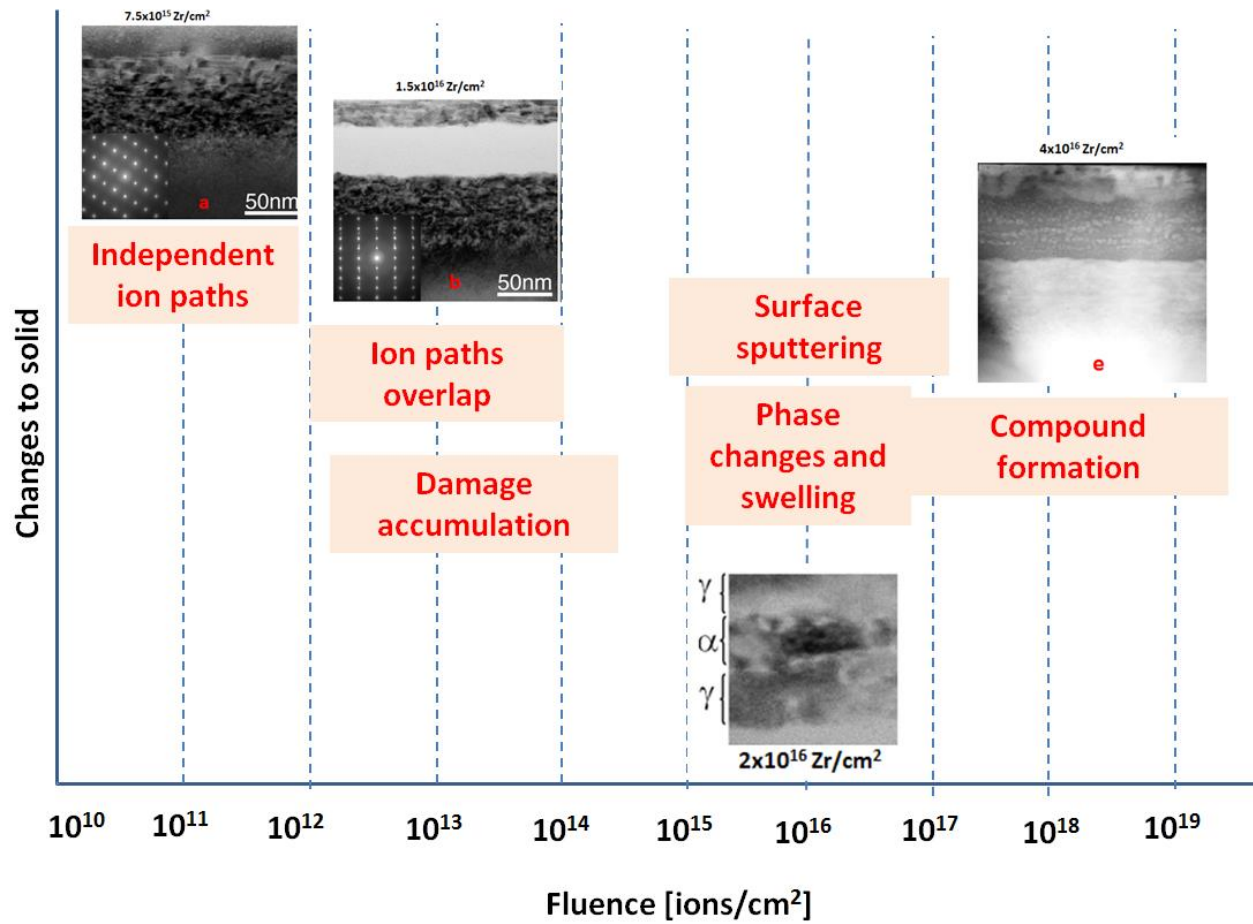


Figure 72 A schematic representation of the changes to a solid caused by increasing ion fluence.

The HRTEM images obtained from the subsurface region of as-irradiated sample and the annealed sample at 900 C for 60 minutes (Fig. 57 and 63) show that the  $\alpha$ -Al<sub>2</sub>O<sub>3</sub> phase sandwiched by two  $\gamma$ -Al<sub>2</sub>O<sub>3</sub> phases transforms to  $\gamma$ -Al<sub>2</sub>O<sub>3</sub> phase. In absence of irradiation the phase transformation of  $\alpha$ -Al<sub>2</sub>O<sub>3</sub> to  $\gamma$ -Al<sub>2</sub>O<sub>3</sub> phase during a thermal annealing is not thermodynamically favorable. But when the energetic particles travel through the material, the significant amount of deposited energy can be stored in a subsurface region in different forms such as stresses which acts as a thermodynamic driving force when tends to relaxation [199]. In the presence of irradiation, the energy of irradiation should be added to the difference in free energy between the phases outside irradiation to analyze the effect of irradiation on phase stability. Therefore thermodynamical concepts cannot be directly applied for the materials.

Essentially if there is a single process of amorphous to  $\gamma$ -Al<sub>2</sub>O<sub>3</sub> transformation in substrate or in subsurface crystalline, a kinetics study could be proposed based on cross-cut or Arrhenius method. However the results showed that very complicated processes such as a stress-related phase transformation govern the amorphous $\rightarrow\gamma\rightarrow\alpha$  transformation. The difference in activation energy resulting in different studies may originate from the nature of the thin film. The thin film synthesized with ion irradiation at cryogenic temperatures produces a thin layer of amorphous region on top of a highly damaged region. A thin film produced by ion irradiation at room temperature produces an amorphous region sandwiched by two highly damaged regions. A thin film produced using CVD or other similar techniques are associated an amorphous layer lying loosely

on top of a crystalline substrate. The surface energies of the amorphous layer in all these cases are completely different.

Figure 73 shows a plot of effect of free energy for a hypothetical system indicating that under irradiation condition free energies of phases could be different from the free energy during a thermal condition. Most of the energies introduced by energetic ions during ion irradiation stored by stress tend to be released by a phenomenon that is known as recovery (stress relaxation). These stored energies in form of stress can be released by stress relaxation such as vacancy, interstitial, and dislocation movement or by recrystallization of the strained regions into new strain-free grains. Therefore stress relaxation acts as a thermodynamic driving force.

Also at higher fluences of ion the concentration of point defects increases due to Frenkel pairs recombination and defect clusters collapse into dislocation loops, which have much lower energies.

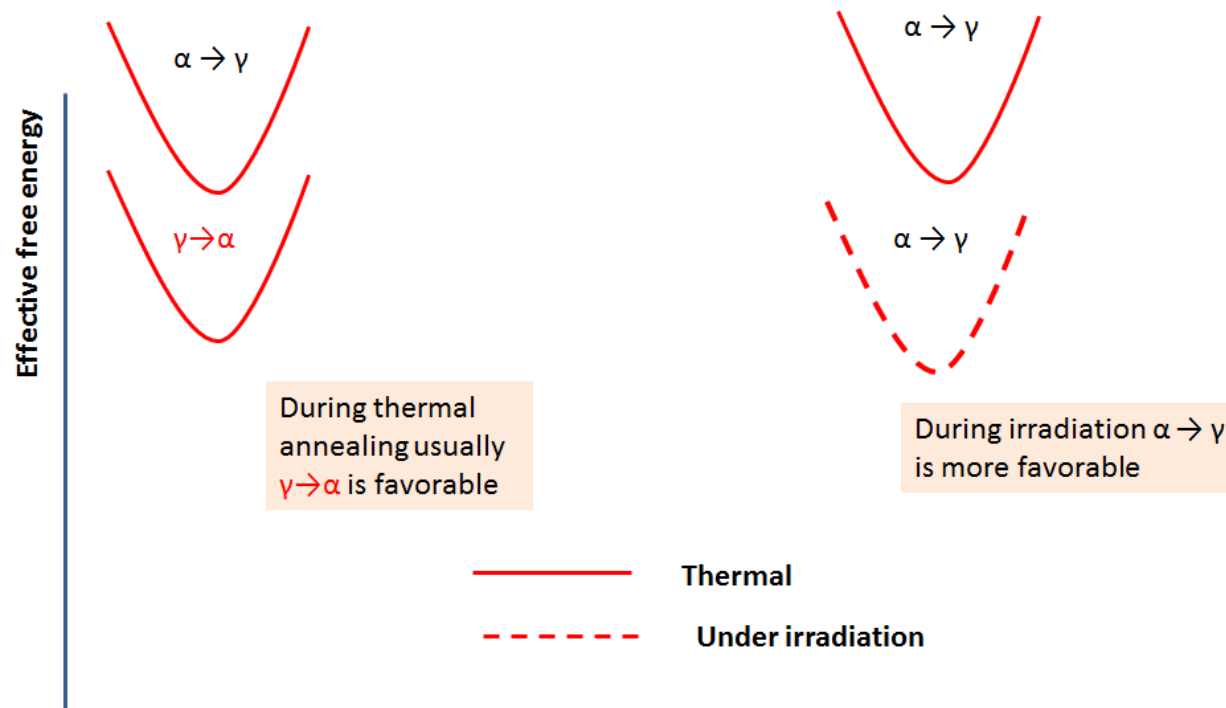


Figure 73 Plot of effect of free energy for a hypothetical system. Irradiation condition alters phases free energies

### 4.3 Ion-beam induced epitaxially recrystallization (IBIER) in $\alpha$ -Al<sub>2</sub>O<sub>3</sub>, due to oxygen irradiation effect on Zr-implanted $\alpha$ -Al<sub>2</sub>O<sub>3</sub>

Figure 74a shows a bright-field (BF) image and a selected area electron diffraction (SAED) pattern obtained from a cross-sectional TEM samples of  $\alpha$ -Al<sub>2</sub>O<sub>3</sub> irradiated with 175 keV Zr<sup>+</sup> ions to a fluence of  $7.5 \times 10^{15}$  Zr/cm<sup>2</sup>. Also shown is SRIM calculated profiles for the Zr displacement damage dose (in units of dpa) as a function of target sample depth and the implanted Zr concentration versus depth. Figure 74b shows TEM-BF and SAED as well as SRIM calculated profiles for  $\alpha$ -Al<sub>2</sub>O<sub>3</sub> irradiated with 175 keV Zr<sup>+</sup> ions to a fluence of  $7.5 \times 10^{15}$  Zr/cm<sup>2</sup> plus 55 keV O<sup>+</sup> ions to a fluence of  $1.1 \times 10^{16}$  O/cm<sup>2</sup> at room temperature. These results reveal a damaged but crystalline surface region extending to about 150 nm from the surface. Fig. 74b shows that subsequent oxygen implantation has no major effect on the extent of damage for this fluence of zirconium.



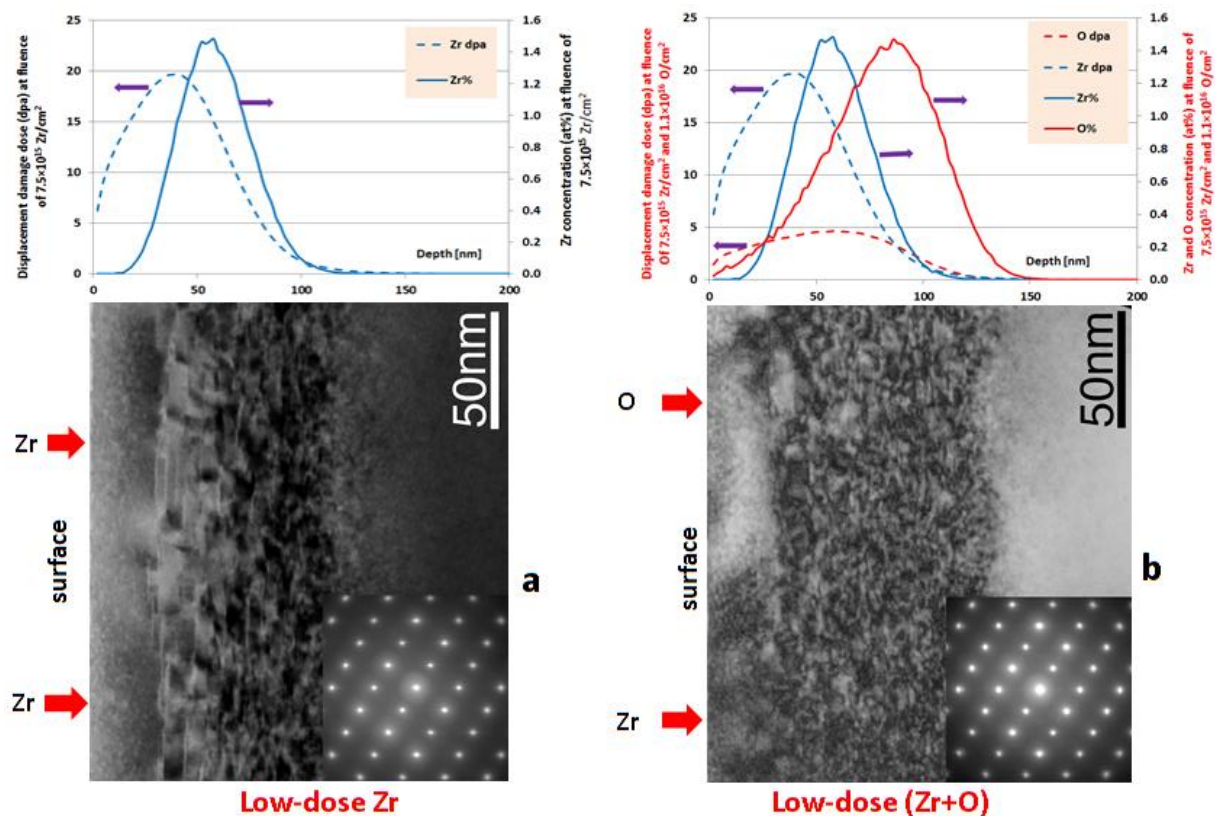


Figure 74 TEM cross section images and SAED patterns obtained from  $\alpha$ - $\text{Al}_2\text{O}_3$  samples irradiated with: (a) 175 keV  $\text{Zr}^+$  ions to a fluence of  $7.5 \times 10^{15} \text{ Zr}^+/\text{cm}^2$  and (b) 175 keV  $\text{Zr}^+$  ions to a fluence of  $7.5 \times 10^{15} \text{ Zr}^+/\text{cm}^2$  plus 55 keV  $\text{O}^+$  to a fluence of  $1.1 \times 10^{16} \text{ O}^+/\text{cm}^2$ . These are “low- dose” samples in the sense that the Zr displacement damage dose is less than the threshold dose for amorphization. Also shown are SRIM calculated profiles for the Zr displacement damage dose (in units of dpa) as a function of target sample depth and the implanted Zr concentration versus depth. The label “surface” indicates the  $\alpha$ - $\text{Al}_2\text{O}_3$  sample surface and the arrows indicate the direction of the incident ions.

Figure 75a, shows RBS-C spectra obtained from  $\alpha$ -Al<sub>2</sub>O<sub>3</sub> irradiated with 175 keV Zr<sup>+</sup> ions to a fluence of  $1.5 \times 10^{16}$  Zr/cm<sup>2</sup>. Figure 75b shows the RBS-C for the same sample subsequently irradiated with 55 keV O<sup>+</sup> to a fluence of  $2.3 \times 10^{16}$  O/cm<sup>2</sup>. For reference, aligned RBS-C spectra are shown in both Figs. 75a, b from unirradiated (virgin) single crystal  $\alpha$ -Al<sub>2</sub>O<sub>3</sub> samples. For the irradiated samples, the aligned spectra overlap the random spectra, suggesting the presence of a random scattering surface layer. The oxygen irradiation produced a slight broadening of the aligned spectra.

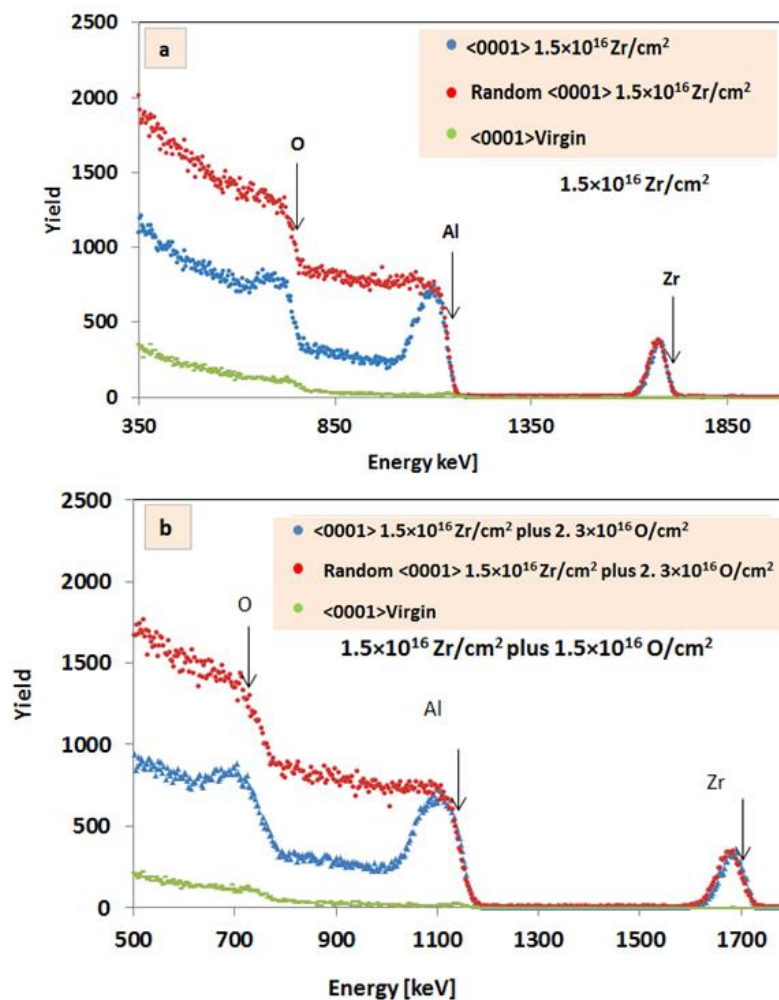


Figure 75 RBS-C spectra obtained from  $\alpha$ -Al<sub>2</sub>O<sub>3</sub> samples irradiated with: (a) 175 keV Zr<sup>+</sup> ions to a fluence of  $7.5 \times 10^{15}$  Zr/cm<sup>2</sup> and (b) 175 keV Zr<sup>+</sup> ions to a fluence of  $7.5 \times 10^{15}$  Zr/cm<sup>2</sup> plus 55 keV O<sup>+</sup> to a fluence of  $1.1 \times 10^{16}$  O/cm<sup>2</sup>. For reference, aligned RBS-C spectra are shown in both and from unirradiated (virgin) single crystal  $\alpha$ -Al<sub>2</sub>O<sub>3</sub> samples. These are “high dose” samples in the sense that the Zr displacement damage dose is in excess of the threshold dose for amorphization. Arrows labeled “Zr”, “Al”, “O” indicate the surface elastic scattering energies for Zr, Al, and O atoms respectively.

Figure 76a shows a TEM cross-sectional bright-field (BF) image obtained from a "high-dose" sample of  $\alpha$ -Al<sub>2</sub>O<sub>3</sub> irradiated with 175 keV Zr<sup>+</sup> ions to a fluence of  $1.5 \times 10^{16}$  Zr<sup>+</sup>/cm<sup>2</sup>. The TEM image in Fig. 76a shows the presence of a subsurface amorphous layer, extending from ~20 to ~65 nm. This amorphous region is sandwiched between two highly damaged regions. The three regions are similar to those reported for  $\alpha$ -Al<sub>2</sub>O<sub>3</sub> irradiated with Zr ions to a fluence of  $4 \times 10^{16}$  Zr/cm<sup>2</sup> (175 keV, 25 °C) [215]. Figure 76b shows a TEM bright-field (BF) image obtained from a cross-sectional sample of  $\alpha$ -Al<sub>2</sub>O<sub>3</sub> irradiated with 175 keV Zr<sup>+</sup> ions to a fluence of  $1.5 \times 10^{16}$  Zr/cm<sup>2</sup> plus 55 keV O<sup>+</sup> ions to a fluence of  $2.3 \times 10^{16}$  O/cm<sup>2</sup>. In Fig. 76, The SRIM calculated Zr% and Zr displacement damage dose (in units of dpa) versus target depth are also shown above the TEM images. The SRIM profiles indicate that the values of dpa and Zr% at the interface between the near-surface damaged region and buried amorphous region are ~33 dpa and ~0.2% Zr, respectively, for the sample irradiated with 175 keV Zr<sup>+</sup> ions to a fluence of  $1.5 \times 10^{16}$  Zr/cm<sup>2</sup> (Fig.76a). The corresponding values at the interface between the buried amorphous region and the deeper damage region are ~25dpa and ~2.7 % Zr.

The TEM micrographs in Figs. 76a and b reveal that the amorphous region adjacent to the near-surface damaged region has recrystallized during the subsequent implantation of oxygen. Approximately 20 nm of the amorphous alumina has crystallized; however, no growth of the deeper damaged layer into the amorphous region is observed.

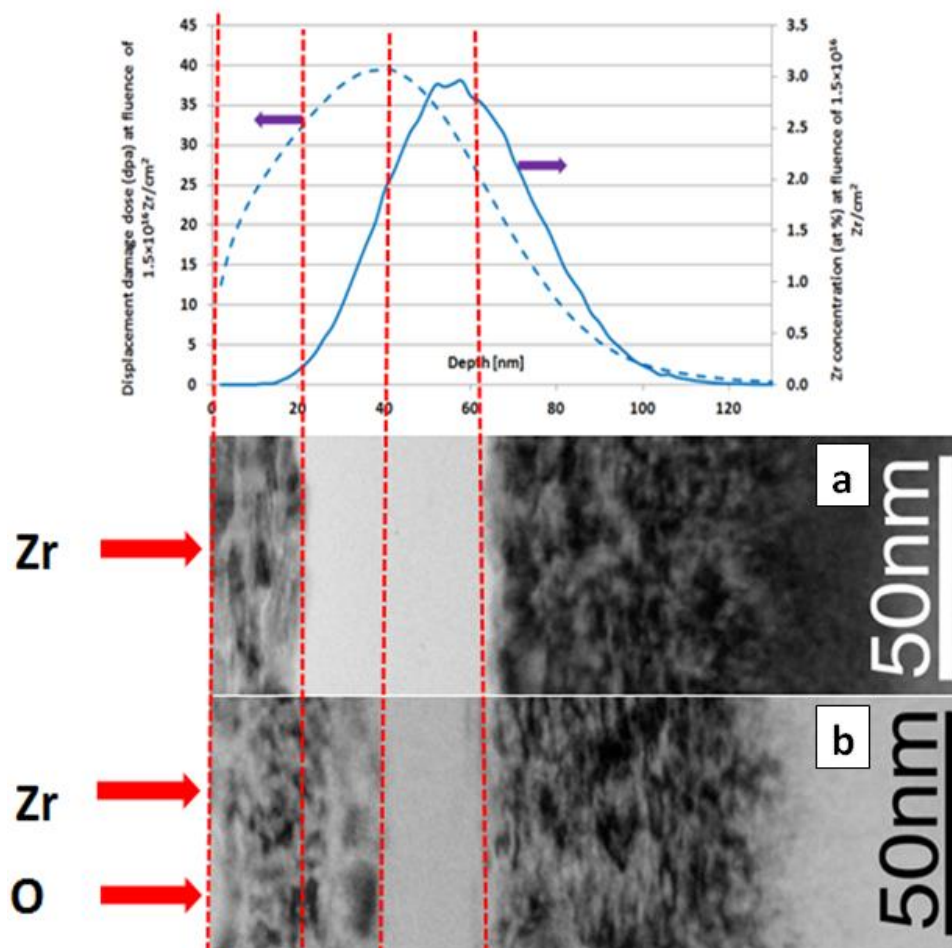


Figure 76 TEM cross-sectional bright-field (BF) images obtained from "high-dose" samples of  $\alpha\text{-Al}_2\text{O}_3$  irradiated with: (a) 175 keV  $\text{Zr}^+$  ions to a fluence of  $1.5 \times 10^{16} \text{ Zr}^+/\text{cm}^2$  and (b) 175 keV  $\text{Zr}^+$  ions to a fluence of  $1.5 \times 10^{16} \text{ Zr}^+/\text{cm}^2$  plus 55 keV  $\text{O}^+$  ions to a fluence of  $2.3 \times 10^{16} \text{ O}^+/\text{cm}^2$ . Also shown are SRIM calculated profiles for the Zr displacement damage dose (in units of dpa) as a function of target sample depth and the implanted Zr concentration versus depth. Comparing the two TEM-BF images, it is apparent that the buried amorphous region in the  $\alpha\text{-Al}_2\text{O}_3$  substrate is recrystallized during the subsequent oxygen implantation.

Thus, the crystallization of the amorphous phase initiated at the interface between the near-surface damaged region and amorphous region grew toward the deeper damaged region. The recrystallized region contains disorder, perhaps in the form of subgrains. This disorder and the thickness of this layer cause the RBS-C spectra of Figure 75b to be similar to those of Figure 75a.

Figure 77a shows a cross-sectional TEM image of the microstructure in “high dose”  $\alpha$ -Al<sub>2</sub>O<sub>3</sub> irradiated with 175 keV Zr<sup>+</sup> ions to a fluence of  $1.5 \times 10^{16}$  Zr/cm<sup>2</sup> plus 55 keV O<sup>+</sup> ions to a fluence of  $2.3 \times 10^{16}$  O/cm<sup>2</sup>. In addition, Fig. 77 shows nano-beam electron diffraction (NBED) patterns obtained from various regions of the ion irradiated microstructure. The NBED pattern of the near- surface region contains spots that are not present in the pattern for the sample that was irradiated with zirconium only. The nano-beam pattern from the deeper damaged region is consistent with an  $\alpha$ -Al<sub>2</sub>O<sub>3</sub> phase (B= $\langle 11\bar{2}0 \rangle$ ). The arrows in nano-beam electron diffraction pattern obtained from the subsurface and recrystallized regions of the high-dose sample irradiated by  $1.5 \times 10^{16}$  Zr<sup>+</sup>/cm<sup>2</sup> plus  $2.3 \times 10^{16}$  O<sup>+</sup>/cm<sup>2</sup>, indicate the presence of a phase that is not  $\alpha$ -Al<sub>2</sub>O<sub>3</sub>.

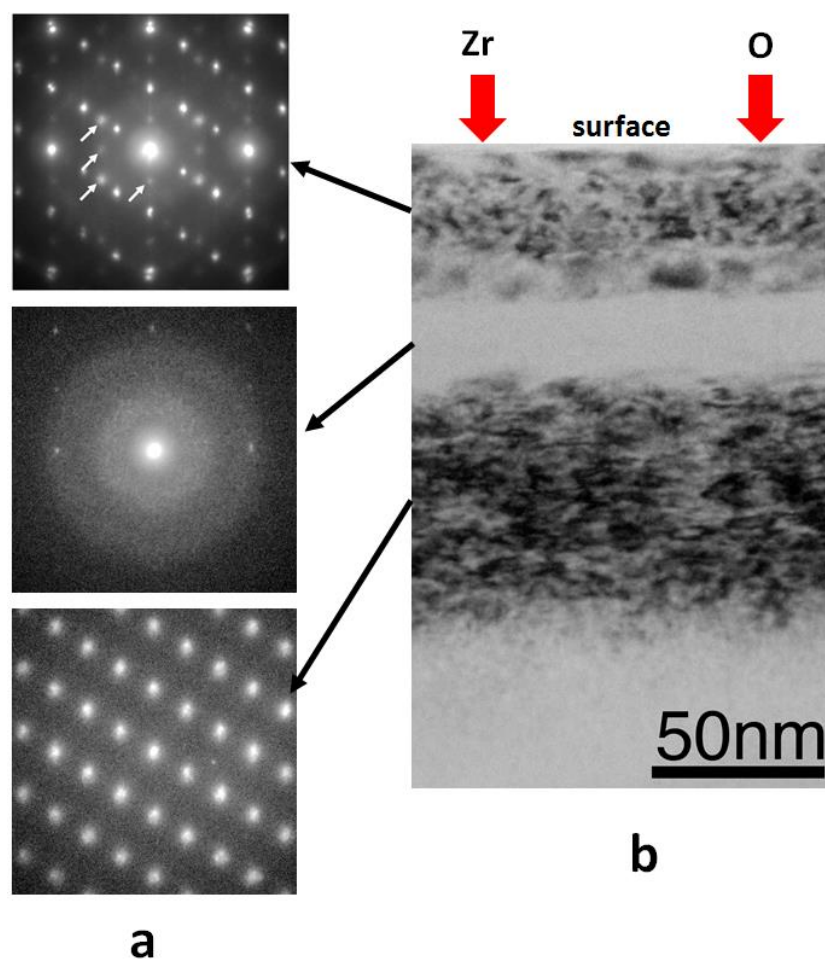


Figure 77 (a) Nano-beam electron diffraction (NBED) patterns obtained from different regions of a "high-dose"  $\alpha$ -Al<sub>2</sub>O<sub>3</sub> sample irradiated with 175 keV Zr<sup>+</sup> ions to a fluence of  $1.5 \times 10^{16}$  Zr<sup>+</sup>/cm<sup>2</sup> plus 55 keV O<sup>+</sup> ions to a fluence of  $2.3 \times 10^{16}$  O<sup>+</sup>/cm<sup>2</sup>; (b) cross-sectional TEM-BF image from the same sample. The NBED pattern from the deeper damaged region is consistent with an  $\alpha$ -Al<sub>2</sub>O<sub>3</sub> phase ( $B = \langle 11\bar{2}0 \rangle$ ). The arrows in the uppermost NBED pattern, in (a) obtained from the near-surface damaged and recrystallized regions, indicate the presence of a phase that is not  $\alpha$ -Al<sub>2</sub>O<sub>3</sub>. The structure of this phase is identified in Figure 78.

The same nano-beam electron diffraction pattern as in Figure 77a, but with indexing of some of the principal reflections is shown in Figure 78. Indexing indicates that both  $\alpha$ -  $\text{Al}_2\text{O}_3$  and  $\gamma$ -  $\text{Al}_2\text{O}_3$  phases are present in  $\text{Al}_2\text{O}_3$  and they are responsible for this diffraction pattern. Figure 78 shows that  $\alpha$ -  $\text{Al}_2\text{O}_3$  and  $\gamma$ -  $\text{Al}_2\text{O}_3$  phases are arranged with a special crystallographic relationship. The incident beam direction is  $[110]$  for  $\alpha$ - phase  $\text{Al}_2\text{O}_3$  and  $[1\bar{1}\bar{2}]$  for  $\gamma$ - phase  $\text{Al}_2\text{O}_3$ . The orientation relationship between  $\gamma$ - and  $\alpha$ -  $\text{Al}_2\text{O}_3$  indicated in Figure 78 shows epitaxy between the phases with  $(111)_\gamma \parallel (0001)_\alpha$  and  $[112]_\gamma \parallel [11\bar{2}0]_\alpha$ .



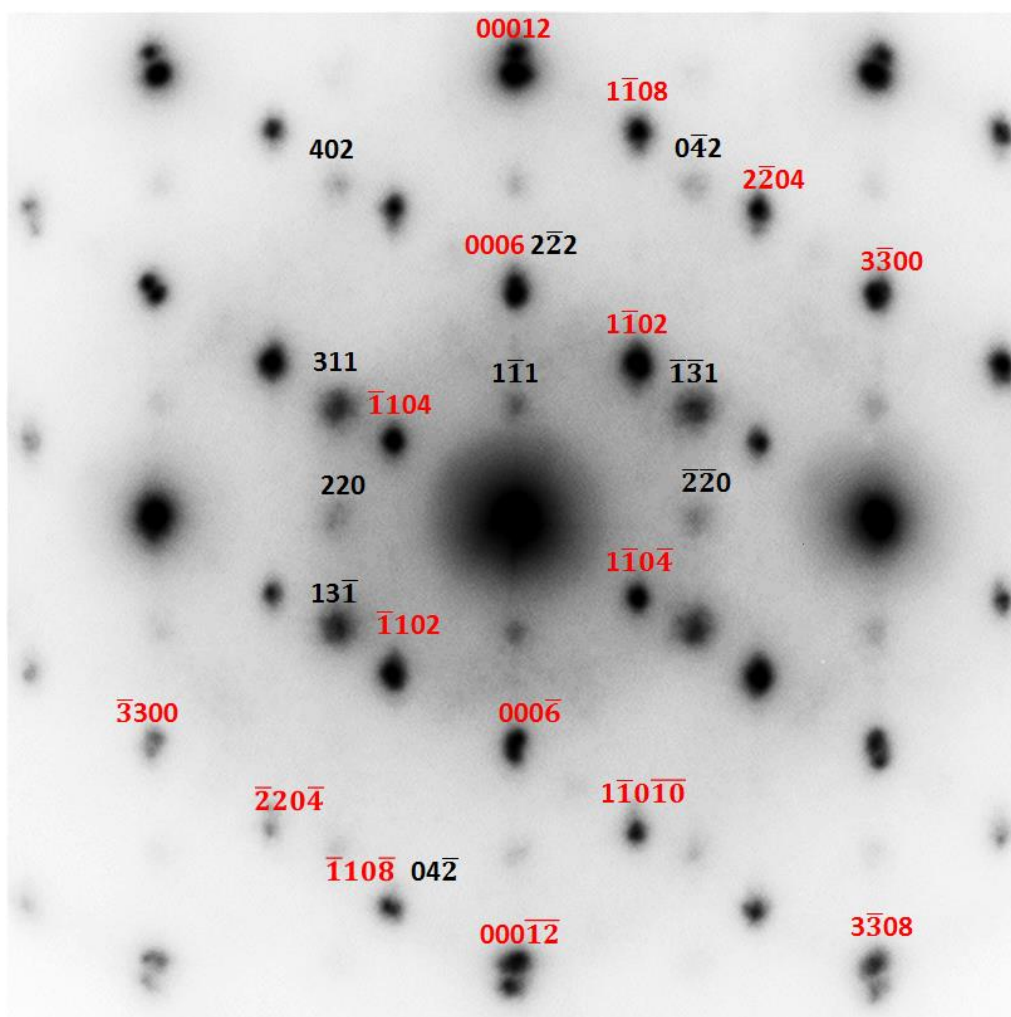


Figure 78 The same NBED pattern as the uppermost pattern in Fig. 77a, with indexing of some of the principal reflections (displayed using reverse contrast). Indexing the individual reflections reveals that two phases of  $\text{Al}_2\text{O}_3$  are responsible for this diffraction pattern. In particular both  $\alpha$ - $\text{Al}_2\text{O}_3$  and  $\gamma$ - $\text{Al}_2\text{O}_3$  are present and they are arranged with a special crystallographic relationship. The incident beam direction is  $[11\bar{2}0]$  for  $\alpha$ -phase  $\text{Al}_2\text{O}_3$  and  $[1\bar{1}\bar{2}]$  for  $\gamma$ -phase  $\text{Al}_2\text{O}_3$ . The red and black indices correspond  $\alpha$ - $\text{Al}_2\text{O}_3$  and  $\gamma$ - $\text{Al}_2\text{O}_3$ , respectively.

Figure 79 shows the zirconium and oxygen ions distribution and corresponding dpa for  $\alpha$ -  $\text{Al}_2\text{O}_3$  irradiated with 175 keV zirconium ions to a fluence of  $1.5 \times 10^{16} \text{ Zr/cm}^2$  followed by 55 keV oxygen ions to a fluence of  $2.3 \times 10^{16} \text{ O/cm}^2$ . The model used for the SRIM calculations, assumes that the densities for the highly-damaged and amorphous regions are 3.98 and 3.1, respectively [7, 211]. The TEM results were also used to determine the depth of damaged and amorphous regions for this model.

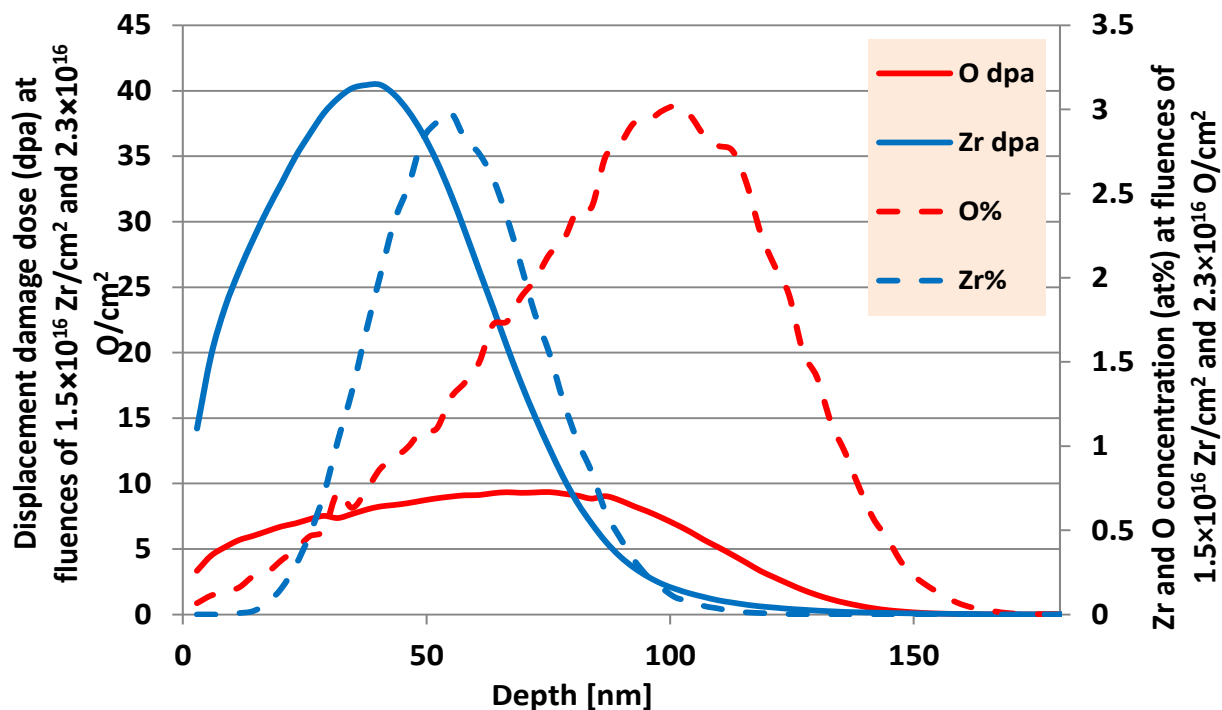


Figure 79 SRIM calculated range and displacement damage dose (in units of dpa) dpa versus target depth. For Al<sub>2</sub>O<sub>3</sub> irradiated with 175 keV Zr<sup>+</sup> ions to a fluence of  $1.5 \times 10^{16}$  Zr<sup>+</sup>/cm<sup>2</sup>, followed by irradiation with 55 keV O<sup>+</sup> ions to a fluence of and  $2.3 \times 10^{16}$  O<sup>+</sup>/cm<sup>2</sup>. For the oxygen SRIM calculation, densities of 3.98 and 3.1 g/cm<sup>3</sup> were used for the highly-damaged and amorphous regions of the Al<sub>2</sub>O<sub>3</sub>, respectively.

SRIM calculated nuclear and electronic energy loss for oxygen during implantation into pre-Zr-implanted sapphire along with TEM cross section images of high-dose samples ( $\alpha$ - Al<sub>2</sub>O<sub>3</sub> irradiated with 175 keV zirconium ions to a fluence of  $1.5 \times 10^{16}$  Zr/cm<sup>2</sup> and the same sample irradiated with 55 keV oxygen ions to a fluence of  $2.3 \times 10^{16}$  O/cm<sup>2</sup>) are shown in Figure 33. The model for calculation assumes that the

sapphire substrate contains a buried amorphous layer with a lower density ( $3.1 \text{ g/cm}^3$ ) compared to the density of pristine  $\alpha\text{-Al}_2\text{O}_3$  ( $3.98 \text{ g/cm}^3$ ). Figure 80 shows that the recrystallization occurred at the subsurface crystalline/amorphous interface where the electronic energy loss is slightly higher than nuclear energy loss. This observation suggests that the energy loss by excitation/ionization processes for lighter ions could be important drivers for the recrystallization process.

Comparing Fig. 33 and 80a, it is apparent that the ballistic (nuclear) energy loss dominates for entire range, at Zr ion irradiation into sapphire. It suggests that at the heavier ion irradiation, the nuclear process is primarily responsible for the lattice damage that results in amorphization in the region from about 25 nm to 65 nm. The electronic collisions produce much smaller energy transfer and few or no displacements.

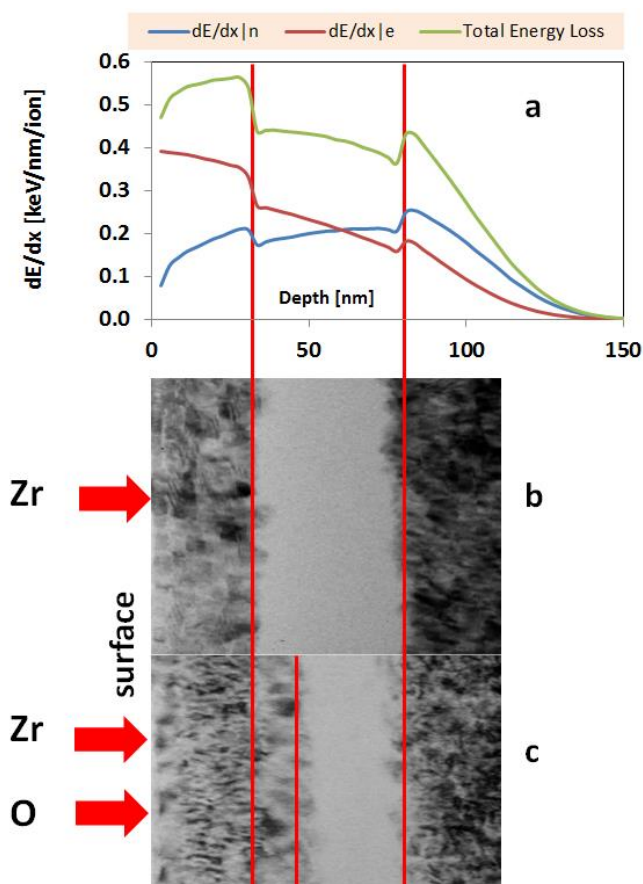


Figure 80 (a) SRIM calculated nuclear and electronic energy loss for  $\text{Al}_2\text{O}_3$  irradiated with 55 keV  $\text{O}^+$  ions, after the formation of buried amorphous layer due to prior "high dose" irradiation with  $\text{Zr}^+$  ions; (b) TEM cross-section BF image obtained from "high dose" sample irradiated with 175 keV  $\text{Zr}^+$  ions to a fluence of  $1.5 \times 10^{16} \text{ Zr}^+/\text{cm}^2$ ; (c) TEM cross-section BF image obtained from a "high dose" sample irradiated with 175 keV  $\text{Zr}^+$  ions to a fluence of  $1.5 \times 10^{16} \text{ Zr}^+/\text{cm}^2$  plus 55 keV  $\text{O}^+$  ions to a fluence of  $2.3 \times 10^{16} \text{ O}^+/\text{cm}^2$ . The model for the SRIM calculation in (a) assumes that the  $\text{Al}_2\text{O}_3$  substrate contains a buried amorphous layer with a lower density ( $3.1 \text{ g/cm}^3$ ) compared to the density of pristine  $\alpha\text{-Al}_2\text{O}_3$  ( $3.98 \text{ g/cm}^3$ ).

In this study, we observed two effects: (1) a recrystallization of an ion-beam-induced buried amorphous region in  $\alpha$ -Al<sub>2</sub>O<sub>3</sub> to form another polymorph of Al<sub>2</sub>O<sub>3</sub>, specifically the cubic phase,  $\gamma$ -Al<sub>2</sub>O<sub>3</sub> and (2) the recrystallization of the amorphous region was confined to the surface crystalline/amorphous interface of the amorphous layer.

#### **4.4 Optical study of Zr-implanted $\alpha$ -Al<sub>2</sub>O<sub>3</sub> samples followed by oxygen irradiation**

Optical methods (absorption and photoluminescence) are powerful techniques for characterizing defects in the oxygen sublattice in oxides. Levy and Dienes [216, 217] first reported the coloration of Al<sub>2</sub>O<sub>3</sub> by neutron irradiation in a reactor. Arnold et al. [218] ascribed the optical absorption band at 204 nm to irradiation-produced defects, observed after irradiation of their samples with light ions (H<sup>+</sup>, D<sup>+</sup>, He<sup>+</sup>) but they did not identify the defect(s). Evans and Stapelbroek [219] measured the absorption and emission spectra in 14-MeV neutron irradiated Al<sub>2</sub>O<sub>3</sub> and ascribed them to F<sup>+</sup> centers. Pogatshnik et al. [220] developed a model for energy transitions associated with single and paired anion vacancies in irradiated sapphire. Using this model and data from 3.8 MeV iron-implanted single crystals  $\alpha$ -Al<sub>2</sub>O<sub>3</sub>, Chen et al. [221] identified the absorption and emission bands for single F-type centers and aggregates of such centers. Table 10 summarizes the absorption and emission bands associated with specific lattice defects in single crystals  $\alpha$ -Al<sub>2</sub>O<sub>3</sub>.

*Table 10 The absorption and emission bands associated with specific lattice defects in single crystals  $\alpha$ -Al<sub>2</sub>O<sub>3</sub> [221]*

Defect type	Absorption		Emission		Number of oxygen vacancies	Number of trapped electrons
	eV	nm	eV	nm		
F	6.06	205	3.0	420	1	2
F <sup>+</sup>	4.8	258	3.8	325	1	1
	5.5	225				
	6.1	203				
F <sub>2</sub>	4.1	300	3.85	322	2	4
F <sub>2</sub> <sup>+</sup>	3.5	355	3.27	379	2	3
F <sub>2</sub> <sup>2+</sup>	2.7	455	2.25	550	2	2

The most common point defects in the oxygen sub-lattices in Al<sub>2</sub>O<sub>3</sub> are F-type centers and aggregates thereof. The F-center is one oxygen vacancy with two trapped electrons; and F<sup>+</sup>-center is a vacancy with one trapped electron. These may cluster in the form of F<sub>2</sub> (two F-centers), F<sub>2</sub><sup>+</sup> (two vacancies with 3 trapped electrons) and F<sub>2</sub><sup>2+</sup> (two trapped electrons). Dalal et al. observed absorption bands at higher energies of 6.8 and 6.97 eV obtained from  $\alpha$ -Al<sub>2</sub>O<sub>3</sub> samples implanted with He, Ne, and Ar ions [222]. These bands are outside the range of most commonly-available detection systems.

Previous studies have used optical absorption to identify the residual damage in the oxygen sublattice for  $\alpha$ -Al<sub>2</sub>O<sub>3</sub> irradiated with different ions at different fluences. Kozakiewicz et al. conducted an optical absorption study for  $\alpha$ -Al<sub>2</sub>O<sub>3</sub> implanted with 100 keV O<sup>+</sup>, Al<sup>+</sup>, and Cr<sup>+</sup> ions to fluences between  $4 \times 10^{15}$  and  $1 \times 10^{17}$  ions/cm<sup>2</sup>. They found that implantation of Al ions generated both F and F<sup>+</sup>-centers very efficiently whereas Cr-implantation produces mainly the F<sup>+</sup> center and few F centers. Implantation of oxygen produced the UV band near 200 nm only at large fluences [223]. Chen et al. irradiated  $\alpha$ -Al<sub>2</sub>O<sub>3</sub> single crystals with 3.8 MeV Fe<sup>2+</sup> ions to fluences of  $0.5 \times 10^{16}$  and  $2 \times 10^{16}$ /cm<sup>2</sup>. The optical absorption spectra contained the strong peak centered near 200 nm, identified as F and/or F<sup>+</sup>-centers, but the presence of other species was not obvious. Photoluminescence with excitation at 240 nm clearly produced luminescence not only from the F center but also from the F<sup>+</sup> center. Photoluminescence of the annealed samples showed presence of F<sup>2</sup> centers [221].

Optical absorption mainly gives information about F and F<sup>+</sup> centers. In single crystal  $\alpha$ -Al<sub>2</sub>O<sub>3</sub>, the absorption peak for F-centers occurs at ~6.06 eV and the peak for F<sup>+</sup>-center is at ~6.1 eV. This separation is less than the resolution of most current optical spectrometers. A measurement by another technique is necessary to confirm the presence or absence of the F-type centers. As shown in Table 1 the emission bands of these defects are well separated. The emission bands at 3.8, 3.0, and 3.85 eV have been ascribed to electronic relaxations at F<sup>+</sup>, F, and F<sup>2</sup> color centers, respectively.

The luminescence of single crystal  $\alpha$ -Al<sub>2</sub>O<sub>3</sub> subjected to the irradiation of energetic hydrogen and helium has studied by Jardin et al. They found that the number of



$F^+$  centers increased with increasing fluence for low fluence implantation. At high fluences, the F-centers are completely annihilated and the  $F^+$ -centers are partially eliminated. They proposed a model based on the conversion between F and  $F^+$  defects and destruction of both luminescent species resulting from the radiation-induced damage [224].

In this research, optical absorption and luminescent was used to characterize the retained defects in the O-sublattice. The estimates of the number of retained oxygen vacancies were compared to the number generated, as calculated with SRIM-2013, to determine the fraction of vacancies retained as F-type centers. Optical absorption spectra were obtained using a double beam Varian Cary 5000 spectrophotometer in the 190–800 nm wavelength range at room temperature. The density of F centers per square centimeter (noted  $N_F$ ) was determined by using Smakula's formula [225]. The photoluminescence was measured for irradiation at 255 nm by a Varian Cary Eclipse 6000 spectrophotometer at room temperature.

Figure 81 contains the optical absorption spectra for the following samples:

- (1) Single crystal  $\alpha$ - $Al_2O_3$  irradiated with 175 keV zirconium ions to a fluence of  $7.5 \times 10^{15} \text{ Zr}^+/\text{cm}^2$
- (2) Single crystal  $\alpha$ - $Al_2O_3$  irradiated with 175 keV zirconium ions to a fluence of  $1.5 \times 10^{16} \text{ Zr}^+/\text{cm}^2$
- (3) Single crystal  $\alpha$ - $Al_2O_3$  irradiated with 175 keV zirconium ions to a fluence of  $2 \times 10^{16} \text{ Zr}^+/\text{cm}^2$

- (4) Single crystal  $\alpha$ -Al<sub>2</sub>O<sub>3</sub> irradiated with 175 keV zirconium ions to a fluence of  $7.5 \times 10^{15}$  Zr<sup>+</sup>/cm<sup>2</sup> followed by 55 keV O<sup>+</sup> ions to fluences of  $1.1 \times 10^{16}$  O/cm<sup>2</sup>
- (5) Single crystal  $\alpha$ -Al<sub>2</sub>O<sub>3</sub> irradiated with 175 keV zirconium ions to a fluence of  $1.5 \times 10^{16}$  Zr<sup>+</sup>/cm<sup>2</sup> followed by 55 keV O<sup>+</sup> ions to fluences of  $2.3 \times 10^{16}$  O/cm<sup>2</sup>

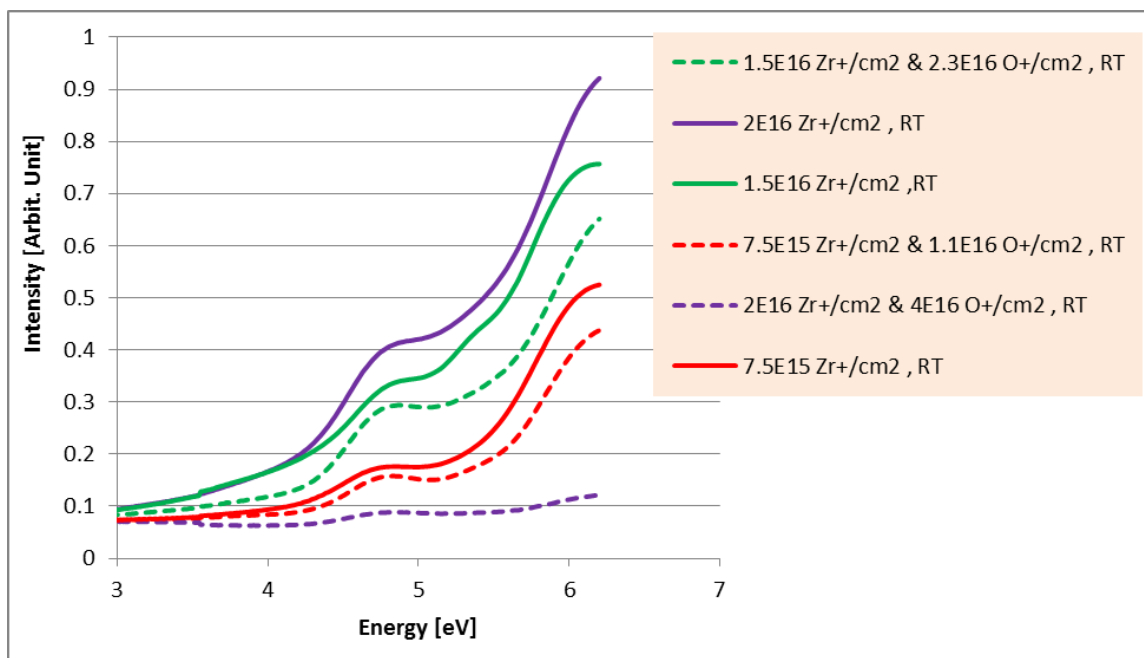


Figure 81 Optical absorption spectra with the absorption from a virgin crystal subtracted

The band located at about 4.8 eV clearly shows the presence of F<sup>+</sup> centers. The ~6 eV band could originate from F-centers, F<sup>+</sup>-centers, or a combination of the two types. The photoluminescence spectra (Figure 82) obtained from 4.86 eV, confirm that both types of oxygen vacancies are present in all implanted samples. From an analysis of the change in the ratio of the absorption at ~6 eV (F + F<sup>+</sup>) to that at ~4.8 eV (F<sup>+</sup>), it is

concluded that F-center production is favored at all fluences, but the fraction of  $F^+$ -centers increases with fluence. This observation agrees with the reported result that F centers defects were preferentially produced at higher defect generated densities [222]. Kozakiewicz et al. also concluded that  $F^+$  center increases as the mass of implanting ion increased [223]. A similar analysis showed that subsequent oxygen ion implantation decreased the total number of F-type centers and increased the number of  $F^+$ -centers relative to the number of F-centers. The decrease in total number of oxygen vacancy is expected as the newly injected oxygen is captured by the vacancies and/or because of IBIER. Arnold et al. found that implanting oxygen into sapphire created a large absorption peak at  $\sim 4.8$  eV, corresponding to the formation of  $F^+$ -centers [218].

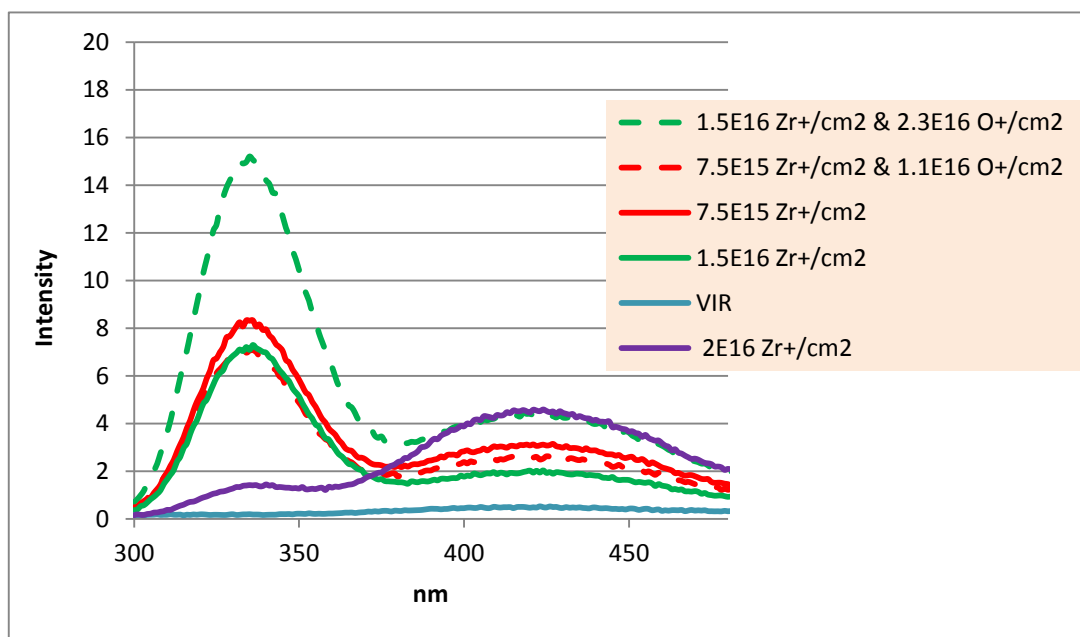


Figure 82 Photoluminescence of Zr and Zr + O irradiated sapphire

The absorption coefficient ( $\mu$ ) is given by  $\log(I_{in}/I_{out}) = \mu t/2.3$  where  $t$  is the path length. Since the absorption curves given in Figure 81, have the absorption from the virgin crystal subtracted, the true path length for these values is very much less than the millimeter thickness of the crystal. An estimate of the damage path length has been obtained by using the simulated range distribution of the damage that can be extracted from SRIM-2013 calculations. The true absorbing path length ( $t$ ) is taken as the FWHM of the oxygen vacancy distribution. The implant/damage width,  $t$ , is only about 62 nm for the samples irradiated with zirconium only and 68 nm for the dual implants. This means the absorption coefficient is extremely large compare with the values of about 2 for OA in normal colour centre using mm thick samples. Hence we expect strong interactions between defects and changes in the F/F+ dynamic balance. Table 2 shows the result of true absorption coefficient of the induced bands of the samples.

The average density of F-type centers in the region of the displacement cascades expected in the samples can be estimated by means of Smakula's equation (eqn.4.4.1) assuming that all F-type centers contribute to the absorption in these regions.

$$N_F = 0.87 \times 10^{17} n \mu_{\max} W_{1/2}/f (n^2 + 2)^2 \quad (4.4.1)$$

In Smakula's equation,  $f$  is the oscillator strength and for the F band is  $\sim 1$ ,  $n$  is the refractive index of sapphire at the wavelength corresponding to the absorption band peak. Refractive index values of 1.76 are typical for visible light, but for UV it will be slightly greater. Indeed truly amorphous sapphire has an index nearer 1.64 rather than 1.76. Since Zr is element 40 compared with Al that is only 13, the dopants will raise the index. In this calculation refractive index was chosen 1.8 because of present of Zr ions at the implanted

region. The width (in eV) at half maximum of the optical absorption band characterized by the maximum optical density ( $W_{1/2}$ ) has a value of ~0.6 eV [226]. The maximum absorption coefficients ( $\mu_m$ ) of the induced bands are given in the Table 11. The concentrations of F centres, i.e., retained oxygen vacancies, calculated using Smakula's equation are given in Table 12.

*Table 11 True absorption coefficient of the induced bands*

sample	$\mu_{\max}[\text{cm}^{-1}]$
$1.5\text{E}16 \text{ Zr}^+/\text{cm}^2$ & $2.3\text{E}16 \text{ O}^+/\text{cm}^2$	220423
$7.5\text{E}15 \text{ Zr}^+/\text{cm}^2$ & $1.1\text{E}16 \text{ O}^+/\text{cm}^2$	148101
$7.5\text{E}15 \text{ Zr}^+/\text{cm}^2$	194782
$1.5\text{E}16 \text{ Zr}^+/\text{cm}^2$	280802
$2\text{E}16 \text{ Zr}^+/\text{cm}^2$	529851

*Table 12 The concentration of F-type centres estimated by Smakula's equation*

Sample	$N_{(F+F^+)} (\text{cm}^{-3})$
$7.5\text{E}15 \text{ Zr}^+/\text{cm}^2$ & $1.1\text{E}16 \text{ O}^+/\text{cm}^2$	$5.07\text{E}+20$
$7.5\text{E}15 \text{ Zr}^+/\text{cm}^2$	$6.66\text{E}+20$
$1.5\text{E}16 \text{ Zr}^+/\text{cm}^2$	$9.61\text{E}+20$
$1.5\text{E}16 \text{ Zr}^+/\text{cm}^2$ & $2.3\text{E}16 \text{ O}^+/\text{cm}^2$	$7.54\text{E}+20$
$2\text{E}16$	$1.81\text{E}+21$

The concentrations of F-type defects ( $F + F^+$ ) given in Table 3 lie in the range of  $5.07 \times 10^{20}$  to  $1.8 \times 10^{21}$  centers/ $\text{cm}^3$ , i.e., about 1% of the total oxygen content of sapphire. These values are in the range of  $10^{20}$  to  $10^{21}$  centers/ $\text{cm}^3$  reported for MgO implanted with a number of ions [227].

The concentrations represent only a small fraction of the oxygen ions displaced during implantation. Assuming than ~99% of the damage is dynamically annealed during the cascade “cool-down” period, the values represent about 1% of those remaining as F-type centers. These centers represent isolated oxygen vacancies. At the relatively high fluences used in this study, there is considerable overlapping of the displacement cascades that may give rise to extended defects such as interstitial dislocations, nanometer-sized clusters, defects trapped at dislocations, etc. Some of the displaced oxygen may reside in interstitial positions as  $\text{O}^{2-}$  leaving a vacancy without a trapped electron(s). This defect has an optical absorption band near 7.0 eV, outside the range of the instrument used here.

The apparent “damage efficiency” reported for this study is much lower than values of 8 to 30% reported by Agnew for ion irradiation of sapphire at room temperature [228]. Averbach et al. found a decrease in damage efficiency with increasing ion mass for a variety of irradiations [229]. Pells concluded that the reduction in damage deficiency is the result of Frenkel pair combination within a displacement cascade [230]. The mass of irradiation ion (Zr) and the fluences used in the present study are higher than those used in these earlier studies, and a decrease on damage efficiency (number of retained defects) is expected.

#### **4.5 Dual effect of oxygen irradiation and thermal annealing on Zr-implanted $\alpha$ -Al<sub>2</sub>O<sub>3</sub>**

Figure 83 shows a bright-field TEM image of  $\alpha$ -Al<sub>2</sub>O<sub>3</sub> samples irradiated with 175 keV Zr ions to a fluence of  $2 \times 10^{15}$  followed by irradiation with O<sup>+</sup> ions to a fluence of  $3 \times 10^{16}$  O/cm<sup>2</sup> at room temperature. Comparing Figs. 54 and 83, it shows that the amorphous region adjacent to the surface damaged region has recrystallized during the subsequent irradiation of oxygen. Approximately 20 nm of the amorphous alumina has crystallized epitaxially on the surface damaged alumina substrate; however, no growth of the deeper damaged layer into the amorphous region is observed. It is interesting that the thickness of the amorphous region remain almost the same by pushing the deeper damaged region toward the bulk alumina. Thus, the crystallization of the amorphous phase initiated at the interface between near-surface damaged and amorphous regions and grew into the surface region.

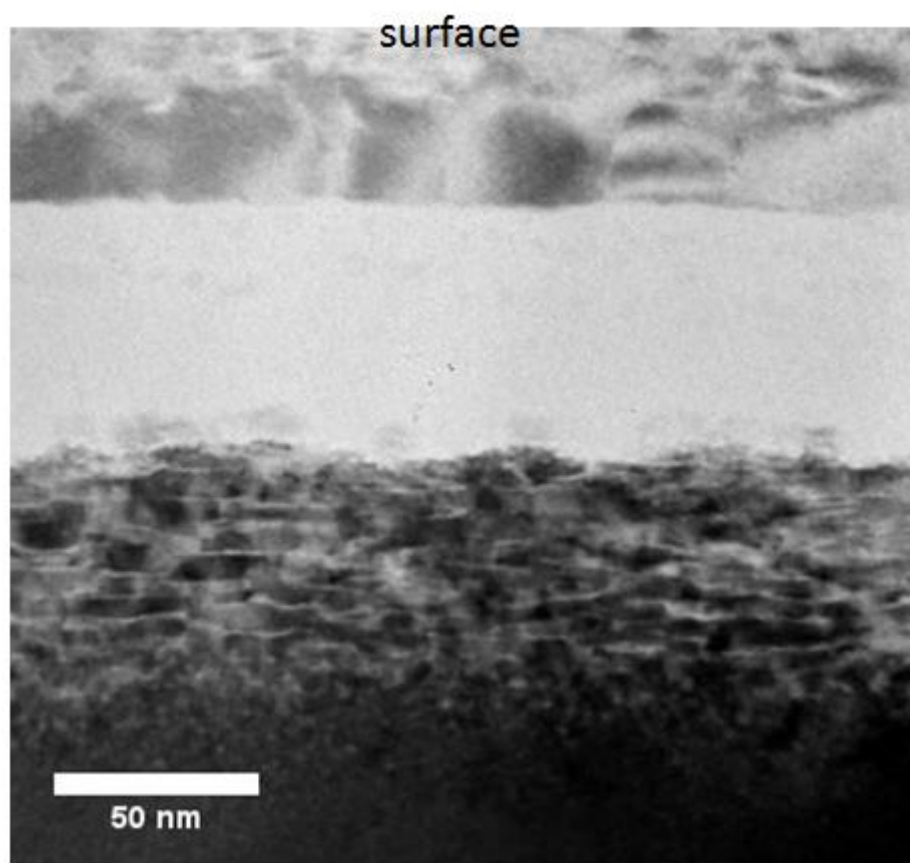


*Figure 83 The bright-field image for the sample irradiated with 175 keV  $\text{Zr}^+$  ions to a fluence of  $2 \times 10^{16} \text{ Zr/cm}^2$  plus 48 keV  $\text{O}^+$  ions to a fluence of  $3 \times 10^{16} \text{ O/cm}^2$*

Figure 84 show the RBS-C for the same sample ( $\alpha\text{-Al}_2\text{O}_3$  sample irradiated with 175 keV  $\text{Zr}^+$  ions to a fluence of  $2 \times 10^{16} \text{ Zr/cm}^2$  plus 48 keV  $\text{O}^+$  ions to a fluence of  $3 \times 10^{16} \text{ O/cm}^2$ ). Figure 85 show a closer view of the Al-sublattice of the spectra in Figure 84. There is still an overlapped random and aligned spectrum where the energy is less than 1075 keV. Comparing Figures 55 and 85, it suggests that a part of amorphous



region is recrystallized by subsequent room temperature irradiation with 48 keV oxygen ions. This is similar to the effect of ion beam-induced epitaxial crystallization (IBIEC) reported previously for the  $\alpha$ - $\text{Al}_2\text{O}_3$  sample irradiated with 175 keV  $\text{Zr}^+$  ions to a fluence of  $1.5 \times 10^{16} \text{ Zr/cm}^2$  plus 55 keV  $\text{O}^+$  ions to a fluence of  $2.3 \times 10^{16} \text{ O/cm}^2$ .

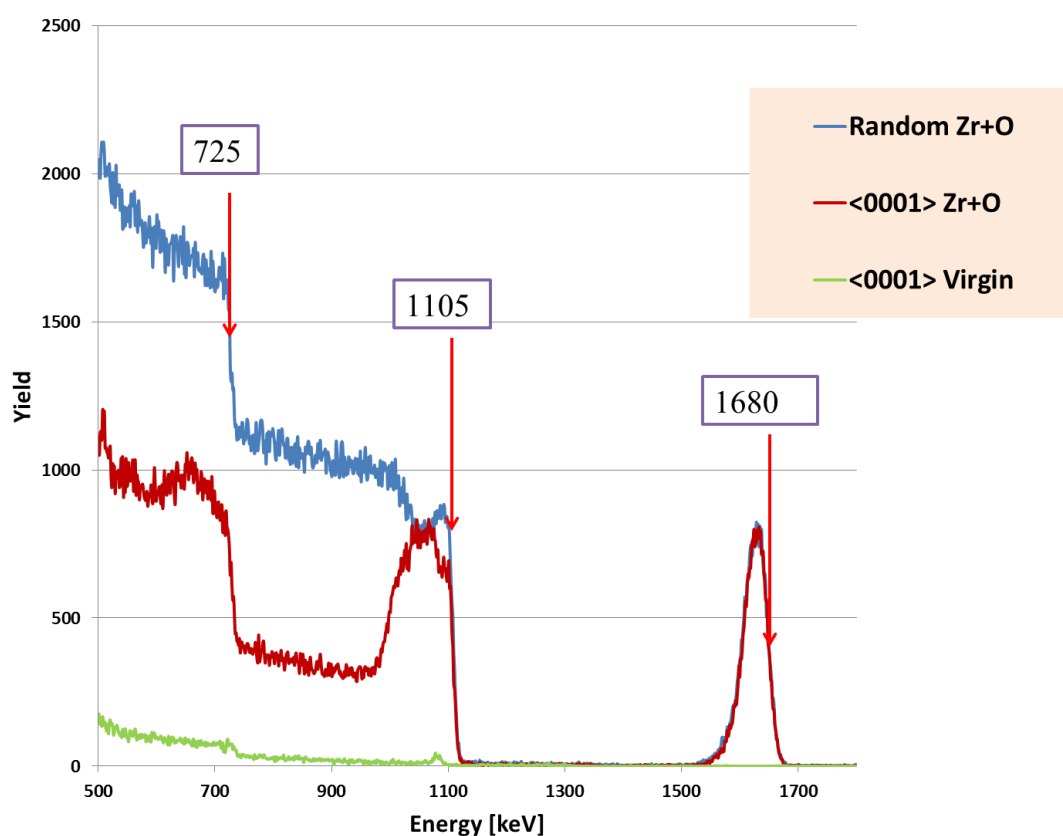


Figure 84 RBS-C spectra using 2 MeV  $\text{He}^+$  obtained from  $\alpha$ - $\text{Al}_2\text{O}_3$  sample irradiated with 175 keV  $\text{Zr}^+$  ions to a fluence of  $2 \times 10^{16} \text{ Zr/cm}^2$  plus 48 keV  $\text{O}^+$  ions to a fluence of  $3 \times 10^{16} \text{ O/cm}^2$ . The RBS-chamber had IBM geometry with detector scattering angle of  $+170^\circ$  with a detector resolution of about 15 keV. Arrows labeled “Zr”, “Al”, “O” indicate the surface elastic scattering energies for Zr, Al, and O atoms respectively.

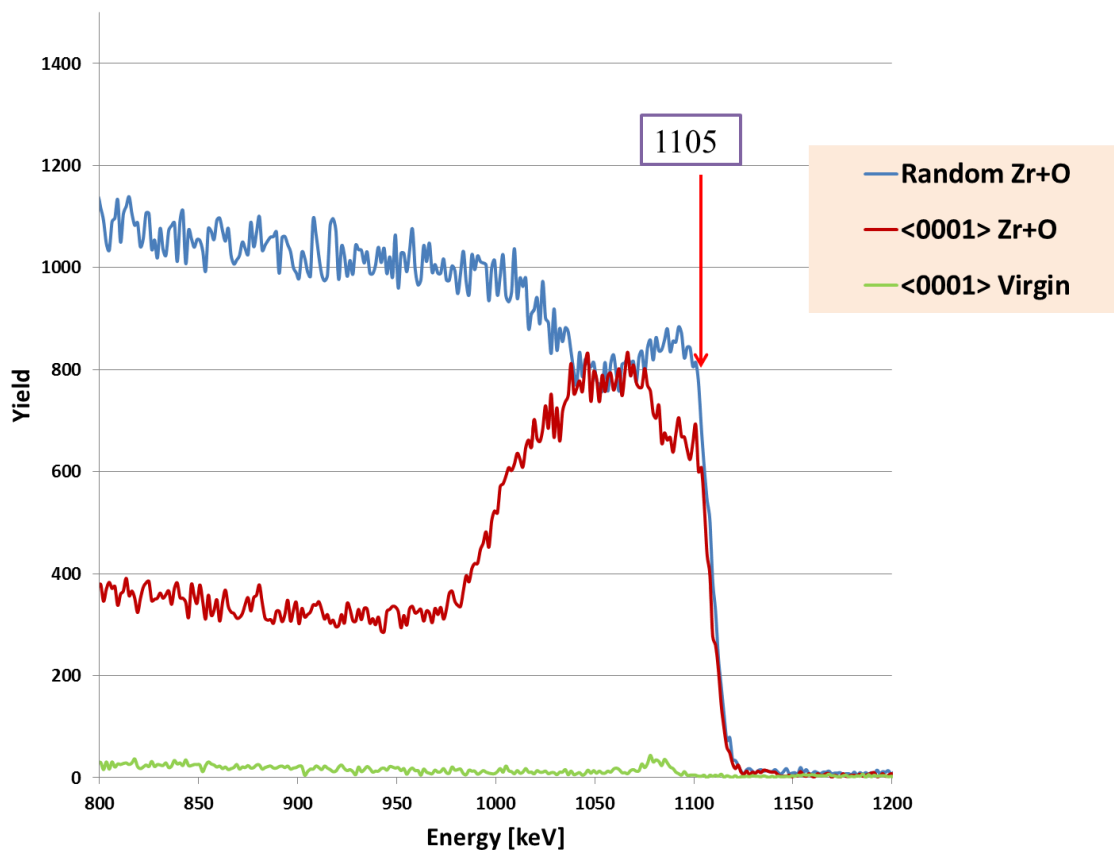
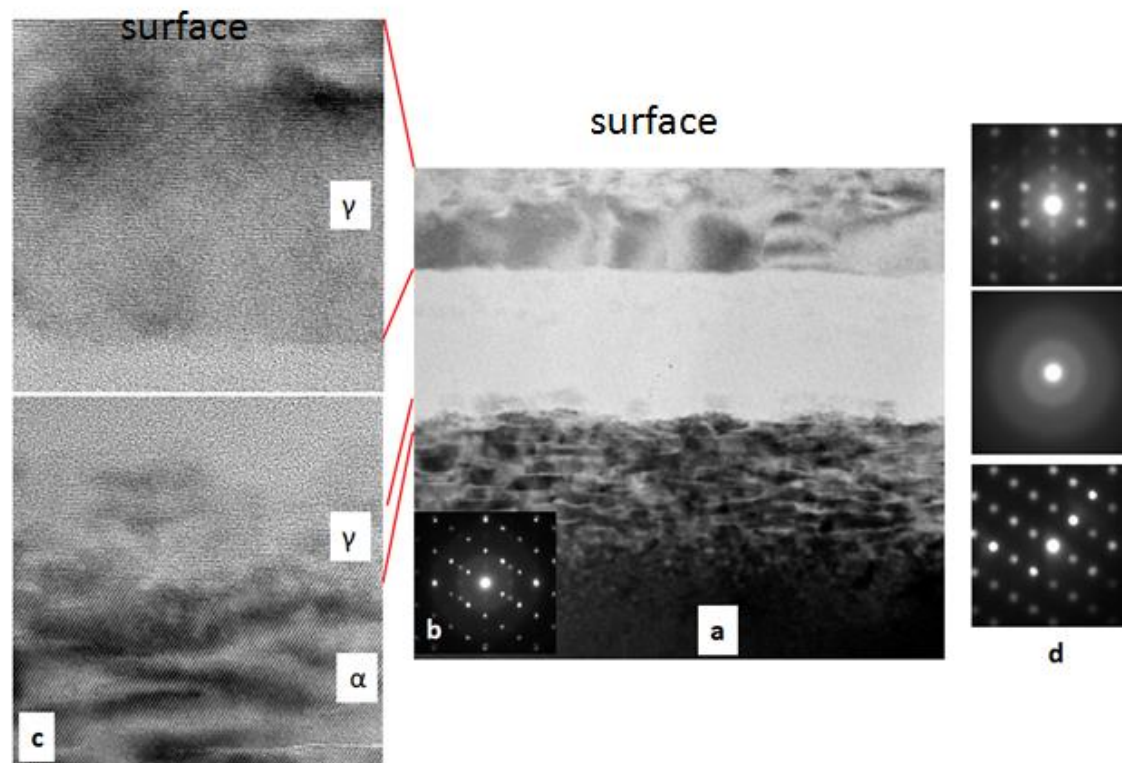


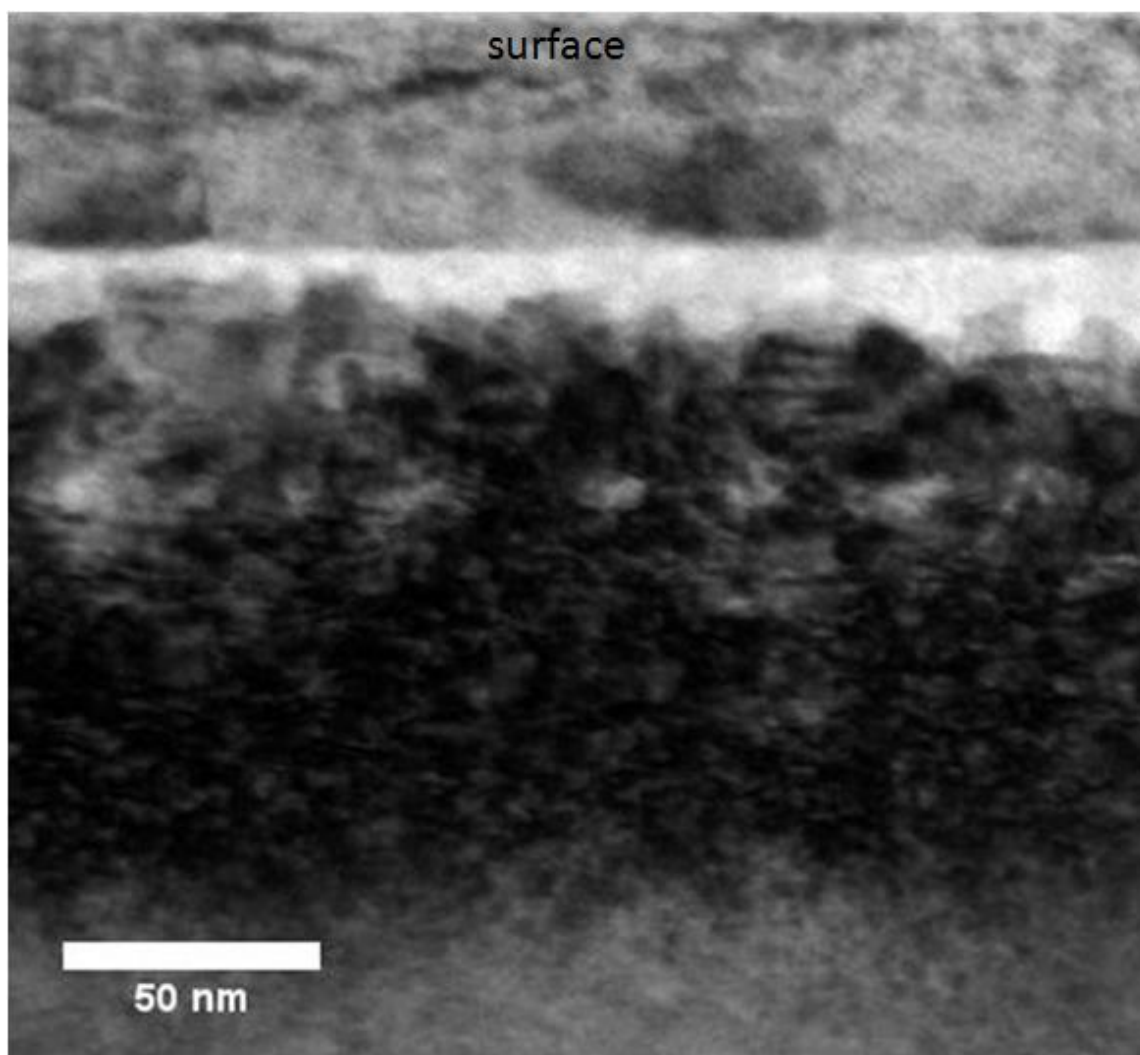
Figure 85 A closer view of Al-sublattice in the RBS-C spectra using 2 MeV  $\text{He}^+$  obtained from  $\alpha\text{-Al}_2\text{O}_3$  samples irradiated with 175 keV  $\text{Zr}^+$  ions to a fluence of  $2 \times 10^{16} \text{ Zr/cm}^2$  plus 48 keV  $\text{O}^+$  ions to a fluence of  $3 \times 10^{16} \text{ O/cm}^2$ . The RBS-chamber had IBM geometry with detector scattering angle of  $+170^\circ$  with a detector resolution of about 15 keV. Arrow labeled “Al” indicates the surface elastic scattering energy for Al atom.

Figure 86a shows the same bright-field TEM image demonstrated in Fig. 83, along with high resolution transmission electron microscopy (HRTEM) image obtained from the subsurface region and NBED pattern obtained from different regions. The HRTEM images obtained from the crystalline sub-surface region and the recrystallized region adjacent to the deeper damaged regions reveal the presence of  $\gamma$ - $\text{Al}_2\text{O}_3$  phase (Fig.86 c). The NBED pattern obtained from the subsurface regions (Fig. 86d) confirms the presence of  $\gamma$ - $\text{Al}_2\text{O}_3$  phase. The NBED pattern obtained from the deeper damaged region is consistent with  $\alpha$ - $\text{Al}_2\text{O}_3$  phase (beam direction  $(\vec{B}) = \langle 11\bar{2}0 \rangle$ ). The NBED pattern from the middle region shows evidence diffuse rings, indicative of an amorphous  $\text{Al}_2\text{O}_3$  region. Fig. 86 b shows the selected area electron diffraction (SAED) pattern obtained from this sample indicating the presence of  $\alpha$ - $\text{Al}_2\text{O}_3$ ,  $\gamma$ - $\text{Al}_2\text{O}_3$  and amorphous regions in the sample.



*Figure 86 (a) cross-sectional TEM-BF image obtained from the as-irradiated  $\alpha$ - $\text{Al}_2\text{O}_3$  sample irradiated with  $2 \times 10^{16} \text{ Zr}^+/\text{cm}^2$  and  $3 \times 10^{16}$  (b) SAED pattern obtained from the sample (c) High resolution transmission electron transmission microscopy (HRTEM) image obtained from the subsurface, amorphous and deeper damaged regions and (d) NBED patterns obtained from different regions.*

Figure 87 shows a bright-field TEM image of annealed  $\alpha$ -Al<sub>2</sub>O<sub>3</sub> sample at 800°C for 30 minutes previously irradiated with 175 keV Zr ions to a fluence of  $2 \times 10^{15}$  followed by irradiation with O<sup>+</sup> ions to a fluence of  $3 \times 10^{16}$  O/cm<sup>2</sup> at room temperature. Comparing as irradiated sample (Fig.83) with this sample (Fig.87) the thickness of the crystalline region adjacent to surface remain the same, but the amorphous region start to epitaxially grow on the deeper damaged region. The thickness of the remained amorphous layer shows that the recrystallization is significant at 800 °C for 30 minutes. Comparing Fig. 58 and Fig. 87, it shows that oxygen irradiation eases the recrystallization process specifically at the interface between the amorphous and the deeper damaged regions during thermal annealing.



*Figure 87 The bright-field image for the sample irradiated with 175 keV  $Zr^+$  ions to a fluence of  $2 \times 10^{16}$   $Zr/cm^2$  plus 48 keV  $O^+$  ions to a fluence of  $3 \times 10^{16}$   $O/cm^2$  and annealed at 800 °C for 30 minutes.*

Figure 88 shows the RBS-C spectra for the samples irradiated with  $2 \times 10^{16}$   $\text{Zr}^+/\text{cm}^2$  plus  $3 \times 10^{16}$   $\text{O}^+/\text{cm}^2$  and annealed at 800 °C for 30 minutes. Figure 89 is the same spectra but at a closer view for the Al-sublattice. The overlapped region for aligned and random spectra from in Fig. 89 suggests an amorphous region in the sample.

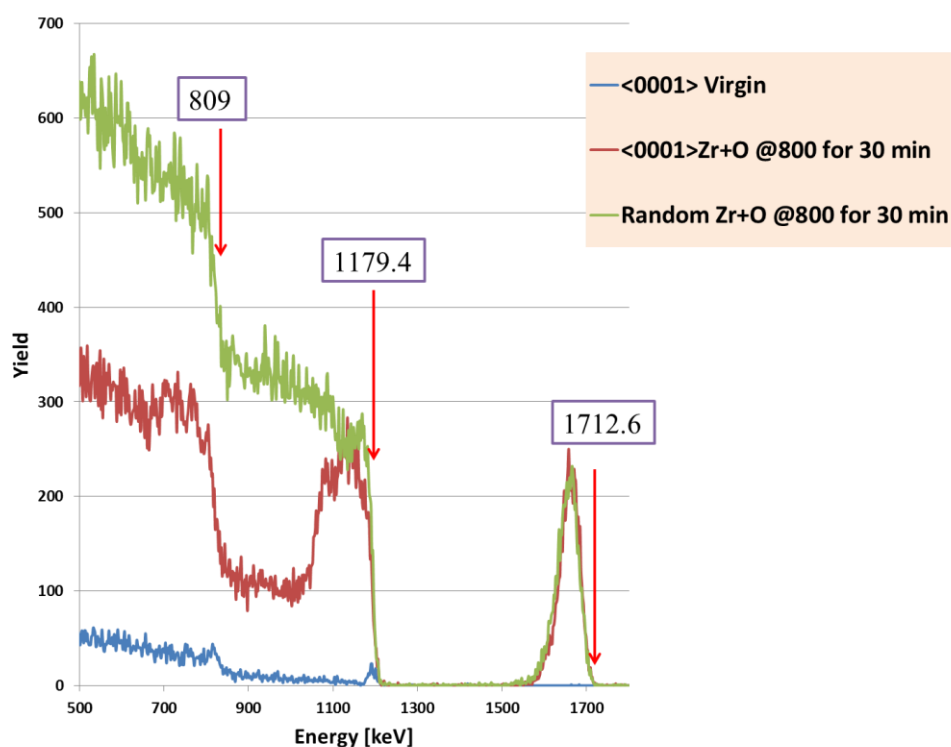


Figure 88 RBS-C spectra using 2 MeV  $\text{He}^+$  obtained from  $\alpha\text{-Al}_2\text{O}_3$  samples irradiated with 175 keV  $\text{Zr}^+$  ions to a fluence of  $2 \times 10^{16}$   $\text{Zr}/\text{cm}^2$  plus 48 keV  $\text{O}^+$  ions to a fluence of  $3 \times 10^{16}$   $\text{O}/\text{cm}^2$  and annealed at 800 °C for 30 minutes. The RBS-chamber had IBM geometry with detector scattering angle of  $-165^\circ$  with a detector resolution of about 15 keV. Arrows labeled “Zr”, “Al”, “O” indicate the surface elastic scattering energies for Zr, Al, and O atoms respectively.

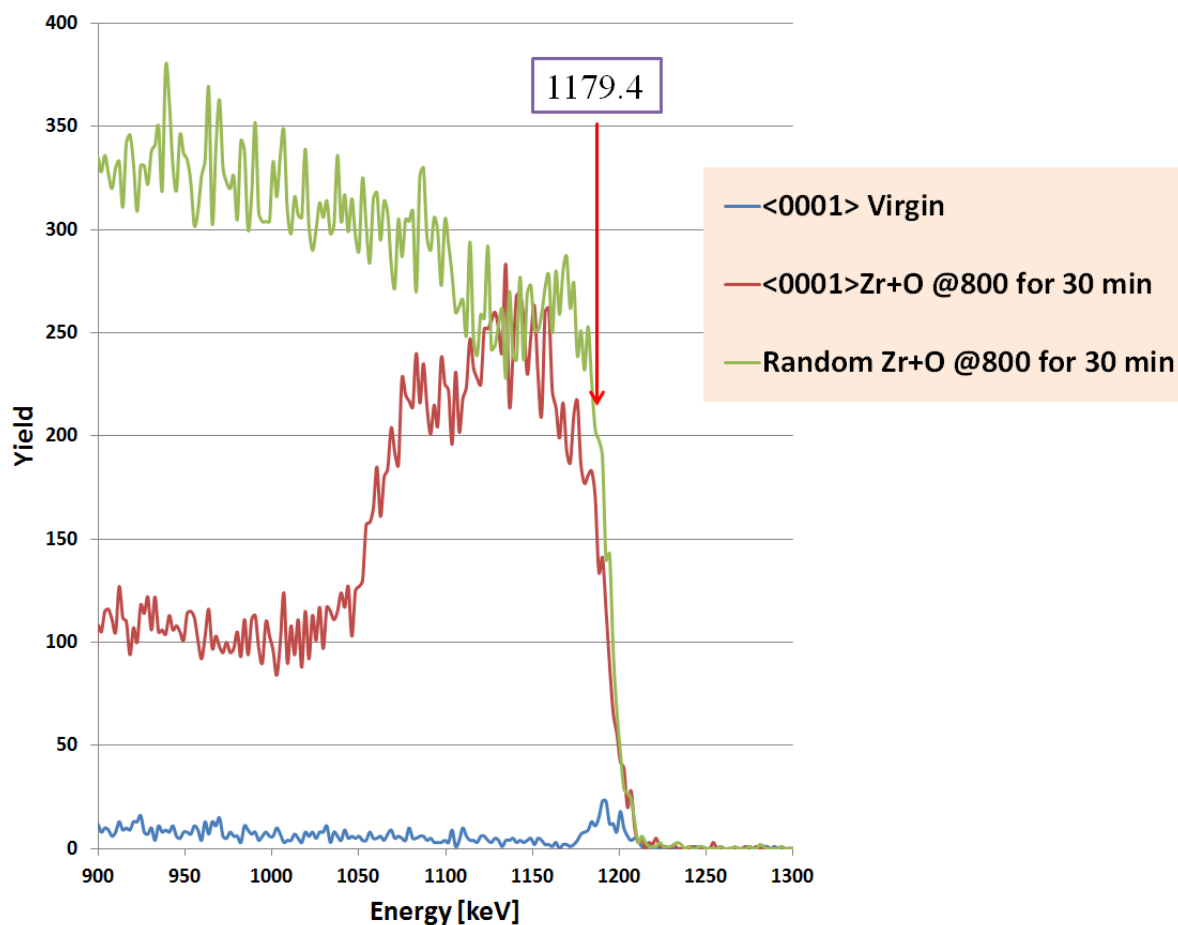
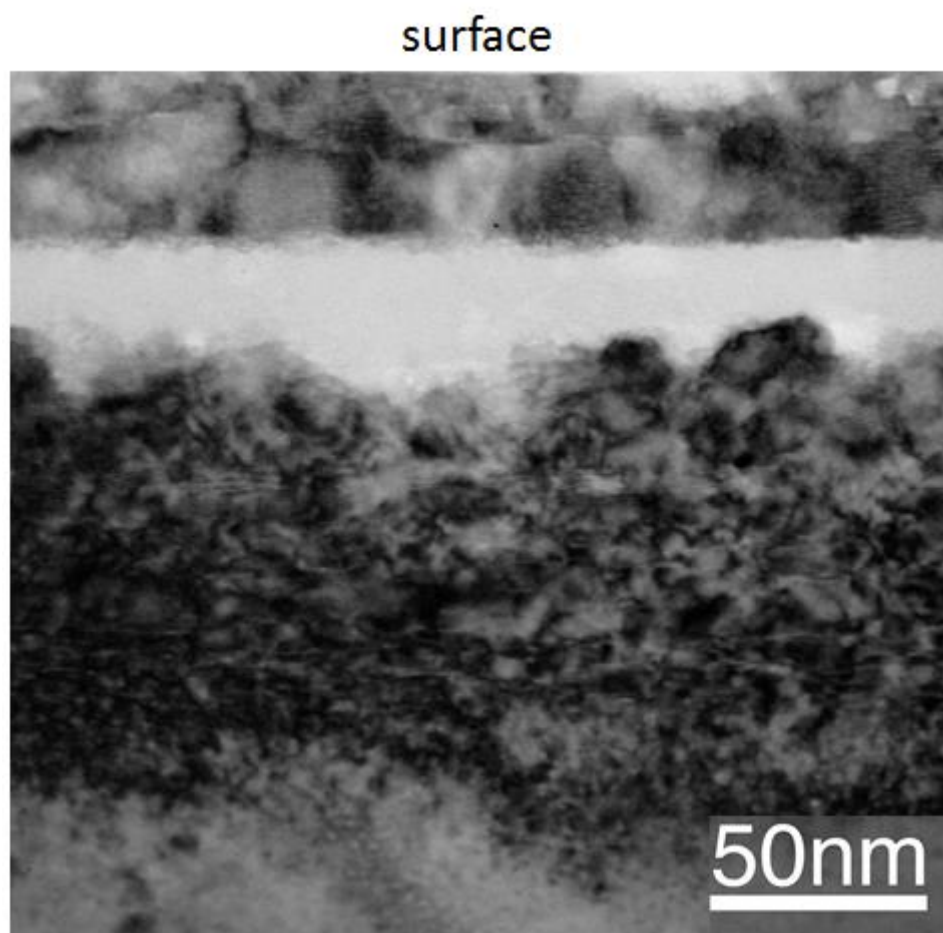


Figure 89 A closer view of Al-sublattice in the RBS-C spectra using 2 MeV  $\text{He}^+$  obtained from  $\alpha\text{-Al}_2\text{O}_3$  samples irradiated with 175 keV  $\text{Zr}^+$  ions to a fluence of  $2 \times 10^{16}$   $\text{Zr}/\text{cm}^2$  plus 48 keV  $\text{O}^+$  ions to a fluence of  $3 \times 10^{16}$   $\text{O}/\text{cm}^2$  and annealed at 800 °C for 30 minutes. The RBS-chamber had IBM geometry with detector scattering angle of  $-165^\circ$  with a detector resolution of about 15 keV. Arrow labeled “Al” indicates the surface elastic scattering energy for Al atom.



Figure 90 shows a bright-field TEM image of annealed  $\alpha$ -Al<sub>2</sub>O<sub>3</sub> sample at 900°C for 60 minutes previously irradiated with 175 keV Zr ions to a fluence of  $2 \times 10^{15}$  followed by irradiation with O<sup>+</sup> ions to a fluence of  $3 \times 10^{16}$  O/cm<sup>2</sup> at room temperature.

Figure 91a shows the same bright-field TEM image demonstrated in Fig. 90, along with HRTEM image obtained from the same sample and NBED patterns obtained from different regions present in the sample. The HRTEM images and NBED patterns (Fig. 91 b, c) indicates the presence of  $\gamma$ -Al<sub>2</sub>O<sub>3</sub> phase in the crystalline sub-surface region and  $\alpha$ -Al<sub>2</sub>O<sub>3</sub> phase in the recrystallized region adjacent to the deeper damaged region. Fig. 91b shows a very small  $\gamma$ -Al<sub>2</sub>O<sub>3</sub> phase region in the interface between the amorphous region and the deeper recrystallized region. The NBED pattern obtained from the deeper damaged region is consistent with  $\alpha$ -Al<sub>2</sub>O<sub>3</sub> phase (beam direction  $(\vec{B}) = \langle 11\bar{2}0 \rangle$ ). The NBED pattern from the middle region shows evidence diffuse rings, indicative of an amorphous Al<sub>2</sub>O<sub>3</sub> region. Comparing Fig. 61 and Fig. 90, it shows that oxygen irradiation affect the recrystallization process significantly at the interface between the amorphous and the deeper damaged regions during thermal annealing. The increasing of the amorphous width in this sample compare with the similar samples annealed at lower temperatures or shorter times is attributed to densification of recrystallized region adjacent to the deeper damaged region due to  $\gamma$ -phase to  $\alpha$ -phase transformation.



*Figure 90 The bright-field image for the sample irradiated with 175 keV  $Zr^+$  ions to a fluence of  $2 \times 10^{16}$   $Zr/cm^2$  plus 48 keV  $O^+$  ions to a fluence of  $3 \times 10^{16}$   $O/cm^2$  and annealed at 800 °C for 30 minutes.*

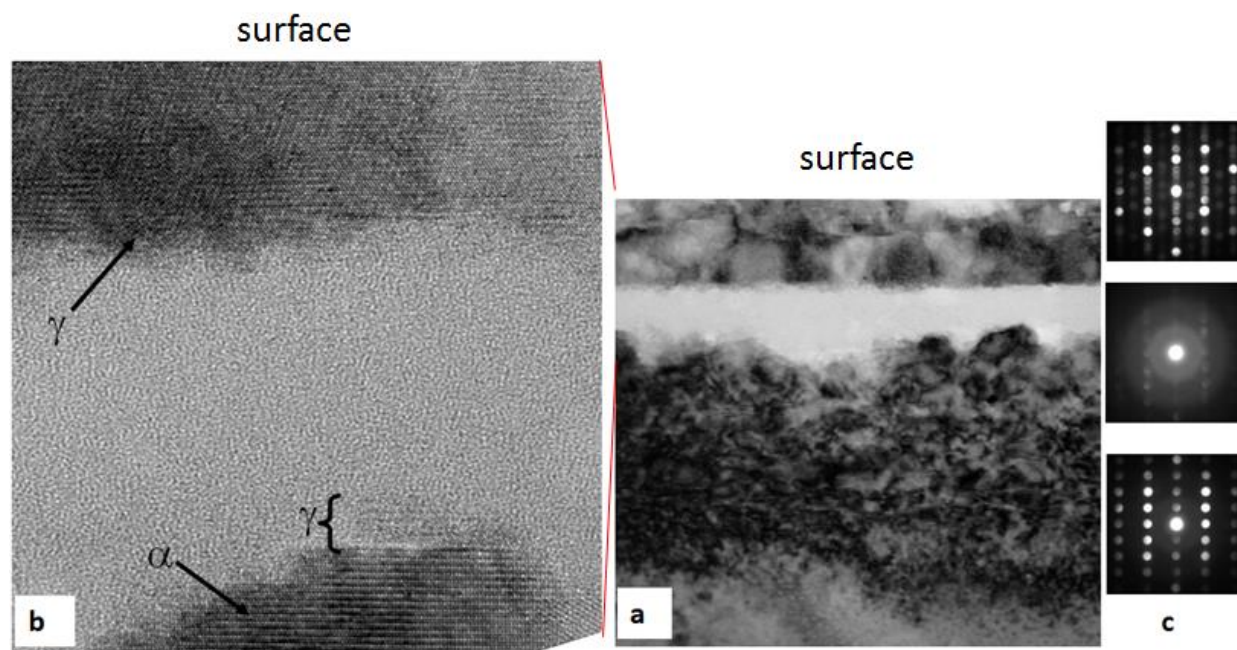
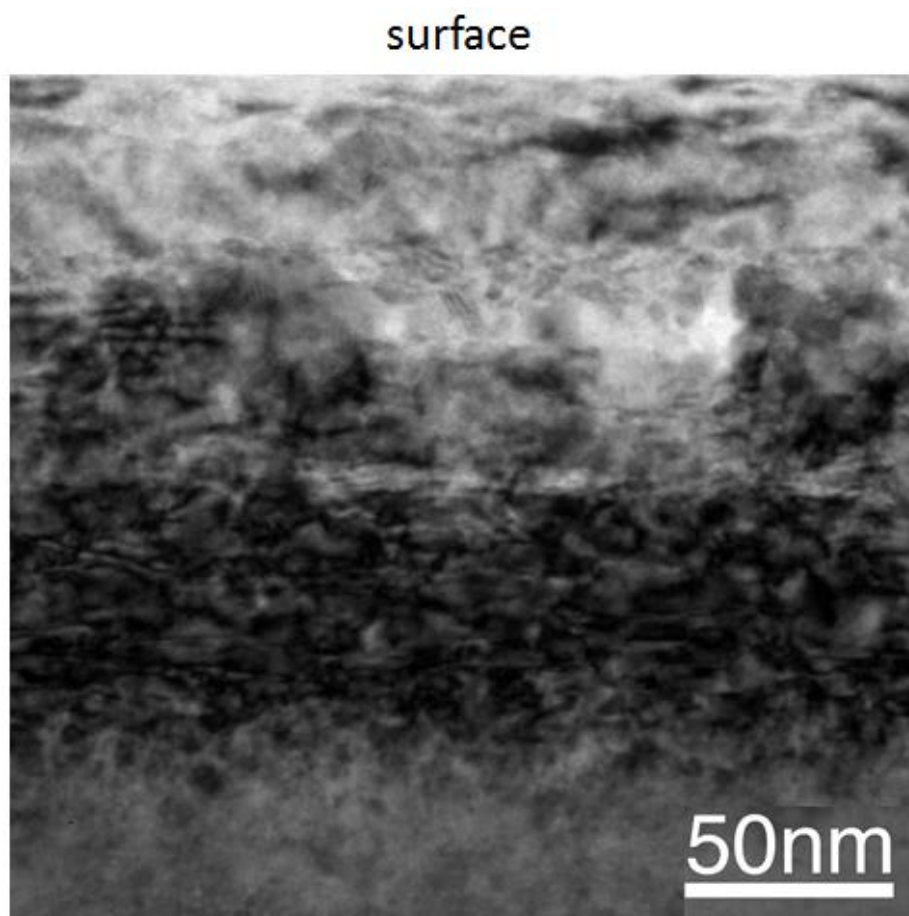


Figure 91 (a) Cross-sectional TEM-BF image obtained from  $\alpha$ - $\text{Al}_2\text{O}_3$  sample irradiated with 175 keV  $\text{Zr}^+$  ions to a fluence of  $2 \times 10^{16} \text{ Zr/cm}^2$  plus 48 keV  $\text{O}^+$  ions to a fluence of  $3 \times 10^{16} \text{ O/cm}^2$  and annealed at 900 °C for 60 minutes. (b) HRTEM image and (c) NBED patterns obtained from the affected regions.

Figure 92 shows a bright-field TEM image of annealed  $\alpha$ -Al<sub>2</sub>O<sub>3</sub> sample at 1000°C for 30 minutes previously irradiated with 175 keV Zr ions to a fluence of  $2 \times 10^{16}$  followed by irradiation with O<sup>+</sup> ions to a fluence of  $3 \times 10^{16}$  O/cm<sup>2</sup> at room temperature.



*Figure 92 The bright-field image for the sample irradiated with 175 keV Zr<sup>+</sup> ions to a fluence of  $2 \times 10^{16}$  Zr/cm<sup>2</sup> plus 48 keV O<sup>+</sup> ions to a fluence of  $3 \times 10^{16}$  O/cm<sup>2</sup> and annealed at 1000 °C for 30 minutes.*

Figure 92 show the RBS-C spectra for the samples implanted with  $2 \times 10^{16} \text{ Zr}^+/\text{cm}^2$  plus  $3 \times 10^{16} \text{ O}^+/\text{cm}^2$  and annealed at  $1000^\circ\text{C}$  for 30 minutes. Figure 84 is a closer view for the Al-sublattice in the spectra illustrated at Figure 83.

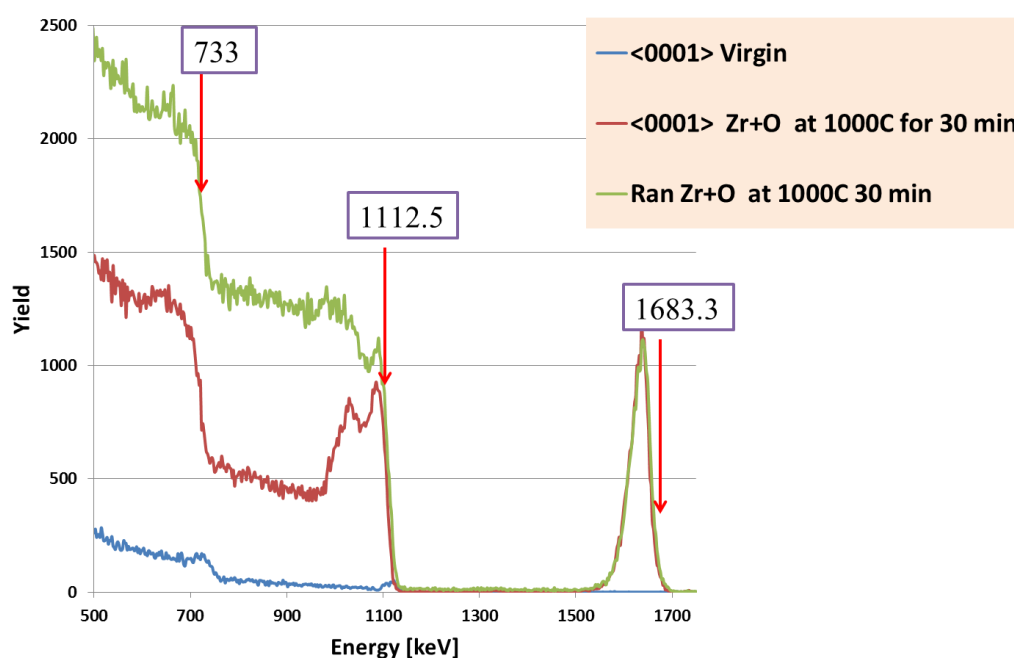


Figure 93 RBS-C spectra using  $2 \text{ MeV He}^+$  obtained from  $\alpha\text{-Al}_2\text{O}_3$  samples irradiated with  $175 \text{ keV Zr}^+$  ions to a fluence of  $2 \times 10^{16} \text{ Zr}/\text{cm}^2$  plus  $48 \text{ keV O}^+$  ions to a fluence of  $3 \times 10^{16} \text{ O}/\text{cm}^2$  and annealed at  $1000^\circ\text{C}$  for 30 minutes. The RBS-chamber had IBM geometry with detector scattering angle of  $-165^\circ$  with a detector resolution of about  $15 \text{ keV}$ . Arrows labeled “Zr”, “Al”, “O” indicate the surface elastic scattering energies for Zr, Al, and O atoms respectively.

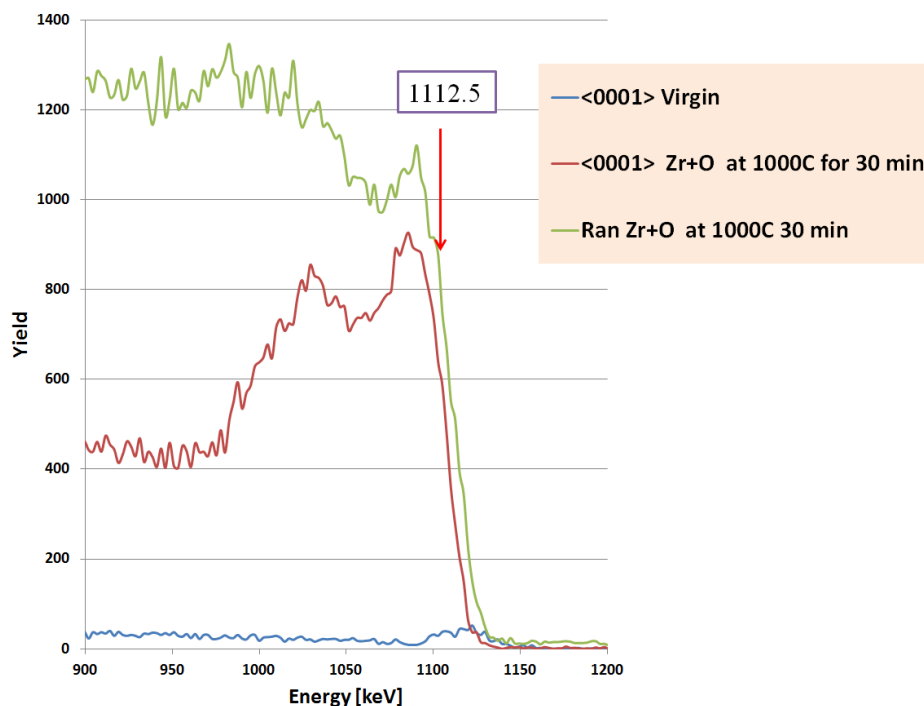
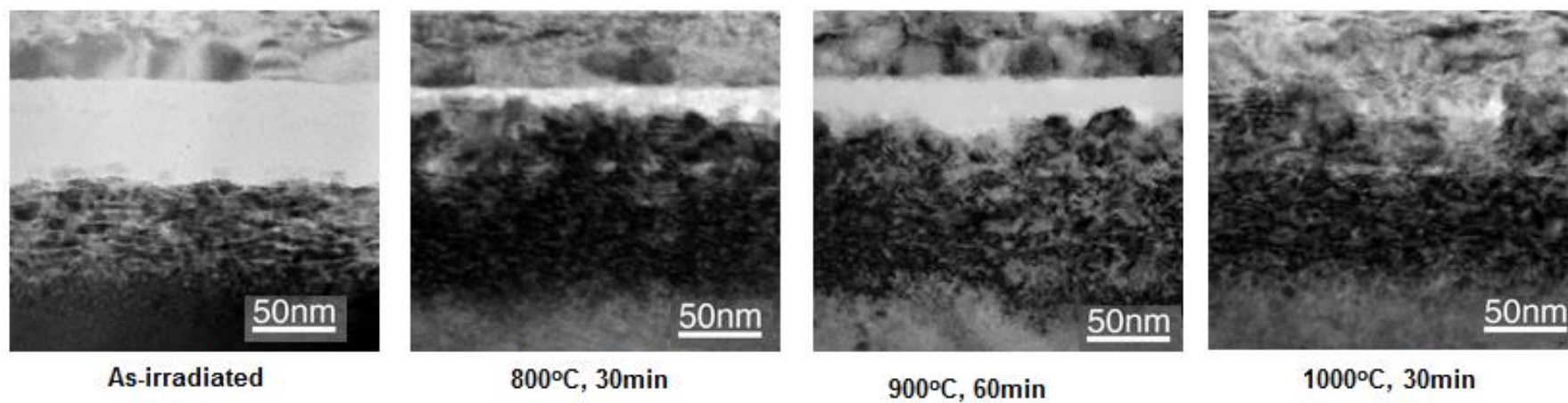


Figure 94 A closer view of Al-sublattice in the RBS-C spectra using 2 MeV  $\text{He}^+$  obtained from  $\alpha\text{-Al}_2\text{O}_3$  samples irradiated with 175 keV  $\text{Zr}^+$  ions to a fluence of  $2 \times 10^{16} \text{ Zr/cm}^2$  plus 48 keV  $\text{O}^+$  ions to a fluence of  $3 \times 10^{16} \text{ O/cm}^2$  and annealed at 1000 °C for 30 minutes. The RBS-chamber had IBM geometry with detector scattering angle of  $-165^\circ$  with a detector resolution of about 15 keV. Arrow labeled “Al” indicates the surface elastic scattering energy for Al atom.

Figure 95 shows the TEM bright-field images for all the samples that have been irradiated with 175 keV  $\text{Zr}^+$  ions to a fluence of  $2 \times 10^{16} \text{ Zr/cm}^2$  plus 48 keV  $\text{O}^+$  ions to a fluence of  $3 \times 10^{16} \text{ O/cm}^2$  before and after annealing at different temperatures and times. Figure 95 shows also that during the thermal annealing of  $2 \times 10^{16} \text{ Zr}^+/\text{cm}^2$  plus  $3 \times 10^{16} \text{ O}^+/\text{cm}^2$  samples recrystallization at the interface between the deeper damaged and the amorphous regions is remarkable.



*Figure 95 The TEM bright-field image for the samples irradiated with 175 keV  $Zr^+$  ions to a fluence of  $2 \times 10^{16}$   $Zr/cm^2$  plus 48 keV  $O^+$  ions to a fluence of  $3 \times 10^{16}$   $O/cm^2$  before and after annealing at different temperatures and times*

Figure 96 shows BF-TEM, HRTEM, and NBED patterns indicating the effect of O irradiation and annealing on Zr-irradiated sample. Irradiation of the pre-Zr-irradiated sample with 48 keV oxygen ions produces a very thin layer of  $\gamma$ -Al<sub>2</sub>O<sub>3</sub> on top of highly damaged but still crystalline of  $\alpha$ -Al<sub>2</sub>O<sub>3</sub>. The subsurface region consists of an  $\alpha$ -Al<sub>2</sub>O<sub>3</sub> layer sandwiched by two  $\gamma$ -Al<sub>2</sub>O<sub>3</sub> layers whilst irradiation of the  $\alpha$ -Al<sub>2</sub>O<sub>3</sub> with 175 keV to a fluence of  $1.5 \times 10^{16}$  Zr/cm<sup>2</sup> produces a defected  $\alpha$ -Al<sub>2</sub>O<sub>3</sub> subsurface. The formation of  $\alpha$ -Al<sub>2</sub>O<sub>3</sub> layer sandwiched by two  $\gamma$ -Al<sub>2</sub>O<sub>3</sub> layers is attributed to stress relaxation of this stressed layer that adjacent to a free surface and an amorphous region. Irradiation of this sample with 48 keV oxygen ions to a fluence of  $3 \times 10^{16}$  O/cm<sup>2</sup> transfers the stressed  $\alpha$ -Al<sub>2</sub>O<sub>3</sub> layer (sandwiched by two  $\gamma$ -Al<sub>2</sub>O<sub>3</sub> layers) to  $\gamma$ -Al<sub>2</sub>O<sub>3</sub> phase. The HRTEM images and NBED patterns obtained from these layers show that the surface layer completely transforms to  $\gamma$ -phase and solid phase epitaxial growth of  $\gamma$ -phase occurs at the bottom interface.

Annealing of this sample at 900 °C for 60 minute, results in phase transformation of majority of deeper  $\gamma$ -Al<sub>2</sub>O<sub>3</sub> layer to  $\alpha$ -Al<sub>2</sub>O<sub>3</sub> phase. The HRTEM images and NBED patterns obtained from these layers show that there is no phase transformation at subsurface. The HRTEM images obtained from the annealed sample confirms the presence of twins at the subsurface region.



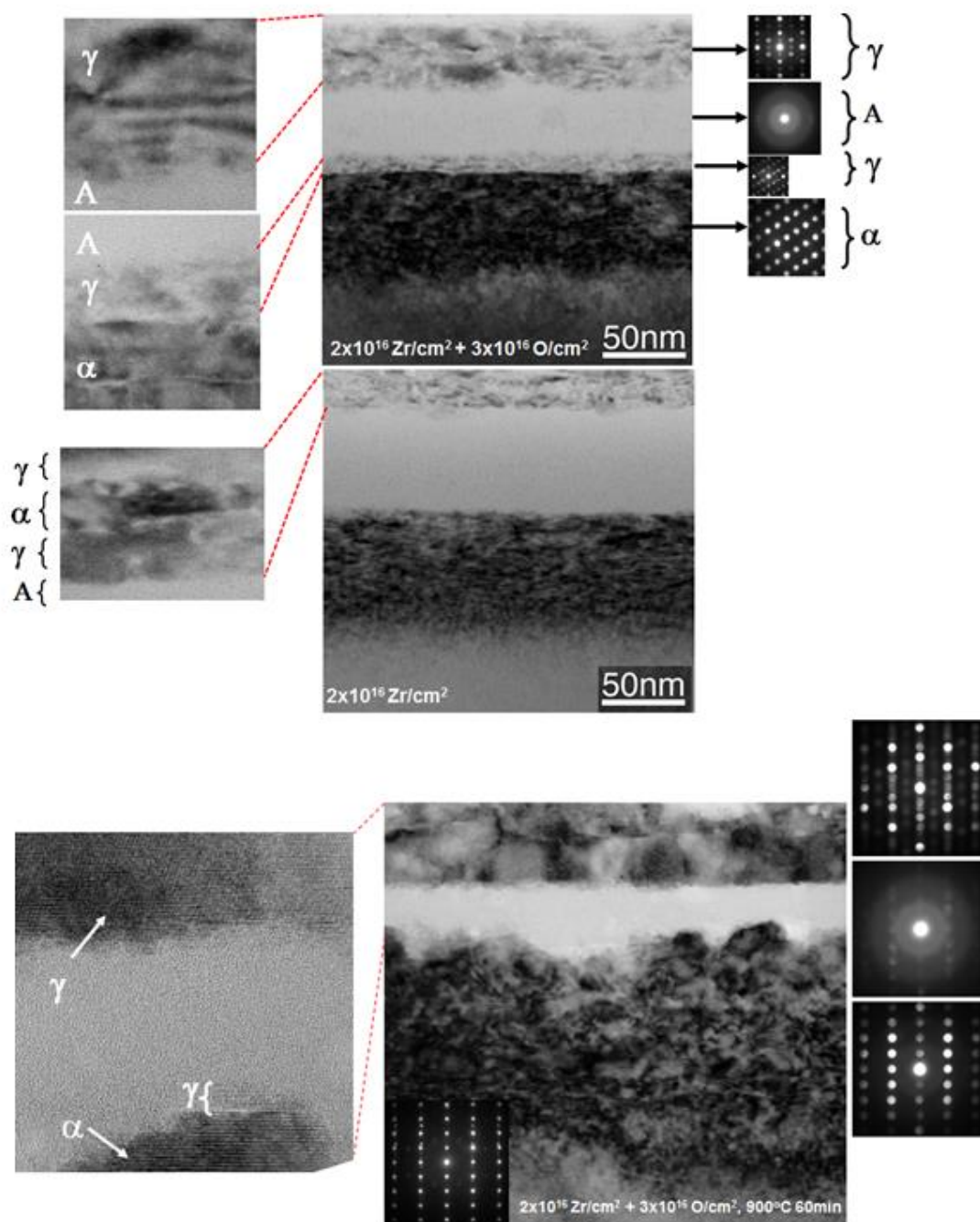


Figure 96 BF-TEM, HRTEM, and NBED patterns showing the effect of O irradiation and annealing on Zr-irradiated sample

## Chapter 5

### Conclusions and recommendation

#### 5.1 Conclusions

The structure of single crystal  $\alpha$ -Al<sub>2</sub>O<sub>3</sub> irradiated with 175 keV zirconium ions to fluences of  $2 \times 10^{15}$ - $4 \times 10^{16}$  Zr/cm<sup>2</sup> at room temperature, was investigated using Rutherford backscattering spectroscopy with ion channeling (RBS-C), scanning transmission electron microscopy (STEM), transmission electron microscopy (TEM), electron energy loss spectroscopy (EELS), Nano-beam electron diffraction (NBED) pattern, selected area electron diffraction (SAED) pattern, optical absorption (OA) and photoluminescence (PL) .

The threshold fluence for amorphization of single crystal  $\alpha$ -Al<sub>2</sub>O<sub>3</sub> (sapphire) due to ion irradiation with 175 keV zirconium ions has been determined to be about  $1.5 \times 10^{16}$  Zr<sup>+</sup>/cm<sup>2</sup> corresponding to ~ 40 dpa and ~2.5% peak Zr-concentration which is a lower damage energy than that reported for implantation with ions of similar mass and energy.

Buried amorphous layers were observed in samples irradiated with 175 keV Zr<sup>+</sup> to fluences of  $1.5 \times 10^{16}$  Zr<sup>+</sup>/cm<sup>2</sup> and higher, at room temperature. The buried amorphous regions for all the samples irradiated with 175 keV Zr<sup>+</sup> ions to fluences above the threshold fluence for amorphization were sandwiched between two highly-damaged crystalline regions. Nano-beam electron diffraction for the sample irradiated with 175 keV Zr<sup>+</sup> ions to a fluence of  $1.5 \times 10^{16}$  Zr<sup>+</sup>/cm<sup>2</sup> confirmed that both the near-surface

damaged layer and the deeper damaged layer remained crystalline, but the buried amorphous region is lacking in long-range atomic order.

The microstructure of single crystal  $\alpha$ -Al<sub>2</sub>O<sub>3</sub> irradiated with 175 keV Zr<sup>+</sup> ions to a fluence of  $4 \times 10^{16}$  Zr/cm<sup>2</sup> at room temperature was studied using RBS-C, EELS, and Z-contrast images obtained from an aberration-corrected STEM. The amorphous region contained Zr-clusters and exhibited short-range order corresponding to  $\gamma$ -Al<sub>2</sub>O<sub>3</sub>. The EELS measurements showed that the amorphous region is deficient in oxygen.

Irradiation of an  $\alpha$ -Al<sub>2</sub>O<sub>3</sub> sample with 175 keV Zr<sup>+</sup> to a fluence of  $2 \times 10^{16}$  Zr<sup>+</sup>/cm<sup>2</sup>, produced a crystalline region consists of an  $\alpha$ -Al<sub>2</sub>O<sub>3</sub> layer sandwiched with two  $\gamma$ -Al<sub>2</sub>O<sub>3</sub> layers on the near-surface damaged region. Post irradiation of this sample with 48 keV O<sup>+</sup> to a fluence of  $3 \times 10^{16}$  O<sup>+</sup>/cm<sup>2</sup> at room temperature transformed the stressed  $\alpha$ -Al<sub>2</sub>O<sub>3</sub> region completely to  $\gamma$ -Al<sub>2</sub>O<sub>3</sub>. Growth of the metastable polymorph  $\gamma$ -Al<sub>2</sub>O<sub>3</sub> was observed at the interface between amorphous and deeper-surface damaged crystalline regions, as a result of this oxygen ions irradiation.

Irradiation of 175 keV Zr<sup>+</sup> ions to a fluence of  $1.5 \times 10^{16}$  Zr/cm<sup>2</sup> into single crystal  $\alpha$ -Al<sub>2</sub>O<sub>3</sub> at room temperature produced a buried amorphous region extending from ~25 to ~65 nm from the (0001) surface. Subsequent irradiation of oxygen at room temperature induced an epitaxially recrystallization adjacent to the near-surface region. The thickness of this recrystallized region was approximately 20 nm. NBED pattern obtained from the recrystallized region confirmed the presence of  $\gamma$ -phase. The IBIER induced  $\gamma$ -phase, grew from the surface damage layer/amorphous interface and ceased growth at a position

where the implanted-Zr concentration is  $\geq 2$  at. %. No change in the amorphous/deeper damage region was detected after the oxygen implantation.

The presence of both F and F<sup>+</sup> centers were indicated by optical absorption (OA) and photoluminescence (PL) measurements for the samples irradiated with 175 keV Zr<sup>+</sup> ions to fluences of  $7.5 \times 10^{15}$ ,  $1.5 \times 10^{16}$  Zr<sup>+</sup>/cm<sup>2</sup> and  $2 \times 10^{16}$  Zr<sup>+</sup>/cm<sup>2</sup>. The OA spectra showed that the concentration of F and F<sup>+</sup> centers increases with increasing fluence. The OA results obtained from  $\alpha$ -Al<sub>2</sub>O<sub>3</sub> samples irradiated with 175 keV Zr<sup>+</sup> ions to fluences of  $7.5 \times 10^{15}$  Zr<sup>+</sup>/cm<sup>2</sup> and  $1.5 \times 10^{16}$  Zr<sup>+</sup>/cm<sup>2</sup> followed by irradiation with 55 keV O<sup>+</sup> ions to fluences of  $1.1 \times 10^{16}$  O<sup>+</sup>/cm<sup>2</sup> and  $2.3 \times 10^{16}$  O<sup>+</sup>/cm<sup>2</sup> respectively, showed decrease in both F and F<sup>+</sup> centers concentration resulting from oxygen irradiation. The F-type center concentrations for these samples were calculated using Smakula's equation.

The problems regarding kinetics of phase transformation during annealing of thin films of amorphous alumina was investigated. An amorphous film was created during irradiation with 175 keV Zr<sup>+</sup> ions to a fluence of  $2 \times 10^{16}$  Zr/cm<sup>2</sup> at room temperature. The samples were annealed in pure Ar ambient at three temperatures of 800, 900, and 1000 °C for different times. The results showed that samples undergo multiple processes of phase transformation, during irradiation and thermal annealing. These complicated processes make the kinetics study impossible or at least very difficult. Under irradiation part of the energy introduced by energetic ions is stored in form of biaxial stresses. Energetic ions implanted into the affected area expand the material near the surface and this also leads to biaxial compressive stresses. During irradiation-induced amorphization or phase

transformation, stress can arise from incompatibilities between the film and the substrate due to differences in thermal expansion, phase transformations with volume changes, densification of the film, and epitaxial effects. For instance, irradiation of  $\alpha\text{-Al}_2\text{O}_3$  with energetic ions undergoes positive volume due to introduction of a number of defects such as vacancies and interstitial atoms.

The effect of oxygen irradiation on pre-Zr-implanted samples before and after thermal annealing in pure Ar ambient at three temperatures of 800, 900, and 1000 °C for different times was studied using TEM, HRTEM, and RBS-C. The results showed that during thermal annealing the amorphous region adjacent to the deeper damaged region recrystallizes to  $\alpha\text{-Al}_2\text{O}_3$  whilst the near-surface region remained in form of  $\gamma\text{-Al}_2\text{O}_3$ . It was found that recrystallization at higher temperature is significant.

In addition, little if any redistribution in depth of Zr is observed at temperatures up to 1000 °C based on the RBS-C results obtained from the samples.

## 5.2 Recommendation

Phase transformation study in samples that irradiated with Zr ions at low temperatures is an interesting area that helps to understand more about microstructure of irradiated  $\alpha\text{-Al}_2\text{O}_3$ . Irradiation of  $\alpha\text{-Al}_2\text{O}_3$  with relatively low fluences at cryogenic temperatures produces an amorphous region all the way to the surface. Study of dpa and Zr% at the interface between amorphous and the highly damaged region can be compared with the samples that irradiated at room temperature. In addition to this work, recrystallization of the amorphous region using post irradiation with oxygen and/or annealing at Ar ambient can complete the fundamental studies of  $\alpha\text{-Al}_2\text{O}_3$  microstructures

produced by irradiation with Zirconium ions. Due to this fact that irradiation of  $\alpha\text{-Al}_2\text{O}_3$  with Zr at cryogenic temperature produces an amorphous region that is not sandwiched by two crystalline regions, the kinetic study seems to be less complicated compare with the samples irradiated at room temperature.

It is shown in this research that irradiation of  $\alpha\text{-Al}_2\text{O}_3$  with Zr to a fluence of  $4 \times 10^{16} \text{ Zr/cm}^2$  produces Zr clusters in the amorphous region. Thermal annealing of such samples could be quite interesting due to presence of these clusters. These clusters can act as barriers to decelerate the phase transformation or act as nucleation sites to increase the speed of phase transformation.

Regarding this fact that effect of sputtering during irradiation with high fluence is significant, study of sputtering effect in  $\alpha\text{-Al}_2\text{O}_3$  irradiated with high fluence Zr is recommended for future work.

**List of References**

- [1] C. McHargue, M. Lewis, B. Appleton, H. Naramoto, C. White, and J. Williams, "ALTERATION OF SURFACE PROPERTIES BY ION IMPLANTATION," *Science of hard materials*, p. 451, 1983.
- [2] C. R. A. Catlow, R. James, W. C. Mackrodt, and R. F. Stewart, "DEFECT ENERGETICS IN ALPHA-AL<sub>2</sub>O<sub>3</sub> AND RUTILE TiO<sub>2</sub>," *Physical Review B*, vol. 25, pp. 1006-1026, 1982 1982.
- [3] E. R. Dobrovinskaja, L. A. Lytvynov, and V. V. Pishchik, *Sapphire: Material, Manufacturing, Applications*: Springer London, Limited, 2009.
- [4] D. F. Moore, *Principles and applications of tribology*: Pergamon Press, 1975.
- [5] L. Dring and B. C. E. N. J., *Ceramic to Metal Seals for High-temperature Thermionic Converters*: Defense Technical Information Center, 1963.
- [6] A. M. Fox, *Optical Properties of Solids*: Oxford University Press, 2001.
- [7] I. Levin and D. Brandon, "Metastable alumina polymorphs: Crystal structures and transition sequences," *Journal of the American Ceramic Society*, vol. 81, pp. 1995-2012, Aug 1998.
- [8] M. L. Kronberg, "PLASTIC DEFORMATION OF SINGLE CRYSTALS OF SAPPHIRE - BASAL SLIP AND TWINNING," *Acta Metallurgica*, vol. 5, pp. 507-524, 1957 1957.
- [9] B. Holm, R. Ahuja, Y. Yourdshahyan, B. Johansson, and B. I. Lundqvist, "Elastic and optical properties of alpha- and kappa-Al<sub>2</sub>O<sub>3</sub>," *Physical Review B*, vol. 59, pp. 12777-12787, May 15 1999.
- [10] C. J. McHargue, P. S. Sklad, and C. W. White, "THE STRUCTURE OF ION-IMPLANTED CERAMICS," *Nuclear Instruments & Methods in Physics Research Section B-Beam Interactions with Materials and Atoms*, vol. 46, pp. 79-88, Feb 1990.
- [11] P. S. Santos, H. S. Santos, and S. P. Toledo, "Standard transition aluminas. Electron microscopy studies," *Materials Research*, vol. 3, pp. 104-114, 2000.
- [12] K. Jiang, *Al<sub>2</sub>O<sub>3</sub> thin films: relation between structural evolution, mechanical properties and stability*: Universitätsbibliothek, 2011.
- [13] P. S. Sklad, J. C. McCallum, C. J. McHargue, and C. W. White, "THE AMORPHOUS-TO-GAMMA TRANSFORMATION IN ION-IMPLANTED AL<sub>2</sub>O<sub>3</sub>," *Nuclear Instruments & Methods in Physics Research Section B-Beam Interactions with Materials and Atoms*, vol. 46, pp. 102-106, Feb 1990.
- [14] J. M. Schneider, W. D. Sproul, and A. Matthews, "Phase formation and mechanical properties of alumina coatings prepared at substrate temperatures less than 500 degrees C by ionized and conventional sputtering," *Surface & Coatings Technology*, vol. 94-5, pp. 179-183, Oct 1997.
- [15] J. M. Schneider, W. D. Sproul, and A. Matthews, "Reactive ionized magnetron sputtering of crystalline alumina coatings," *Surface & Coatings Technology*, vol. 98, pp. 1473-1476, Jan 1998.
- [16] O. Zywitzki and G. Hoetzsch, "Influence of coating parameters on the structure and properties of Al<sub>2</sub>O<sub>3</sub> layers reactively deposited by means of pulsed magnetron sputtering," *Surface & Coatings Technology*, vol. 86-7, pp. 640-647, Dec 15 1996.



- [17] O. Zywitzki and G. Hoetzs, "Correlation between structure and properties of reactively deposited Al<sub>2</sub>O<sub>3</sub> coatings by pulsed magnetron sputtering," *Surface & Coatings Technology*, vol. 94-5, pp. 303-308, Oct 1997.
- [18] S. Q. Cao, A. J. Pedraza, D. H. Lowndes, and L. F. Allard, "GAMMA-AL<sub>2</sub>O<sub>3</sub> FORMATION FROM PULSED-LASER IRRADIATED SAPPHIRE," *Applied Physics Letters*, vol. 65, pp. 2940-2942, Dec 5 1994.
- [19] R. S. Zhou and R. L. Snyder, "STRUCTURES AND TRANSFORMATION MECHANISMS OF THE ETA, GAMMA AND THETA TRANSITION ALUMINAS," *Acta Crystallographica Section B-Structural Science*, vol. 47, pp. 617-630, Oct 1 1991.
- [20] B. K. Gan and C. U. o. T. S. o. P. Sciences, *Crystallographic Transformations Involved in the Decomposition of Gibbsite to Alpha-alumina*: School of Physical Sciences, Curtin University of Technology, 1996.
- [21] C. Pecharroman, I. Sobrados, J. E. Iglesias, T. Gonzalez-Carreno, and J. Sanz, "Thermal evolution of transitional aluminas followed by NMR and IR spectroscopies," *Journal of Physical Chemistry B*, vol. 103, pp. 6160-6170, Jul 29 1999.
- [22] D. G. Brandon and W. D. Kaplan, *Microstructural characterization of materials*: John Wiley, 2008.
- [23] M. Halvarsson, J. E. Trancik, and S. Ruppi, "The microstructure of CVD kappa-Al<sub>2</sub>O<sub>3</sub> multilayers separated by thin intermediate TiN or TiC layers," *International Journal of Refractory Metals & Hard Materials*, vol. 24, pp. 32-38, 2006 2006.
- [24] G. Paglia, C. U. o. T. D. o. A. Physics, and C. U. o. T. D. o. A. Chemistry, *Determination of the Structure of Y-alumina Using Empirical and First Principle Calculations Combined with Supporting Experiments*: Curtin University of Technology., 2004.
- [25] L. Smrcok, V. Langer, and J. Krestan, "gamma-Alumina: a single-crystal X-ray diffraction study," *Acta Crystallographica Section C-Crystal Structure Communications*, vol. 62, pp. I83-I84, Sep 2006.
- [26] C. S. John, N. C. M. Alma, and G. R. Hays, "CHARACTERIZATION OF TRANSITIONAL ALUMINA BY SOLID-STATE MAGIC ANGLE SPINNING ALUMINUM NMR," *Applied Catalysis*, vol. 6, pp. 341-346, 1983 1983.
- [27] K. Shirasuka, H. Yanagida, and G. Yamaguchi, "COD ID: 1200015," *Crystallography Open Database*, 2012-10-11 1976.
- [28] M. H. Lee, C. F. Cheng, V. Heine, and J. Klinowski, "Distribution of tetrahedral and octahedral Al sites in gamma alumina," *Chemical Physics Letters*, vol. 265, pp. 673-676, Feb 14 1997.
- [29] K. Sohlberg, S. J. Pennycook, and S. T. Pantelides, "Hydrogen and the structure of the transition aluminas," *Journal of the American Chemical Society*, vol. 121, pp. 7493-7499, Aug 25 1999.
- [30] B. Ealet, M. H. Elyakhlofi, E. Gillet, and M. Ricci, "ELECTRONIC AND CRYSTALLOGRAPHIC STRUCTURE OF GAMMA-ALUMINA THIN-FILMS," *Thin Solid Films*, vol. 250, pp. 92-100, Oct 1 1994.

- [31] K. P. Sinha and A. P. B. Sinha, "VACANCY DISTRIBUTION AND BONDING IN SOME OXIDES OF SPINEL STRUCTURE," *Journal of Physical Chemistry*, vol. 61, pp. 758-761, 1957 1957.
- [32] E. J. W. Verwey, "The structure of the electrolytical oxide layer on aluminium," *Zeitschrift Fur Kristallographie*, vol. 91, pp. 317-320, Sep 1935.
- [33] V. Jayaram and C. G. Levi, "THE STRUCTURE OF DELTA-ALUMINA EVOLVED FROM THE MELT AND THE GAMMA- DELTA-TRANSFORMATION," *Acta Metallurgica*, vol. 37, pp. 569-578, Feb 1989.
- [34] B. C. Lippens and J. H. Deboer, "STUDY OF PHASE TRANSFORMATIONS DURING CALCINATION OF ALUMINUM HYDROXIDES BY SELECTED AREA ELECTRON DIFFRACTION," *Acta Crystallographica*, vol. 17, pp. 1312-&, 1964 1964.
- [35] R. Ahuja, J. M. Osorio-Guillen, J. S. de Almeida, B. Holm, W. Y. Ching, and B. Johansson, "Electronic and optical properties of gamma-Al<sub>2</sub>O<sub>3</sub> from ab initio theory," *Journal of Physics-Condensed Matter*, vol. 16, pp. 2891-2900, Apr 28 2004.
- [36] C. M. Fang, R. Metselaar, H. T. Hintzen, and G. de With, "Structure models for gamma-aluminum oxynitride from ab initio calculations," *Journal of the American Ceramic Society*, vol. 84, pp. 2633-2637, Nov 2001.
- [37] G. W. Watson and D. J. Willock, "The enumeration of structures for gamma-alumina based on a defective spinel structure," *Chemical Communications*, pp. 1076-1077, Jun 21 2001.
- [38] C. Wolverton and K. C. Hass, "Phase stability and structure of spinel-based transition aluminas," *Physical Review B*, vol. 63, Jan 1 2001.
- [39] I. V. Markov, *Crystal Growth for Beginners: Fundamentals of Nucleation, Crystal Growth and Epitaxy*: World Scientific, 2003.
- [40] M. J. Aziz, *THE MECHANISM OF SOLID-PHASE EPITAXY* vol. 222, 1992.
- [41] W. Zhou, D. K. Sood, R. G. Elliman, and M. C. Ridgway, "ION-BEAM-INDUCED EPITAXIAL CRYSTALLIZATION OF SAPPHIRE," *Nuclear Instruments & Methods in Physics Research Section B-Beam Interactions with Materials and Atoms*, vol. 80-1, pp. 1104-1108, Jun 1993.
- [42] N. Yu, P. C. McIntyre, M. Nastasi, and K. E. Sickafus, "High-quality epitaxial growth of gamma-alumina films on alpha-alumina sapphire induced by ion-beam bombardment," *Physical Review B*, vol. 52, pp. 17518-17522, Dec 15 1995.
- [43] N. Yu and M. Nastasi, "Ion beam induced epitaxial recrystallization of alumina thin films deposited on sapphire," *Nuclear Instruments & Methods in Physics Research Section B-Beam Interactions with Materials and Atoms*, vol. 106, pp. 579-582, Dec 1995.
- [44] J. J. De Yoreo and P. G. Vekilov, "Principles of crystal nucleation and growth," in *Biomineralization*. vol. 54, P. M. Dove, J. J. DeYoreo, and S. Weiner, Eds., ed, 2003, pp. 57-93.
- [45] J. Schmelzer, *Nucleation Theory and Applications*: Wiley, 2005.

- [46] J. M. Andersson, E. Wallin, U. Helmersson, U. Kreissig, and E. P. Munger, "Phase control of Al<sub>2</sub>O<sub>3</sub> thin films grown at low temperatures," *Thin Solid Films*, vol. 513, pp. 57-59, Aug 14 2006.
- [47] S. Ansell, S. Krishnan, J. K. R. Weber, J. J. Felten, P. C. Nordine, M. A. Beno, D. L. Price, and M. L. Saboungi, "Structure of liquid aluminum oxide," *Physical Review Letters*, vol. 78, pp. 464-466, Jan 20 1997.
- [48] Y. Waseda, K. Sugiyama, and J. M. Toguri, "DIRECT DETERMINATION OF THE LOCAL-STRUCTURE IN MOLTEN ALUMINA BY HIGH-TEMPERATURE X-RAY-DIFFRACTION," *Zeitschrift Fur Naturforschung Section a-a Journal of Physical Sciences*, vol. 50, pp. 770-774, Aug 1995.
- [49] S. K. Lee, S. B. Lee, S. Y. Park, Y. S. Yi, and C. W. Ahn, "Structure of Amorphous Aluminum Oxide," *Physical Review Letters*, vol. 103, Aug 28 2009.
- [50] B. T. Poe, P. F. McMillan, B. Cote, D. Massiot, and J. P. Coutures, "SiO<sub>2</sub>-Al<sub>2</sub>O<sub>3</sub> LIQUIDS - INSITU STUDY BY HIGH-TEMPERATURE AL-27 NMR-SPECTROSCOPY AND MOLECULAR-DYNAMICS SIMULATION," *Journal of Physical Chemistry*, vol. 96, pp. 8220-8224, Oct 1992.
- [51] S. K. Lee, S. B. Lee, S. Y. Park, Y. S. Yi, and C. W. Ahn, "Structure of Amorphous Aluminum Oxide," *Physical Review Letters*, vol. 103, p. 095501, 08/24/ 2009.
- [52] H. Uchi, T. Kanno, and R. S. Alwitt, "Structural features of crystalline anodic alumina films," *Journal of the Electrochemical Society*, vol. 148, pp. B17-B23, Jan 2001.
- [53] L. P. H. Jeurgens, W. G. Sloof, F. D. Tichelaar, and E. J. Mittemeijer, "Thermodynamic stability of amorphous oxide films on metals: Application to aluminum oxide films on aluminum substrates," *Physical Review B*, vol. 62, pp. 4707-4719, Aug 15 2000.
- [54] D. K. Avasthi and G. K. Mehta, *Swift Heavy Ions for Materials Engineering and Nanostructuring*: Springer London, Limited, 2011.
- [55] R. Chattopadhyay, *Advanced Thermally Assisted Surface Engineering Processes*: Springer, 2004.
- [56] C. A. Harper, *Handbook of ceramics, glasses, and diamonds*: McGraw-Hill, 2001.
- [57] J. F. Ziegler, J. P. Biersack, and M. D. Ziegler, *SRIM, the Stopping and Range of Ions in Matter*: SRIM Company, 2008.
- [58] S. X. Wang, L. M. Wang, and R. C. Ewing, "Irradiation-induced amorphization: Effects of temperature, ion mass, cascade size, and dose rate," *Physical Review B*, vol. 63, Jan 1 2001.
- [59] R. M. Drosd, *A Model of the Recrystallization Mechanism of Amorphous Silicon Layers Created by Ion Implantation*: University of California, Berkeley, 1979.
- [60] E. D. Specht, D. A. Walko, and S. J. Zinkle, "AMORPHIZATION OF AL<sub>2</sub>O<sub>3</sub> BY ION-INDUCED DENSITY REDUCTION," *Nuclear Instruments & Methods in Physics Research Section B-Beam Interactions with Materials and Atoms*, vol. 84, pp. 323-330, Feb 1994.
- [61] L. M. Wang, S. X. Wang, R. C. Ewing, A. Meldrum, R. C. Birtcher, P. N. Provencio, W. J. Weber, and H. Matzke, "Irradiation-induced nanostructures,"

- Materials Science and Engineering a-Structural Materials Properties Microstructure and Processing*, vol. 286, pp. 72-80, Jun 30 2000.
- [62] M. R. Benam, H. A. R. Aliabad, and S. M. Hosseini, "Effect of substituted IIIB transition metals on the energy gap of  $\alpha$ - $\text{Al}_2\text{O}_3$  by first-principle calculations," *Physica Status Solidi a-Applications and Materials Science*, vol. 203, pp. 2223-2228, Jul 2006.
  - [63] G. W. Brindley, "THE REACTION SERIES, GIBBSITE- CHI ALUMINA- KAPPA ALUMINA- CORUNDUM 2," *American Mineralogist*, vol. 46, pp. 1187-1190, 1961 1961.
  - [64] G. W. Brindley and K. Hunter, "THE THERMAL REACTIONS OF NACRITE AND THE FORMATION OF METAKAOLIN, GAMMA-ALUMINA, AND MULLITE," *American Mineralogist*, vol. 40, pp. 775-775, 1955 1955.
  - [65] G. W. Brindley and M. Nakahira, "EVIDENCE FOR A VARIABLE LONG-RANGE ORDER IN NEARLY ANHYDROUS GAMMA ALUMINA," *Nature*, vol. 183, pp. 1620-1620, 1959 1959.
  - [66] R. H. R. Castro, S. V. Ushakov, L. Gengembre, D. Gouvea, and A. Navrotsky, "Surface energy and thermodynamic stability of gamma-alumina: Effect of dopants and water," *Chemistry of Materials*, vol. 18, pp. 1867-1872, Apr 4 2006.
  - [67] P. L. Chang, F. S. Yen, K. C. Cheng, and H. L. Wen, "Examinations on the critical and primary crystallite sizes during theta- to alpha-phase transformation of ultrafine alumina powders," *Nano Letters*, vol. 1, pp. 253-261, May 2001.
  - [68] A. Duevel, E. Romanova, M. Sharifi, D. Freude, M. Wark, P. Heitjans, and M. Wilkening, "Mechanically Induced Phase Transformation of gamma- $\text{Al}_2\text{O}_3$  into alpha- $\text{Al}_2\text{O}_3$ . Access to Structurally Disordered gamma- $\text{Al}_2\text{O}_3$  with a Controllable Amount of Pentacoordinated Al Sites," *Journal of Physical Chemistry C*, vol. 115, pp. 22770-22780, Nov 24 2011.
  - [69] S. M. Hosseini, H. A. R. Aliabad, and A. Kompany, "First-principles study of the optical properties of pure alpha- $\text{Al}_2\text{O}_3$  and La aluminates," *European Physical Journal B*, vol. 43, pp. 439-444, Feb 2005.
  - [70] L. Ji, J. Lin, and H. C. Zeng, "Thermal processes of volatile  $\text{RuO}_2$  in nanocrystalline  $\text{Al}_2\text{O}_3$  matrixes involving gamma  $\rightarrow$  alpha phase transformation," *Chemistry of Materials*, vol. 13, pp. 2403-2412, Jul 2001.
  - [71] A. K. Khattak, M. Afzal, M. Saleem, G. Yasmeen, and R. Ahmad, "Surface modification of alumina by metal doping," *Colloids and Surfaces a-Physicochemical and Engineering Aspects*, vol. 162, pp. 99-106, Mar 15 2000.
  - [72] C. P. Khattak, S. Digregorio, F. Schmid, and J. Lagowski, "ION-IMPLANTATION AND GROWTH OF 3 IN DIAMETER HEM-GAAS," *Journal of the Electrochemical Society*, vol. 134, pp. C232-C232, Apr 1987.
  - [73] C. P. Khattak and F. Schmid, "GROWTH OF NEAR-NET-SHAPED SAPPHIRE DOMES USING THE HEAT-EXCHANGER METHOD," *Materials Letters*, vol. 7, pp. 318-321, Jan 1989.
  - [74] C. P. Khattak and F. Schmid, "Growth of the world's largest sapphire crystals," *Journal of Crystal Growth*, vol. 225, pp. 572-579, May 2001.

- [75] E. E. Kis, G. A. Lomic, G. C. Boskovic, and R. P. Marinkovic-Neducin, "Accelerated polymorphic transformations of alumina," *Reaction Kinetics and Catalysis Letters*, vol. 63, pp. 323-328, Mar 1998.
- [76] E. Kiss, S. Ratkovic, D. Vujicic, and G. Boskovic, "Accelerated polymorphous transformations of alumina induced by copper ions impede spinel formation," *Indian Journal of Chemistry Section a-Inorganic Bio-Inorganic Physical Theoretical & Analytical Chemistry*, vol. 51, pp. 1669-1676, Dec 2012.
- [77] K. Kosuge and A. Ogata, "Effect of SiO<sub>2</sub> addition on thermal stability of mesoporous gamma-alumina composed of nanocrystallites," *Microporous and Mesoporous Materials*, vol. 135, pp. 60-66, Nov 2010.
- [78] K. N. P. Kumar, J. Tranto, B. N. Nair, J. Kumar, J. W. Hoj, and J. E. Engell, "EFFECT OF SINTERING ATMOSPHERE ON THE PORE-STRUCTURE STABILITY OF CERIUM-DOPED NANOSTRUCTURED ALUMINA," *Materials Research Bulletin*, vol. 29, pp. 551-558, May 1994.
- [79] J. H. Kwak, J. Hu, A. Lukaski, D. H. Kim, J. Szanyi, and C. H. F. Peden, "Role of pentacoordinated Al<sup>3+</sup> ions in the high temperature phase transformation of gamma-Al<sub>2</sub>O<sub>3</sub>," *Journal of Physical Chemistry C*, vol. 112, pp. 9486-9492, Jun 26 2008.
- [80] J. H. Kwak, C. H. F. Peden, and J. Szanyi, "Using a Surface-Sensitive Chemical Probe and a Bulk Structure Technique to Monitor the gamma- to theta-Al<sub>2</sub>O<sub>3</sub> Phase Transformation," *Journal of Physical Chemistry C*, vol. 115, pp. 12575-12579, Jun 30 2011.
- [81] C. Legros, C. Carry, S. Lartigue-Korinek, and P. Bowen, "Phase transformation and densification of nanostructured alumina. Effect of seeding and doping," in *Diffusion in Materials: Dimat 2004, Pts 1 and 2*. vol. 237-240, M. Danielewski, R. Filipek, R. Kozubs, W. Kucza, P. Zieba, and Z. Zurek, Eds., ed, 2005, pp. 665-670.
- [82] C. Legros, F. Herbst, C. Carry, P. Bowen, and Ttp, "Effect of Ti-doping on the sintering behaviour of transition alumina," in *Euro Ceramics VII, Pt 1-3*. vol. 206-2, ed, 2002, pp. 357-360.
- [83] C. Legros, F. Herbst, S. Lartigue-Korinek, C. Carry, and P. Bowen, "Sintering of nanostructured alumina : influence of various parameters," *Revue De Metallurgie-Cahiers D Informations Techniques*, vol. 99, pp. 1073-1080, Dec 2002.
- [84] I. Levin, L. A. Bendersky, D. G. Brandon, and M. Ruhle, "Cubic to monoclinic phase transformations in alumina," *Acta Materialia*, vol. 45, pp. 3659-3669, Sep 1997.
- [85] J. C. McCallum, C. W. White, P. S. Sklad, and C. J. McHargue, "ANNEALING ENVIRONMENT EFFECTS IN SOLID-PHASE EPITAXIAL REGROWTH OF FE-IMPLANTED AL<sub>2</sub>O<sub>3</sub>," *Nuclear Instruments & Methods in Physics Research Section B-Beam Interactions with Materials and Atoms*, vol. 46, pp. 137-143, Feb 1990.
- [86] C. J. McHargue, *MECHANICAL-PROPERTIES OF DIAMOND AND DIAMOND-LIKE FILMS* vol. 73, 1991.

- [87] C. J. McHargue, *INDENTATION TESTING OF THIN-FILMS AND HARD MATERIALS* vol. 266, 1991.
- [88] C. J. McHargue, G. C. Farlow, M. B. Lewis, and J. M. Williams, "IMPLANTATION OF GASES INTO SAPPHIRE," *Nuclear Instruments & Methods in Physics Research Section B-Beam Interactions with Materials and Atoms*, vol. 19-2, pp. 809-812, Feb 1987.
- [89] C. J. McHargue, G. C. Farlow, P. S. Sklad, C. W. White, A. Perez, N. Kornilios, and G. Marest, "IRON-ION IMPLANTATION EFFECTS IN SAPPHIRE," *Nuclear Instruments & Methods in Physics Research Section B-Beam Interactions with Materials and Atoms*, vol. 19-2, pp. 813-821, Feb 1987.
- [90] C. J. McHargue, D. L. Joslin, J. E. Pawel, L. Romana, and C. W. White, "DESIGN OF METAL SAPPHIRE INTERFACES FOR ENHANCED ADHESION," *Surface & Coatings Technology*, vol. 65, pp. 198-202, Jul 1994.
- [91] C. J. McHargue, D. L. Joslin, and C. W. White, "ION-BEAM MIXING IN INSULATOR SUBSTRATES," *Nuclear Instruments & Methods in Physics Research Section B-Beam Interactions with Materials and Atoms*, vol. 91, pp. 549-557, Jun 1994.
- [92] C. J. McHargue, D. L. Joslin, J. M. Williams, and M. E. Ohern, *SURFACE MODIFICATION OF SAPPHIRE FOR ENHANCED INFRARED WINDOW PERFORMANCE* vol. 17, 1994.
- [93] C. J. McHargue, A. Perez, and J. C. McCallum, "THE CHEMICAL-STATE OF IRON IONS IMPLANTED INTO SILICON-CARBIDE," *Nuclear Instruments & Methods in Physics Research Section B-Beam Interactions with Materials and Atoms*, vol. 59, pp. 1362-1365, Jul 1991.
- [94] C. J. McHargue, P. S. Sklad, J. C. McCallum, C. W. White, A. Perez, E. Abonneau, and G. Marest, "THE RESIDUAL CHARGE STATE OF TIN IMPLANTED INTO SAPPHIRE," *Nuclear Instruments & Methods in Physics Research Section B-Beam Interactions with Materials and Atoms*, vol. 46, pp. 74-78, Feb 1990.
- [95] C. J. McHargue, P. S. Sklad, J. C. McCallum, C. W. White, A. Perez, and G. Marest, "THE STRUCTURE OF  $Al_2O_3$  IMPLANTED WITH IRON AT 77 K," *Nuclear Instruments & Methods in Physics Research Section B-Beam Interactions with Materials and Atoms*, vol. 46, pp. 144-148, Feb 1990.
- [96] C. J. McHargue and J. M. Williams, "ION-IMPLANTATION EFFECTS IN SILICON-CARBIDE," *Nuclear Instruments & Methods in Physics Research Section B-Beam Interactions with Materials and Atoms*, vol. 80-1, pp. 889-894, Jun 1993.
- [97] O. Mekasuwandumrong, P. Praserttham, M. Inoue, V. Pavarajarn, and W. Tanakulrungsank, "Phase transformation behavior of nanocrystalline chi-alumina powder obtained by thermal decomposition of AIP in inert organic solvent," *Journal of Materials Science*, vol. 39, pp. 2417-2421, Apr 1 2004.
- [98] O. Mekasuwandumrong, P. Tantichuwet, C. Chaisuk, and P. Praserttham, "Impact of concentration and Si doping on the properties and phase

- transformation behavior of nanocrystalline alumina prepared via solvothermal synthesis," *Materials Chemistry and Physics*, vol. 107, pp. 208-214, Feb 15 2008.
- [99] K. J. Morrissey, K. K. Czanderna, C. B. Carter, and R. P. Merrill, "GROWTH OF ALPHA-AL<sub>2</sub>O<sub>3</sub> WITHIN A TRANSITION ALUMINA MATRIX," *Journal of the American Ceramic Society*, vol. 67, pp. C88-C90, 1984 1984.
  - [100] K. Okada, A. Hattori, Y. Kameshima, and A. Yasumori, "Concentration effect of Cs<sup>+</sup> additive on the gamma-Al<sub>2</sub>O<sub>3</sub>-to-alpha-Al<sub>2</sub>O<sub>3</sub> phase transition," *Materials Letters*, vol. 42, pp. 175-178, Jan 2000.
  - [101] K. Okada, A. Hattori, Y. Kameshima, A. Yasumori, and R. N. Das, "Effect of monovalent cation additives on the gamma-Al<sub>2</sub>O<sub>3</sub>-to-alpha-Al<sub>2</sub>O<sub>3</sub> phase transition," *Journal of the American Ceramic Society*, vol. 83, pp. 1233-1236, May 2000.
  - [102] K. Okada, A. Hattori, T. Taniguchi, A. Nukui, and R. N. Das, "Effect of divalent cation additives on the gamma-Al<sub>2</sub>O<sub>3</sub>-to-alpha-Al<sub>2</sub>O<sub>3</sub> phase transition," *Journal of the American Ceramic Society*, vol. 83, pp. 928-932, Apr 2000.
  - [103] M. Ozawa and M. Kimura, "EFFECT OF CERIUM ADDITION ON THE THERMAL-STABILITY OF GAMMA-ALUMINA SUPPORT," *Journal of Materials Science Letters*, vol. 9, pp. 291-293, Mar 1990.
  - [104] M. Ozawa, M. Kimura, and A. Isogai, "THERMAL-STABILITY AND CHARACTERIZATION OF GAMMA-AL<sub>2</sub>O<sub>3</sub> MODIFIED WITH RARE-EARTHS," *Journal of the Less-Common Metals*, vol. 162, pp. 297-308, Sep 1990.
  - [105] M. Ozawa and Y. Nishio, "Thermal stabilization of gamma-alumina with modification of lanthanum through homogeneous precipitation," *Journal of Alloys and Compounds*, vol. 374, pp. 397-400, Jul 14 2004.
  - [106] M. Ozawa and S. Suzuki, "ESR OBSERVATION OF MN<sup>2+</sup> IMPREGNATED ON LA-MODIFIED ALUMINA SURFACE," *Journal of Materials Science Letters*, vol. 13, pp. 435-437, Mar 15 1994.
  - [107] M. Ozawa, S. Suzuki, C. K. Loong, J. W. Richardson, and R. R. Thomas, "Structural phase transitions and lean NO removal activity of copper-modified alumina," *Applied Surface Science*, vol. 121, pp. 441-444, Nov 1997.
  - [108] G. Paglia, C. E. Buckley, A. L. Rohl, B. A. Hunter, R. D. Hart, J. V. Hanna, and L. T. Byrne, "Tetragonal structure model for boehmite-derived gamma-alumina," *Physical Review B*, vol. 68, Oct 1 2003.
  - [109] P. Palmero and M. Lombardi, "Sintering of a nano-crystalline metastable alumina," *Journal of Thermal Analysis and Calorimetry*, vol. 97, pp. 191-196, Jul 2009.
  - [110] P. Palmero, M. Lombardi, L. Montanaro, M. Azar, J. Chevalier, V. Garnier, and G. Fantozzi, "Effect of Heating Rate on Phase and Microstructural Evolution During Pressureless Sintering of a Nanostructured Transition Alumina," *International Journal of Applied Ceramic Technology*, vol. 6, pp. 420-430, 2009 2009.
  - [111] D. W. Schaefer, R. A. Shelleman, K. D. Keefer, and J. E. Martin, "EQUILIBRIUM STRUCTURE AND RIGIDITY OF ALUMINA POLYMERS," *Physica A*, vol. 140, pp. 105-113, Dec 1986.

- [112] R. A. Shelleman and G. L. Messing, "LIQUID-PHASE-ASSISTED TRANSFORMATION OF SEEDED GAMMA-ALUMINA," *Journal of the American Ceramic Society*, vol. 71, pp. 317-322, May 1988.
- [113] R. A. Shelleman, G. L. Messing, and M. Kumagai, "ALPHA-ALUMINA TRANSFORMATION IN SEEDED BOEHMITE GELS," *Journal of Non-Crystalline Solids*, vol. 82, pp. 277-285, Jun 1986.
- [114] L. Shen, C. Hu, Y. Sakka, and Q. Huang, "Study of phase transformation behaviour of alumina through precipitation method," *Journal of Physics D-Applied Physics*, vol. 45, May 30 2012.
- [115] K. Sohlberg, S. J. Pennycook, and S. T. Pantelides, "The bulk and surface structure of gamma-alumina," *Chemical Engineering Communications*, vol. 181, pp. 107-135, 2000 2000.
- [116] D. H. Trinh, K. Back, G. Pozina, H. Blomqvist, T. Selinder, M. Collin, I. Reineck, L. Hultman, and H. Hogberg, "Phase transformation in kappa- and gamma-Al<sub>2</sub>O<sub>3</sub> coatings on cutting tool inserts," *Surface & Coatings Technology*, vol. 203, pp. 1682-1688, Mar 15 2009.
- [117] H. L. Wen, Y. Y. Chen, F. S. Yen, and C. Y. Huang, "Size characterization of theta- and alpha-Al<sub>2</sub>O<sub>3</sub> crystallites during phase transformation," *Nanostructured Materials*, vol. 11, pp. 89-101, Feb 1999.
- [118] Q. Wen, D. R. Clarke, N. Yu, and M. Nastasi, "EPITAXIAL REGROWTH OF RUBY ON SAPPHIRE FOR AN INTEGRATED THIN-FILM STRESS SENSOR," *Applied Physics Letters*, vol. 66, pp. 293-295, Jan 16 1995.
- [119] Y. Q. Wu, Y. F. Zhang, G. Pezzotti, and J. K. Guo, "Influence of AlF<sub>3</sub> and ZnF<sub>2</sub> on the phase transformation of gamma to alpha alumina," *Materials Letters*, vol. 52, pp. 366-369, Feb 2002.
- [120] J. R. Wynnyckyj and C. G. Morris, "A SHEAR-TYPE ALLOTROPIC TRANSFORMATION IN ALUMINA," *Metallurgical Transactions B-Process Metallurgy*, vol. 16, pp. 345-353, Jun 1985.
- [121] Q. Xu, K. C. Kharas, B. J. Croley, and A. K. Datye, "The Contribution of Alumina Phase Transformations to the Sintering of Pd Automotive Catalysts," *Topics in Catalysis*, vol. 55, pp. 78-83, Mar 2012.
- [122] R.-J. Yang, P.-C. Yu, C.-C. Chen, and F.-S. Yen, "Growth Thermodynamics of Nanoscaled alpha-Alumina Crystallites," *Crystal Growth & Design*, vol. 9, pp. 1692-1697, Apr 2009.
- [123] F. S. Yen, J. L. Chang, and P. C. Yu, "Relationships between DTA and DIL characteristics of nanosized alumina powders during theta- to alpha-phase transformation," *Journal of Crystal Growth*, vol. 246, pp. 90-98, Dec 2002.
- [124] F. S. Yen, P. L. Chang, P. C. Yu, and R. J. Yang, "Characterization on microstructure homogeneity of  $\theta$ -Al<sub>2</sub>O<sub>3</sub> powder systems during phase transformation," *Key Engineering Materials*, vol. 351, pp. 81-87, 2007.
- [125] F. S. Yen, H. S. Lo, H. L. Wen, and R. J. Yang, "theta- to alpha-phase transformation subsystem induced by alpha-Al<sub>2</sub>O<sub>3</sub>-seeding in boehmite-derived nano-sized alumina powders," *Journal of Crystal Growth*, vol. 249, pp. 283-293, Feb 2003.



- [126] D. D. Ragan, *The Effect of Cation Dopants on the Phase Transformations in Alumina*: University of California, Santa Barbara, 1999.
- [127] S. W. Wang, A. Y. Borisevich, S. N. Rashkeev, M. V. Glazoff, K. Sohlberg, S. J. Pennycook, and S. T. Pantelides, "Dopants adsorbed as single atoms prevent degradation of catalysts," *Nature Materials*, vol. 3, pp. 143-146, Mar 2004.
- [128] D. R. Clarke, "Epitaxial phase transformations in aluminum oxide," *Physica Status Solidi a-Applied Research*, vol. 166, pp. 183-196, Mar 16 1998.
- [129] C. W. White, L. A. Boatner, P. S. Sklad, C. J. McHargue, J. Rankin, G. C. Farlow, and M. J. Aziz, "ION-IMPLANTATION AND ANNEALING OF CRYSTALLINE OXIDES AND CERAMIC MATERIALS," *Nuclear Instruments & Methods in Physics Research Section B-Beam Interactions with Materials and Atoms*, vol. 32, pp. 11-22, May 1988.
- [130] D. D. Ragan, T. Mates, and D. R. Clarke, "Effect of yttrium and erbium ions on epitaxial phase transformations in alumina," *Journal of the American Ceramic Society*, vol. 86, pp. 541-545, Apr 2003.
- [131] N. Yu, T. W. Simpson, P. C. McIntyre, M. Nastasi, and I. V. Mitchell, "DOPING EFFECTS ON THE KINETICS OF SOLID-PHASE EPITAXIAL-GROWTH OF AMORPHOUS ALUMINA THIN-FILMS ON SAPPHIRE," *Applied Physics Letters*, vol. 67, pp. 924-926, Aug 14 1995.
- [132] C. W. White, *Ion Implantation and Annealing of Crystalline Oxides*: North-Holland, 1989.
- [133] J. C. McCallum, T. W. Simpson, and I. V. Mitchell, "TIME-RESOLVED REFLECTIVITY MEASUREMENTS OF THE AMORPHOUS-TO-GAMMA AND GAMMA-TO-ALPHA PHASE-TRANSITIONS IN ION-IMPLANTED AL<sub>2</sub>O<sub>3</sub>," *Nuclear Instruments & Methods in Physics Research Section B-Beam Interactions with Materials and Atoms*, vol. 91, pp. 60-62, Jun 1994.
- [134] T. W. Simpson, Q. Z. Wen, N. Yu, and D. R. Clarke, "Kinetics of the amorphous  $\rightarrow$ gamma  $\rightarrow$ alpha transformations in aluminum oxide: Effect of crystallographic orientation," *Journal of the American Ceramic Society*, vol. 81, pp. 61-66, Jan 1998.
- [135] L. E. Rehn, J. Greene, and F. A. Smidt, *Processing and Characterization of Materials Using Ion Beams*: Materials Research Society, 1989.
- [136] D. K. Sood and D. X. Cao, "ANNEALING BEHAVIOR OF ALPHA-AXIS SAPPHIRE AMORPHIZED BY HIGH-DOSE INDIUM ION-IMPLANTATION," *Nuclear Instruments & Methods in Physics Research Section B-Beam Interactions with Materials and Atoms*, vol. 46, pp. 194-201, Feb 1990.
- [137] *Radiation Effects in Solids: [Proceedings of the NATO Advanced Study Institute on Radiation Effects in Solids : Erice, Sicily, Italy, 17-29 July 2004]*, 2007.
- [138] F. Spaepen, "Interfaces and stresses in thin films," *Acta Materialia*, vol. 48, pp. 31-42, Jan 1 2000.
- [139] C. W. White, G. C. Farlow, C. J. McHargue, P. S. Sklad, M. P. Angelini, and B. R. Appleton, "FORMATION OF AMORPHOUS LAYERS IN AL<sub>2</sub>O<sub>3</sub> BY ION-IMPLANTATION," *Nuclear Instruments & Methods in Physics Research Section B-Beam Interactions with Materials and Atoms*, vol. 7-8, pp. 473-478, 1985 1985.

- [140] Y. Sina, C. J. McHargue, G. Duscher, and Y. Zhang, "The effect of zirconium implantation on the structure of sapphire," *Journal Name: Nuclear Instruments and Methods in Physics Research Section B: Beam Interactions with Materials and Atoms; Journal Volume: 286*, p. Medium: X; Size: 190, 2012.
- [141] Y. Sina, P. D. Townsend, C. J. McHargue, and E. J. da Costa Alves, "The defect structure of sapphire produced by implantation of Zr and Zr plus O: threshold fluence for amorphization and optical properties," in *Physica Status Solidi C: Current Topics in Solid State Physics, Vol 10, No 2*. vol. 10, C. Stanek, Ed., ed, 2013, pp. 202-207.
- [142] R. C. Ewing, A. Meldrum, L. M. Wang, and S. X. Wang, "Radiation-induced amorphization," *Transformation Processes in Minerals*, vol. 39, pp. 319-361, 2000 2000.
- [143] L. W. Hobbs, C. E. Jesurum, and B. Berger, "Rigidity constraints in amorphization of multiply-polytopic multiply-connected ceramic structures," in *Microstructural Processes in Irradiated Materials*. vol. 540, S. J. Zinkle, G. E. Lucas, R. C. Ewing, and J. S. Williams, Eds., ed, 1999, pp. 717-728.
- [144] W. J. Weber, L. M. Wang, N. Yu, and N. J. Hess, "Structure and properties of ion-beam-modified (6H) silicon carbide," *Materials Science and Engineering: A*, vol. 253, pp. 62-70, 9/30/ 1998.
- [145] H. Inui, H. Mori, and H. Fujita, "ELECTRON-IRRADIATION INDUCED CRYSTALLINE AMORPHOUS TRANSITION IN CERAMICS," *Acta Metallurgica*, vol. 37, pp. 1337-1342, May 1989.
- [146] H. Inui, H. Mori, and H. Fujita, "ELECTRON-IRRADIATION-INDUCED CRYSTALLINE TO AMORPHOUS TRANSITION IN ALPHA-SIC SINGLE-CRYSTALS," *Philosophical Magazine B-Physics of Condensed Matter Statistical Mechanics Electronic Optical and Magnetic Properties*, vol. 61, pp. 107-124, Jan 1990.
- [147] H. Inui, H. Mori, and T. Sakata, "HIGH-RESOLUTION ELECTRON-MICROSCOPY STUDY OF ELECTRON-IRRADIATION-INDUCED CRYSTALLINE-TO-AMORPHOUS TRANSITION IN ALPHA-SIC SINGLE-CRYSTALS," *Philosophical Magazine B-Physics of Condensed Matter Statistical Mechanics Electronic Optical and Magnetic Properties*, vol. 66, pp. 737-748, Dec 1992.
- [148] H. Inui, H. Mori, A. Suzuki, and H. Fujita, "ELECTRON-IRRADIATION-INDUCED CRYSTALLINE-TO-AMORPHOUS TRANSITION IN BETA-SIC SINGLE-CRYSTALS," *Philosophical Magazine B-Physics of Condensed Matter Statistical Mechanics Electronic Optical and Magnetic Properties*, vol. 65, pp. 1-14, Jan 1992.
- [149] P. J. Burnett and T. F. Page, "CRITERIA FOR MECHANICAL PROPERTY MODIFICATIONS OF CERAMIC SURFACES BY ION-IMPLANTATION," *Radiation Effects and Defects in Solids*, vol. 97, pp. 283-296, 1986 1986.
- [150] J. O. Orwa, J. L. Peng, J. C. McCallum, D. N. Jamieson, S. Rubanov, and S. Prawer, "Microstructure evolution in carbon-ion implanted sapphire," *Journal of Applied Physics*, vol. 107, Jan 15 2010.

- [151] E. M. Hunt and J. M. Hampikian, "Formation and thermal stability of aluminium nanoparticles synthesized via yttrium ion implantation into sapphire," *Journal of Materials Science*, vol. 32, pp. 3393-3399, Jul 1 1997.
- [152] Z. Werner, M. Pisarek, M. Barlak, R. Ratajczak, W. Starosta, J. Piekoszewski, W. Szymczyk, and R. Groetzschel, "Chemical effects in Zr- and Co-implanted sapphire," *Vacuum*, vol. 83, pp. S57-S60, May 1 2009.
- [153] C. J. McHargue, G. C. Farlow, G. M. Begun, J. M. Williams, C. W. White, B. R. Appleton, P. S. Sklad, and P. Angelini, "DAMAGE ACCUMULATION IN CERAMICS DURING ION-IMPLANTATION," *Nuclear Instruments & Methods in Physics Research Section B-Beam Interactions with Materials and Atoms*, vol. 16, pp. 212-220, Jun 1986.
- [154] C. J. McHargue, "Ion beam modification of ceramics," *Materials Science and Engineering a-Structural Materials Properties Microstructure and Processing*, vol. 253, pp. 94-105, Sep 30 1998.
- [155] C. J. McHargue, C. W. White, P. S. Sklad, M. E. Ohern, D. L. Joslin, and G. C. Farlow, *STRUCTURE-MECHANICAL PROPERTY RELATIONSHIPS IN ION-IMPLANTED CERAMICS* vol. 46-7, 1990.
- [156] C. J. McHargue, G. C. Farlow, P. S. Sklad, C. W. White, A. Perez, N. Kornilios, and G. Marest, "IRON-ION IMPLANTATION EFFECTS IN SAPPHIRE," *Nuclear Instruments & Methods in Physics Research Section B-Beam Interactions with Materials and Atoms*, vol. 19-20, pp. 813-821, Feb 1987.
- [157] C. J. McHargue, S. X. Ren, B. Lucas, T. Y. Tsui, L. F. Allard, and J. Hunn, *Hardness and elastic modulus of nanocomposites of iron in sapphire prepared by ion implantation and annealing*, 1996.
- [158] C. J. McHargue, S. X. Ren, P. S. Sklad, L. F. Allard, and J. Hunn, "Preparation of manometer-size dispersions of iron in sapphire by ion implantation and annealing," *Nuclear Instruments & Methods in Physics Research Section B-Beam Interactions with Materials and Atoms*, vol. 116, pp. 173-177, Aug 1996.
- [159] C. J. McHargue, P. S. Sklad, C. W. White, J. C. McCallum, A. Perez, and G. Marest, "MICROSTRUCTURAL AND CHEMICAL EFFECTS IN AL<sub>2</sub>O<sub>3</sub> IMPLANTED WITH IRON AT 77-K AND ANNEALED IN OXIDIZING OR REDUCING ATMOSPHERES," *Journal of Materials Research*, vol. 6, pp. 2160-2177, Oct 1991.
- [160] M. Ohkubo, T. Hioki, and J. Kawamoto, "MAGNETIC-PROPERTIES OF FE-IMPLANTED SAPPHIRE," *Journal of Applied Physics*, vol. 62, pp. 3069-3071, Oct 1 1987.
- [161] M. Ohkubo, T. Hioki, N. Suzuki, T. Ishiguro, and J. Kawamoto, "STRUCTURE AND MAGNETIC-PROPERTIES OF FE-IMPLANTED SAPPHIRE," *Nuclear Instruments & Methods in Physics Research Section B-Beam Interactions with Materials and Atoms*, vol. 39, pp. 675-679, Mar 1989.
- [162] G. C. Farlow, P. S. Sklad, C. W. White, and C. J. McHargue, "MICROSTRUCTURAL DEVELOPMENT IN THE NEAR-SURFACE REGION DURING THERMAL ANNEALING OF AL<sub>2</sub>O<sub>3</sub> IMPLANTED WITH

- CATIONIC IMPURITIES," *Journal of Materials Research*, vol. 5, pp. 1502-1519, Jul 1990.
- [163] C. J. McHargue, E. Alves, C. Marques, and L. C. Ononye, "Comparison of the damage in sapphire due to implantation of boron, nitrogen, and iron," *Journal of Nuclear Materials*, vol. 389, pp. 311-316, May 31 2009.
  - [164] C. J. McHargue, E. Alves, L. C. Ononye, and C. Marques, "Structure and optical properties of sapphire implanted with boron at room temperature and 1000 degrees C," *Nuclear Instruments & Methods in Physics Research Section B-Beam Interactions with Materials and Atoms*, vol. 250, pp. 81-84, Sep 2006.
  - [165] G. C. Farlow, C. J. McHargue, C. W. White, and B. R. Appleton, "ANNEALING STUDIES OF ALPHA-AL<sub>2</sub>O<sub>3</sub> IMPLANTED WITH BROMINE," *Radiation Effects and Defects in Solids*, vol. 97, pp. 257-264, 1986 1986.
  - [166] B. R. Appleton, H. Naramoto, C. W. White, O. W. Holland, C. J. McHargue, G. Farlow, J. Narayan, and J. M. Williams, "ION-IMPLANTATION, ION-BEAM MIXING, AND ANNEALING STUDIES OF METALS IN AL<sub>2</sub>O<sub>3</sub>, SIC AND SI<sub>3</sub>N<sub>4</sub>," *Nuclear Instruments & Methods in Physics Research Section B-Beam Interactions with Materials and Atoms*, vol. 1, pp. 167-175, 1984 1984.
  - [167] C. J. McHargue, G. C. Farlow, C. W. White, J. M. Williams, B. R. Appleton, and H. Naramoto, "THE AMORPHIZATION OF CERAMICS BY ION-BEAMS," *Materials Science and Engineering*, vol. 69, pp. 123-127, 1985 1985.
  - [168] H. Naramoto, C. W. White, J. M. Williams, C. J. McHargue, O. W. Holland, M. M. Abraham, and B. R. Appleton, "ION-IMPLANTATION AND THERMAL ANNEALING OF ALPHA-AL<sub>2</sub>O<sub>3</sub> SINGLE-CRYSTALS," *Journal of Applied Physics*, vol. 54, pp. 683-698, 1983 1983.
  - [169] E. Alves, R. C. da Silva, M. F. da Silva, and J. C. Soares, "Lattice location and annealing behaviour of Pt and W implanted sapphire," *Nuclear Instruments & Methods in Physics Research Section B-Beam Interactions with Materials and Atoms*, vol. 147, pp. 226-230, Jan 1999.
  - [170] C. Donnet, G. Marest, N. Moncoffre, and J. Tousset, "EFFECTS OF ANNEALING ENVIRONMENT ON SURFACE CHEMICAL-PHASES OF IRON-IMPLANTED SINTERED ALUMINA," *Nuclear Instruments & Methods in Physics Research Section B-Beam Interactions with Materials and Atoms*, vol. 59, pp. 1177-1182, Jul 1991.
  - [171] H. Abe, S. Yamamoto, and H. Naramoto, "Amorphization in aluminum oxide induced by ion irradiation," *Nuclear Instruments & Methods in Physics Research Section B-Beam Interactions with Materials and Atoms*, vol. 127, pp. 170-175, May 1997.
  - [172] C. Marques, E. Alves, C. McHargue, L. C. Ononye, T. Monteiro, J. Soares, and L. F. Allard, "Influence of annealing atmosphere on the behavior of titanium implanted sapphire," *Nuclear Instruments & Methods in Physics Research Section B-Beam Interactions with Materials and Atoms*, vol. 191, pp. 644-648, May 2002.
  - [173] E. Alves, C. Marques, R. C. da Silva, T. Monteiro, J. Soares, C. McHargue, L. C. Ononye, and L. F. Allard, "Structural and optical studies of Co and Ti implanted

- sapphire," *Nuclear Instruments & Methods in Physics Research Section B-Beam Interactions with Materials and Atoms*, vol. 207, pp. 55-62, May 2003.
- [174] A. P. Mouritz, D. K. Sood, D. H. Stjohn, M. V. Swain, and J. S. Williams, "ION-IMPLANTATION OF LOW MELTING-POINT METALS INTO SAPPHIRE," *Nuclear Instruments & Methods in Physics Research Section B-Beam Interactions with Materials and Atoms*, vol. 19-20, pp. 805-808, Feb 1987.
  - [175] T. Kobayashi and T. Terai, "Electrical property of high-fluence metal ion implanted sapphire and its thermal annealing effects," *Nuclear Instruments & Methods in Physics Research Section B-Beam Interactions with Materials and Atoms*, vol. 141, pp. 441-445, May 1998.
  - [176] T. Kobayashi, A. Nakanishi, K. Fukumura, and G. Langouche, "Fine iron particles formed in a sapphire crystal by the ion implantation technique," *Journal of Applied Physics*, vol. 83, pp. 4631-4641, May 1 1998.
  - [177] E. Alves, C. Marques, R. C. da Silva, T. Monteiro, and C. McHargue, "Ion beam processing of sapphire single crystals," *Surface & Coatings Technology*, vol. 203, pp. 2357-2362, Jun 15 2009.
  - [178] S. X. Ren, C. J. McHargue, L. F. Allard, Y. Chen, J. D. Hunn, B. N. Lucas, and R. K. Williams, "Microstructural characterization of iron implanted sapphire nanocomposites," in *Microstructure of Irradiated Materials*. vol. 373, I. M. Robertson, L. E. Rehn, S. J. Zinkle, and W. J. Phythian, Eds., ed, 1995, pp. 305-310.
  - [179] D. Ila, E. K. Williams, S. Sarkisov, D. B. Poker, and D. K. Hensley, "Change in the optical properties of sapphire induced by ion implantation," in *Atomistic Mechanisms in Beam Synthesis and Irradiation of Materials*. vol. 504, J. C. Barbour, S. Roorda, D. Ila, and M. Tsujioka, Eds., ed, 1998, pp. 381-385.
  - [180] A. Turos, H. Matzke, and P. Rabette, "THE THERMAL-BEHAVIOR OF PT-AL<sub>2</sub>O<sub>3</sub> CATALYSTS STUDIED WITH THE CHANNELING TECHNIQUE," *Physica Status Solidi a-Applied Research*, vol. 64, pp. 565-575, 1981 1981.
  - [181] C. J. McHargue, J. D. Hunn, D. L. Joslin, E. Alves, M. F. daSilva, and J. C. Soares, "Etching of amorphous Al<sub>2</sub>O<sub>3</sub> produced by ion implantation," *Nuclear Instruments & Methods in Physics Research Section B-Beam Interactions with Materials and Atoms*, vol. 127, pp. 596-598, May 1997.
  - [182] L. J. Romana, P. S. Sklad, C. W. White, J. C. McCallum, A. Choudhury, L. L. Horton, and C. J. McHargue, "FORMATION AND ANNEALING BEHAVIOR OF AN AMORPHOUS LAYER INDUCED BY TIN IMPLANTATION INTO SAPPHIRE," *Surface & Coatings Technology*, vol. 51, pp. 415-419, Apr 15 1992.
  - [183] C. J. McHargue and L. J. Romana, "Influence of tin ion implantation on the damage and annealing kinetics of sapphire," *Nuclear Instruments & Methods in Physics Research Section B-Beam Interactions with Materials and Atoms*, vol. 166, pp. 193-197, May 2000.
  - [184] L. Romana, P. Thevenard, S. Ramos, B. Canut, L. Gea, M. Brunel, L. L. Horton, and C. J. McHargue, "FORMATION OF SMALL METALLIC PRECIPITATES OF NIOBIUM IN ALPHA-AL<sub>2</sub>O<sub>3</sub> IMPLANTED WITH NIOBIUM IONS," *Surface & Coatings Technology*, vol. 51, pp. 410-414, Apr 15 1992.

- [185] E. Alves, C. Marques, G. Safran, and C. J. McHargue, "Temperature behavior of damage in sapphire implanted with light ions," *Nuclear Instruments & Methods in Physics Research Section B-Beam Interactions with Materials and Atoms*, vol. 267, pp. 1464-1467, May 1 2009.
- [186] I. D. Sharp, Q. Xu, D. O. Yi, C. W. Yuan, J. W. Beeman, K. M. Yu, J. W. Ager, III, D. C. Chrzan, and E. E. Haller, "Structural properties of Ge nanocrystals embedded in sapphire," *Journal of Applied Physics*, vol. 100, Dec 1 2006.
- [187] E. Alves, M. F. da Silva, J. G. Marques, J. C. Soares, and K. Freitag, "Chemical effects on the amorphization of sapphire," *Nuclear Instruments & Methods in Physics Research Section B-Beam Interactions with Materials and Atoms*, vol. 141, pp. 353-357, May 1998.
- [188] P. S. Sklad, J. D. McCallum, S. J. Pennycook, C. J. McHargue, C. W. White, and A. Perez, *MICROSTRUCTURAL CHARACTERIZATION OF ALPHA-AL<sub>2</sub>O<sub>3</sub> IMPLANTED WITH IRON* vol. 138, 1989.
- [189] P. S. Sklad, P. Angelini, and J. Sevely, "EXTENDED ELECTRON-ENERGY LOSS FINE-STRUCTURE ANALYSIS OF AMORPHOUS AL<sub>2</sub>O<sub>3</sub>," *Philosophical Magazine a-Physics of Condensed Matter Structure Defects and Mechanical Properties*, vol. 65, pp. 1445-1461, Jun 1992.
- [190] G. Effenberg, *Selected Systems from Al-B-C to B-Hf-W*: Springer, 2009.
- [191] D. A. Jerebtsov, G. G. Mikhailov, and S. V. Sverdina, "Phase diagram of the system: Al<sub>2</sub>O<sub>3</sub>-ZrO<sub>2</sub>," *Ceramics International*, vol. 26, pp. 821-823, 2000 2000.
- [192] H. M. Ondik, H. F. McMurdie, A. C. Society, and P. E. D. D. Center, *Phase diagrams for zirconium and zirconia systems*: American Ceramic Society, 1998.
- [193] S. J. Bull and T. F. Page, "THERMAL EFFECTS ON THE MICROSTRUCTURE AND MECHANICAL-PROPERTIES OF ION-IMPLANTED CERAMICS," *Journal of Materials Science*, vol. 26, pp. 3086-3106, Jun 1 1991.
- [194] R. Hellborg, H. J. Whitlow, and Y. Zhang, *Ion Beams in Nanoscience and Technology*: Springer Berlin Heidelberg, 2009.
- [195] C. J. McHargue, J. D. Hunn, E. Alves, M. F. da Silva, and J. C. Soares, "Influence of oxygen ion implantation on the damage and annealing kinetics of iron-implanted sapphire," *Nuclear Instruments & Methods in Physics Research Section B-Beam Interactions with Materials and Atoms*, vol. 166, pp. 188-192, May 2000.
- [196] P. S. Sklad, L. Romana, C. J. McHargue, C. W. White, and J. C. McCallum, "THE EFFECT OF POSTIMPLANTATION ANNEALING ON THE MICROSTRUCTURE OF AL<sub>2</sub>O<sub>3</sub> IMPLANTED WITH IRON AT - 185-DEGREES-C," *Nuclear Instruments & Methods in Physics Research Section B-Beam Interactions with Materials and Atoms*, vol. 59, pp. 1187-1194, Jul 1991.
- [197] X. Xiang, X. T. Zu, S. Zhu, L. M. Wang, V. Shutthanandan, P. Nachimuthu, and Y. Zhang, "Photoluminescence of SnO<sub>2</sub> nanoparticles embedded in Al<sub>2</sub>O<sub>3</sub>," *Journal of Physics D-Applied Physics*, vol. 41, Nov 21 2008.
- [198] S. I. Maydet and K. C. Russell, "PRECIPITATE STABILITY UNDER IRRADIATION - POINT-DEFECT EFFECTS," *Journal of Nuclear Materials*, vol. 64, pp. 101-114, 1977 1977.

- [199] J. A. Thornton and D. W. Hoffman, "STRESS-RELATED EFFECTS IN THIN-FILMS," *Thin Solid Films*, vol. 171, pp. 5-31, Apr 1 1989.
- [200] T. Hioki, A. Itoh, M. Ohkubo, S. Noda, H. Doi, J. Kawamoto, and O. Kamigaito, "MECHANICAL PROPERTY CHANGES IN SAPPHIRE BY NICKEL ION-IMPLANTATION AND THEIR DEPENDENCE ON IMPLANTATION TEMPERATURE," *Journal of Materials Science*, vol. 21, pp. 1321-1328, Apr 1986.
- [201] R. G. Elliman, S. T. Johnson, A. P. Pogany, and J. S. Williams, "ION-BEAM INDUCED EPITAXIAL CRYSTALLIZATION OF SILICON," *Nuclear Instruments & Methods in Physics Research Section B-Beam Interactions with Materials and Atoms*, vol. 7-8, pp. 310-315, 1985 1985.
- [202] R. G. Elliman, J. S. Williams, S. T. Johnson, and A. P. Pogany, "CHARACTERIZATION OF MEV NEON DAMAGE IN SILICON," *Nuclear Instruments & Methods in Physics Research Section B-Beam Interactions with Materials and Atoms*, vol. 15, pp. 439-442, Apr 1986.
- [203] J. S. Williams, M. C. Ridgway, R. G. Elliman, J. A. Davies, S. T. Johnson, and G. R. Palmer, "MEV ION-BEAM ANNEALING OF SEMICONDUCTOR STRUCTURES," *Nuclear Instruments & Methods in Physics Research Section B-Beam Interactions with Materials and Atoms*, vol. 55, pp. 602-606, Apr 1991.
- [204] L. C. Feldman and J. W. Mayer, *Fundamentals of surface and thin film analysis*: North-Holland, 1986.
- [205] S. J. Pennycook and P. P. D. Nellist, *Scanning Transmission Electron Microscopy: Imaging and Analysis*: Springer New York, 2011.
- [206] L. J. Allen, A. J. D'Alfonso, S. D. Findlay, J. M. LeBeau, N. R. Lugg, and S. Stemmer, "Elemental mapping in scanning transmission electron microscopy," in *Electron Microscopy and Analysis Group Conference 2009*. vol. 241, R. T. Baker, Ed., ed, 2010.
- [207] J. Ayache, L. Beaunier, J. Boumendil, G. Ehret, and D. Laub, *Sample Preparation Handbook for Transmission Electron Microscopy: Techniques*: Springer London, Limited, 2010.
- [208] J. Wiley and S. Inc, *Characterization of Materials*: John Wiley & Sons, Incorporated, 2012.
- [209] W. M. Mueller, *Energetics In Metallurgical Phenomena*: Gordon and Breach, 1965.
- [210] S. J. Zinkle and C. Kinoshita, "Defect production in ceramics," *Journal of Nuclear Materials*, vol. 251, pp. 200-217, Nov 1997.
- [211] R. Lizarraga, E. Holmstroem, S. C. Parker, and C. Arrouvel, "Structural characterization of amorphous alumina and its polymorphs from first-principles XPS and NMR calculations," *Physical Review B*, vol. 83, Mar 14 2011.
- [212] R. Brydson, "Multiple scattering theory applied to ELNES of interfaces," *Journal of Physics D-Applied Physics*, vol. 29, pp. 1699-1708, Jul 14 1996.
- [213] G. Carter and W. A. Grant, "Amorphisation of solids by ion implantation," *Nuclear Instruments and Methods in Physics Research*, vol. 199, pp. 17-35, 8/1/ 1982.

- [214] R. Smith, *Atomic and Ion Collisions in Solids and at Surfaces: Theory, Simulation and Applications*: Cambridge University Press, 2005.
- [215] Y. Sina, C. J. McHargue, G. Duscher, and Y. Zhang, "The effect of zirconium implantation on the structure of sapphire," *Nucl. Instrum. Methods Phys. Res. Sect. B-Beam Interact. Mater. Atoms*, vol. 286, pp. 190-195, Sep 1 2012.
- [216] P. W. Levy, "COLOR CENTERS AND RADIATION-INDUCED DEFECTS IN  $Al_2O_3$ ," *Physical Review*, vol. 123, pp. 1226-&, 1961 1961.
- [217] P. W. Levy and G. J. Dienes, "IRRADIATION INDUCED OPTICAL ABSORPTION IN  $Al_2O_3$ ," *Physical Review*, vol. 94, pp. 1409-1409, 1954 1954.
- [218] G. W. Arnold, G. B. Krefft, and C. B. Norris, "ATOMIC DISPLACEMENT AND IONIZATION EFFECTS ON OPTICAL-ABSORPTION AND STRUCTURAL-PROPERTIES OF ION-IMPLANTED  $Al_2O_3$ ," *Applied Physics Letters*, vol. 25, pp. 540-542, 1974 1974.
- [219] B. D. Evans and M. Stapelbroek, "OPTICAL-PROPERTIES OF THE  $F^+$  CENTER IN CRYSTALLINE  $Al_2O_3$ ," *Physical Review B*, vol. 18, pp. 7089-7098, 1978 1978.
- [220] G. J. Pogatshnik, Y. Chen, and B. D. Evans, "A MODEL OF LATTICE-DEFECTS IN SAPPHIRE," *Ieee Transactions on Nuclear Science*, vol. 34, pp. 1709-1712, Dec 1987.
- [221] Y. Chen, M. M. Abraham, and D. F. Pedraza, "RADIATION-DAMAGE IN  $Al_2O_3$  CRYSTALS IMPLANTED WITH 3.8 MEV  $Fe^{2+}$  IONS," *Nuclear Instruments & Methods in Physics Research Section B-Beam Interactions with Materials and Atoms*, vol. 59, pp. 1163-1166, Jul 1991.
- [222] M. L. Dalal, M. Rahmani, and P. D. Townsend, "UV ABSORPTION OF ION-IMPLANTED SAPPHIRE," *Nuclear Instruments & Methods in Physics Research Section B-Beam Interactions with Materials and Atoms*, vol. 32, pp. 61-65, May 1988.
- [223] A. G. Kozakiewicz, A. T. Davidson, and T. E. Derry, "VUV optical absorption in sapphire crystals following implantation with 100 keV  $O^+$ ,  $Al^+$  and  $Cr^+$  ions," *Nuclear Instruments & Methods in Physics Research Section B-Beam Interactions with Materials and Atoms*, vol. 191, pp. 582-585, May 2002.
- [224] C. Jardin, B. Canut, and S. M. M. Ramos, "The luminescence of sapphire subjected to the irradiation of energetic hydrogen and helium ions," *Journal of Physics D-Applied Physics*, vol. 29, pp. 2066-2070, Aug 14 1996.
- [225] P. D. Townsend, Kelly, J.C., *Colour Centres and Imperfections in Insulators and Semiconductors*. Chatto and Windus for Sussex University Press, 1973.
- [226] P. D. Townsend, "The study of radiation damager in sapphire and ruby by optical methods," PhD thesis, Reading, 1961.
- [227] A. Perez, "ION-IMPLANTATION EFFECTS IN CRYSTALLINE INORGANIC INSULATORS," *Nuclear Instruments & Methods in Physics Research Section B-Beam Interactions with Materials and Atoms*, vol. 1, pp. 621-627, 1984.
- [228] P. Agnew, "DISPLACEMENT DAMAGE EFFICIENCY IN SAPPHIRE," *Nuclear Instruments & Methods in Physics Research Section B-Beam Interactions with Materials and Atoms*, vol. 65, pp. 305-310, Mar 1992.



- [229] R. S. Averback, R. Benedek, and K. L. Merkle, "ION-IRRADIATION STUDIES OF THE DAMAGE FUNCTION OF COPPER AND SILVER," *Physical Review B*, vol. 18, pp. 4156-4171, 1978 1978.
- [230] G. P. Pells, "RADIATION-DAMAGE EFFECTS IN ALUMINA," *J. Am. Ceram. Soc.*, vol. 77, pp. 368-377, Feb 1994.

**Vita**

Younes Sina was born in 1965 in Mahabad, Iran. Younes Sina started his PhD in the Materials Science and Engineering program in 2009. Starting spring semester 2010 Younes joined Center for materials processing (CMP) working on fundamental studies in heavy ions irradiation in  $\alpha\text{-Al}_2\text{O}_3$  under direction of his advisor professor Carl J. McHargue.

Younes received his Chemical Engineering B.Sc. in 1989, and his Industrial Engineering M.Sc. with a focus on economic evaluation of nuclear power plants in 1996 both in Iran. Between 1989 and 2006, Younes worked as an academic member in a research institute.

Parallel to his study in UTK he taught physics courses in Pellissippi community college as an adjunct instructor for about three years.

During his Ph.D. program, Younes published three papers and presented two of them at international conferences. The first one “the effect of zirconium implantation on the structure of sapphire” that was presented for International conference on Radiation Effect in Insulators (REI-16) held in China received an award in recognition of an outstanding poster. The second paper “the defect structure of sapphire produced by implantation of Zr and Zr plus O: threshold fluence for amorphization and optical properties” was an invited article for International Conference on Defects in Insulating Material (ICDIM 2012) in Santa Fe, New Mexico. Younes’s recent works about phase transformation study of Zr-ion irradiation and phase transformation in sapphire with

collaboration of Kyushu Institute of Technology in Japan and ion beam laboratory in Portugal are submitted for publication.